DEPARTAMENTO DE ASTROFISICA

Universidad de La Laguna

Design of an integral field spectrograph for the European Solar Telescope

Memoria que presenta
Ariadna Z. Calcines Rosario
para optar al grado de
Doctora en Ciencias Físicas.

INSTITUTO Ð ASTROFISICA Ð CANARIAS
febrero de 2013

Examination date: March $5^{th}, 2013$.
Thesis supervisor :
Dr. D. Manuel Collados Vera

© **Ariadna Z. Calcines Rosario**, 2013
ISBN: xx-xxx-xxxx-x
Depósito legal: TF-xxxx/2013

A mis abuelos, con todo mi corazón.
To my grandfathers, with all my heart.

Summary

The Sun is one of the 400,000 millions of stars of the Milky Way. Because of its physical characteristics, it houses a planetary system, the Solar System. This condition seems to be attractive enough to justify its study, however, no doubt, there exist many other reasons.

It is the only star that can be spatially resolved, due to its proximity to the Earth. High spatial resolution is, therefore, an essential condition for solar telescopes. In addition, high spectral resolution provides information about the spectral lines and other physical properties encoded in the spectrum. Nevertheless, it does not provide a wide information about the magnetic field, which governs its activity, as well as the physical phenomena that take place in its different layers. This formation is obtained using polarimetry, from the Stokes parameters. The combination of these two important techniques, spectroscopy and polarimetry, applied simultaneously, offers a broad information about the Sun, facilitating the understanding of the phenomena that take place in it and the Physics that governs it. Due to the analogies of the Sun with the other stars, the results obtained from its study can be extrapolated to stellar physics. Thus, understanding the Sun helps us to understand the stellar evolution. On the other hand, it plays an important role in the Sun-Earth relation. These reasons justify the necessity and relevance of its study.

Despite being the nearest star, there still are nowadays many unknowns about the processes that take place within it, as well as the origin and evolution of the observed phenomena. It is important to understand the evolution of the magnetic field and its structures observed at different heights. It is not known accurately how the energy is transported from the photosphere to the chromosphere and which is the cause of the temperature increase between these two layers. To answer these and other questions it is needed the development of advanced instrumentation. Spatial resolution, which allows to resolve details on the Sun, is limited by the primary mirror diameter. Present ground-based telescopes have diameters until 1.6 metres. Nevertheless, this value is not enough to resolve other structures predicted by theory.

Because of this and, motivated by the idea of going into the solar investigation and being able to explain the physics of the Sun, 15 countries of the European Union, led by Spain, have joined to design the greatest technological challenge until the date in ground-based solar instrumentation: the European Solar Telescope (EST). It presents a primary mirror with a diameter of 4 metres and it is provided with a wide variety of state-of-the-art instruments, which can also operate simultaneously. One of those instruments is the spectrograph described in this thesis.

In general, long-slit spectrographs use one centred slit, through which the image of the Sun is displaced. This instrument presents eight entrance slits, what allows to observe a field of view eight times larger in the same integration time. There are different ways to generate these slits. The simplest one is to place a mask at the telescope image focal plane and to scan as in the case of a single slit. The disadvantage is that, doing it this way, two adjoining points in the field of view would be observed in different time exposures and, thus, under different atmospheric conditions. This problem is solved using integral field spectroscopy. This technique is being implemented in the new generation spectrographs for the largest

night-time telescopes, however it is still a novelty for solar instruments. The application of this technique, known as 3D spectroscopy, allows to observe a bidimensional field of view, to decompose it into one or more slits and to obtain the spectrum of every point of the field of view simultaneously. There are also different alternatives of integral field units, which can be even combined between them. After studying all of them, we have chosen the application of the image slicer concept. A new design of image slicer, called MuSICa (Multi-Slit Image slicer based on collimator-Camera), has been specifically developed for EST. The requirements and characteristics of the design make of it a state-of-the-art integral field unit, which considerably enhances the value and performance of the instrument.

A prototype for GRIS, the spectrograph of the GREGOR solar telescope, has been designed too. The implementation of an integral field unit at GRIS will improve its performance, as well as being a feasibility study for EST.

Since in the Sun, as in every star, a different optical depth is associated to each wavelength, the study of many spectral lines allows to analyse what is happening at different heights at the same time. One of the requirements for this instrument is the simultaneous observation of eight spectral lines, five from the visible spectral range and three from the near-infrared one.

The coupling of a bidimensional field of view scanning system makes possible the observation of a larger field of view as a mosaic of sequential integrations. The design of this subsystem is polarimetrically compensated and can also be used as a focusing mechanism.

The design of this spectrograph also contemplates the possibility to couple a polarimeter, offering two different modes of observation and converting this instrument into a 5D spectrograph that offers spatial (along two orthogonal directions), spectral and temporal information, as well as the Stokes parameters $(x,y,\lambda,t,(I,Q,U,V))$.

Several ambicious requirements and specifications are added to the technological complexity of this instrument, which must be fulfilled simultaneously. These requirements include high spatial (0.1 arcsec in 2 pixels) and spectral ($R=\frac{\lambda}{\delta\lambda}\sim 300{,}000$) resolutions, the reorganisation of a field of view of 80 arcsec^2 into eight slits of 200 arcsec length by 0.05 arcsec width and the simultaneous observation of different combinations of wavelengths associated to the science programmes. Each wavelength is observed with a different detector, so that there can not exist overlapping at the image focal plane. All the wavelengths should be observed with high efficiency and a good optical quality. The instrument is telecentric: the exit pupil is sent to infinity and the monochromatic beams illuminate homogeneously the detectors.

This thesis describes the design of an integral field, multi-slit, multi-wavelength, high-resolution spectrograph for the European Solar Telescope. It satisfies the different mentioned requirements and, coupled to the telescope, will be a useful tool for the study of the Sun from the Earth.

Resumen

Entre los 400.000 millones de estrellas de La Vía Láctea se encuentra el Sol, cuyas características físicas hacen posible que albergue un sistema planetario, El Sistema Solar. Esta condición parece suficientemente atractiva para justificar su estudio aunque, sin duda, existen otras razones que lo avalan.

Por su proximidad a La Tierra, es la única estrella que puede ser resuelta espacialmente. La alta resolución espacial es, por tanto, una condición imprescindible en los telescopios solares. Asimismo la alta resolución espectral proporciona información sobre las líneas espectrales y otras propiedades físicas codificadas en el espectro. Sin embargo, no aporta demasiada información sobre el campo magnético, el cual rige su actividad y gobierna los fenómenos físicos que tienen lugar en sus diferentes capas. Esta información puede obtenerse con polarimetría, a partir de los parámetros de Stokes. La combinación de estas dos importantes técnicas, espectroscopía y polarimetría, aplicadas de manera simultánea, aporta una amplia información sobre el Sol, facilitando el entendimiento de los fenómenos que tienen lugar en él y la Física que lo rige. Dadas las analogías del Sol con las demás estrellas, los resultados obtenidos de su estudio pueden ser extrapolados a física estelar, luego entender el Sol nos ayuda a entender la evolución de las estrellas. Por otra parte, el Sol juega un papel muy importante en las relaciones Sol-Tierra. Esta razón, combinada con las anteriores, justifican la necesidad e importancia de su estudio.

A pesar de ser la estrella más próxima, existen, aún hoy, muchas incógnitas sobre los procesos físicos que tienen lugar en su interior y el origen y evolución de los fenómenos observados. Es importante entender la evolución del campo magnético y de sus estructuras observadas a diferentes alturas. No se conoce con exactitud cómo es transportada la energía desde la fotosfera hasta la cromosfera y cuál es el motivo del aumento de la temperatura entre estas dos capas. Para responder estas y otras preguntas es necesario el desarrollo de instrumentación avanzada. La resolución espacial que permite resolver detalles en el Sol está limitada por el diámetro del espejo primario. Los telescopios terrestres actuales presentan diámetros de hasta 1,6 metros. Sin embargo, este valor no es suficiente para resolver otras estructuras predichas por la teoría. Ante estas necesidades y, motivados por la idea de profundizar en la investigación del Sol y ser capaces de explicarlo físicamente, 15 países de la Unión Europea, liderados por España, se han unido para diseñar el mayor reto tecnológico hasta la fecha en Física Solar terrestre: el Telescopio Solar Europeo (EST), con 4 metros de diámetro y provisto de una gran variedad de instrumentos de vanguardia, que pueden, además, operar de manera simultánea. Uno de esos instrumentos es el espectrógrafo descrito en esta tesis.

Generalmente, los espectrógrafos de rendija larga utilizan una única rendija centrada a través de la cual se va desplazando la imagen del Sol. El instrumento propuesto presenta ocho rendijas de entrada, lo que permite observar un campo de visión del Sol ocho veces mayor en el mismo tiempo de integración. Hay diferentes maneras de generar esas rendijas. La más sencilla es colocar una máscara en el plano focal imagen del telescopio y realizar el barrido análogamente al caso de una única rendija. El inconveniente es que, de este modo, dos puntos contiguos del campo de visión se observarían en diferentes instantes de tiempo

y, por tanto, bajo distintas condiciones atmosféricas. Para solucionar este problema se ha aplicado espectroscopía de campo integral, una técnica que está siendo implementada en los espectrógrafos de nueva generación para los grandes telescopios nocturnos y que es, sin embargo, una novedad para instrumentos solares. La aplicación de esta técnica, conocida como espectroscopía 3D, permite observar un campo bidimensional, descomponerlo en una o más rendijas y obtener el espectro de todos los puntos del campo simultáneamente. Hay, asimismo, diferentes alternativas de unidades de campo integral que pueden ser, además, combinadas entre sí. Tras el estudio de todas ellas, nos hemos decantado por la aplicación del concepto de *image slicer*. Se ha desarrollado un nuevo diseño de *image slicer*, llamado MuSICa ("Multi-Slit Image slicer based on collimator-Camera "), específicamente para EST. Los requisitos y las características del diseño lo convierten en una unidad de campo integral de vanguardia que enriquece considerablemente el valor y las prestaciones del instrumento.

Se ha diseñado también un prototipo de MuSICa para GRIS, el espectrógrafo del telescopio solar GREGOR. La implementación de una unidad de campo integral en GRIS mejorará las características del instrumento, además de ser un estudio de viabilidad para EST.

Puesto que en el Sol, como en las demás estrellas, a cada longitud de onda se le asocia una profundidad óptica, el estudio de varias líneas espectrales permite estudiar lo que ocurre a diferentes alturas al mismo tiempo. Uno de los requisitos es la observación simultánea de ocho líneas espectrales, cinco del rango espectral visible y tres del infrarrojo cercano.

El acoplamiento de un sistema de barrido bidimensional hace posible la observación de un campo de visión mayor en integraciones secuenciales. El diseño de este subsistema está polarimétricamente compensado y puede ser además utilizado como un mecanismo de enfoque.

El espectrógrafo ha sido diseñado contemplando la posibilidad de acoplar un polarímetro, ofreciendo así dos modos de observación y convirtiéndose en un espectrógrafo 5D que ofrecería información espacial a lo largo de dos direcciones, espectral, temporal y los parámetros de Stokes $(x,y,\lambda,t,(I,Q,U,V))$.

A la complejidad tecnológica que presenta este instrumento se añaden una serie de requisitos y especificaciones ambiciosas que deben cumplirse simultáneamente. Estos requisitos incluyen alta resolución espacial (0,1 segundos de arco en 2 píxeles) y espectral ($R= \frac{\lambda}{\delta\lambda}\sim 300.000$), la reorganización de un campo de visión de 80 segundos de arco cuadrados en ocho rendijas de 200 segundos de arco de largo por 0,05 de ancho y la observación simultánea de diversas combinaciones de longitudes de onda asociadas a diferentes programas científicos. Dado que cada longitud de onda es observada con un detector diferente, no puede existir solapamiento en el plano focal imagen. Todas las longitudes de onda deben observarse con una eficiencia alta y una buena calidad óptica. El instrumento es, además, telecéntrico, por lo que la pupila de salida es enviada al infinito y los diferentes haces monocromáticos iluminan los detectores de un modo homogéneo.

Esta tesis describe el diseño de un espectrógrafo de campo integral, multi-rendija, multi-longitud de onda, de alta resolución, para el Telescopio Solar Europeo, que satisface los diferentes requisitos mencionados y que será una herramienta útil para el estudio del Sol desde La Tierra.

Contents

1

Introduction

The Sun is one of the 400,000 millions of stars of the Milky Way. It is located near the galaxy equatorial plane, at a distance of around 10 kiloparsecs from its nucleus, over an internal border of one of its spiral arms. It is a small yellow star, with a spectral type G2V. It presents a geometry approximately spherical modified by a slight polar flatness. The Sun does not rotate as a rigid body and its structure, like that of other stars, is in shells. Its chemical composition is: $\sim$71% of its total mass of hydrogen, element that prevails over the others, $\sim$27.1% of helium and $\sim$1.9% of heavy metals: oxygen, carbon, iron, neon, nitrogen, silicon, magnesium and sulfur, listed in decreasing order. One of its most attractive points is the magnetic activity governed by cycles. It presents a bipolar magnetic field coupled to the plasma by the Lorentz force.

The Sun is a common star. However, its physical characteristics make possible to house a planetary system: the Solar System, in which, furthermore, the habitability conditions exist. The Sun, placed nearly at the centre of this planetary system, is the most important element. It contains around 98.6% of its total mass and is its greatest source of energy. Its external temperature has been estimated around 5,800 K and its age is approximately 4,600 millions of years. However, it still has combustible to live 5,000 millions more. Its evolution is known: it will move away from the Main Sequence and become a red giant until it collapses due to its own weight and finishes its life like a white dwarf (Fig. 1.1).

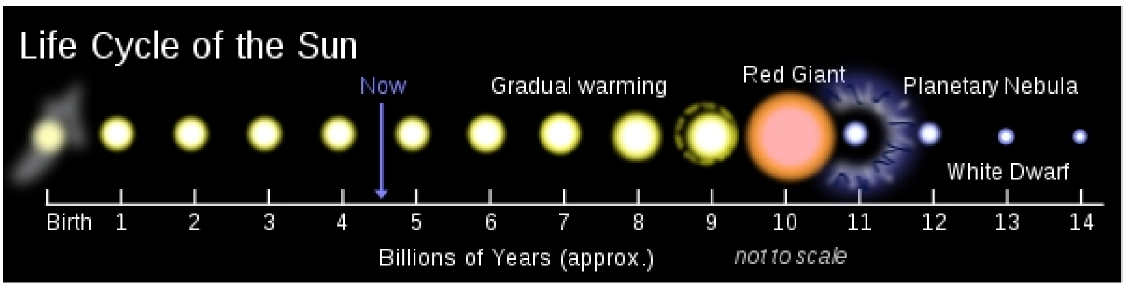

Figure 1.1: Sketch of the Sun's expected evolution. Figure from Prof. Hanson's lecture notes, University of Cincinnati.

Due to its proximity to the Earth, the Sun is the only star that can be spatially resolved from ground-based telescopes. Because of this, its study is very important to verify many physical theories, not only applicable to it, but results can also be extrapolated to the studies of other stars, due to their analogies. If the importance of the studies about the Sun-Earth relations are also added, all these reasons justify the relevance of the Sun's study.

There are different techniques to obtain information about our closest star. Currently two of the most important ones are: Spectroscopy and Polarimetry.

In the XVIIth century Isaac Newton discovered that, if a white light beam passes through a prism, the beam is decomposed in its constituent wavelengths generating the colours of the rainbow. In addition, the white light beam is again recovered if a second prism is added. This physical phenomenon for which waves with different frequency are separated after going through a material is known as dispersion, which is the base of spectroscopy. Dispersion affects all waves and it is produced by all materials as a function of their index of refraction. The angle of incidence of the light over a material in general is not the same that the output one. The difference between the output and input angles, δ, is called angular deviation. It increases with the index of refraction, n, which is itself, a function of wavelength. Thus, $\delta = \delta(\lambda)$ and each wavelength, λ, will suffer a different angular deviation, being the dispersion lower for red wavelengths than for blue ones.

As a result of the dispersion, the spectrum is obtained, as the spectral decomposition of the incoming beam. There are other disperser elements that offer higher dispersion than a prism. They replicate the spectral decomposition of the incident light with varying separation between the wavelengths. Each spectral decomposition is known as diffraction order, m. There is, however, a configuration for which dispersion is not produced and all the wavelengths are overlapped. It is known as zero order. In the spectrum, the different diffraction orders are distributed symmetrically at both sides of the zero order (see Fig. 1.2).

Every atom can emit or absorb electromagnetic radiation only in some frequencies that are characteristic of each chemical element and spectra can be in emission or absorption. The emission spectrum of an element is produced by the electromagnetic waves emitted by its atoms, in gaseous state, when a photon is able to stimulate it. If the same element receives electromagnetic radiation such that it absorbs in some frequencies, the spectrum of absorption is obtained. The relation between the emission and absorption spectra is given by the Kirchoff's law, which indicates that all the elements absorb radiation in the same wavelengths in which they emit it.

Since 1666, the application of this phenomenon has evolved in time until the current concept of spectroscopy. A wide information about the observed source can be obtained by decomposing its light after making it pass through a disperser element. The information about chemical composition, effective temperature, gravity, metallicity or rotation velocity is encoded in the spectrum. This observational technique of light decomposition is used in different fields. Specifically in Astronomy, it is applied to all types of celestial objects, including the Sun.

The magnetic field is one of the most attractive characteristics of the Sun and, spectroscopy, despite offering a wide information about the observed object, does not allow to

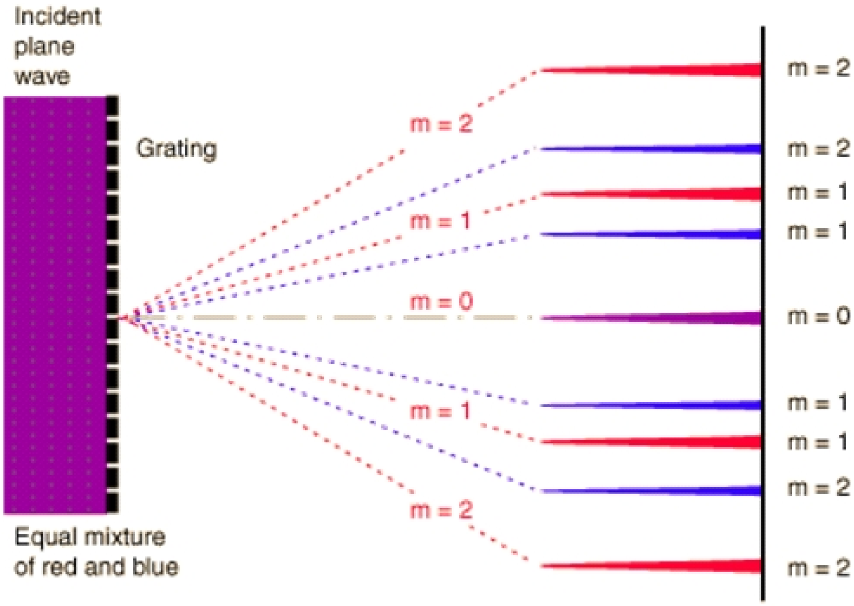

Figure 1.2: Symmetry of the spectrum with respect to the zero order. The different diffraction orders are equidistanly distributed at both sides of the zero order. The bigger the diffraction order is, the more separated the lines are in the spectrum. Unknown source.

study the magnetic field in depth. For this purpose polarimetry (del Toro Iniesta, 2003) is applied.

The phenomenon of light polarisation is known since the $XVII^{th}$ century, after Christian Huygens' (1629-1695) studies. Nevertheless, his work was not developed more in depth until beginning of the XIX^{th} century by Jean Baptiste Biot (1774-1862) and Thomas Johann Seebeck (1770-1831). These studies provided experimental evidences that confirmed that light can be considered as a transverse electromagnetic wave. This means a wave that oscillates perpendicularly to its propagation direction.

Polarisation is a phenomenon that can be produced in electromagnetic waves and for which the oscillation of the electric field vector is restricted to a certain plane, called polarisation plane. The orientation of the wave's electric field and its temporal variation describe the state of polarisation. There are three types of polarisation: linear, elliptical or circular. They are sketched in Fig. 1.3. In this figure, Z-axis represents the propagation direction of the wave, and the plane xy is the oscillation plane. The total electric field vector (E_{sum}) is the sum of its two orthogonal components (E_x and E_y) and φ is the relative phase between them. For a phase delay $\varphi = 0$ and equal components ($E_x = E_y$), the total electric field vector describes a line oriented 45° what defines the linear polarisation. In the second case, for $\varphi = \frac{\pi}{2}$, the magnitud of the electric field is constant and its orientation varies with time defining the shape of a circle. This is circular polarisation. In general, the electric field (E_{sum}) describes an ellipse and the state of polarisation is, in this case, elliptical.

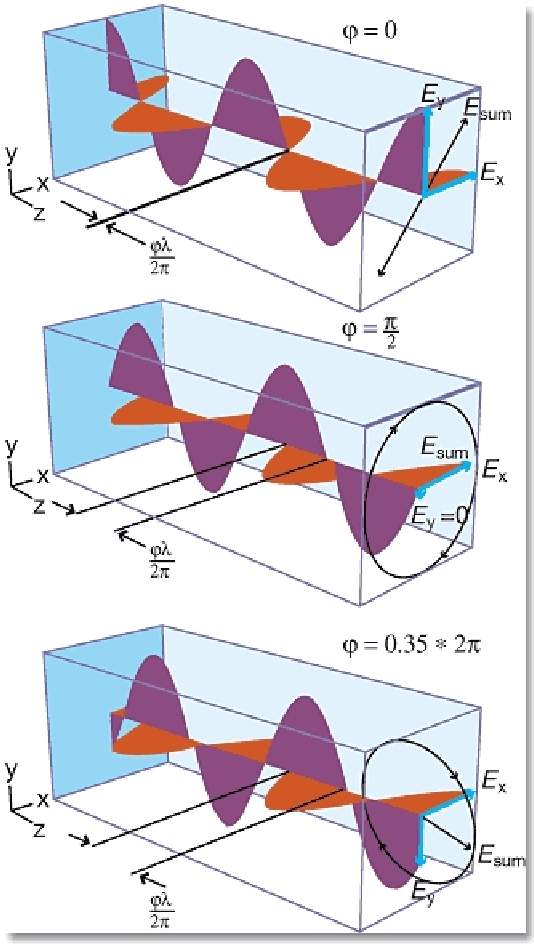

Figure 1.3: Sketch of the different types of polarisation: linear, circular and eliptical. In this figure, Z-axis represents the propagation direction of the wave, and the plane xy is the oscillation plane of the electric field. The total electric field vector is the sum (E_{sum}) of its two orthogonal components (E_x and E_y) and φ is the relative phase between them. For a phase delay $\varphi = 0$ and equal components ($E_x = E_y$), the total electric field vector describes a line oriented 45° what defines the linear polarisation. In the second case, for $\varphi = \frac{\pi}{2}$, the magnitud of the electric field is constant and its orientation varies with time defining the shape of a circle. This is circular polarisation. In general, the electric field (E_{sum}) describes an ellipse and the state of polarisation is, in this case, elliptical. This figure has been extracted from "Polarizing views"(Guimond & Elmore, 2004).

The state of polarisation is parametrised by four quantities that can be measured with a polarimeter. These quantities are the four Stokes parameters (I, Q, U, V), formulated by George Gabriel Stokes in 1852 to describe the polarisation state of electromagnetic radiation. The first parameter, I, is the total wave intensity, Q and U represent the linear polarisation and V, the circular one.

Spectroscopy and polarimetry are two excellent techniques to study the Sun. They can also be combined to obtain more information at the same time. Its combination is known as spectropolarimetry (Trujillo-Bueno et al., 2000).

1.1 Science Objectives

The Sun is composed by layers. These, from the inner to the outer ones, are: core, radiative zone, convective zone, photosphere, chromosphere and corona (see Fig. 1.4). The last three layers conform the solar atmosphere. In between the upper chromosphere and the corona the transition region is found. It is a thin and very irregular layer in which the temperature changes rapidly from 25,000 to 1 $\times 10^6$ K, separating the hot corona from the much cooler chromosphere.

The interior of the Sun is too dense to be observed. The photons generated in it are unable to stream out into space and to the Earth. The deepest solar layer that can be observed is the photosphere. Since the photosphere is the surface of the Sun that can be observed in visible light (Schmelz & Brown, 1992), it was the first solar layer to be studied. It is a thin layer with a thickness of $\sim$ 400 km. The photosphere density is approximately $2 \times 10^{-4}\, kg/m^3$. Its effective temperature is 5,800 K, however in its immediately upper layer, the chromosphere, a strongly increase of temperature occurs until 20,000 K. This increase has not been explained yet and the chromosphere represents one of the most interesting challenges of the Sun to be analysed.

The chromosphere is more transparent than the photosphere, and it normally can not be seen by the naked eye because the light from the photosphere of the Sun overpowers it.

According to theoretical models, the thickness of the chromosphere is around 2,200 and 5,000 km and it presents an irregular thickness and a deviation of spherical symmetry. Its density varies over almost seven orders of magnitude from a value of $1.0 \times 10^{-11}\, kg/m^3$ at its boundary with the solar transition region, and increases to a value of $2.0 \times 10^{-4}\, kg/m^3$ where it merges with the photosphere.

The magnetic field activity, manifested in photosphere and chromosphere through several magnetic field structures, makes these solar layers an interesting point of study.

In the photosphere, the magnetic field is found to occur in discrete concentrations of intense field, like sunspots or pores. The most common solar feature in the chromosphere are spicules, long thin structures of luminous gas which appear like the blades of a huge field of fiery grass growing upwards from the photosphere below. Spicules rise to the top of the chromosphere and then sink back down again over the course of about 10 minutes. Another feature found in the chromosphere are fibrils, horizontal wisps of gas similar in extent to spicules but with about twice the duration. Finally, solar prominences rise up through the chromosphere from the photosphere, sometimes reaching altitudes of 150,000 kilometres. These gigantic plumes of gas are the most spectacular solar phenomena, aside from the less frequent solar flares.

According to the importance and interest of photosphere and chromosphere, the instrument described in this thesis has been optimised for these solar layers. Provided with several technical advances and applying spectro-polarimetric techniques, one of its goals is the study of all these magnificent phenomena to offer a more detailed analysis and provide the physical explanation of all the aspects that nowadays continue being unknown.

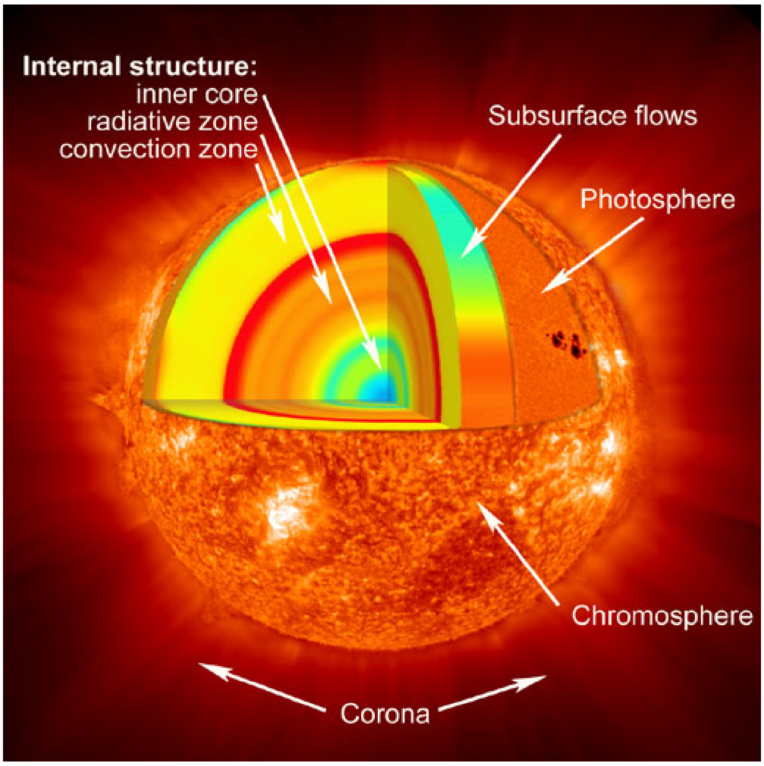

Figure 1.4: Structure of the Sun in layers. The Sun presents an internal structure composed by: core, radiative zone and convection zone. And an atmosphere, composed by the three most external layers: photosphere, chromosphere and corona. Figure obtained from the NASA webpage.

Some of the science programmes that impose the most restrictive requirements and for which the instrument has been optimised are shown in Table 1.1. These programmes, as well as their associated combination of spectral lines, have been defined by the EST project Science Group (EST Science Group, 2011).

1. Flux tube:

   Solar Magnetic Flux Tubes (MFT) are magnetic field concentrations in discrete areas near the surface of the Sun. They are caused by surrounding convective motion which brings together small components of magnetic fields. They are mainly observed in the surrounding of sunspots, however, other smaller arrangements are found in the lanes between granules where downdrafts occur. The tubes have diameters of a few hundred kilometres or smaller and yield strengths of 1 or 2 kG.

   The small-scale tubes of the photosphere may be thought of as elementary building blocks of solar magnetism and understanding them has implications for a wider understanding of solar and stellar magnetic phenomena. In addition, they are believed to play an important role in the irradiance variations of the Sun and the heating of the chromosphere and corona through a variety of dynamical processes, including the channeling of waves and shock fronts.

Table 1.1: This table presents the science programmes that impose the most restrictive requirements and for which the instrument has been optimised. Each program requires a specific combination of wavelengths that should be observed simultaneously. This table has been defined by the EST project Science Group (EST Science Group, 2011).

λ (Å)	Line	Flux tube	Network elements	Magnetic canopies	Hanle effect	Flares	Planets	Sunspots
3933	Ca II K				x	x		
3968	Ca II H				x	x		
3970	H_ε					x		
4102	H_δ					x		
4227	Ca I						x	
5172-5183	Mg Ib	x						
5247-5250	Fe I	x						
5576	Fe I		x					
5890	Na ID2						x	
5896	Na ID1			x			x	
6302-6303	Fe I	x	x					
6563	H_α					x		
7665-7699	K ID						x	
7770	O I triplet				x			
8498	Ca II			x				
8542	Ca II	x		x	x	x		
10827	Si I	x				x		
10829-10830	He I	x						
15260	Mn I	x						
15650	Fe I	x	x	x				
22200-22320	Ti I							x

Flux tubes are observed as small bright points in the continuum and spectral lines. Except for sunspots, the areas in which the magnetic field is concentrated are too small to have been resolved by conventional observations (Keller, 1992) although indications exist that they may have been resolved in some cases (Lagg et al., 2010). High resolution spectropolarimetry is used to study their magnetic properties, however aspects as their formation are still not well understood. Their study with the 4-m European Solar Telescope (EST) and the instrument described in this thesis is then important to understand this phenomenon. The evolution and eventual disappearance of flux tubes would be a natural consequence of their interaction with convective motions if they are a surface phenomenon, as suggested by recent numerical simulations. On the other hand, the persistence of these structures suggests that they are rooted somewhere below the solar surface, which would require different mechanisms for the disappearance of the flux.

2. Network elements:

   It is known that small-scale magnetic fields outside sunspots are found everywhere on the Sun (Harvey, 1971). The network elements correspond to the strongest magnetic elements at the boundaries of supergranulation cells. They are observed in different solar layers, like the photosphere or chromosphere.

   The structure and dynamics of the features on the solar surface are a result of magneto-convective processes and the chromospheric network is formed by magnetic field lines related to supergranulation cells in the photosphere below. Their study is relevant since these small-scale magnetic elements in the quiet photospheric network are believed to play a key role in the energy flow from the solar surface to the upper layers of the atmosphere.

3. Magnetic canopies:

   One of the most intriguing features of the solar chromosphere is its fibrilar topology in almost all chromospheric structures. The magnetic canopy is a layer of magnetic field which is directed parallel to the solar surface and located in the low chromosphere, overlying a field-free region of the photosphere (Steiner, 2000). Magnetic flux tubes rise in the vertical direction from the photospheric level and present a horizontally spreading magnetic field.

   Magnetic canopies can be theoretically inferred from a magnetohydrostatic extrapolation of the easily observable photospheric magnetic field. A thorough investigation of these fibrilar structures requires ultra-high resolution imaging and highest spatial resolution spectro-polarimetric measurements, since the average width of the fibrils is comparable to or smaller than the diffraction limit of a 1 metre class telescope. EST will study their detailed magnetic structure and their short and long term dynamics.

4. Hanle effect:

   The Sun also results to be an excellent laboratory for atomic physics. Some examples are the Hanle and Zeeman effects, which are presented in the spectral lines profile and allow to determine different characteristics of the magnetic field. The Hanle effect is a quantum phenomenon that consists in the modification of the light polarisation due to the action of a weak magnetic field over an atom or molecule. The presence of the field breaks partially the degeneration of the sublevels of energy and, from this effect, information about the chromospheric and coronal magnetic field can be obtained.

The second solar spectrum is the linearly polarised solar spectrum that is produced by coherent scattering processes. The information encoded in it presents a great potential for magnetic field diagnostics through the Hanle effect, which represents the influence of magnetic fields on the scattering polarisation (Stenflo et al., 2002a).

5. Flares:

   Solar flares are the most powerful magnetic events in the solar system. They are associated to the solar photosphere, chromosphere and corona. Flares are rapid and intense eruptions of magnetic energy on the solar surface that occur when magnetic energy that has been built up in the solar atmosphere is suddenly released. They emit radiation across the entire electromagnetic spectrum, from radio to gamma-rays, and are also intimately associated with the acceleration of particles into interplanetary space and with coronal mass ejections. The total flare energy is compatible with the amount of magnetic energy available in magnetic active regions, for example the coronal connections of a sunspot group,where most flares take place. Flares of all sizes tend strongly to occur in magnetic active regions and are associated with strong magnetic fields in the neighbourhood of magnetic polarity inversion lines, which is the dividing line between regions of positive and negative vertical component of the photospheric magnetic field, sometimes also called a neutral line.

   A small fraction of flares occur in so-called spotless regions (Dodson & Hedeman, 1970), and large-scale filament eruptions with flare-like properties can happen anywhere on the quiet Sun (Harvey et al., 1986). It is not yet possible to predict the time or location of a solar flare. Several statistical studies have attempted to identify active-region magnetic properties that are correlated with active region flare productivity, or can even act as solar flare forecasters. They represent the rapid transformation of the magnetic energy into thermal energy, particle acceleration and mass flows.

   Although they are nowadays viewed as high-energy processes which take place mainly in the corona, the response of the photosphere and chromosphere to the flare energy transport is very complex and the energy radiated from the lower atmosphere forms an important part of the flare energy budget. It is therefore essential that the photospheric and chromospheric signatures and processes involved are well understood.

6. Sunspots:

   When observing the Sun with appropriate filtration, the most immediately visible features are usually its sunspots (Scharmer et al., 2008), which are well-defined surface areas that appear darker than their surroundings because of lower temperatures. Sunspots are regions of intense magnetic activity where convection is inhibited by strong magnetic fields, reducing energy transport from the hot interior to the surface. They are magnetic structures associated to the photosphere and they are one of the most evident manifestation of the magnetic activity in the solar atmosphere, whose sizes are 30-40 arcseconds, what is equivalent to $20-30\times10^3$ kilometres. These structures are not presented isolated, but in groups, as pairs with opposite magnetic polarity. They have two polarities that are the same within an hemisphere and during a cycle. The magnetic polarity of the leading sunspot alternates every solar cycle. A typical sunspot presents two different zones: the central part, called umbra, whose size is 15-20 arcseconds and where the magnetic field is predominantly vertical, with a value on the order of 2,500 to 3,500 G and a surrounding area, the penumbra, with a size of 8-10 arcseconds and an inclined magnetic field with a value of 2,200-2,300 G. The umbra is much darker than the quiet photosphere with a factor 0.1 to 0.2 times its intensity and presents a lower temperature, between 4,000 and 5,000 K. The average intensity of the penumbra is a factor 0.75 of the photosphere one, where its brightness filaments present an intensity similar than the photosphere one and the dark filaments one half of this value.

The number of sunspots visible on the Sun is not constant, but varies over an 11-year cycle known as the solar cycle.

The Sunspot science programme only requires the additional observation of the Ti I spectral lines at 22300 Å. These lines can be observed only in sunspots and are, thus, exce-llent candidates to study the physical conditions prevailing in these solar structures. It is clear that there exist other spectral lines that are also of interest to study sunspots, like, for instance, the magnetically sensitive photospheric Fe I lines at $5247-5250$ Å, $6301-6032$ Å or the Si I 10827 Å line, as well as the chromosperic Hα, Ca H & K, Ca II IR or He 10830 Å. Since the measurement of all these spectral lines is also required by other programmes and, consequently, they must be observable with the spectrographs of EST, we will only centre on the Ti I lines for the sunspot programme.

7. Planets:

   Although EST is a solar telescope, the science requirements also include a second priority programme for the observation of some planets, like Mercury, Venus or Jupiter.

   Mercury is the prime example of non-solar science for a solar telescope. Its inner orbit places it at a maximum of 20 degrees elongation of the Sun, leaving all night instruments on the necessity of observing it low over the horizon through huge air masses and for brief periods of time during the day and through the year. Thus its observation is very difficult to night-time telescopes while a solar telescope can observe Mercury all day long for almost all year round.

   A similar problem happens with Venus, which can still be considered as a planet imposing similar geometry constrains to night-time telescopes as Mercury. There is growing interest on the observation of the powerful winds appearing in the high layers of the Venus or Jupiter atmospheres. The high resolution of the solar spectrographs like that of this thesis, is suitable to measure the velocity of the wind in their atmospheres.

A different combination of wavelengths of simultaneous observation is associated to each science programme, which are shown in Table 1.1. This selection takes into account the characteristics associated to each wavelength and the information that can be obtained of them.

- Ca II K 3933 Å and Ca II H 3968 Å:

  the cores of these spectral lines are formed in the medium-high chromosphere. They are useful to study the solar chromosphere at different heights.

  These are two Fraunhofer lines, absorption lines in the optical spectrum of the Sun that were originally observed by Joseph von Fraunhofer (1787-1826).

- H_ε at 3970 Å:

  the Balmer series is characterised by the electron transitioning from $n > 3$ to $n = 2$ (or viceversa), where n refers to the radial quantum number or principal quantum number of the electron. The transitions are named sequentially by Greek letter: $n = 3$ to $n = 2$ is called H_α, 4 to 2 is H_β, 5 to 2 is H_γ, and 6 to 2 is H_ε, specifically this line at 3970 Å. The Balmer series is particularly useful in Astronomy because the Balmer lines appear in numerous stellar objects due to the abundance of hydrogen in the universe, and therefore are commonly seen and relatively strong compared to lines from other elements. The spectral classification of stars, which is primarily a determination of surface temperature, is based on the relative strength of spectral lines, and the Balmer series in particular are very important. Other characteristics of a star can be determined by close analysis of its spectrum include surface gravity (related to physical size) and composition. Since the hydrogen is the majority element in the Sun, the Balmer lines are good candidates to be studied.

- H_δ at 4102 Å:

  this spectral line was defined as 'h' line by Joseph von Fraunhofer (1787-1826) and corresponds to the δ line of the Balmer series of the hydrogen atom. The visible spectrum of light from hydrogen displays five prominent spectral lines, 3970 Å, 4102 Å, 4340 Å, 4860 Å and 6563 Å, which correspond to emissions of photons by atoms in excited states transitioning to the quantum level described by the principal quantum number n equal to 2 (or the corresponding opposite absorption transition).

- Ca I at 4227 Å:

  the Ca II line at 4227 Å is a preferred line for the exploration of scattering polarisation and the determination of the weak magnetic fields in the lower chromosphere (Anusha et al., 2011a). Its study is important because this line exhibits the largest degree of linear polarisation in the visible spectrum near the limb. Historically this was the first line in which scattering polarisation was detected with confidence (Brückner, 1963). Also the Hanle effect was first detected on the solar disk in this line (Stenflo, 1982).

- Mg Ib at 5172 – 5183 Å:

  these are very deep lines formed in the low chromosphere, however they can reach the middle of this layer and can allow the observation of high layers of the atmosphere.

- Fe I at 5247 – 5250 Å:

  these lines both belong to multiplet number 1 of Fe and have approximately the same oscillator strength, equivalent width, and excitation potential. They differ mainly in their effective Landé factors, 3.0 for the 5250 Å and 2.0 for the 5247 Å. These are important lines with which the magnetic, velocity, and brightness structure of the spatially unresolved basic magnetic elements in active-region of plages can be studied (Frazier & Stenflo, 1978a).

- Fe I at 5576 Å:

  this spectral line is important for velocity measurements without the Zeeman effect contribution, because of its landè factor is equal to zero.

- Na I D2 at 5890 Å and Na I D1 at 5896 Å:

  these lines correspond to the doublet of Sodium. They are used to study the polarisation signatures of the Hanle and Zeeman effects (Stenflo et al., 2002b), as well as the study of the quantum theory of polarised line formation when both fine-structure and hyperfine-structure effects are important. The D1 and D2 lines form the sodium doublet, the centre wavelength of which (5893 Å) is given the designation letter ıDȷ. This historical designation for this line has stuck and is given to all the transitions between the ground state and the first excited state of the other alkali atoms as well. The D1 and D2 lines correspond to the fine splitting of the excited states.

- Fe I at 6302 – 6303 Å:

  these lines of neutral iron are associated to the middle photosphere. They are a couple of magnetic lines with a strong magnetic sensitivity and a Landé factor of 1.67 and 2.5.

- $H\alpha$ at 6563 Å:

  the $H\alpha$ line is formed in the middle-high chromosphere. It is the most used spectral line to observe this layer. This Balmer transition line of neutral hydrogen, centred at 6563 Å is historically important in flares. It is used for the study of filaments and, if they are observed against the border, prominences too.

- K I D at 7665 – 7699 Å:

  the K I D line at 7699 Å has been used to study the energy provided by MAG (magneto-acoustic-gravity) waves at photospheric layers.

- O I triplet at 7770 Å:

  oxygen is probably the most abundant element in the universe, next after hydrogen and helium. This neutral oxygen triplet lines at 7770 Å, as well as other atomic lines, are used for abundance studies of the Sun and solar-type stars (Kiselman, 1993a).

- Ca II at 8498 Å and Ca II at 8542 Å:

  the cores of these two lines are formed in the high chromosphere. They are an alternative to the Ca II H&K lines and, although the instrument has a worse spectral resolution at these wavelengths, they present a higher flux, what makes them easier to be studied.

- Si I at 10827 Å:

  although this spectral line presents a middle magnetic sensitivity, it is very useful because it can be observed simultaneously with the He I 10830 Å line, making it possible to obtain information about the photosphere and chromosphere in the same measurement.

- He I at 10829 – 10830 Å:

  this is a triplet line formed in high chromosphere. According to the Saha's ionisation equation, helium can not be ionised at chromospheric temperatures. Thus the presence of these lines indicates the possible existence of an unknown mechanism, either radiative or collisional, for their formation.

- Mn I at 15260 Å:

  this photospheric line has a particular fine structure. With it, the presence of intense magnetic fields (1kG) and weak ones (a few hG) can be measured in a single pixel.

- Fe I at 15650 Å:

  this spectral line is associated to the deep photosphere. The relevance of its study is because it is the most sensitive line to the magnetic field of all the spectral range between the visible and the near infrared.

- Ti I at 22200 – 22320 Å:

  these lines of neutral titanium can only be observed in sunspots and are ideal to study the physical conditions of these solar features (Rueedi et al., 1995).

1.2 Spectrographs

Astronomy is an observational science and the knowledge about the nature and evolution of celestial objects is based on the results of the observations. One of the observational techniques that offers more information is spectroscopy. Because of that, spectrographs are very important instruments used in different science fields. Specifically for the study of the Sun, it is one of the most useful tools. Telescopes collect the light from an astronomical object in order to measure its position, brightness or spatial distribution. However, it is possible to obtain more information with the spectrum, namely the distribution of light intensity as a function of wavelength. A spectrograph is an instrument used to disperse the light of an emitting source in order to get the information about its physical characteristics encoded in the spectrum. This technique is usually applied in Astronomy since it allows to obtain the temperature, chemical composition and the movement of a star and, in an indirect way: the age, evolutive state, mass, luminosity and distance.

Despite the first spectrum was observed in the XVIIth century, it was not until the XIXth when its chemical and physical interpretation took place. Thereafter and, thanks to Wollaston's and Fraunhofer's studies, the spectrographs became an important tool for the study of the Sun.

1.2.1 Spectrograph elements

The elements of a spectrograph are: entrance slit, collimator element, disperser element, camera element and detector (see Fig. 1.5). Basically, a spectrograph selects a specific field of view (FoV) using a slit at the telescope image focal plane, limiting the size on the sky and over a celestial object that is going to be observed. The collimator element, which can be a lens or a mirror, collimates the beam. For each point of the slit, the rays are driven parallel to each other. All the rays are contained within an aperture defined by the pupil diameter. The disperser element is usually located at the pupil position. Before the detector, it is needed to focus the beams. This is done by the camera. Each wavelength will be focused in a different place of the spectrograph image focal plane.

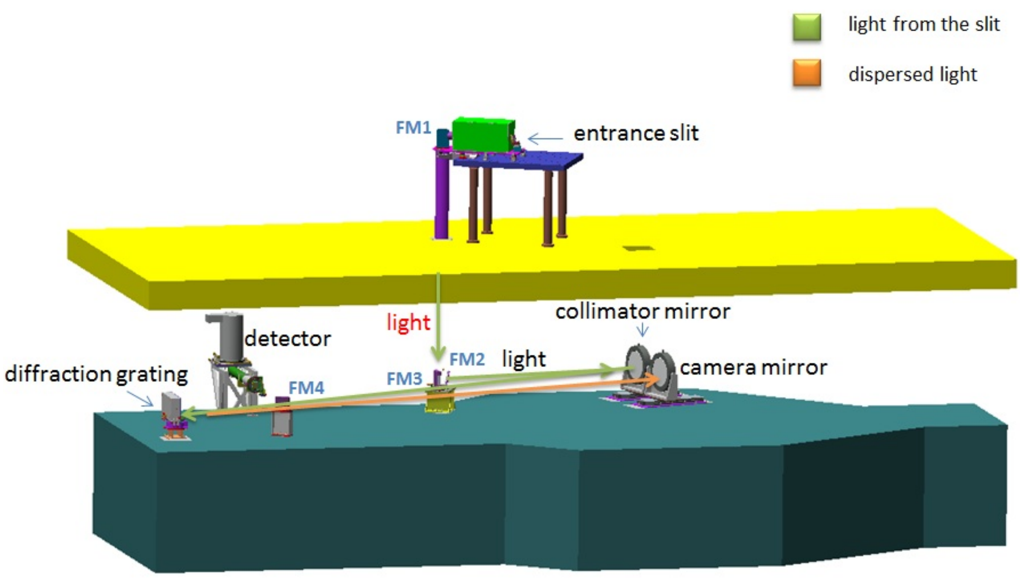

Figure 1.5: Elements of a spectrograph. This design corresponds to the spectrograph of the GREGOR solar telescope, where the slit is in a different floor than the other optical elements. The entrance slit selects the field of view for which the spectrum will be obtained. The light is driven to the lower floor using a folding mirror (FM1). Two flat mirrors, FM2 and FM3, orient the beam adequately and send it to the collimator mirror, which collimates the light before the disperser element, which in this case is an echelle diffraction grating. The beam is then decomposed spectrally and the camera mirror focuses each wavelength in a different location of the image focal plane forming the spectrum of the incoming light. For this spectrograph, a folding mirror, FM4, drives the beam focused by the camera element to the detector.

Slit

The slit is placed at the telescope image focal plane and it limits the observed field of view, which is the angular area of the sky selected to illuminate the instrument.

The field of view of an optical system is often expressed as the maximum angular size of the object as seen from the entrance pupil. The maximum image height is also used. For finite conjugate systems, the maximum object height is useful. In astronomy the field of view is usually expressed as an angular area viewed by the instrument, in square arcseconds.

If the physical entrance slit width is W_s, its image through the system,W'_s, can be defined by Eq. 1.1 (Gray, 1976).

$$W'_s = W_s \cdot \mathit{\Gamma}_T, \tag{1.1}$$

where $\mathit{\Gamma}_T$ is the total magnification of the system, including the ratio between the camera and collimator mirrors focal lengths (f_{cam}, f_{col}, respectively), the anamorphic magnification, γ_{an}, and, in some cases, as for the proposed instrument, the magnification of the reimaging system, $\Gamma_{R.S.}$, which will change the focal-ratio of the beam before the detectors (Eq. 1.2).

$$\mathit{\Gamma}_T = \frac{f_{cam}}{f_{col}} \cdot \gamma_{an} \cdot \Gamma_{R.S.} \tag{1.2}$$

In an optical system, the size of the object is modified by the difference between the focal lengths of camera and collimator elements. This modification can be calculated as the ratio between them. In addition, the angle of incidence, Θ_i, of the beam over the disperser element is different to the angle with which the beam is diffracted, Θ_o, which happens in general, in most of the cases. The ratio between the trigonometric cosine function of the input and output angles with respect to the diffraction grating defines the anamorphic magnification, defined in Eq.1.3. This expression is shown in (Schroeder, 1987), Chapter 13, where γ_{an} is denoted as 'r', Θ_i as α and Θ_o as β.

$$\gamma_{an} = \frac{\cos\theta_i}{\cos\theta_o} \tag{1.3}$$

The focal-ratio is a dimensionless number obtained from the ratio of the lens or powered mirror focal length and the diameter of the beam that illuminates it. It is a quantitative measure of the lens or powered mirror speed, this is, a measure of how fast the beam is focused. The result of this ratio, $\sharp$, is the f-number and is commonly used to give an equivalent of the focal-ratio, F/$\sharp$.

In some instruments, the focal-ratio needs to be changed before the detector, in order to have the appropriate scale. This is done using a reimaging system that could be either a reflective or refractive system or even a combination of them. The magnification of the reimaging system, $\Gamma_{R.S.}$, is defined by the ratio between the final focal-ratio, $(focal-ratio)_f$, produced by it, and the previous focal-ratio of the beam, $(focal-ratio)_p$, as defined by Eq. 1.4.

$$\Gamma_{R.S.} = \frac{(focal - ratio)_f}{(focal - ratio)_p} \tag{1.4}$$

The slit width, W_s, should be set so that the projected slit width seen by the detector should be well sampled by the detector resolution.

Solar spectrographs use a slit-jaw imaging system to have a reference of the position of the slit in the telescope field of view. This allows the pass of the light through the slit to the spectrograph and the rest of the light is reflected to produce an image of the observed field of view and the location of the slit over it.

Collimator element

The collimator element is used to collect the light, previously dispersed by diffraction in all directions by the slit, and collimate it, this is, send all the rays associated to each point of the slit, parallel to each other.

The collimator element can be a lens, working then in transmission, or a powered mirror, for reflective systems. The conicity of the mirrors may be different: parabola, sphere or hyperbola.

Disperser element

The disperser element is the most important piece of a spectrograph, since without it there is no dispersion. It decomposes the incident beam into their constituent wavelengths. There are different types of disperser elements: prisms, diffractions gratings, grisms or VPH.

- Prism:

  It was the first element used for the spectral decomposition of the light. Optically it is a transparent medium limited by two sides not parallel between them, so that each wavelength of a polychromatic beam, following the Snell's law, presents a different output angle. The angular deviation is bigger for smaller wavelengths. These are also more absorbed by the glass and they have a larger optical path within the prism, what reduces their intensity.

  When light enters a prism, it is no longer travelling in air, and its speed decreases. If the incident wavefront is travelling at an angle to the surface of the prism, which is easy to arrange because of its angled faces, then the propagation of the part of the wavefront in the prism is retarded, thus bending the wavefront and changing its direction of propagation through the prism. This phenomenon is referred to as refraction. If the prism is illuminated by a polychromatic beam, this occurs in a different way for each wavelength and a spectral separation is obtained.

  The prism is a very versatile optical element that can be used for different applications. As a disperser, prisms produce a very low dispersion that is not enough for very high resolution solar spectrographs, like the one that is the subject of this thesis, where the simultaneous observation of eight wavelengths is required. In this case in which different science cases are considered and a great versatility is essential, a prism is not a valid option.

- Diffraction grating:

  The diffraction grating is an excellent choice to disperse the polychromatic light into its constituent monochromatic components for high orders or even for working at different diffractive orders, as in the case of multi-wavelength spectrographs.

  It can be described as a collection of reflecting or transmitting elements separated by a distance comparable to the wavelength under study. So, it may be thought of as a collection of diffracting elements, such as a pattern of transparents slits or apertures in an opaque screen, or a collection of reflecting grooves on a substrate or blank.

  Upon diffraction, an electromagnetic wave incident on a grating will have its electric field amplitude, or phase, or even both, modified in a predictable way in the region near the surface of the grating. When monochromatic collimated light is incident on a grating surface, it is diffracted into discrete directions. Each grating groove can be thought as being a very small, slit-shaped source of diffracted light. The light diffracted by each groove combines to form set of diffracted wavefronts. The usefulness of a grating depends on the fact that there exists a unique set of discrete angles along which, for a given spacing, d, between grooves, the diffracted light from each facet is in phase with the light diffracted from any other facet, leading to constructive interference. When light passes through a narrow aperture, it will spread out on the other side.

  A grating can be manufactured to work in reflection or transmission. There are different types of diffraction gratings. For high resolution spectrographs, echelle gratings are used. Their grooves have a high inclination with respect to the base of the grating, of the order of 60°. They work at high diffraction orders with a superb spectral resolution.

- Grism:

  A grism or Carpenter's prism is a combination of a prism and a grating arranged in a way such that light at a chosen central wavelength passes straight through. It is formed by replicating a transmission grating onto the hypotenuse face of a right-angle prism.

  The dispersion of a grism is not linear, since the dispersive effects of the prism and grating are superimposed.

- VPH:

  Volume Phase Holographic Gratings (VPH) diffract light by refractive index modulations within a thin layer of material between two glass substrates.

  The diffracting mechanism arises from modulations in the refractive index in the form of fringe planes running parallel to each other through the depth of the grating material and oriented so that the fringes terminate at the surfaces of the volume (Barden et al., 1998).

Two critical parameters in the performance of this type of grating are the intensity of the refractive index modulation and the depth of the grating layer. A VPH grating is formed in a layer of transmissive material, usually dichromated gelatin, which is sealed between two layers of clear glass or fused silica. The phase of incident light is modulated as it passes through the optically thick film. Light is diffracted at angles corresponding to the classical grating equation as a function of the incident angle and the frequency of the index modulation at the surface of the grating.

Good efficiency over moderately broad angular and spectral bandwidths can be achieved, but peak efficiency is usually decreased with increased bandwidth.

Every volume-phase holographic grating is a genuine holographic master, not a mechanical replication, what increases the price. In addition, although they can achieve higher diffractive efficiencies in many applications than currently available surface gratings. On the other hand, in the present, the sizes of this type of gratings are up to 75 mm, what is too small for astronomical high spectral resolution spectrographs, which generally have pupil diameters of at least 150 mm located over the diffraction grating.

For a very high spectral resolution spectrograph like that of this thesis, in which several wavelengths are to be observed together at different high diffraction orders, the most appropriate choice for the disperser element is an echelle diffraction grating. Several aspects of the diffraction gratings are interesting to be studied, as their characteristics and types, its mathematical description or its efficiency. These aspects are analysed in the next sections.

Camera element

The dispersed light should be focused on the detector to obtain the spectrum of the observed source. This is the function of the camera element. As well as for the collimator, the camera element can work in transmission using a lens (or even a combination of them) or in reflection, using a powered mirror. The main problem of using a refractive camera is the chromatic aberration so, in multi-wavelength spectrographs, a camera per wavelength is used, what limits the versatility of the instruments for different combinations of wavelengths. Another option is to use an achromatic doublet to avoid the dependence on wavelength, however the throughput associated to its transmission could be lower than the corresponding to a mirror with an appropriate coating. For the design of the instrument described in this thesis mirrors have been considered for both, collimator and camera elements.

Collimator and camera elements form an imaging system, which produces an image of the slit on the detector. In the case of monochromatic light, a simple image of the slit would be produced and a continuum spectrum in the case of dispersed white light. The focal ratio of the camera can be the same as that of the collimator and telescope, for 1 : 1 systems, or also a different one, if a magnification is required.

Detector

The detector is an element in increasing evolution. The developments in the sizes of the pixel have allowed improvements in the resolution and the observed field of view.

The eye was the first detector used in spectroscopy. During the XIX^{th} century the photographic plate replaced the eye. In 1969 a new type of detector, called charge coupled device (CCD), was invented at AT&T Bell Labs by Willard Boyle and George E. Smith, but was not before the end of 1980 when CCDs were applied to solar physics.

A CCD is a device for the transfer of electrical charge to an area where it can be manipulated, for example for its conversion into a digital value. This is achieved by shifting the signals between stages within the device one at a time. CCDs move charge between capacitive bins in the device, with the shift allowing for the transfer of charge between bins. In a CCD there is a photoactive region (an epitaxial layer of silicon), and a transmission region made out of a shift register. An image is projected onto the capacitor array (the photoactive region), causing each capacitor to accumulate an electric charge proportional to the light intensity at that location. The general functioning of a CCD can be divided into two phases: exposure and readout. During the first phase, the CCD passively collects incoming photons, storing electrons in its cells. After the exposure time is passed, the cells are read out one line at a time. The emergence of the charge coupled devices was so important that in January 2006, Boyle and Smith were awarded the National Academy of Engineering Charles Stark Draper Prize and in 2009 they were awarded the Nobel Prize for Physics.

The parameters that characterise a CCD are:

1. Pixel size:

   the pixel size, τ, has commonly a value between 10 and 20 μm. The pixel size delimits the size of the smallest image that can be detected. It is an important parameter, since it is related to the spatial and spectral resolution.

2. Spatial resolution:

   according to the Shanon's sampling Theorem, the sampling to measure a signal has to be the size of the smallest detail divided by 2. The smallest angular detail that can be observed, α_{min}, is given by the Rayleigh Criteria (Hecht, 2000), which is defined by Eq. 1.5.

$$\alpha_{min} = 1.22 \cdot \frac{\lambda}{D} \tag{1.5}$$

   The resolution element of a detector is defined using two pixels, as described in Eq. 1.6 attending to the Rayleigh Criteria or as shown in Eq. 1.7 if the cutoff frequency is considered.

$$2 \cdot \tau = 1.22 \cdot \frac{\lambda}{D} \cdot f_{ef} \tag{1.6}$$

$$2 \cdot \tau \approx \frac{\lambda}{D} \cdot f_{ef} \tag{1.7}$$

Where f_{ef} is the effective focal length, which is defined as the focal length of the optical system for the same focal-ratio and the entrance pupil diameter. Equations 1.5 and 1.6 are shown in (Hecht, 2000), Chapter 10, where α_{min} is denoted as $(\Delta\varphi)_{min}$ and $2{\cdot}\tau$ is denoted as $(\Delta l)_{min}$.

3. Number of pixels:

   the number of pixels is directly related to the field of view. Let's assume a detector with N pixels in the horizontal direction with a sampling of $\Delta\alpha_x$ and M pixels in the orthogonal direction with a sampling $\Delta\alpha_y$. The field of view (FoV), can be defined by these parameters, as shown in Eq. 1.8.

$$FoV = N \cdot \Delta\alpha_x \cdot M \cdot \Delta\alpha_y \tag{1.8}$$

4. Quantum efficiency:

   it is defined as the ratio between the number of electrons generated by the light and the number of received photons.

5. Zero level:

   the zero level is the number of electrons generated with a zero time exposure.

6. Dark current:

   the dark level is the number of generated electrons without illuminating photons and with a time exposure different to zero. Cooling reduces the dark current, improving the sensitivity of the CCD to low light intensities.

7. Readout noise:

   Even in the absence of illumination there is a noise known as readout noise, σ. If two dark images are taken, the noise associated to them would be σ_1 and σ_2. Then, the readout noise can be calculated as defined in Eq. 1.9.

$$\sigma = \frac{\sigma_s}{\sqrt{2}} \tag{1.9}$$

   where σ_s is defined by Eq. 1.10 (P. Léna & Mignard, 1998).

$$\sigma_s^2 = \sigma_1^2 + \sigma_2^2 \tag{1.10}$$

8. Well depth:

   this parameter gives how many electrons fit on the potential well.

9. Digitalization:

   this is the conversion factor that offers the electrons per count.

10. Flatness and Linearity:

    it is desirable a homogeneous behaviour of the different pixels and a linear response, what makes important the flatness and linearity of a detector.

1.2.2 Types of diffraction gratings

There are different types of diffraction gratings. They can be plane or curve like the concave gratings. In addition, they can be characterised by its grooves, according to their number and angle of inclination with respect to the base of the grating, shape and size.

A concave reflective grating can be modeled as a concave mirror that disperses the light. It can reflect and focus light by virtue of its concavity and to disperse light by virtue of its groove pattern. Compared with plane gratings, they offer one important advantage: they provide the focusing (imaging) properties to the grating that otherwise must be supplied by other optical elements.

This type of gratings also presents some disadvantages, like aberrations, which is an important point to be minimised in all optical systems. For a ruled concave grating, the facet angles are not aligned identically and the effective blaze wavelength varies from one side of the grating to the other. Concave gratings also present difficulty in the alignment control.

The most used gratings for Astronomy are reflective plane ruled. This type of diffraction grating is characterised by the shape and density of its grooves.

The groove profile has a significant effect on the light intensity diffracted from the grating. While ruled gratings may have triangular or trapezoidal groove profiles, holographic gratings usually have sinusoidal (or nearly sinusoidal) groove profiles.

Ideally, the groove facet should be flat with smooth straight edges, and be generally free from irregularities, with a quality better than $\lambda/10$.

For plane ruled gratings, the inclination of the grooves with respect to the base of the grating is smaller than 10°. For high resolution spectrographs, another type of diffraction gratings is used, where the angle of inclination is around 60°. These are the Echelle gratings.

1.2.3 Characteristics of a diffraction grating

An Echelle diffraction grating is characterised by 3 constant parameters: the blaze angle,φ_B, the groove density, σ, and the total number of grooves, N. The blaze angle is the angle of inclination of the grooves with respect to the base of the diffraction grating. The groove density is the number of grooves per mm and N is the number of grooves of the grating.

There is a specific configuration, called Littrow, in which the grating angles of incidence, Θ_i, and diffraction, Θ_o, are the same. The beam diffracted by the grating returns following the same optical path both, using reflective collimator and camera elements or refractive ones. In practice, this configuration is generally used with a small variation of the output angle, what is known as quasi-Littrow configuration. The diffraction gratings working in quasi-Littrow configuration at high resolution can be classified based on the blaze angle attending to Eq. 1.11.

$$\tan \varphi_B = q \tag{1.11}$$

where q the integer number closest to the numerical result obtained from Eq. 1.11. So the grating is classified as R_q. This is a usual way to characterise a grating based on one of its constant parameters.

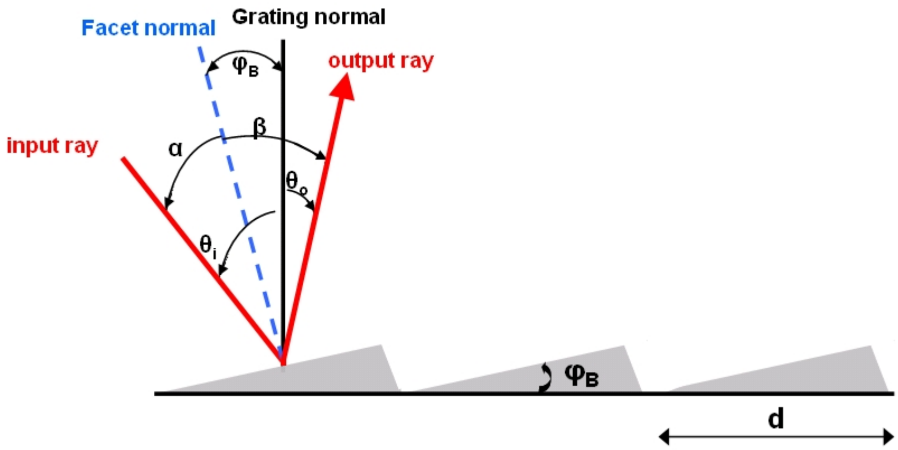

Figure 1.6: Sketch of the angles of a diffraction grating using two different references: the facet normal, for which α and β are the input and output angles respectively, and the grating normal, for which these angles are θ_i and θ_o. The angles are measured with respect to the normal. The inclination of each groove with respect to the base of the grating is the blaze angle, φ_B, a characteristic parameter of a diffraction grating.

1.2.4 Mathematical description

As described in previous sections, a diffraction grating is a repetitive collection of diffractive elements that produce periodic alterations in the phase, amplitude, or even in both, of an incoming wave. When monochromatic collimated light is incident on a grating surface, it is diffracted into discrete directions. The light diffracted by each groove combines to form set of diffracted wavefronts. The usefulness of a grating depends on the fact that there exists a unique set of discrete angles along which, for a given spacing (d) between grooves, the diffracted light from each facet is in phase with the light diffracted from any other facet, leading to constructive interference.

The mathematical description of a diffraction grating considers the incidence angle on the grating and its corresponding output angle, the wavelength, since the dispersion is a function of it, the diffraction order and the characteristics of the own grating, like the blaze angle or the separation between grooves. All these important parameters are related in the grating equation, which describes the physical behaviour of a diffraction grating. There are two different references that can be assumed for the angles. The first and most used one is the normal to the grating. In this case the grating equation can be expressed by Eq. 1.12.

$$m \cdot \lambda = d(\sin \Theta_i + \sin \Theta_o) \tag{1.12}$$

where m is the diffraction order, λ is the considered wavelength, d is the groove size, Θ_i and Θ_o are, respectively, the input and output angles with respect to the grating normal. Equation 1.12 is presented in (Hecht, 2000), Chapter 10. There are some differences in the nomenclature. The groove size, d, is denoted as a, and the output grating angle, Θ_o, as Θ_m. In addition, there is a difference in the sign that affects the input angle, Θ_i. This sign is introduced to consider that the angles Θ_i and Θ_o are measured in different sense with respect to the reference, as shown in Fig. 1.6. Thus, the absolute value of Θ_i is used. However, in Equation 1.12, the angle is introduced with the corresponding sign with respect to the considered reference.

Another possibility is to take as the reference the normal to the grating grooves (see Fig. 1.6). In this case, the angles, called α and β respectively, are related to the last ones through the blaze angle, φ_B. The grating equation can also be written on the following way, according to Fig. 1.13.

$$m \cdot \lambda = d(\sin(\varphi_B + \alpha) + \sin(\varphi_B + \beta)) \tag{1.13}$$

For Littrow configuration, Θ_i is equal to Θ_o and the light is diffracted back in the direction from which it came. The grating equation, then, takes the following expression presented in Eq. 1.14.

$$m \cdot \lambda = 2 \cdot d \cdot \sin(\Theta) \tag{1.14}$$

with $\Theta = \Theta_i = \Theta_o$.

1.2.5 Efficiency

The study of the grating efficiency is, itself, the analysis of the energy distribution of the incoming wave after being dispersed. Each wavelength at different integer orders will have an associated percentage of luminosity that is commonly known as grating efficiency and defined by Eq. 1.15.

$$Eff = (\frac{sin(x)}{x})^2 \tag{1.15}$$

with:

$$x = \frac{k \cdot a \cdot p}{2} \tag{1.16}$$

$$k = \frac{2\pi}{\lambda} \tag{1.17}$$

$$a = d \cdot \cos\varphi_B \tag{1.18}$$

$$p = \sin\alpha + \sin\beta \tag{1.19}$$

This corresponds to the theoretical absolute grating efficiency, normalised to 1. The experimental value is a 10% lower than the theoretical one. Even so, the grating efficiency has to be multiplied by the reflectivity of its coating to obtain the throughput associated to the grating for each wavelength. Eq. 1.15 is presented in (Schroeder, 1987), Chapter 13, where 'x' is denoted as 'γ' *and* '$d \cdot \cos\varphi_B$' is denoted as 'b'.

The wavelength for which the efficiency is maximum is called blaze wavelength, λ_B. It is a very important characteristic of a diffraction grating, however it is not considered as a different grating constant because it can be calculated once the blaze angle and the groove density are known.

1.2.6 Types of spectrographs

Spectrographs can be classified based on its optical configuration:

1. Czerny-Turner

   In this configuration (Fig. 1.7) the incident light is diverging from a source or slit, and collimated by a concave mirror. The diffracted light is focused by the camera mirror, that is also a second concave mirror.

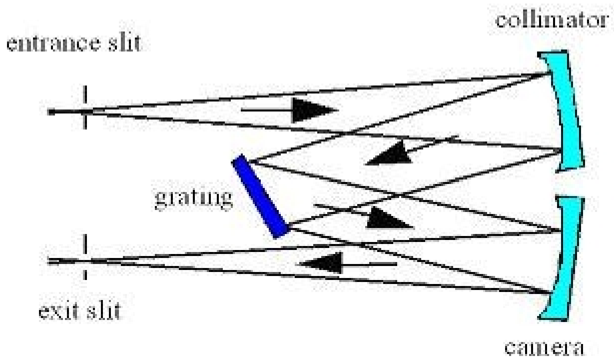

Figure 1.7: Layout of the Czerny-Turner configuration. This figure belongs to the Diffraction Grating Handbook, 6^{th} Edition, Newport Corporation.

2. Ebert-Fastie

   This configuration (Fig. 1.8) is a special case of a Czerny-Turner mount in which the collimator and camera mirrors form part of a single conic surface.

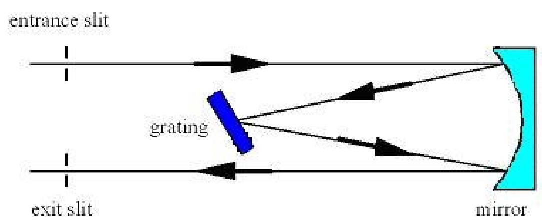

Figure 1.8: Layout of the Ebert-Fastie configuration. This figure belongs to the Diffraction Grating Handbook, 6^{th} Edition, Newport Corporation.

3. Monk-Gillieson

   In this configuration (Fig. 1.9), as a difference with the last cases, the plane grating is illuminated by converging light and after it an exit slit is got. The grating diffracts the light, which converges toward the exit slit.

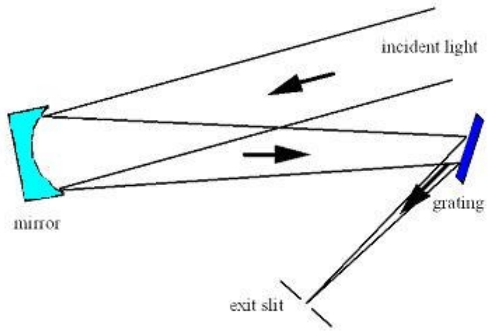

Figure 1.9: Layout of the Monk-Gillieson configuration. This figure belongs to the Diffraction Grating Handbook, 6^{th} Edition, Newport Corporation.

4. Littrow

   In Littrow configuration the incidence and output angles with respect to the grating are the same and equal to the blaze angle. The beam follows the same input and output optical path in different directions. If a reflective diffraction grating is considered, the same lens works as collimator and camera elements, as shown in the sketch of Fig. 1.10. If the incidence grating angle is very similar to the blaze angle and there is a small variation between the input and output grating angles, then the configuration is defined as quasi-Littrow and Ebert configuration when these angles are appreciably different.

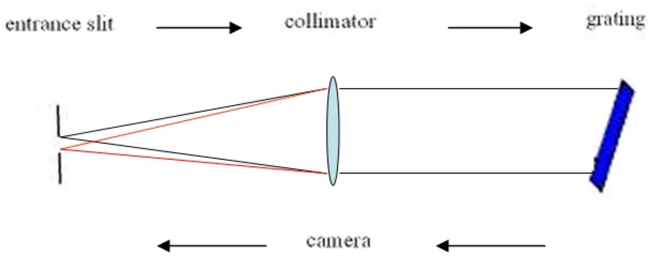

Figure 1.10: In this sketch, the beam schematised in black represents the Littrow configuration, in which the beam returns following exactly the same optical path. And the red beam, for which there is a small variation respect to the Littrow condition, represents the quasi-Littrow configuration.

1.2.7 Spectral resolution

The spectral resolution, R_T, of a spectrograph is limited by three elements: slit, grating and detector, whose resolution elements are $\delta\lambda_s$, $\delta\lambda_g$ and $\delta\lambda_d$, respectively.

The slit resolution element is defined by Eq. 1.20.

$$\delta\lambda_s = W_s \cdot \frac{f_{cam}}{f_{col}} \cdot L^{-1} \tag{1.20}$$

the factor L^{-1} corresponds to the reciprocal linear dispersion in units of Å/mm. The direct linear dispersion, in mm/ Å, is calculated using Eq. 1.21.

$$L = \frac{m \cdot f_{cam}}{d \cdot \cos\Theta_o \cdot \cos(\Theta_i - \Theta_o)^2} \tag{1.21}$$

In this equation, d is the grating constant, inverse of the groove density and m is the diffraction order. The factor $\cos(\Theta_i - \Theta_o)^2$ is usually of the order of 0.99 $\simeq$1. Since this factor does not vary the result, is commonly omitted in Eq. 1.21 and Eq. 1.21 is generally used as shown in Eq. 1.22.

$$L \approx \frac{m \cdot f_{cam}}{d \cdot \cos\Theta_o} \tag{1.22}$$

The reciprocal linear dispersion, L^{-1} is calculated using Eq. 1.23.

$$L^{-1} \approx \frac{d \cdot \cos(\theta_o)}{f_{cam} \cdot m} \tag{1.23}$$

The grating resolution element is defined by Eq. 1.24. N is the total number of lines of the grating illuminated by the projection of the pupil. The bigger the number of lines, the higher the spectral resolution. D_{pup}, defined in Eq. 1.25, is the pupil diameter.

$$\delta\lambda_g = \frac{\lambda}{N \cdot m} \tag{1.24}$$

$$N = \frac{\sigma \cdot D_{pup}}{\cos(\Theta_i)} \tag{1.25}$$

The detector resolution element is defined by Eq. 1.26. Where τ is the linear pixel size and $\Gamma_{R.S.}$ is the magnification of the reimaging system.

$$\delta\lambda_d = \frac{2 \cdot \tau \cdot L^{-1}}{\Gamma_{R.S.}} \tag{1.26}$$

The total resolution element, $\delta\lambda_T$, is a function of these three resoluton elements and is calculated using Eq. 1.28.

$$\delta\lambda_T = f(\delta\lambda_s, \delta\lambda_g, \delta\lambda_d) \tag{1.27}$$

$$\delta\lambda_T = \sqrt{\delta\lambda_s^2 + \delta\lambda_g^2 + \delta\lambda_d^2} \tag{1.28}$$

where $\delta\lambda_s$, $\delta\lambda_g$ and $\delta\lambda_d$ are described by Eqs. 1.20, 1.24 and 1.26, respectively.

The total spectral resolving power is calculated with the total spectral resolution element, as defined in Eq. 1.29.

$$R_T = \frac{\lambda}{\delta\lambda_T} \tag{1.29}$$

The grating spectral resolving power is calculated applying Eq. 1.30.

$$R_g = \frac{\lambda}{\delta\lambda_g} = N \cdot m = \frac{\sigma \cdot D_{pup} \cdot m}{\cos(\Theta_i)} \tag{1.30}$$

Another important parameter is the sampling, S, which defines the spectral interval covered by a pixel. It is defined by Eq. 1.31.

$$S = \frac{L^{-1} \cdot \tau}{\Gamma_{R.S.}} \tag{1.31}$$

1.3 Predisperser

When a polichromatic beam is dispersed, the spectra of its constituent wavelengths can be overlapped at different diffraction orders (see Fig. 1.11). To avoid this overlapping it is needed to filter the wavelengths of interest blocking the contribution of others. Order sorting filters, also called prefilters, are an option to select a spectral range of the incoming light. Predispersers are another alternative. They present the same optical configuration than a spectrograph, usually with shorter focal lengths, and using plane-ruled diffraction gratings. They separate spectrally the entrance beam and use a slit mask at their image focal plane to select the wavelengths of interest at the appropriate diffraction orders.

The design of the predisperser considers parameters like the grating dispersion, its inclination angle or the camera focal length to locate adequately the required wavelengths on the mask. The angle with which the wavelengths illuminate the spectrograph grating can be adjusted by the predisperser so possible overlapping can be avoided and even the grating efficiency can be improved controlling the spectrograph grating angles.

The angles for the predisperser, $\Theta_{i_{pd}}$ and $\Theta_{o_{pd}}$, can be calculated using the grating equation 1.12. The input angle of the spectrograph grating, $\Theta_{i_{sp}}$, depends on the output angle of the predisperser grating and can be calculated using Eq. 4.15.

$$\Theta_{i_{sp}} = \chi - \arctan(\frac{Z_{pd}}{F_{col_{sp}}})\,, \tag{1.32}$$

where χ is the rotated angle of the spectrograph grating, Z_{pd} is the position of the wavelength at the predisperser image focal plane, which can be calculated using Eq. 1.33 and $F_{col_{sp}}$ is the spectrograph collimator focal length.

$$Z_{pd} = F_{cam_{pd}} \cdot \tan(\Theta_{o_{pd}} - \Theta_{i_{pd}})\,, \tag{1.33}$$

Z_{pd} is calculated using the predisperser camera focal length, $F_{cam_{pd}}$ and the predisperser grating input and output angles, $\Theta_{i_{pd}}$ and $\Theta_{o_{pd}}$.

After the coupling between predisperser and spectrograph, the final direct linear dispersion is obtained by multiplying the values for predisperser and spectrograph.

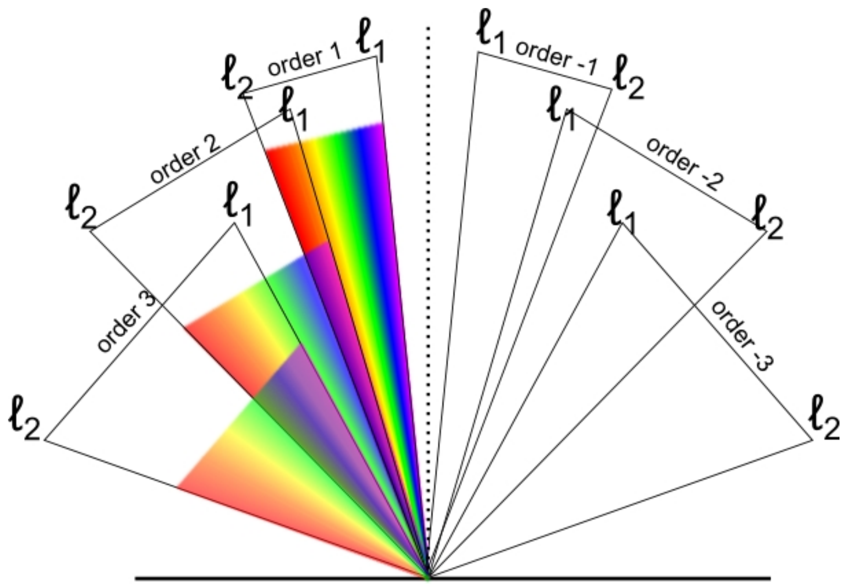

Figure 1.11: Sketch of the distribution of the diffraction orders at both sides of the zero order. Since the dispersion increases with the order, there exist the possibility of wavelengths overlapping, as it is shown in this figure. Unknown source.

1.4 Multi-slit capability and Integral Field Spectroscopy

Generally, spectrographs present one entrance long-slit. However, in order to increase the observed field of view, the number of slits can be increased. There are different ways to generate the multi-slit spectrograph entrance. The easiest way is to place a mask at the telescope image focal plane. In order to observe a larger field of view using a multi-slit mask, it is needed to move the image along the axis perpendicular to the slit length. Each measurement is then done in a different exposure and, thus, with different atmospheric conditions.

In the Sun, the observed small-scale phenomena are constantly evolving with typical temporal scales between seconds and minutes. In order to have spatial continuity in the results, the bidimensional field of view should be measured under the same conditions. This is possible applying Integral Field Spectroscopy (IFS) (Allington-Smith, 2007). IFS reorganises a 2-D field of view into one or more slits using an integral field unit (IFU). The spectra of all the points of the field of view are obtained simultaneously, what provides integrity to the results. This technique is being applied to the new generation of spectrographs dedicated to Astronomy.

The field of view observed using a multi-slit mask at the telescope image focal plane (see Fig. 1.12) can be compared with the bidimensional field of view of Fig. 1.13, using IFS. In the first case the black thin lines represent eight entrance slits. To observe the rest of the field points it is needed to displace the image of the Sun to scan along the X axis. Using an integral field unit, the bidimiensional entrance field of view can be reorganised into eight slits and, to observe a larger field of view, a bidimensional field of view scanning system (along X and Y axis) is needed.

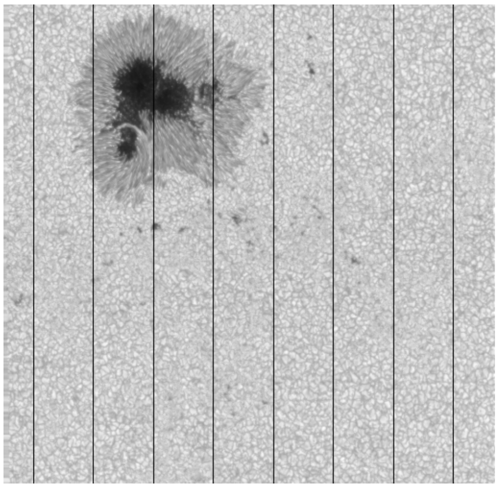

Figure 1.12: Example of the field of view observed using a multi-slit mask at the telescope image focal plane. The 8 black thin lines represent the entrance slits. To observe different field points, it is needed a scanning system to displace the image of the Sun along the X axis. A bidimensional field of view can then be observed but those points observed in different exposures are also measured under different conditions.

1.4.1 Alternatives of integral field unit

There are three alternatives of integral field unit (see Fig. 1.14) that can also be combined. These are: microlenses, optical fibres (commonly used coupled to input, output, or even both, microlenses) and the image slicers.

Microlenses

The microlenses concept is based on the developed techniques carried out by Robert Hooke and Antonie van Leeuwenhoek, in the 17^{th} century. With the advances in technology, this development was applied to other fields, as is the case of Astronomy. The microlenses array was the first option proposed for an integral field unit, at the beginning of 1980, by George Courtes. Microlenses sample the entrance field of view. Each one of the microlenses generate an image of the telescope pupil. The first prototype of an integral field unit using an array of microlenses was designed for the instrument TIGER (Bacon et al., 1995). The basic optical properties of a microlens are the lens diameter and the effective focal length. The disadvantage of this alternative is the overlapping of the spectra on the detector, at the spectrograph image focal plane.

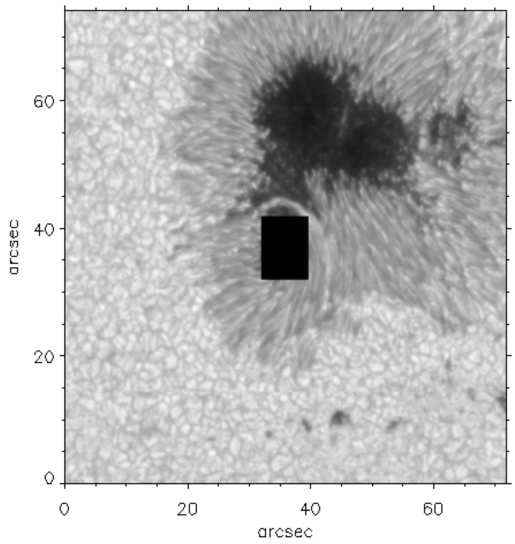

Figure 1.13: Example of the entrance field of view for integral field spectroscopy. A 2-D field of view is observed in a time exposure, getting the spectrum of all the points under the same conditions. For the spectrograph described in this thesis, an 80 arcsec^2 is reorganise into eight slits, each one with 200 arcsec length $\times$ 0.05 arcsec width. To observe a larger field of view a bidimensional scanning system, along x and y axis, is needed.

Optical Fibres

A second alternative for the integral field unit is based on optical fibres. They drive the light within a small area, called core by total internal reflection. The core is surrounded by a transparent layer, known as cladding, whose material presents a lower index of refraction. Inside the fiber the light is multiple times reflected due to incidences with angles that are larger than the critical one. This implies a total reflection of the beam. Only light that enters the fibre within a certain range of angles can travel down the fibre without leaking out. This range of angles is called the acceptance cone of the fibre (Eq. 1.34). The size of this acceptance cone is a function of the refractive index difference between the fibre core and cladding. There is a maximum angle from the fibre axis at which light may enter the fibre so that it will propagate, or travel, in the core of the fibre. The sine of this maximum angle, multiplied by the index of refraction in which the light travels, is the numerical aperture (NA) of the fibre, defined in Eq. 1.34.

$$NA = n \cdot \sin\theta\,, \tag{1.34}$$

where NA is the numerical aperture, n is the index of refraction of the medium in which the light travels and θ is the half-angle of the maximum cone of light.

The numerical aperture of an optical system can be defined as a dimensionless number that characterises the range of angles over which the system can accept or emit light. In the structure of an optical fibre, three or four components, dependending on the type of fibre and the materials, can be distinguished. These, from inside to outside, are: core, cladding, buffer and jacket.

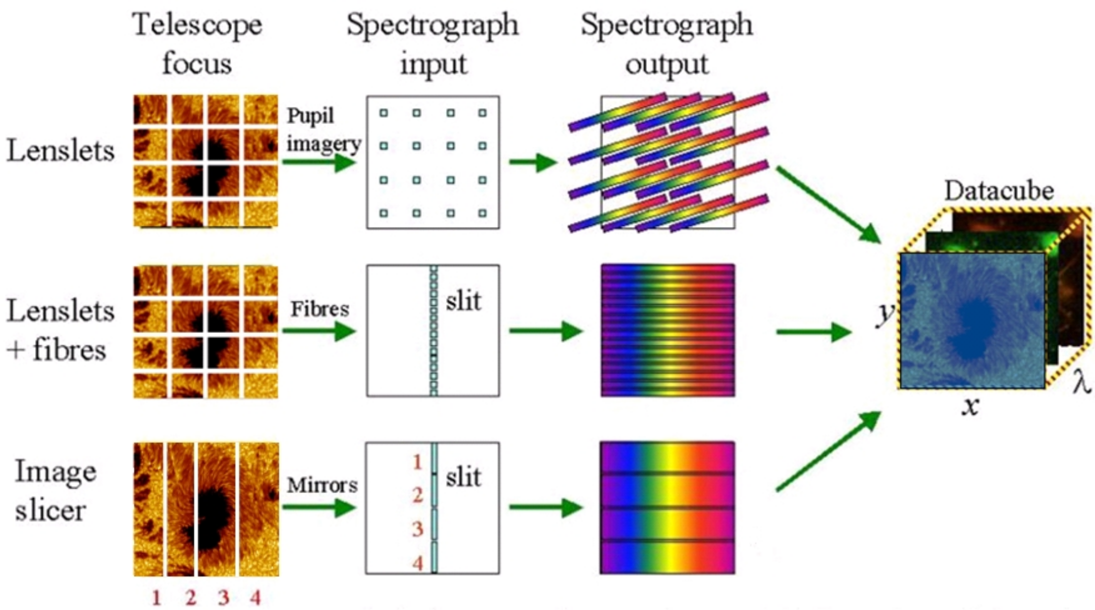

Figure 1.14: Alternatives of integral field unit. Using microlenses the spectra are overlapped at the spectrograph image focal plane. The combination of optical fibres with microlenses avoid this problem but, on the other hand, the fibres are depolarising elements and then, non indicated for instruments with polarimetric capabilities. Rectangular undepolarising fibres are currently under development (Lin, 2012). The focal ratio degradation and the transmission in the infrared spectral range are other negative points in the case of fibres. Image slicers, with a correct design that control the pupil and using the minimum number of surfaces with the best coating for the spectral interval of interest is the best choice for the spectrograph of this thesis.

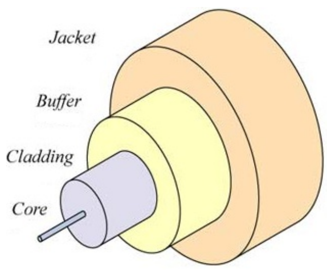

Figure 1.15: Different layers of an optical fibre. Unknown source.

Taking into account the diameter of the core, two types of fibres can be defined: single-mode if the diameter of the core is smaller or equal to 9 μm and multi-mode for diameters on the order of 50 to 62.5 μm. The difference between these two types of fibres is the number of modes that they present. A multi-mode fibre can spread more than one mode of light, even more than one thousand of modes while single-mode, as their name says, have only one way of spreading light.

Optical fibre will only propagate light whose input angle on the core is contained within a certain cone, known as the acceptance cone of the fibre. The half-angle of this cone is called the acceptance angle, θ_{max}. The acceptance angle of a multimode fibre is determined by the index of refraction of core and cladding, n_1 and n_2, respectively, according to Eq. 1.35. This Equation is presented in (Hecht, 2000), Chapter 5, using a different nomenclature, where n is denoted as n_i, n_1 as n_f and n_2 as n_c.

$$n \cdot \sin \theta_{max} = \sqrt{n_1^2 - n_2^2}\,, \tag{1.35}$$

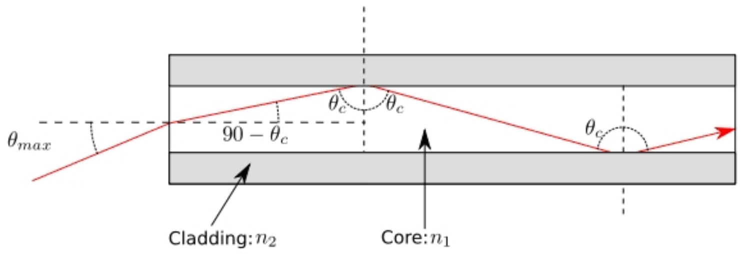

Figure 1.16: Sketch of the acceptance angle of an optical fibre. The maximum angle is a function of the core and cladding index of refraction. Unknown source.

An advantage of using optical fibres is their versatility to rearrange a bidimensional field of view, even with different shapes, in one or more slits. The following figure shows some examples of the reorganisation of several small fields or a larger one into one long slit that, in this case has been duplicated to simulate two orthogonal polarisation modes of the light.

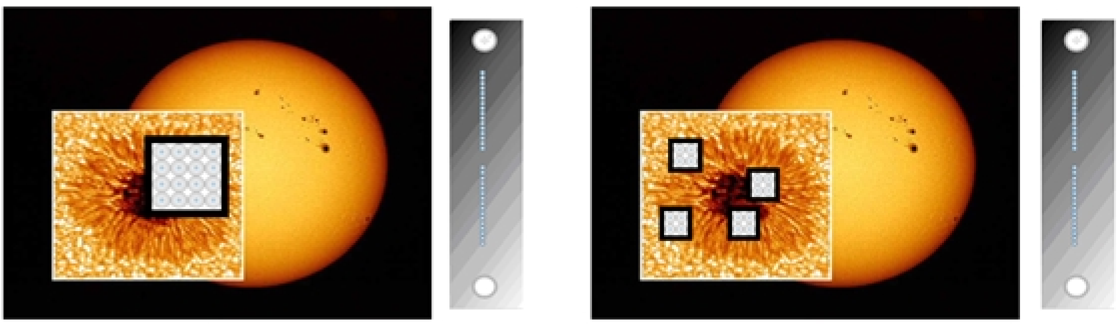

Figure 1.17: Two examples of the versatility of optical fibres to reorganise the entrance field of view. On the left, a bidimensional field of view of the sun is reorganised in one slit. On the right, fibres are used to observe different smaller fields and rearrange them into one slit. In both cases, the slit has been duplicated to simulate two orthogonal states of polarisation of the light.

The most common use of optical fibres in Astronomy is combined with input, output, or even both, arrays of microlenses. The microlenses are used to adjust the focal ratio for a perfect coupling between the telescope, the IFU and the instrument.

On the other hand, one of the disadvantages of this integral field unit alternative is the focal ratio degradation. The input f-ratio is not preserved, however this effect is minor for small f-ratios. The optimum condition for using the fibres is working with the numerical aperture, what also optimises the efficiency. Nevertheless, the transmission of optical fibres is reduced for infrared wavelengths. The other relevant aspect to discard this option is the

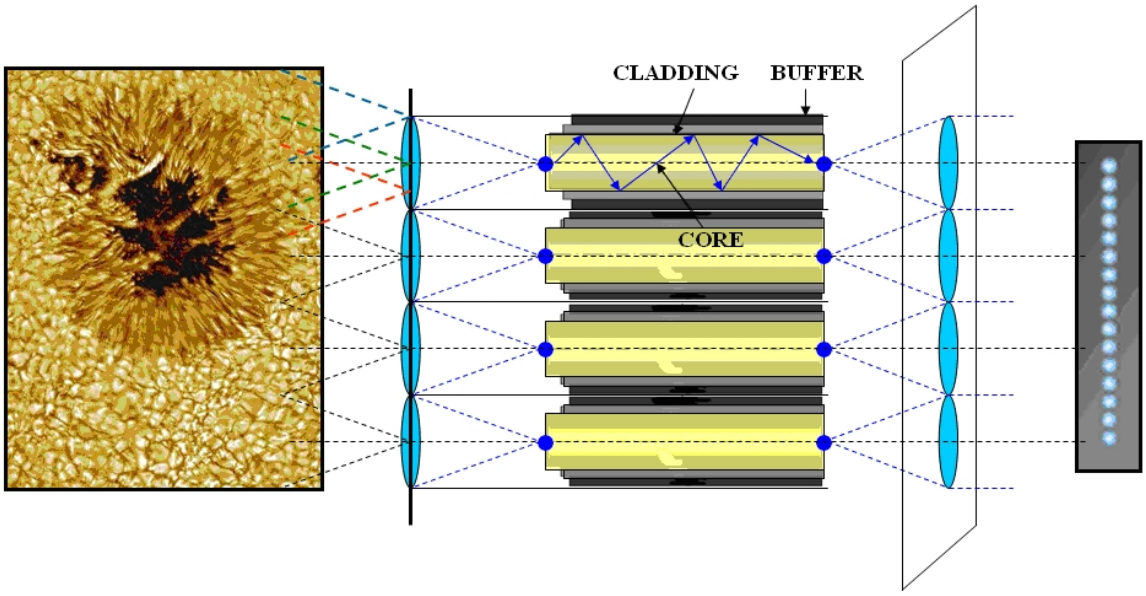

Figure 1.18: Sketch of the coupling between an input array of microlenses, where each one of them produces a pupil image of the field of view and adjusts the input focal-ratio to focus the light on the core, and fibres. The fibres distribute the light and the output microlenses adjust the focal-ratio for the instrument. Finally, a slit is generated as a reorganisation of the bidimensional entrance field of view.

depolarising characteristic of the fibres, however rectangular non-depolarising fibres are currently under development (Lin, 2012). This reason, added to the others, lead us to rule out the option of optical fibres.

Image slicer

Image slicers are the current alternative applied to the new generation spectrographs for the largest telescopes. It is a compact, elegant and high efficiency alternative. It solves some of the critical points of the previous alternatives. There is no spectra overlapping, neither focal-ratio degradation.

The function of an image slicer can be summarised in four steps:

- to cut the bidimensional entrance field of view,
- to control the pupil by imaging it in an intermediate position,
- to focus each piece of the field, one on top of the other, reorganising the field into one or more slits,
- and, for telecentric systems, to send the exit pupil to infinity.

An image slicer is a system composed by two or three arrays of elements, depending on the design. They can use reflective or refractive components, or even a combination of both. Only reflective ones are considered in this proposal.

In general its components are: slicer mirror array, pupil mirror array and focusing mirror array, that can also be found under other names in the literature, but with the same functionality. The first array of mirrors cuts the entrance field in very thin slices, whose width determines the input spatial sampling of the instrument. It is located at the telescope image focal plane. There, the telescope beam is decomposed in different sub-beams, as many as the number of slicer mirrors. These reflect the light corresponding to different parts of the field of view using X and Y-axis tilts. Depending on the design and, to control the position of the pupil to keep the telecentricity, the second array of powered mirrors can be located at the pupil positions (then called pupil mirrors) or a mask could replace them, allowing the light to pass through it to avoid the contribution of scattered light. The last component is common for all the designs of image slicers and consists in an array of powered mirrors that focus the sub-beams, one on top of the others using X and Y-axis tilts, generating the output slit. For telecentric systems this array executes 2 important functions: to focus the beam of each configuration and to send the pupil to infinity.

Thus, the optical path of each sub-beam is such that the light is reflected using one mirror of each array, starting with a part of the image, at the telescope image focal plane, and finishing as a part of the output slit, at the instrument object focal plane. This is called a configuration.

Image slicer is the best choice for the integral field spectrograph of EST.

1.5 Existing solar spectrographs

Solar observations require high spatial, spectral and temporal resolutions. Spectroscopy is one of the most used techniques in solar physics. Currently there are different solutions to make solar spectroscopy.

Single slit spectrographs produce the spectra of the slit points in each exposure. Spectroscopy, thus, is done along one dimension. A larger field of view can be observed using a scanning system along the direction orthogonal to the slit. This concept can be developed together with multi-wavelength capability, as in the cases of the spectrographs of THEMIS (Rayrole & Mein, 1993), VTT (Staiger, 2011), POLIS (Schmidt et al., 2003), TRIPPEL (Kiselman et al., 2011) at the Swedish Solar Tower (SST), ASP (Advanced Stokes Polarimeter), (Skumanich et al., 1997), SPINOR (Socas-Navarro et al., 2006) or ViSP (de Wijn et al., 2012), which allow different combinations of simultaneous wavelengths. However, their configurations are different.

The spectrographs of THEMIS and VTT are preceded by a predisperser. The THEMIS telescope presents a diameter of 90 cm. Its spectrograph allows the observation of up to ten wavelengths simultaneously, opening the possibility to perform 3D inversions of the magnetic field structure in the solar atmosphere (Gelly & THEMIS Team, 2007). The German Vacuum Tower Telescope (VTT) has a diameter of 70 cm. Its spectrograph offers the possibility to observe up to three wavelength regions at the same time, which are selected by the predisperser. Three gratings with different blaze angles are available to optimise the light throughput and, as well as at THEMIS, a number of detectors are available for simultaneous observations of different spectral bands.

POLIS and TRIPPEL are designed to work in Littrow configuration. POLIS, POlarimetric LIttrow Spectrograph (Schmidt et al., 2001), allows the observation of photosphere and chromosphere observing different wavelengths simultaneously, as two Fe I lines at 6301 Å and 6302 Å and the Ca II H line at 3969 Å at the Vacuum Tower Telescope. The TRI-Port Polarimetric Echelle-Littrow spectrograph, TRIPPEL, is one of the instruments of the SST (1 m). It is called like this because it can observe three wavelengths simultaneously.

The Advanced Stokes Polarimeter, ASP, has been designed for the Dunn Solar Telescope (0.76 m) at Sunspot, New Mexico for high spatial resolution quantitative measurement of magnetic fields at multiple heights in the solar atmosphere (Elmore et al., 1992). Multiple CCDs are used for detection followed by video processing to produce spatial maps of the full state of polarisation in restricted regions of the solar spectrum. It measures two spectral regions simultaneously, which include lines sensitive to the Zeeman effect. The Spectro-Polarimeter for Infrared and Optical Regions, SPINOR, is an instrument for the Dunn Solar Telescope at the National Solar Observatory. While ASP only observed in the visible spectral range, SPINOR extends the coverage range to the infrared, from 4000 to 16000 Å. It is provided by different camera lenses for the simultaneous observation of several wavelengths within this interval. The Visible Spectro-Polarimeter, ViSP (Nelson et al., 2010), is one of the first light instruments for the 4-m Advanced Technology Solar Telescope, ATST (Rimmele et al., 2012). It is a slit-based spectro-polarimeter designed to measure three different regions of the solar spectrum within 3800 and 9000 Å in three separate focal planes simultaneously, using different camera lenses like SPINOR.

Some spectrographs can also work like an imaging-spectrograph. This is the case of MSDP (Mein, 1992), whose concept has been adapted to different telescopes since 1970 like the Meudon Solar Tower, the Turret Dome of Pic-du-Midi, the German VTT telescope of Tenerife, the Wroclaw large coronograph, THEMIS (Mein, 2002) and its current adaptation for EST (Sayède et al., 2010), or TUNIS (López Ariste et al., 2010).

Both, MSDP and TUNIS, are based on the subtractive double pass. In subtractive mode, the light passes through the spectrograph twice. The first pass disperses the light and, at the focal plane of the spectrograph, a narrow slit or a mask is applied to the spectrum. The light thus selected with a small bandwidth is sent back to the spectrograph for a second pass with an optically reversed sign for the dispersion. The result is a spectro-image, a monochromatic image of the wide 2-D entrance field of view with a linearly varying wavelength in one spatial dimension where the spectral gradient and the spatial scale are coupled. The MSDP design at THEMIS has capability for simultaneous spectro-imaging in two line profiles. However, its current proposal for the European Solar Telescope (4 m), called NG-MSDP (New Generation Multichannel Subtractive Double Pass) will increase its performance, up to four simultaneous lines. The Tunable Universal Narrow-band Imaging Spectrograph, TUNIS, is currently available at THEMIS telescope and its concept is one of the spectrograph proposals for EST. It aims at recording the 3-dimensional cube of information made by the 2-dimensional imaging and the spectrum at each point. TUNIS also offers a mode using an Hadamard mask (López Ariste et al., 2011a) allowing multiplexing of 31 or 63 wavelengths over the same image point quasi-simultaneously (Calcines et al., 2010a).

Multi-slit spectrographs increase the field of view observed in a time exposure. They can be fed by a mask at the telescope focal plane or using an integral field unit, both ideas have been studied by H. Lin (Lin, 2003a) for the near-infrared spectrograph of the Advanced Technology Solar Telescope (ATST). The current proposal for both, the near-infrared spectrograph of ATST and SPIES, the SpectroPolarimetric Imager for the Energetic Sun (Lin, 2012), which is a project to develop a new class of spectropolarimetric instrument for the study of highly dynamic solar phenomena, is the implementation of integral field spectroscopy using optical fibers.

The integral field spectrograph described in this thesis unifies the advantages of some of the mentioned spectrographs offering integral field spectroscopy using image slicers with multi-slit and multi-wavelength capabilities.

1.6 The European Solar Telescope

Despite the Sun is the only star that can be spatially resolved from the Earth due to its proximity, there are considerable uncertainties that require advanced telescopes and instrumentation. It is because of this that the initiative of The European Solar Telescope, EST, is developed (Fig. 1.19) (Collados et al., 2010). Fifteen countries of the European Union (Austria, Croatia, Czech Republic, France, Germany, Hungary, Italy, Norway, Poland, Slovakia, Spain, Sweden, Switzerland, The Netherlands and United Kingdom) collaborate in the design of the largest solar telescope of the world, together with the American ATST, with an aperture of 4 metres.

EST is a project promoted by the European Association for Solar Telescopes (EAST), a consortium with the aim, among others, of undertaking the development of the telescope, to keep Europe in the frontier of Solar Physics. It will be located in the Canary Islands and its first light is expected at the beginning of the next decade.

Europe has a wide experience in Solar Physics, supported by the Observatorio del Teide, in Tenerife, where the third largest solar telescope is placed, GREGOR (Schmidt et al., 2012), with a 1.5 metres primary mirror that only differs in 10 centimetres from the McMath-Pierce of Kitt Peak and Big Bear telescopes, and the Observatory of El Roque de los Muchachos, in La Palma, where the Swedish 1-metre Solar Telescope (SST) is currently the most highly resolving solar telescope.

EST will be optimised for studies of the magnetic coupling between the deep photosphere and upper chromosphere. This will require diagnostics of the thermal, dynamic and magnetic properties of the plasma over many scale heights, by using multiple wavelength imaging, spectroscopy and spectropolarimetry. To achieve these goals, EST will specialise in high spatial and temporal resolution using instruments that can efficiently produce two-dimensional spectral information. It is provided with a wide variety of imaging instruments, narrow band and broad band and a family of spectrographs focused on different science cases that present 2 different modes of operation: spectroscopic or spectropolarimetric. The multi-purpose grating spectrograph of EST (Calcines et al., 2012a) is composed by a long slit standard spectrograph (LsSS), by two devices based on the subtractive double pass (TUNIS and MSDP) and by an integral field, multi-slit, multi-wavelength, high resolution spectrograph, whose design is presented in this doctoral thesis.

Provided with these characteristics and based on the presented set of wavelengths associated to diverse science programmes, this spectrograph, coupled to the largest solar telescope,

Figure 1.19: European Solar Telescope design

EST, will address several uncertainties and currently still unknown aspects like: how the magnetic field emerges to the surface and evolves, how the energy is transported from the photosphere to the chromosphere and what originates the temperature increase between these two layers, and how the energy is released and deposited in the upper atmosphere. It will study the structure and evolution of magnetic flux focused on the formation and disappearance of kG flux concentrations in the solar photosphere, magnetopauses and current sheets in the solar atmosphere, small-scale flux emergence and magnetic flux cancellations in the quiet Sun, quiet Sun internetwork fields and polar magnetic fields. A second important point of study is the magnetic coupling of photosphere and chromosphere, for which three main aspects will be studied: the magnetic topology of the photosphere and chromosphere, the conversion of mechanical to magnetic energy in the photosphere as well as the magnetic twist and torsion. About the chromospheric structure, dynamics and heating, there are several important issues, like wave propagation from photosphere to chromosphere, energy dissipation in the chromosphere, large-scale chromospheric release of magnetic energy, observational determination of electric currents and Hanle diagnostics of chromospheric fields. In addition other aims are considered, like magnetised plasma processes and dynamics of large-scale magnetic structures, the solar corona, the explosive Sun, highlighting solar flares and space weather, atomic physics based on spectro-polarimetric observations involving atomic physics phenomena and, even, non-solar astrophysics.

The EST science will focus mainly on those aspects related to solar polarimetry on the disk at very high spatial resolution, particularly for the diagnostics of magnetic fields and dynamics of the photosphere and chromosphere.

The optical design (Sánchez-Capuchino et al., 2010), (Sánchez-Capuchino, 2011) of the telescope (Fig. 1.20) presents an on-axis Gregorian configuration. The telescope mechanical configuration is alt-azimutal. F1 is the Gregorian F/1.5 focus generated by the almost

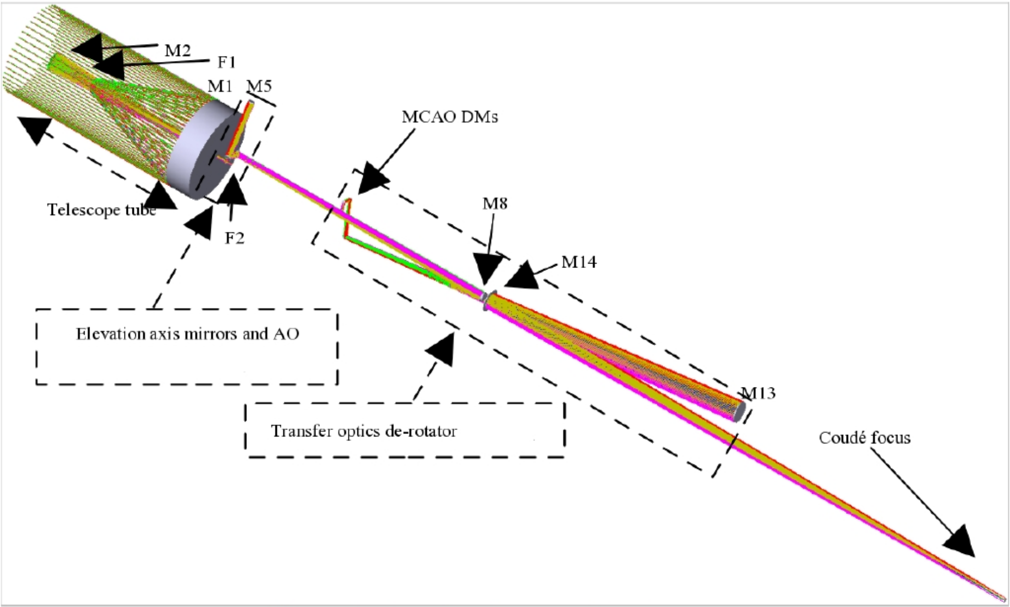

Figure 1.20: Optical layout of the European Solar Telescope (Sánchez-Capuchino et al., 2010), (Sánchez-Capuchino, 2011). F1 is the Gregorian F/1.5 focus generated by the almost parabolic primary mirror, M1. The field of view, 2×2 arcmin^2, is limited by a heat rejecter located there. The focal-ratio at the secondary focus, F2, is F/11.5. M2 is defined as the system pupil and also allows functionalities of tip-tilt mirror. For the purpose of analyzing the polarimetric performance of the rest of the telescope, a truly polarisation-free focus just before the secondary focus F2 is foreseen. M3 and M4 are flat mirrors tilted 45° in perpendicular planes to auto-balance the instrumental polarisation. The telescope elevation axis is located 1.5 m below the primary mirror and is defined by M4 and M5. The transfer optics relaying the secondary focus down to the Science Coudé Focus uses three magnification stages: one to generate the pupil for the AO system, another to generate the focal plane near the MCAO post-focus deformable mirrors and the last one to generate the science coudé focus.

parabolic primary mirror, M1. The field of view, 2×2 arcmin^2, is limited by a heat rejecter located there. The focal-ratio at the second focus, F2, is F/11.5. M2 is defined as the system pupil and also allows functionalities of tip-tilt mirror. For the purpose of analyzing the polarimetric performance of the rest of the telescope, a truly polarisation-free focus just before the secondary focus F2 is foreseen. M3 and M4 are flat mirrors tilted 45° in perpendicular planes to auto-balance the instrumental polarisation. The telescope elevation axis is located 1.5 m below the primary mirror and is defined by M4 and M5. The transfer optics relaying the secondary focus down to the Science Coudé Focus uses three magnification stages: one to generate the pupil for the AO system, another to generate the focal plane near the MCAO post-focus deformable mirrors and the last one to generate the science coudé focus.

The telescope includes Adaptive Optics (AO) and Multiconjugate Adaptive Optics (MCAO) (Soltau et al., 2010) that are integrated in the telescope optical path, described in the EST project internal documentation (Bettonvil et al., 2011a), (Bettonvil et al., 2011b) and (Bettonvil et al., 2011c).

1.7 Objective and structure of the thesis

Because of the importance of the study of the Sun and the understanding of its physical phenomena, not only for Solar Physics, but in general for Stellar Evolution and Sun-Earth relations, the motivation for the development of advanced instrumentation arises. The objective of this thesis is the design of an integral field, high resolution, multi-slit and multi-wavelength spectrograph that, coupled to the largest ground-based solar telescope, EST, pretends to be a powerful tool that allows us to approach the Sun.

Chapter 2 describes the design restrictions that establish the bases for the design. In order to facilitate the understanding of the different subsystems of this complex instrument, these are presented in Chapters 3 and 4 organised in the light path advance direction, explaining how they are coupled. Chapter 3 describes a fundamental module of this instrument: the integral field unit. After analyzing the different alternatives of integral field unit, the image slicer concept has been chosen as the best option according to the characteristics of this spectrograph. A new concept of image slicer has been developed, which undoubtedly increases the spectrograph performances. The design of this instrument also considers the possibility to couple a polarimeter and offer two modes of operation, spectroscopic and spectro-polarimetric. The proposed image slicer is compatible with both modes. The integral field unit entrance field of view is 80 arcsec^2, however a larger field of view, up to 2 $\times$ 2 arcmin^2, can be observed in sequential exposures using a bidimensional field of view scanning system, whose design is also described in this chapter.

Chapter 4 describes the predisperser and spectrograph and, as a special point of interest, the multi-slit mask used to select the combination of simultaneous wavelengths at the predisperser image focal plane, which is also the spectrograph object focal plane. In addition, the reimaging systems used before the detectors to adapt the final focal-ratio are described. These subsystems, perfectly coupled to each other, compose the total instrument layout.

The final performances, including optical designs and calculations, are shown in Chapter 5. Finally, the conclusions obtained from the design study of the proposed instrument, as well as the future perspectives expected for the near-future, are presented in Chapter 6.

2

Design restrictions

In order to satisfy the science requirements, the design has a set of restrictions. All of them are considered and a compromise is finally reached to get the best solution that fulfils the requirements and specifications.

2.1 Instrument Science Requirements and Specifications

It is not often easy to distinguish the instrument requirements and specifications. It is common to find them mixed as if they were the same things. The truth is that, although their definitions are not always clear, they allude to similar things related between them. Technically, the requirements are the conditions imposed to an instrument or at least, what is expected to be reached attending to the science objectives. Then, the specifications are obtained from the requirements as consequences derived from them. In the preliminary design of an instrument, the science motivation can be described as the first step that originates the development of that instrument. The requirements would be the second step to fulfil that motivation and the specifications would be the third step, a derivation of the imposed requirements (Fig. 2.1). These steps are the technical ones. If the scientific steps were also included, then the order would be: science objectives, scientific specifications, technical requirements and technical specifications.

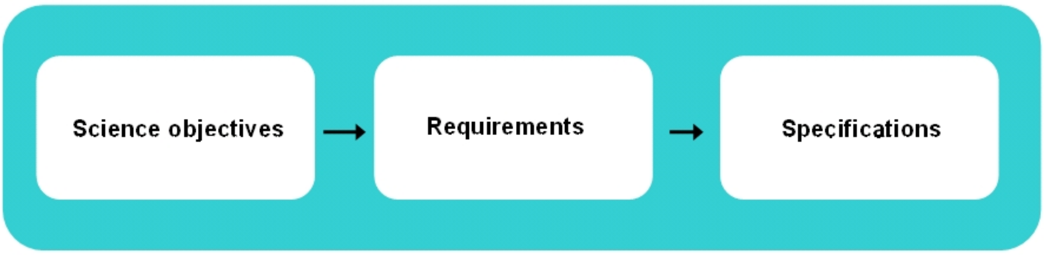

Figure 2.1: The first three steps in the design of an instrument. The science objectives are the motivation to design the instrument. The requirements are the imposed conditions to satisfy the science objectives and the specifications are derived from the requirements.

The requirements are summarised in Table 2.1.

Table 2.1: Requirements for the spectrograph design.

Total spectral resolving power	$\sim$ 300,000
Spatial resolution	0.1 arcsec
Spectral range	3900 – 23000 Å
Number of simultaneous wavelengths	8 (5 visible and 3 IR)

Detectors with the largest size have been considered, whose format is 4k $\times$ 4k. Pixel sizes have been assumed within the standard interval, 10 μm for visible wavelengths and 20 μm for infrared ones. The input sampling defines how thin the entrance field of view is sampled, in this case, literally cut by the image slicer, 0.05 arcsec/slice. The slices in which the field is cut are reorganised one of top of others generating the instrument input slits. Thus, the slices width defines the slits width.

In general for solar physics, and, especially for an instrument with the capabilities of this one, high resolution, both spectral and spatial, are crucial. High spatial resolution is required to observe and study the small structures over the Sun.

In order to resolve adequately the structures associated to the chromosphere and photosphere, a spatial resolution of 0.1 arcsec, what allows resolving structures about 70 km wide at 1 A.U. distance from the Earth and a spectral resolution of $\sim$ 300,000 are required. The higher the spectral resolution, the better the details that can be observed in the spectrum. Spectra with different spectral resolution present the same qualitative behaviour but with the characteristic that the clarity with which the details are observed increases with the resolution.

The instrument must cover a spectral range between 3900 and 23000 Å. This interval has been defined to consider the wavelengths of interest of the main science programmes of Table 1.1 and takes into consideration the spectral interval of the electromagnetic spectrum that can be observed from the Earth, due to its atmosphere.

As it is shown in the examples of Table 1.1, each science programme presents a specific combination of wavelengths to be observed simultaneously. Since in the Sun, as in every star, a different opacity is associated to each spectral line, the multi-wavelength capability applied to this instrument allows the observation of several solar layers and the study of phenomena at different heights at the same time. Specifically, the requirement is to observe eight wavelengths, five from the visible and three from the near-infrared spectral range. This is the maximum number of wavelengths required by the science programmes of Table 1.1. To offer more versatility, the spectrograph can observe different combinations of eight simultaneous wavelengths associated to other programmes that might be proposed.

The specifications for the spectrograph design are shown in Table 2.2. The number of entrance slits has been estimated as the maximum possible assuming detectors with the largest size and considering the required resolution. The field of view is also the largest one compatible with the number of slits, the pixels that the images of them cover over the detector and the sampling. With the field of view (80 arcsec^2) and the number of slits (eight), the field of view per slit is inferred, 0.05 $\times$ 200 arsec^2. The plate scale, 0.05 arcsec/pixel, is a translation of the input sampling, 0.05 arcsec/slit width, through the system. In order to have the appropriate scales on the detectors a focal-ratio conversion is needed, leading to F/10.3 for visible wavelengths and F/20.6 for infrared ones.

Table 2.2: Specifications for the spectrograph design.

Number of entrance slits	8
Field of view	80 arcsec^2
Field of view per slit	0.05 $\times$200 arcsec^2

2.2 Proposed technical solution and conditioning parameters

The proposed technical solution (Calcines, 2011b) is a 1:1 spectrograph with a focal-ratio F/40 based on the Ebert-Fastie configuration, as a special case of the Czerny-Turner one, where collimator and camera elements are off-axis parabolic mirrors that belong to the same on-axis global parabola. After studying different alternatives I have chosen this configuration, since the symmetry of this layout offers very compensated results in terms of optical quality, specially for the multi-wavelength capability. The spectrograph is preceded by a predisperser with the same optical configuration, which acts like a prefilter.

The spectrograph described in this thesis is really very ambitious. The requirements and specifications make it a high level instrument where the compatibility of all these expected parameters is a very hard task. In addition, some other conditioning parameters have been added, as the choice of the diffraction grating.

Commercial diffraction gratings have been considered for costs and efficiency reasons. Theoretical gratings can be manufactured and, at the beginning of the design, theoretical gratings with customised characteristics were calculated. Nevertheless, they imply a very high cost, much more expensive than the catalogue ones. Besides the difference in price, the manufacturer does not guarantee the calculated grating efficiency that can be modified by small differences with respect to the calculated data during the manufacturing process. On the other hand, those gratings offered in a catalogue are already characterised and tested and their response when they are illuminated is known. The difference in costs and the confidence in the grating behaviour are the reasons why commercial diffraction gratings from the Newport catalogue are finally considered. Gratings represent a very restrictive point for the design of this instrument and they drive it in different ways. Their efficiency for the multi-wavelength capability makes it not possible to find a commercial diffraction grating which presents a high efficiency for all the wavelengths, visible and infrared, simultaneously. This means that the grating could be used for the wavelengths separately, with a different orientation for each one, but not for a set of eight wavelengths in a fixed configuration. This limitation leads to a division of the spectral range, which is proposed to be split into four intervals (Table 2.3), two visible ones, called VIS-I, from 3900 to 5600 Å, and VIS-II, from 5600 to 11000 Å, and two infrared intervals, IR-I, from 7000 to 16000 Å, and IR-II, from 10000 to 23000 Å. For this reason, four spectrographs conceptually identical are proposed, with smaller sizes of the optical components and specific gratings optimised for the wavelengths of each interval. The spectral divisions are made using dichroics attending to the commercial gratings efficiencies, whose curves are presented in Chapter 5. The overlapping region (from 7000 Å to 11000 Å) gives the versatility to observe spectral lines in this region in the visible or the near-infrared spectral ranges (Calcines et al., 2010a). A dichroic is an optical element used to divide a beam into two different spectral intervals. It allows the trasmission of a range of wavelengths and reflects the others. This is outlined in Fig. 2.2.

Table 2.3: Spectral range divisions for the four spectrographs.

VIS-I	3900-5600 Å
VIS-II	5600-11000 Å
IR-I	7000-16000 Å
IR-II	10000-23000 Å

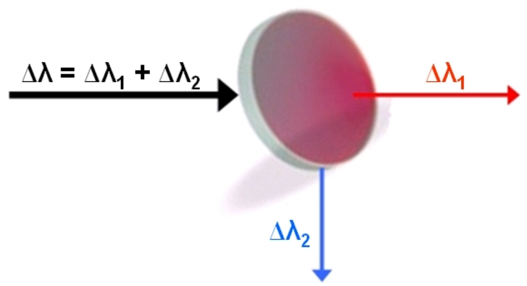

Figure 2.2: Sketch of how a dichroic works. It transmits a specific spectral range and reflects the rest of the incoming beam.

A first dichroic (D1) divides the visible and near-infrared spectral ranges. Then, each spectral interval is itself again divided using another dichroic (D2 and D3). So, three dichroics are needed to generate the foci for the four spectrographs. For the two IR spectrographs special dichroics are needed, in order to allow the pass of specific wavelengths and its approximately multiples, like 8498 Å, 8542 Å, 15260 Å and 15650 Å for IR-I and 10827 Å, 22300 Å for IR-II, as well as other intermediate wavelengths of the interval. These dichroics working on this way are interferential filters designed for the required wavelengths. The ranges have been divided attending to the efficiencies of the commercial gratings, however there is the possibility to extend the spectral range of the VIS-II spectrograph until 11000 Å.

Since the pupil is imaged at the diffraction grating, the grating physical size also conditions the design on this sense. The pupil diameter is then limited by the grating size.

Different focal ratios have been studied. In every case, for a given f-number and a commercial grating, the requirement of resolution, as well as the optical quality, determine the collimator and camera focal lengths. The detector format and size, define the separation between the eight entrance slits, as well as the predisperser mask slits. The spectral resolution determines the width of the input slits images on the detector. To obtain the adequate scales, the pixel size and the spectral resolution determine the final focal-ratio. All these conditioning parameters are presented in the diagram of Fig. 2.3.

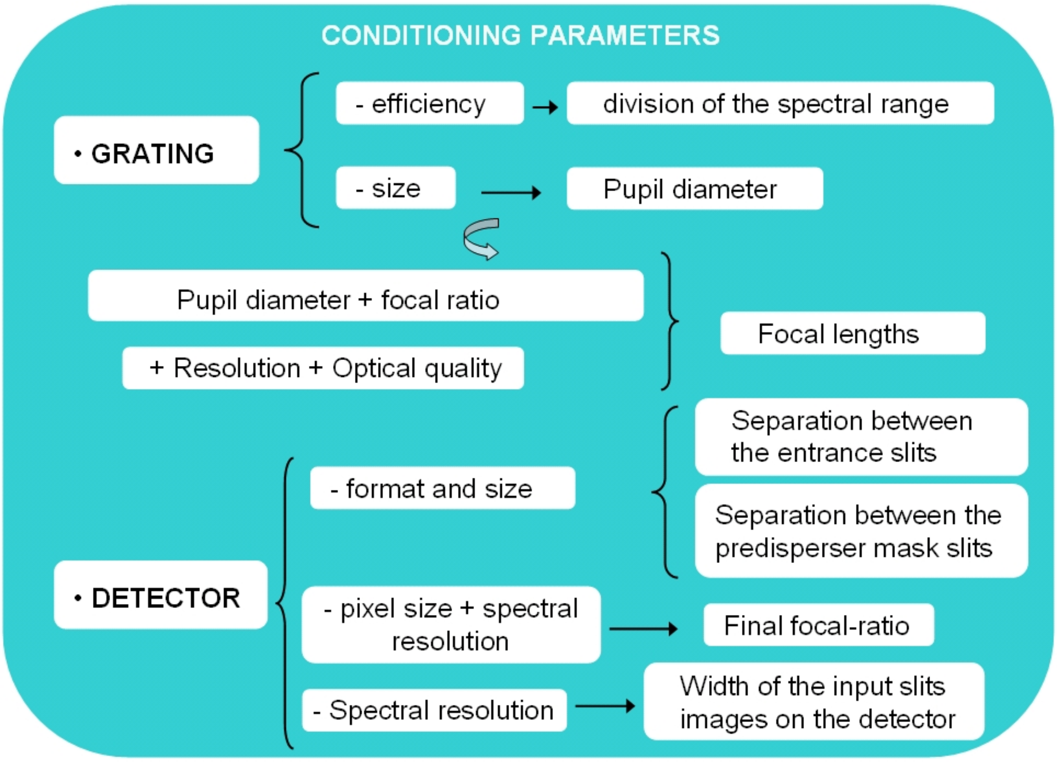

Figure 2.3: Diagram of the conditioning parameters in the spectrograph design.

2.3 Focal-ratio study

Each optical system works best for a specific range of f-numbers in terms of optical quality, resolution or even limited by the physical size of the optical components.

The instrument entrance focal-ratio is given by the telescope, which offers an F/50 beam. The spectrograph final focal-ratio (on the detectors) is determined in order to have the appropriate scale. Different options from F/10 to F/50 for VIS-I and VIS-II and from F/20 to F/50 for IR-I and IR-II have been studied to fit the requirements. The most appropriate focal-ratios for the spectrographs seem to be the final ones, F/10.3 and F/20.6, or the telescope f-number. However, the decision about the focal-ratio has taken into account other parameters. The results obtained from the focal-ratio studies are described below.

2.3.1 Focal-ratio vs. focal length

Since the physical size of the diffraction gratings limits the maximum pupil diameter, for a given focal-ratio it also limits the largest focal lengths. For the studied range of focal-ratios, the maximum focal lengths vary from 2 to 10 metres, as it is shown in Fig. 2.4. This gives a first range of values that will be reduced when introducing other factors as the aberrations or the resolution.

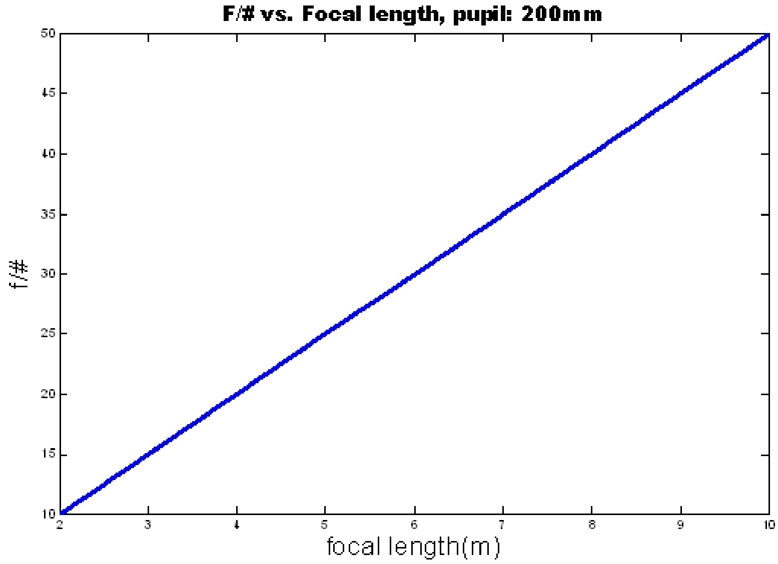

Figure 2.4: F-number versus focal length for a 200 mm pupil diameter.

2.3.2 Focal-ratio conversion before or after the spectrographs

According to the spectrographs requirements, a focal-ratio conversion is required before the detectors, converting the beam into F/10.3 for the visible spectrographs and F/20.6 for the infrared ones. The question is: should the conversion be done before or after the spectrographs? Both options have been studied and compared.

As an example, the VIS-I spectrograph has been evaluated using an entrance F/10 beam, for the lines Ca II K at 3933 Å, Ca II H at 3968 Å and H_ε at 3970 Å, which correspond to the Flares science programmes. These wavelengths are too separated to be observed with the same detector but, using a focal length of 2 metres they are too close to each other to allow using two detectors without vignetting (see Fig. 2.5). The change of the orientation of the grating only moves the wavelengths at the image focal plane with respect to the optical axis, but does not separate them, as it is shown in Fig. 2.6, where the same optical design has been evaluated for three different orientation angles. A larger focal length is needed to increase the separation between the wavelengths at the image focal plane. In addition, an important point is that, with a fast focal-ratio and a short focal length, the beam is focused sharply, what produces aberrations and a good optical quality is not possible without extra optical elements to correct them. Fig. 2.7 shows the spot diagram corresponding to the design presented in Fig. 2.5, which shows the incidence of the rays at the spectrograph image focal plane. The spots, for each field, are so aberrated that the size is much bigger than the Airy disk, which despite being also represented is not visible at this scale. Parabolic mirrors are used for this layout. The aberration that prevails is coma, due to the incidence of off-axis field points with strong angles, what occurs in fast optical systems. In addition, a smaller contribution of distortion exists. The optical quality is not improved using spheres or a different type of conic surface.

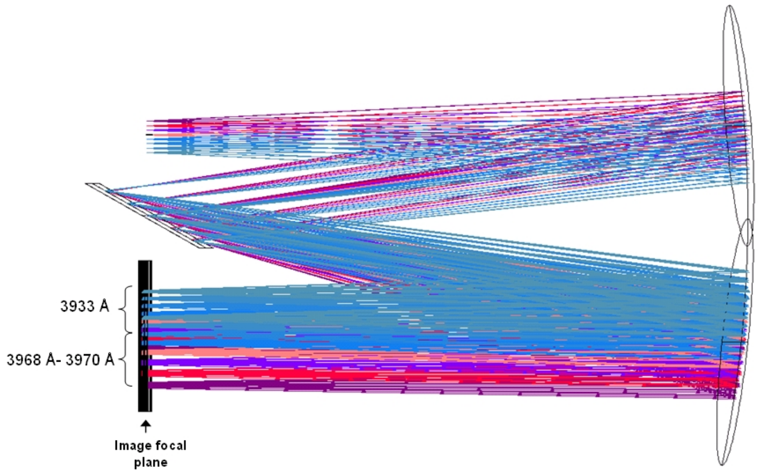

Figure 2.5: Optical design of the VIS-I spectrograph for a 1:1 layout with a focal ratio F/10 and a focal length of 2 m. The colours represent different optical fields. This ZEMAX design is evaluated at the lines Ca II K at 3933 Å, Ca II H at 3968 Å and H_ε at 3970 Å, which correspond to the Flares science programmes. These wavelengths are too separated to be observed within the spectral range of the same detector, but, using a focal length of 2 metres, they are too close to each other to be observed in two different detectors. In this design, there is not enough space between the wavelengths at the image focal plane to allow using two detectors without vignetting. A larger focal length is needed to increase the separation between the wavelengths.

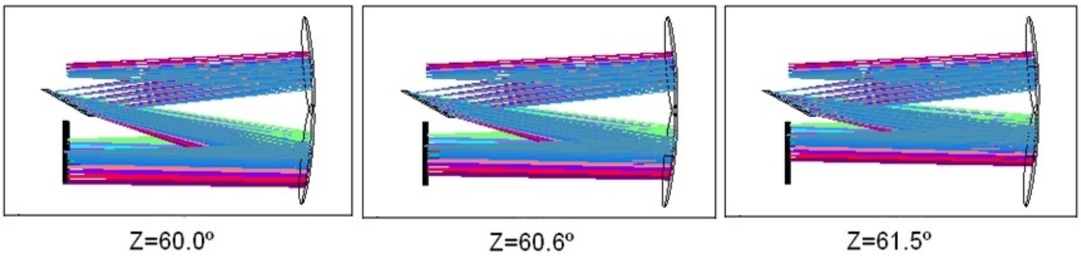

Figure 2.6: The same design (corresponding to the layout of Fig. 2.5) evaluated for three different rotation angles of the diffraction grating. Z is the tilted angle in the grating coordinate break of the ZEMAX file. The angle of the grating modifies the decentred distances of the beams with respect to the optical axis but does not separate them. Using the same image focal plane representation (in black) for all of them, the change in the orientation of the grating leads to a different position of the image at the final focal plane. Three positions (down, centred and up, from left to right) are shown in this example for three angles: 60.0°, 60.6° and 61.5°.

If the same pupil diameter and final focal-ratio are used, the decision of making the focal-ratio conversion before or after the spectrograph does not affect the total spectral resolving power.

The slit width changes with the focal-ratio. The field of view is the same, 0.05 arcsec, however it implies a size of 50 μm for F/50, 40 μm for F/40 and 10 μm for F/10. The slit resolution element, defined by Eq. 1.20, can be calculated for the two focal-ratios, F/40 and F/10, whose camera focal lengths are 8 metres and 2 metres, respectively, using Eqs. 2.1 and 2.2.

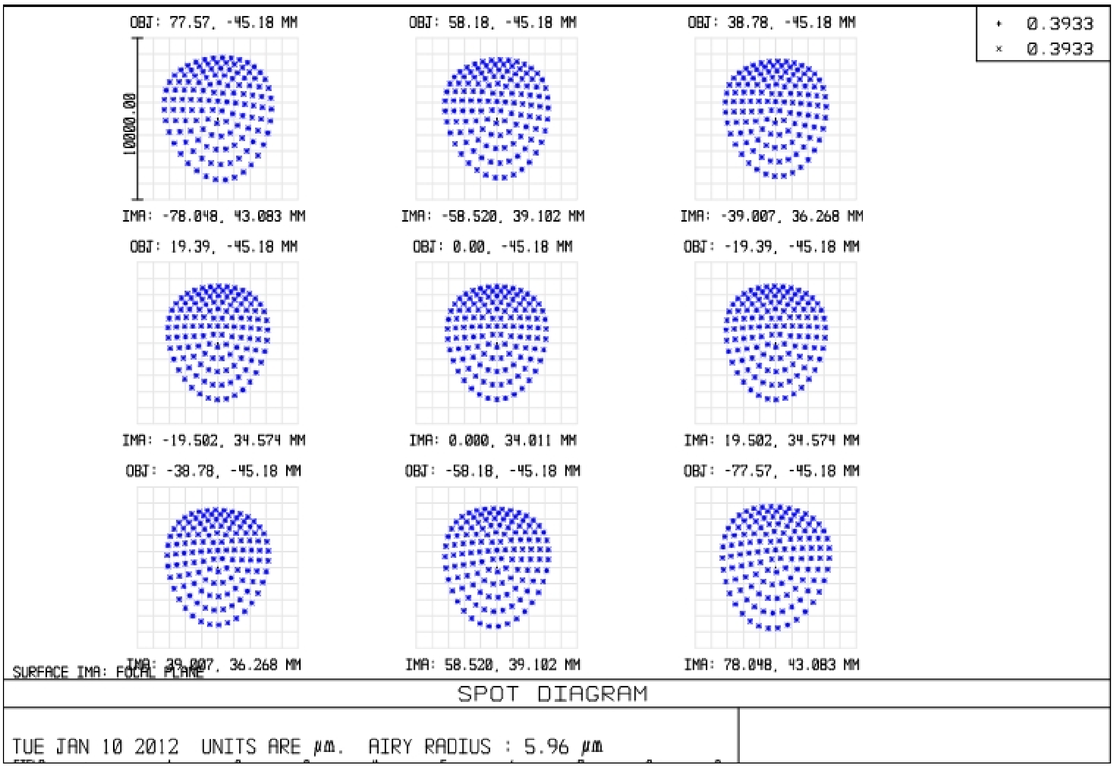

Figure 2.7: Spot diagram associated to the wavelength 3933 Å. The different spots correspond to different field points of one of the eight input slits, represented separately for more clarity. Because of the use of a fast focal-ratio (F/10) and a short focal length (2 m), the beams are focused sharply, what produces aberrations. The Airy disk is also represented but it is not visible due to the large size of the aberrated spots.

$$\delta\lambda_{s40} = W_{s40} \cdot \frac{f_{cam}}{f_{col}} \cdot L_{40}^{-1} \tag{2.1}$$

$$\delta\lambda_{s10} = W_{s10} \cdot \frac{f_{cam}}{f_{col}} \cdot L_{10}^{-1} \tag{2.2}$$

Since 1:1 systems are considered in both cases, the ratio between the collimator and camera focal lengths is 1. The reciprocal linear dispersion, L^{-1}, defined by Eq. 1.23, is a function of the grating constant, d, the diffraction order, m, the output grating angle of the beam, Θ_o, and the camera focal length, f_{cam}. It can be calculated for F/40 and F/10 with Eqs. 2.3 and 2.4. Since the grating is the same, d and m are the same for the different focal-ratios, as well as the grating angles. So, the reciprocal linear dispersion is a function of the camera focal length.

$$L_{40}^{-1} = \frac{d \cdot \cos(\theta_o)}{f_{cam40} \cdot m} \tag{2.3}$$

$$L_{10}^{-1} = \frac{d \cdot \cos(\theta_o)}{f_{cam10} \cdot m} \tag{2.4}$$

The slit resolution elements are then defined by Eqs. 2.5 and 2.6.

$$\delta\lambda_{s_{40}} = 0.040 \cdot \frac{d \cdot \cos\Theta_o}{f_{cam40} \cdot m} \tag{2.5}$$

$$\delta\lambda_{s_{10}} = 0.010 \cdot \frac{d \cdot \cos\Theta_o}{f_{cam10} \cdot m} \tag{2.6}$$

The ratio between Eqs. 2.5 and 2.6 is defined by Eq. 2.7.

$$\frac{\delta\lambda_{s10}}{\delta\lambda_{s40}} = \frac{0.010 \cdot f_{cam40}}{0.040 \cdot f_{cam10}} = 1 \tag{2.7}$$

So, if the focal-ratio and the focal length of a spectrograph are modified, keeping the ratio of Eq. 2.7 for the specific values of the studied optical system, the slit does not limit the spectral resolving power.

The pupil diameter of the two optical systems considered, with a focal-ratio F/10 and 2 metres focal length and F/40 with 8 metres focal length, is 200 mm. The grating spectral resolution, defined by Eq. 1.24 depends on the wavelength, the input grating angle of the beam, the diffraction order, grating grooves density and the pupil diameter. Since these parameters are the same in both cases, the grating is not the limiting cause for the total spectral resolution.

The resolution element associated to the detector is defined by Eq. 1.26, which can be particularised for the considered f-numbers, as shown in Eqs. 2.8 and 2.9.

$$\delta\lambda_{d40} = \frac{2 \cdot \tau \cdot L_{40}^{-1}}{\Gamma_{R.S.40}} \tag{2.8}$$

$$\delta\lambda_{d10} = \frac{2 \cdot \tau \cdot L_{10}^{-1}}{\Gamma_{R.S.10}} \tag{2.9}$$

The pixel size, τ, is the same (10 μm for visible wavelengths). The linear dispersion is calculated at the spectrograph image focal plane. Substituting the expressions for the reciprocal linear dispersion (Eqs. 2.3 and 2.4) and calculating the ratio between the detector resolution elements, the result of Eq. 2.10 is obtained.

$$\frac{\delta\lambda_{d10}}{\delta\lambda_{d40}} = \frac{f_{cam40} \cdot \Gamma_{R.S.40}}{f_{cam10} \cdot \Gamma_{R.S.10}} = \frac{8 \cdot 1}{2 \cdot 4} = 1 \tag{2.10}$$

Thus, the detector resolution element is also the same in both cases. Since the resolution elements of slit, grating and detector are the same, the total resolution element does not change and the total spectral resolving power is not affected by the decision of making the focal-ratio conversion before or after the spectrograph.

After the results obtained in optical quality and location of the simultaneous observed wavelengths, the possibility to make the focal-ratio conversion before the visible spectrographs and illuminate them with the final f-number is ruled out.

In the case of the infrared spectral range, the IR-I spectrograph has been evaluated for a 1:1 system with a focal ratio F/20 and 4 metres focal length for the wavelengths 8498 Å, 8542 Å and 15650 Å. The associated optical design is presented in Fig. 2.8. The colours represent different optical fields. As in the previous design, the wavelengths are not separated enough to be observed in different detectors. It is needed to increase the separation between them considering the mechanical mount of the detectors too. This is possible if the focal length is increased.

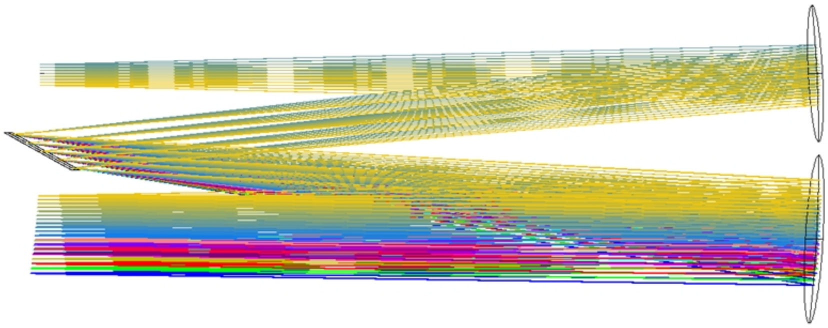

Figure 2.8: Evaluation of the IR-I spectrograph for: 8498 Å, 8542 Å and 15650 Å, using a 1:1 layout with a focal-ratio F/20. The wavelengths are not separated enough to be observed in different detectors. The separation between them should consider the detector size, including the mechanical mount.

The optical quality associated to the design of Fig. 2.8, as in the VIS-I case, is not good and the spot diagram, which is presented in Fig. 2.9, is dominated by aberrations, mainly coma. To improve the optical quality a more gradual beam focusing is required, with larger f-number and focal lengths.

According to the results, either for optical quality or wavelength separation, small f-numbers, F/10 and F/20, are not good alternatives since they do not fulfill the requirements. So, these results are an argument to work with a focal ratio as similar to that of the telescope as possible and use a reimaging system after the spectrograph to have the appropriate scales on the detectors.

2.3.3 Study of focal-ratio alternatives

This section describes the study of several f-numbers analysed for different focal lengths, from 5 metres to the maximum allowed according to Fig. 2.4. The focal ratios F/15, F/20, F/25, F/30 and F/35 do not offer an acceptable optical quality, however this improves for F/35 with the largest considered focal lengths (6.0, 6.5, 7.0 metres). Once the final f-numbers (F/10.3, F/20.6) are ruled out, the best alternative is to use the telescope F/50 to allow the perfect coupling between the telescope and the instrument or, if the F/50 is not the best option in terms of requirements, the most similar one. So, finally, the study has been focused more in depth in three focal-ratios: F/40, F/45 and F/50. Focal numbers larger than 50 have not been considered for the instrument, since they imply a loss of light of the telescope. If the f-numbers of telescope and instrument are the same, the full cone of light offered by the telescope is collected by the instrument. In the case of a telescope f-number larger than that of the instrument, the telescope beam is slower than that of the instrument and all the

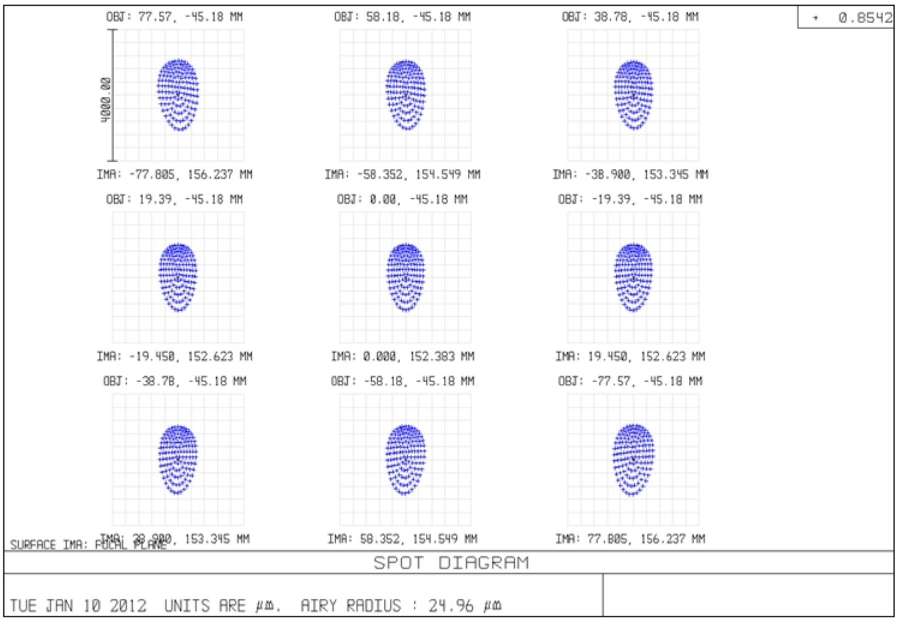

Figure 2.9: Spot diagram of the IR-I spectrograph illuminated by an F/20 beam at 8542 Å. The aberrations of the system, mainly coma, do not lead to a good optical quality.

light of the telescope is collected by the instrument, which still could collect a larger cone of light. For this type of coupling the grating spectral resolution decreases, compared with the case of a coupling where both, telescope and instrument, would have the same focal-ratio, since the projection of the pupil at the spectrograph grating is smaller than the associated to a telescope with the same focal-ratio than the spectrograph. If the telescope f-number is smaller than that of the instrument, the instrument can not collect all the light from the telescope and a fraction of the light is lost.

F/40

For VIS-I the maximum focal length, limited by the physical size of the commercial echelle diffraction gratings, is 8 metres. For 5 and 5.5 metres a good optical quality has not been obtained, because these focal lengths do not offer a slow beam convergence for an object length of 200 arcsec. The spot diagram for 5250 Å using a focal length of 5 metres and eight inputs slits of 200 arcseconds are presented in Fig. 2.10, which shown an optical quality dominated by astigmatism because of the object off-axis distance.

For 7.5 metres the optical quality (Fig. 2.11) improves until almost diffraction limit.

The focal length for a pupil of 200 mm and an F/40 is 8 metres, however a more compact system with 7.5 metres fulfills the requirements, even with a smaller pupil diameter at the diffraction grating. This is the configuration proposed for the VIS-I spectrograph because it represents the most compact system that satisfies the requirements.

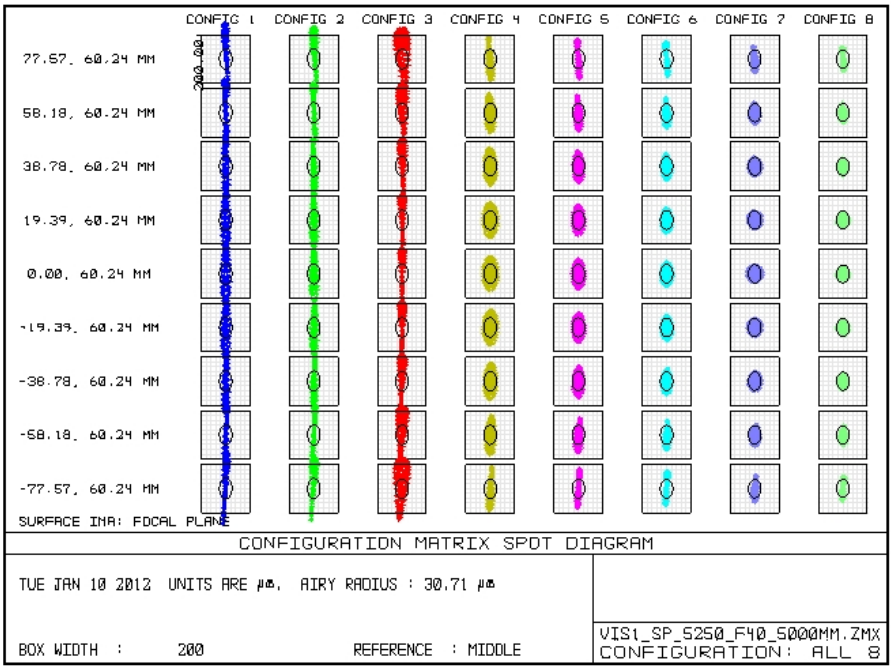

Figure 2.10: Spot diagram associated to the VIS-I spectrograph with a focal length of 5 metres, evaluated at 5250 Å for a focal-ratio F/40 using eight inputs slits of 200 arcsec length each. In this figure, each column represents the different field points of a same slit. The field values are shown on the left. Since the same entrance field of view is considered for all the designs, these field values are the same for all the spot diagrams. On the top of each column the number of configuration is specified, from left to right in increasing order. The number on the left of the first spot of configuration one shows the size of the box that, in this case, is 200 μm, bigger than the Airy disk, whose diameter is 61.42 μm. The spot diagram shows that the system is affected by a strong astigmatism.

F/45

A focal-ratio of F/45 would need a 9 metres focal length to have the same pupil diameter than the F/40 system with a focal length of 8 metres. The optical design for 3933 Å, 3968 Å and 3970 Å offers a diffraction limited optical quality, as it is presented in Fig. 2.12, with an increment in length of 1 metre.

F/50

If the focal-ratio is F/50, which is the telescope one, 10 metres are needed to have the same pupil size. The spot diagram associated to the design with this focal-ratio is presented in Fig. 2.13.

Comparing the three last figures (2.11, 2.12 and 2.13), the larger the f-number the bigger the Airy disk, as it can be seen in the value showed at the bottom of each spot diagram. So the optical quality is also better. However the improvement in the spot diagram implies an increment of ~2.5 metres in the focal length for these three examples corresponding to values between 7.5 and 10 metres.

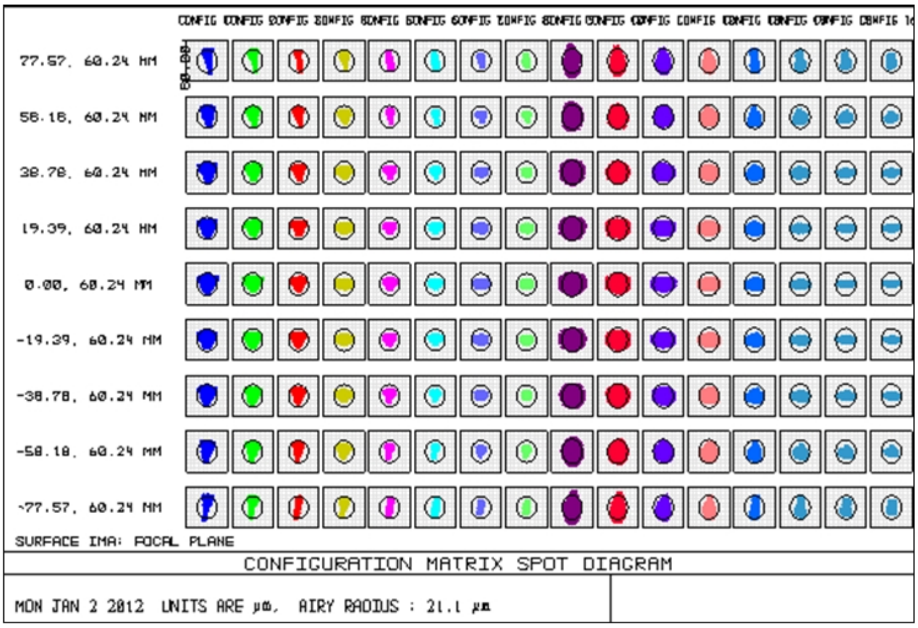

Figure 2.11: Spot diagram for the VIS-I spectrograph, with a focal length of 7.5 metres and eight slits of 200 arcseconds length. The evaluated wavelengths are 3933 Å and 3968 − 3970 Å. The field points, on the left, are the same than those of Fig. 2.10. On the top of each column the number of configuration is specified from left to right in increasing order. Each group of eight configurations is associated to a given wavelength. The Airy disk has a diameter of 42.2 μm.

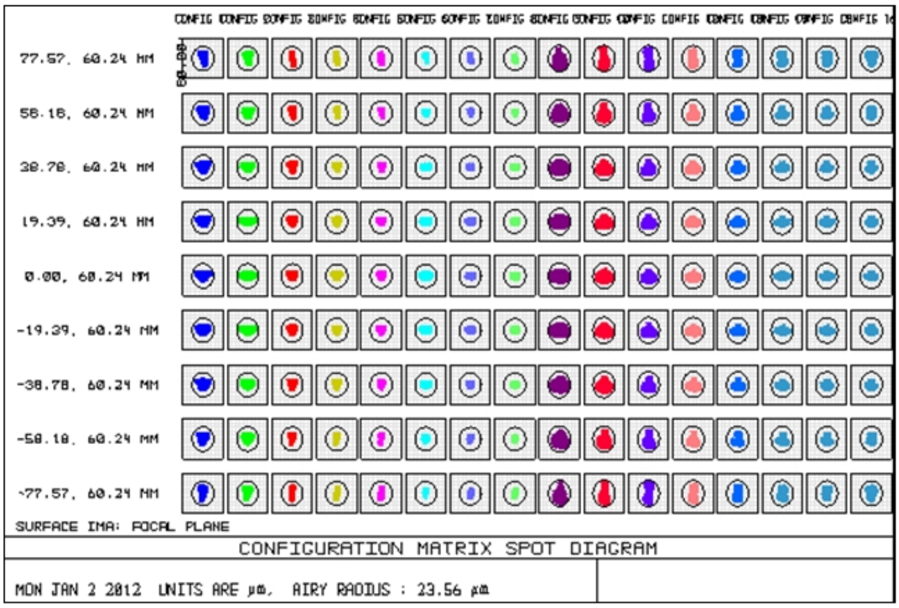

Figure 2.12: Spot diagram for the VIS-I spectrograph for a focal-ratio F/45 and a focal length of 9 metres. The study has been done for 3933 Å and 3968 − 3970 Å in multi-slit configuration. The optical quality is excellent showing the rays contained within the Airy disk, whose diameter is 47.12 μm.

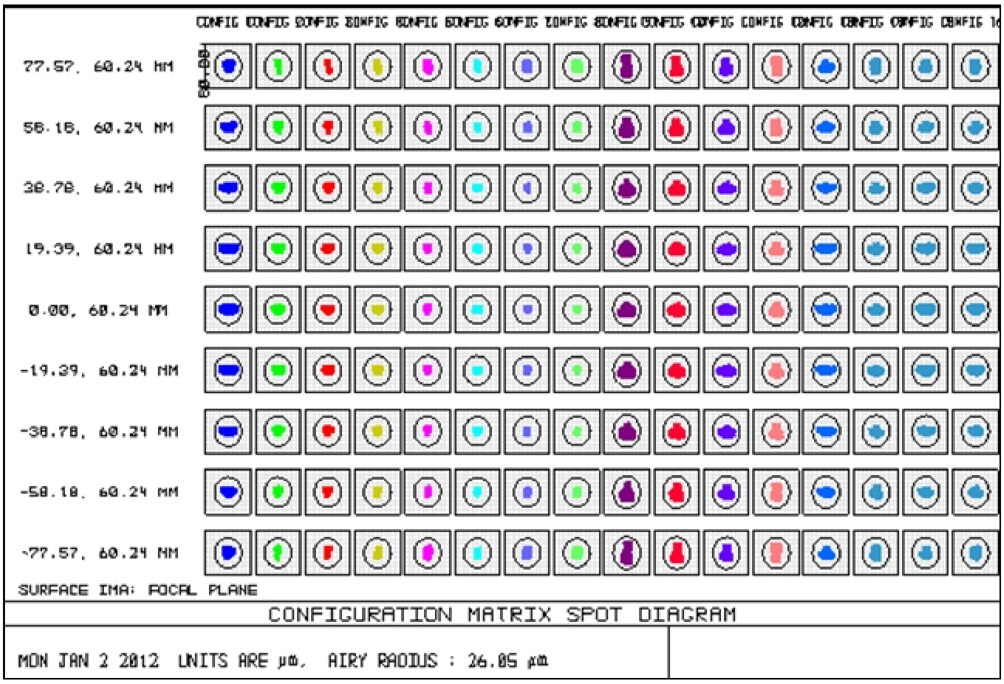

Figure 2.13: VIS-I spectrograph spot diagram for 3933 Å and 3968 – 3970 Å, considering a focal-ratio F/50, 10 metres focal length and eight input slits with 200 arcseconds length. On the top of each column the number of configuration is specified in increasing order from left to right. The box size is 80 μm and the Airy disk has a diameter of 52.1 μm.

Comparison for different science programmes

The considered focal-ratio alternatives have been evaluated for the different science programs. The spot diagrams of Figs. 2.14, 2.15 and 2.16 show the optical quality obtained for the flux tube programme for the alternatives studied: F/40 and 7.5 metres focal length, F/45 and 9.0 metres focal length and F/50 and 10 metres focal length, respectively. Strictly, the comparison should be done with a focal length of 8.0 metres in the case of F/40. Thus, the three alternatives would have the same pupil diameter, but 7.5 metres is enough to fulfill the requirements. The same pupil diameter (187.5 mm) is obtained with a focal length of 8.4 metres for F/45 and 9.4 metres for F/50. Although the optical quality is comparable for the three designs, for a given f-number, the beam diverges with the separation with respect to the object and the longer the focal length, the bigger the camera mirror. Since the linear dispersion is a function of the focal length, it also conditions the camera mirror diameter, as well as the separation of the wavelengths observed at the same time. For a focal-ratio F/40 and 7.5 m focal length, a diameter of 820 mm and a decentred distance with respect to the optical axis of 470 mm is needed, while for F/45 and 9.0 m these numbers are 920 mm and 520 mm and for F/50 with a focal length of 10 m: 1.0 metre and 555 mm respectively. Attending to the calculated values of Table 2.4, the three studied cases, corresponding to F/40, F/45 and F/50, fulfill the requirement of spectral resolution. They have been calculated using a slit width of 0.05 arcsec and a sampling of 0.05 arcsec/pixel. The pupil diameter at the spectrograph grating is calculated for each focal-ratio and focal length.

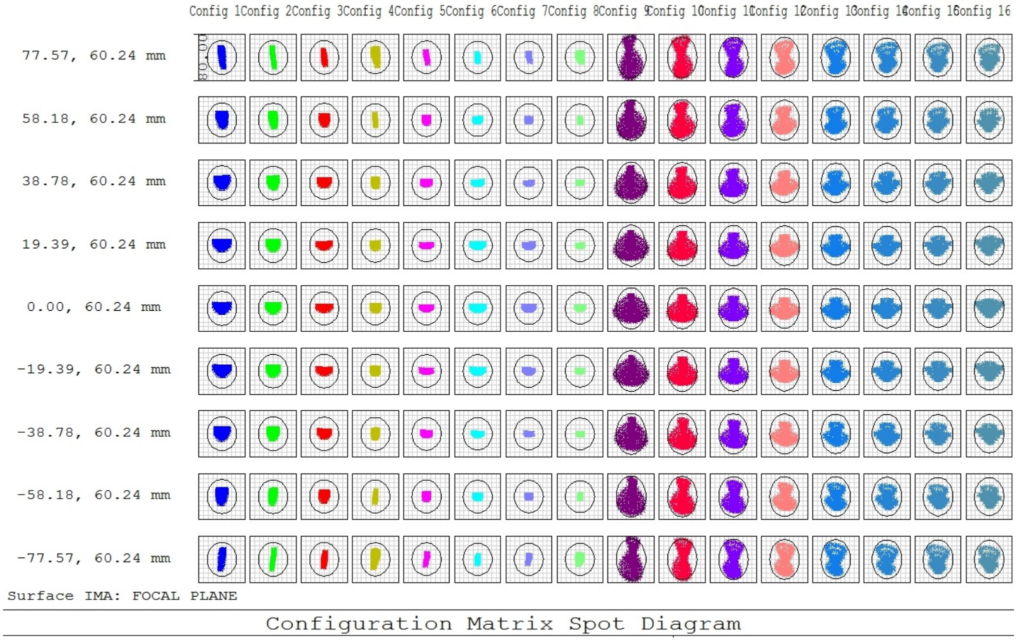

Figure 2.14: Spot diagram of the VIS-I spectrograph evaluated for the flux tube science programme at 5172 Å and 5250 Å, considering a focal-ratio F/40 and 7.5 metres focal length. On the top of each column the number of configuration is specified, from left to right in increasing order.

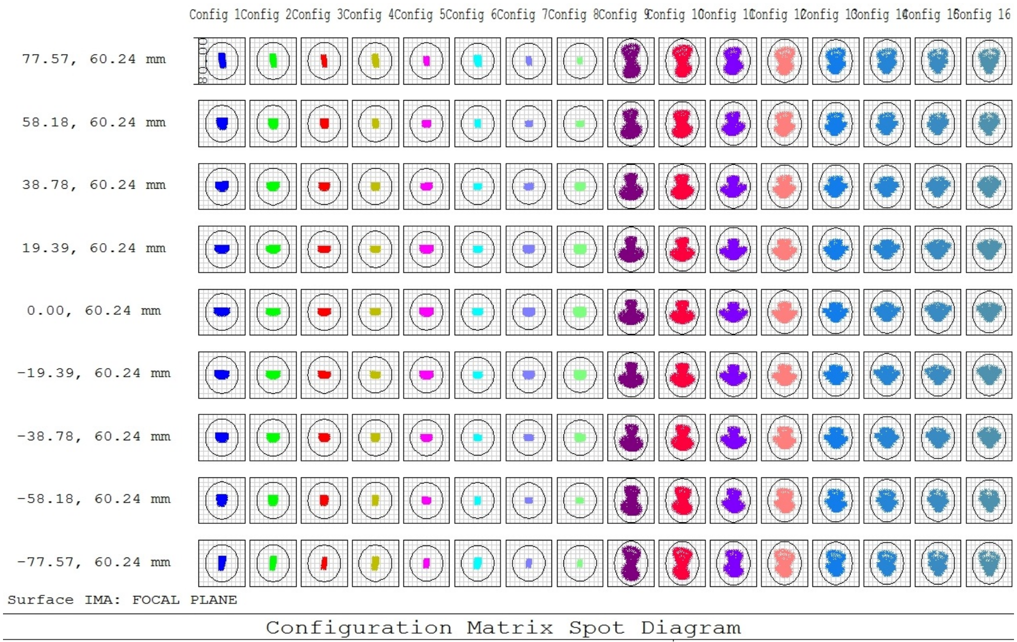

Figure 2.15: Spot diagram of the VIS-I spectrograph evaluated for the flux tube science programme at 5172 Å and 5250 Å, considering a focal-ratio F/45 and 9.0 metres focal length.

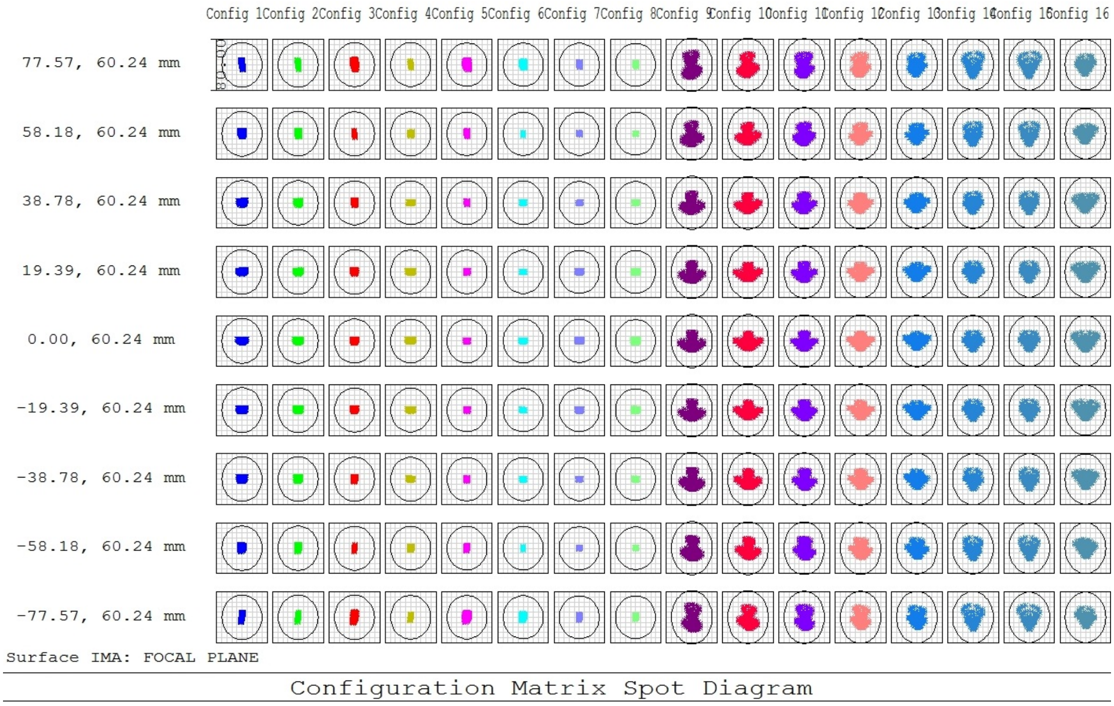

Figure 2.16: Spot diagram of the VIS-I spectrograph evaluated for the flux tube science programme at 5172 Å and 5250 Å, considering a focal-ratio F/50 and 10 metres focal length.

Table 2.4: Calculated parameters associated to the three cases studied (F/40, F/45 and F/50), for a slit width of 0.05 arcsec and a sampling of 0.05 arcsec/pixel. R_g is the grating spectral resolving power and R_T the total one, considering the resolution elements of slit, grating and detector. Focal is the collimator and camera focal lengths that are the same because the spectrographs are 1:1 systems. L^{-1} is the linear dispersion. The efficiency means the grating efficiency, which is the same because the same rotation angle for the grating has been used.

F/♯	focal(m)	pupil diam.(mm)	λ(Å)	efficiency	L^{-1} (Å/mm)	R_g	R_T
40	7.50	187.50	3933	0.77	0.14	1471,000	775,960
45	9.00	200.00	3968	0.77	0.12	1469,000	898,540
50	10.00	200.00	3970	0.77	0.11	1569,000	962,060

The VIS-I spectrograph has five science programmes: network elements, planets, flux tube, Hanle effect and flares. The first and second ones only need the observation of one wavelength, 5576 Å and 4227 Å, respectively. The evaluation of a system with a single wavelength does not represent a great problem. The grating can be rotated to centre the wavelength in the detector and appropriately to have a good optical quality, at least in these three cases of slow enough focal-ratios. This study is focused on the combination of many wavelengths where the optimisation of all of them is not trivial.

The optical quality of Figs. 2.14, 2.15 and 2.16 is very good in all the cases and the spectral resolution is higher than the requirement. Considering all the results, as well as the ones for size and decentring of the camera mirror, for the different combination of wavelengths studied, the F/40 is the most compact system that fulfils the requirements, since it satisfies the different requirements using the shortest focal length. The change from F/40 to F/45 or F/50 with these focal lengths implies: larger focal lengths, bigger camera mirror and a bigger size of the image focal plane.

The spectrographs can be illuminated by a beam whose focal-ratio belongs to a range between F/40 and F/50 satisfying the requirements. Since the F/40 system increases the spectral resolution for the largest wavelength of the interval, this is the one proposed for this instrument.

The Ca II K 3933 Å and Ca II H 3968 Å lines are associated to the study of the Hanle effect and together with Hα 6563 Å, to the Flares programme. For this combination of lines the optical design has been done for the parameters of the VIS-I proposed spectrograph, using the same camera diameter and decentred distance. A focal length of 7.5 m for F/40 (Fig. 2.17) has been considered and 9 and 10 metres for F/45 (Fig. 2.18) and F/50 (Fig. 2.19), respectively. The optical quality obtained in the three cases is similar, however the increase in the Airy radius with larger f-numbers improves the optical quality of the system.

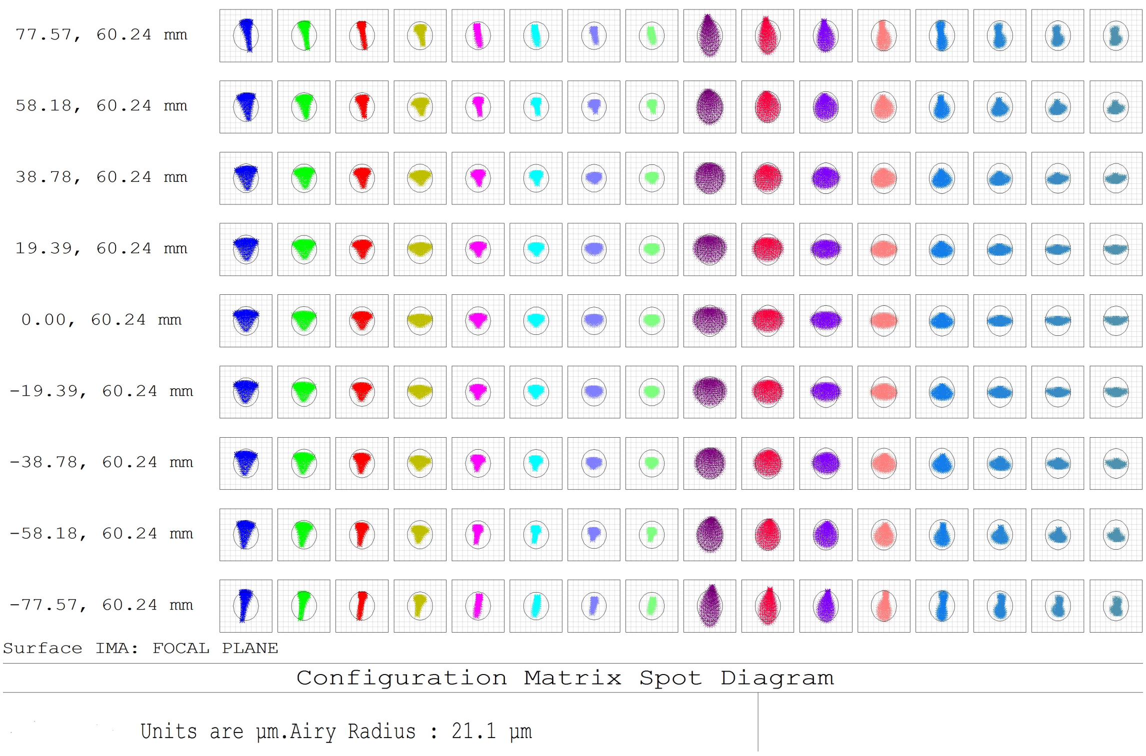

Figure 2.17: Spot diagram of the VIS-I spectrograph evaluated at the Ca II K 3933 Å and Ca II H 3968–3970 Å lines associated to the Hanle effect science programme, for a focal-ratio F/40 and 7.5 metres focal length.

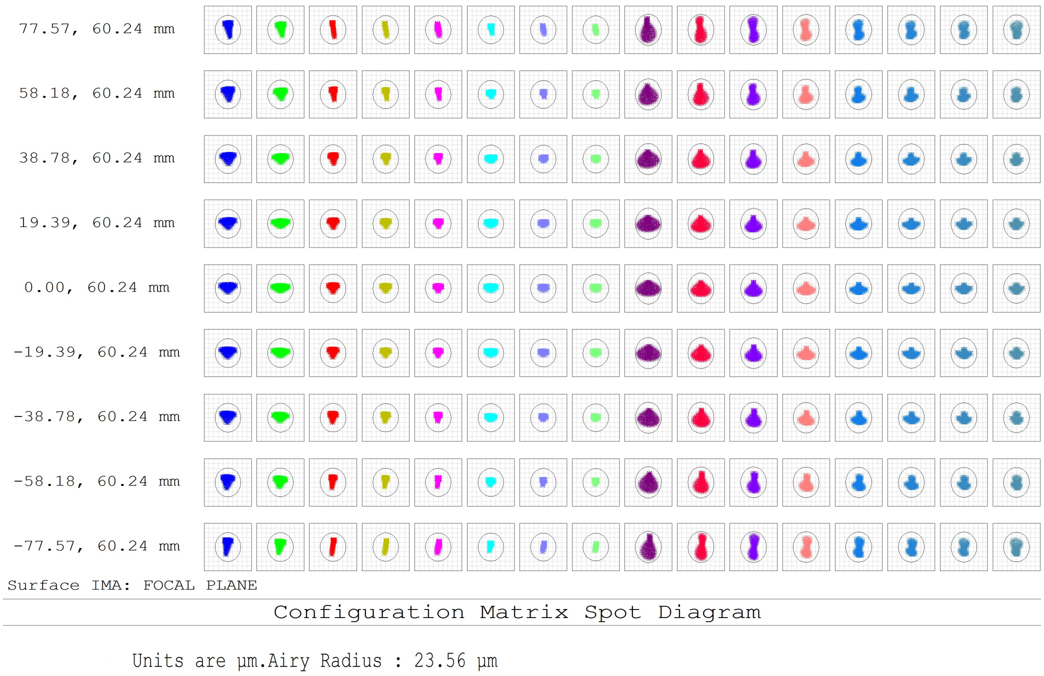

Figure 2.18: Spot diagram of the VIS-I spectrograph evaluated at the Ca II K 3933 Å and Ca II H 3968−3970 Å lines associated to the Hanle effect science program, for a focal-ratio F/45 and 9 metres focal length.

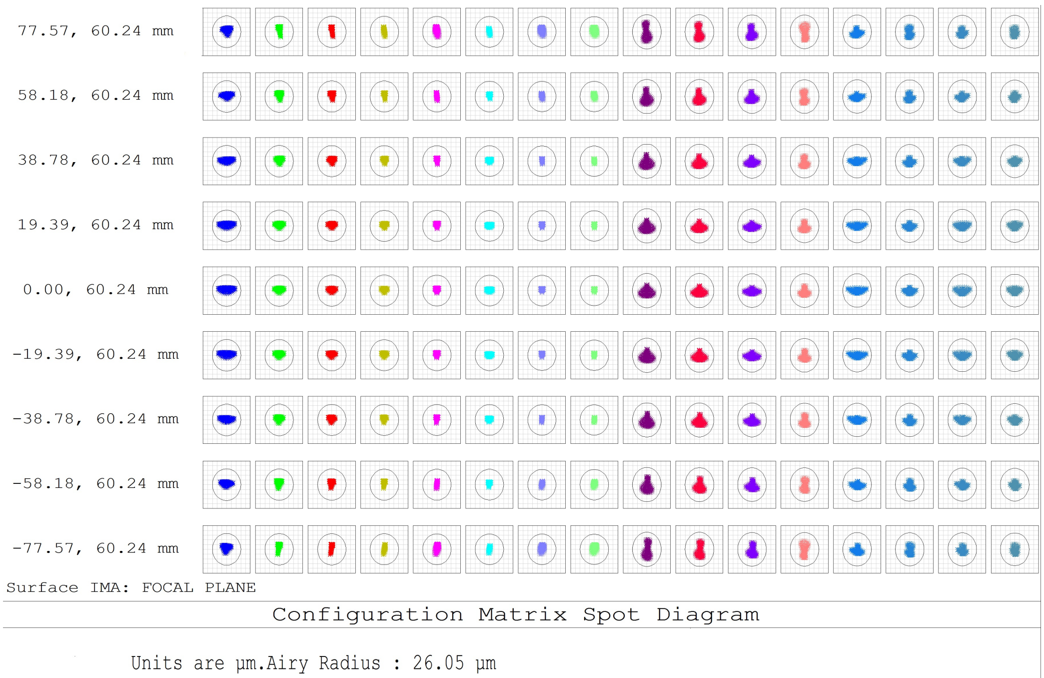

Figure 2.19: Spot diagram of the VIS-I spectrograph evaluated at the Ca II K 3933 Å and Ca II H 3968−3970 Å lines associated to the Hanle effect science programme, for a focal-ratio F/50 and 10 metres focal length.

Study of focal-ratio alternatives keeping the focal length

This section presents the results obtained after the evaluation of the layouts using different f-numbers and the same focal length. Although solar spectrographs present large focal lengths, the shortest ones with which the requirements are satisfied have been considered. In all the cases the spectrograph layout is kept, using the same off-axis mirrors distances and sizes.

The optical quality corresponding to the evaluation of the VIS-I spectrograph at 3933 Å and 3968 – 3970 Å for 7.5 metres focal length is shown in the spot diagrams of Fig. 2.17 for F/40, Fig. 2.20 for F/45 and Fig. 2.21 for F/50. The optical quality is very good in all the cases, improving for larger f-numbers.

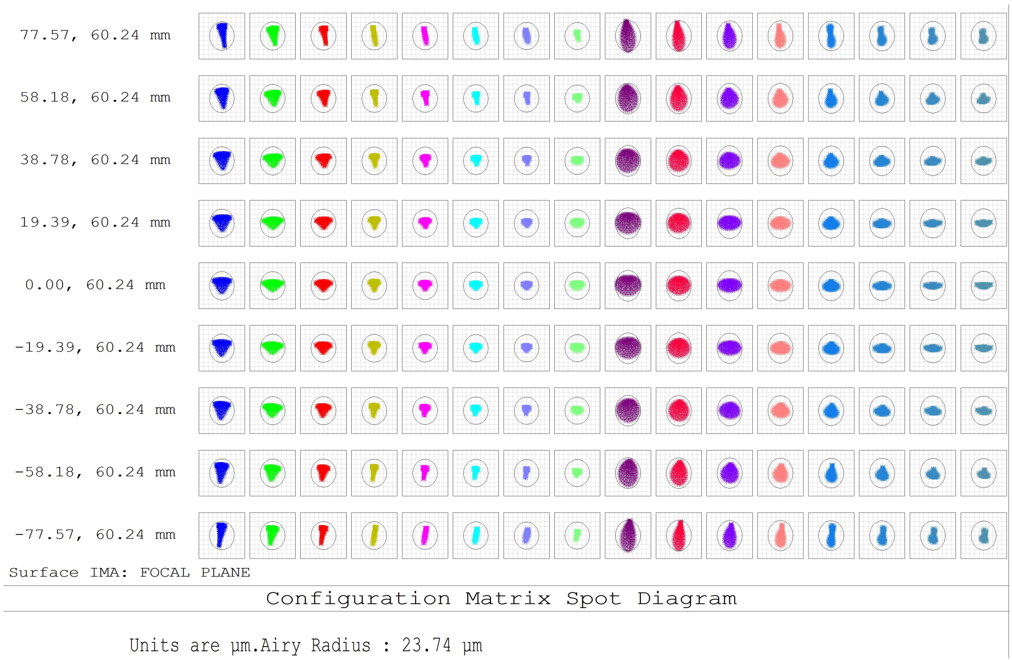

Figure 2.20: Spot diagram of the VIS-I spectrograph evaluated at the Ca II K 3933 Å and Ca II H 3968−3970 Å lines associated to the Hanle effect science programme, for a focal-ratio F/45 and 7.5 metres focal length.

According to these spot diagrams that show an optical quality limited by diffraction and taking into account that the spectral resolving power is larger than 300,000 in the three cases, for these wavelengths, these three alternatives are acceptable. The wavelengths 5172 Å and 5250 Å, associated to the Flux tube programme, have also been studied together to evaluate the VIS-I spectrograph using a focal length of 7.5 metres for F/40 (see the spot diagram of Fig. 2.14), F/45 (Fig. 2.22) and F/50 (Fig. 2.23). The optical quality obtained is diffraction limited.

The combination of 5172 Å and 5250 Å can be observed simultaneously using also the same sizes and off-axis distances for F/40, F/45 and F/50. Other points like the grating efficiency or the spectral resolving power, for the grating and the total one, have also been analysed. From these studies we have inferred that the VIS-I spectrograph can work within the interval of focal-ratios from F/40 to F/50 satisfying all the requirements.

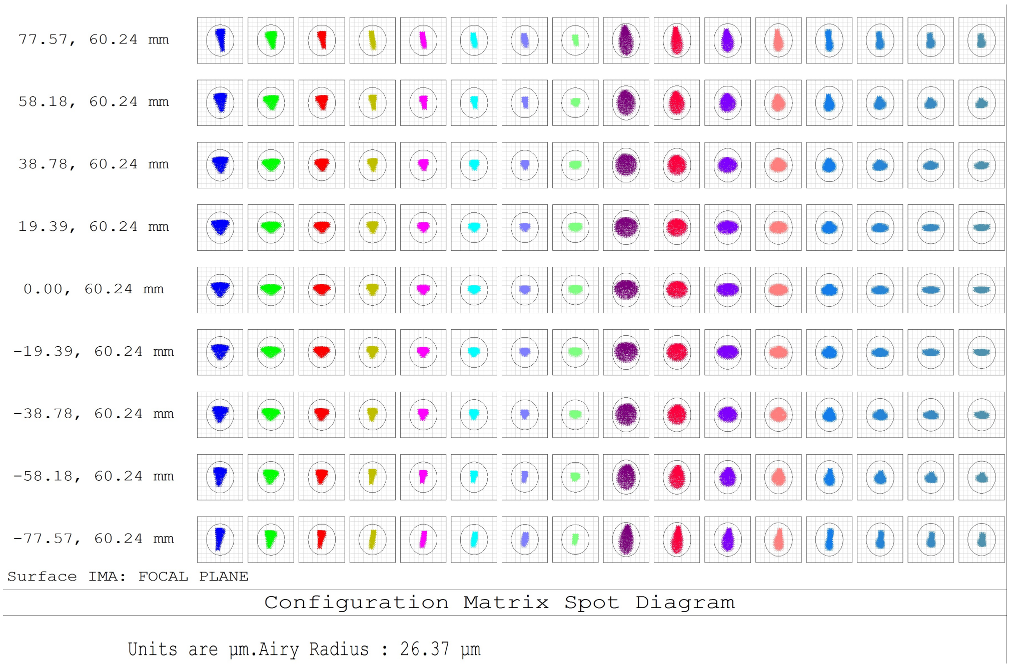

Figure 2.21: Spot diagram of the VIS-I spectrograph evaluated at the Ca II K 3933 Å and Ca II H 3968−3970 Å lines for a focal-ratio F/50 and 7.5 metres focal length.

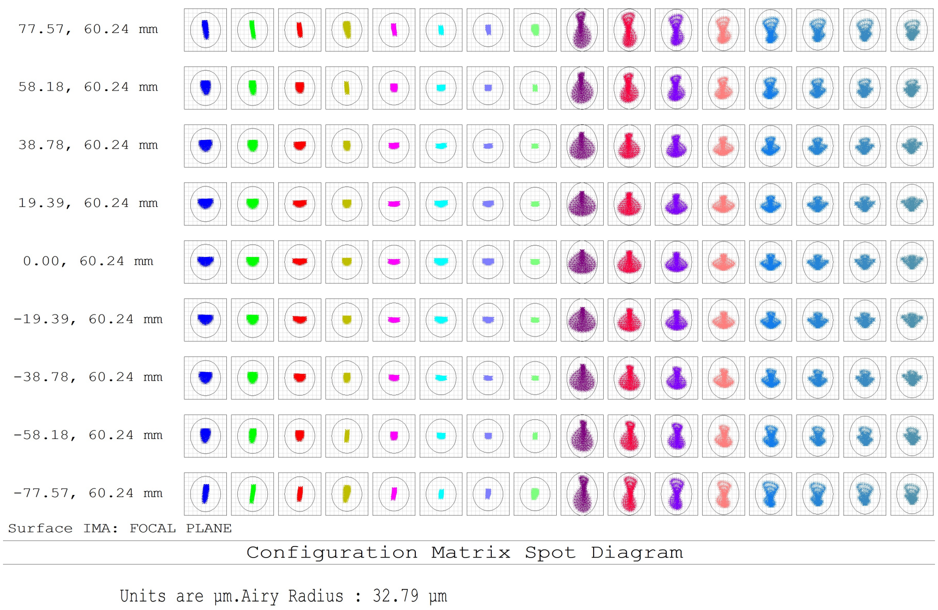

Figure 2.22: Spot diagram of the VIS-I spectrograph evaluated at 5172 Å and 5250 Å, for a focal-ratio F/45 and 7.5 metres focal length.

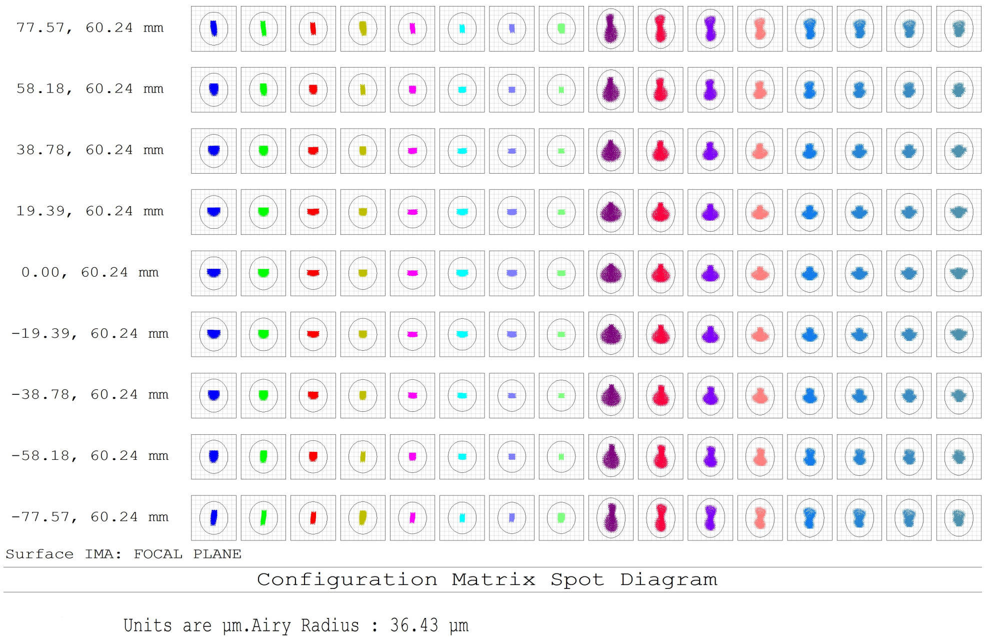

Figure 2.23: Spot diagram of the VIS-I spectrograph evaluated at 5172 Å and 5250 Å, for a focal-ratio F/50 and 7.5 metres focal length.

The science programmes for the VIS-II spectrograph have the following wavelengths associated: for the magnetic canopies and planets programmes, the Na I D1 line at 5896 Å, for the flux tube and network elements programmes, the FeI line at 6302 Å; Hα for the Flares programme at 6563 Å and the O I triplet for the Hanle effect programme at 7770 Å. A single wavelength per programme does not represent a problem to get optical quality, at least for these three focal-ratios, F/40, F/45 and F/50 that, attending to this study are slow enough to offer good optical quality results. Anyway, their designs have also been studied, as well as the spectral resolving power in each case. Again, as it has been explained for VIS-I, the proposed VIS-II spectrograph is the most compact system that satisfies the requirements. Its focal length is 7 metres. So, F/45 and F/50 have been studied too, using the same focal length. The spot diagrams of the VIS-II spectrograph at 6302 Å, associated to the flux tube and network elements programmes, for F/40, F/45 and F/50, are presented in Figs. 2.24, 2.25 and 2.26, respectively. The optical quality is very good and the rays are contained within the Airy disk. The results obtained for 6563 Å, corresponding to the Flares programme, are shown in Figs. 2.27, 2.28 and 2.29, for which the optical quality is also limited by diffraction. Equivalent results have been obtained for the other wavelengths of the VIS-II spectral range.

In addition, a very important point is that the three focal-ratios are possible using the same configuration for the VIS-II spectrograph. This is, the same diameters for the optical surfaces and the same off-axis distances. The spectral resolving power is, in all cases, larger than 300,000. With these results we can conclude that the proposed VIS-II spectrograph can perfectly operate in the range of focal-ratios from F/40 to F/50 using the same configuration and fulfilling the specifications.

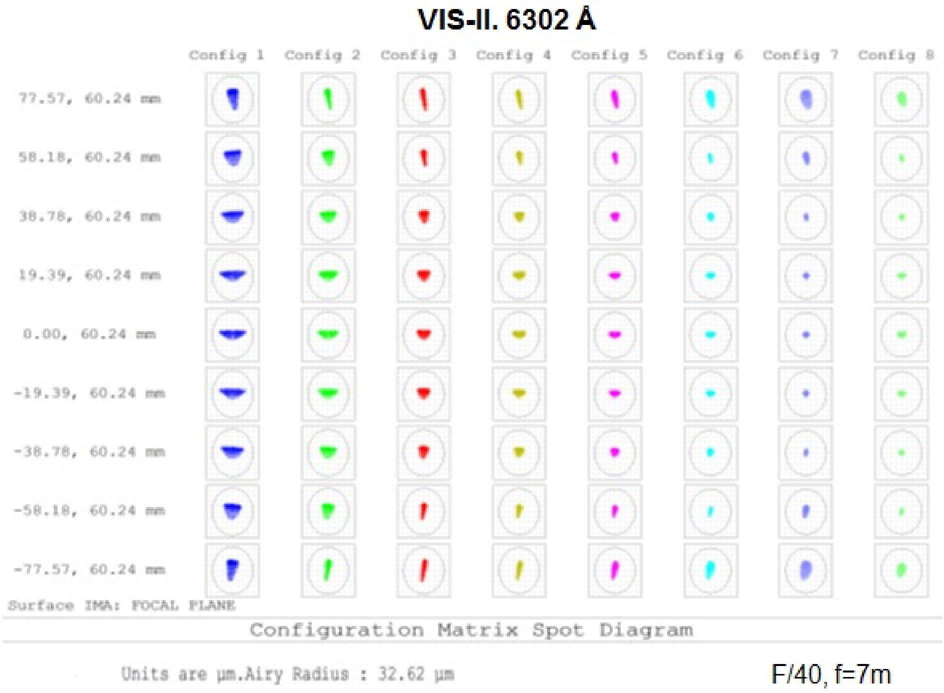

Figure 2.24: Diffraction limited optical quality obtained from the evaluation of the VIS-II spectrograph at 6302 Å, considering a focal-ratio F/40 and 7 metres focal length.

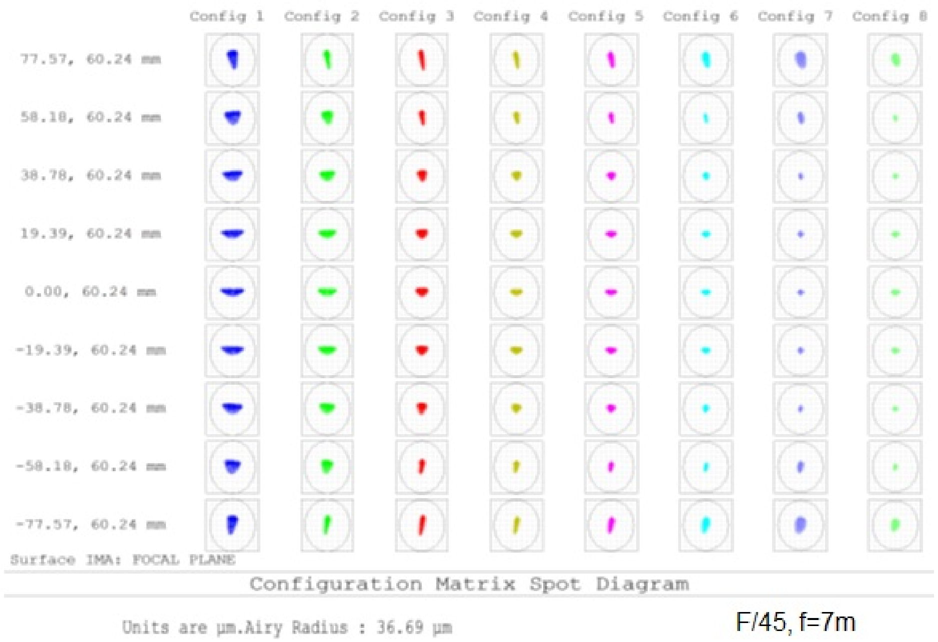

Figure 2.25: Diffraction limited optical quality obtained from the evaluation of the VIS-II spectrograph at 6302 Å, considering a focal-ratio F/45 and 7 metres focal length.

Figure 2.26: Spot diagram at diffraction limit for the VIS-II spectrograph evaluated at 6302 Å for a focal-ratio F/50 and a focal length of 7 metres.

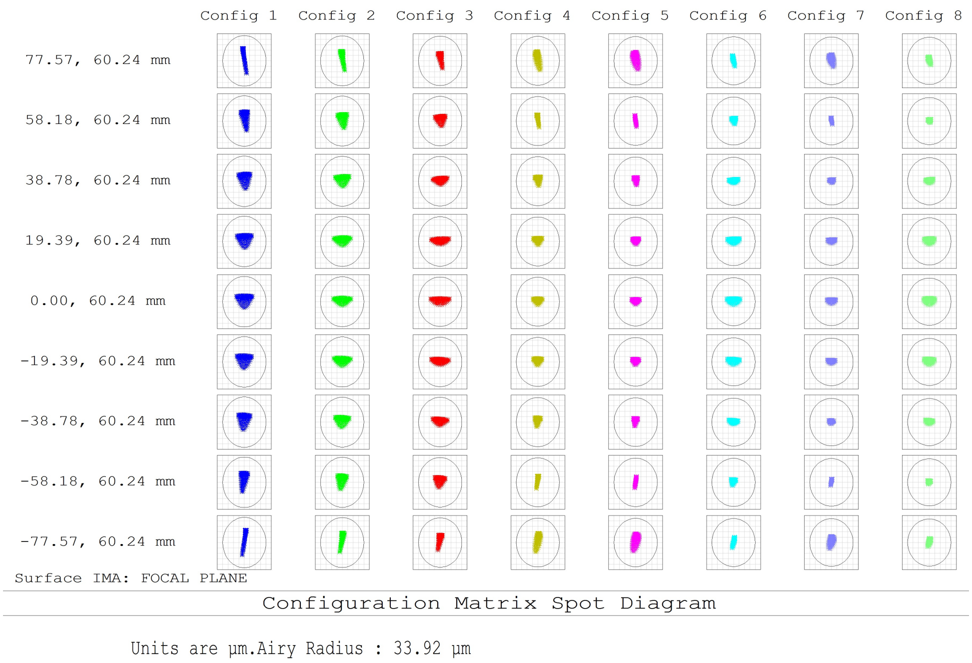

Figure 2.27: Spot diagram of the VIS-II spectrograph evaluated at 6563 Å for a focal-ratio F/40 and a focal length of 7 metres. The optical quality is at diffraction limit.

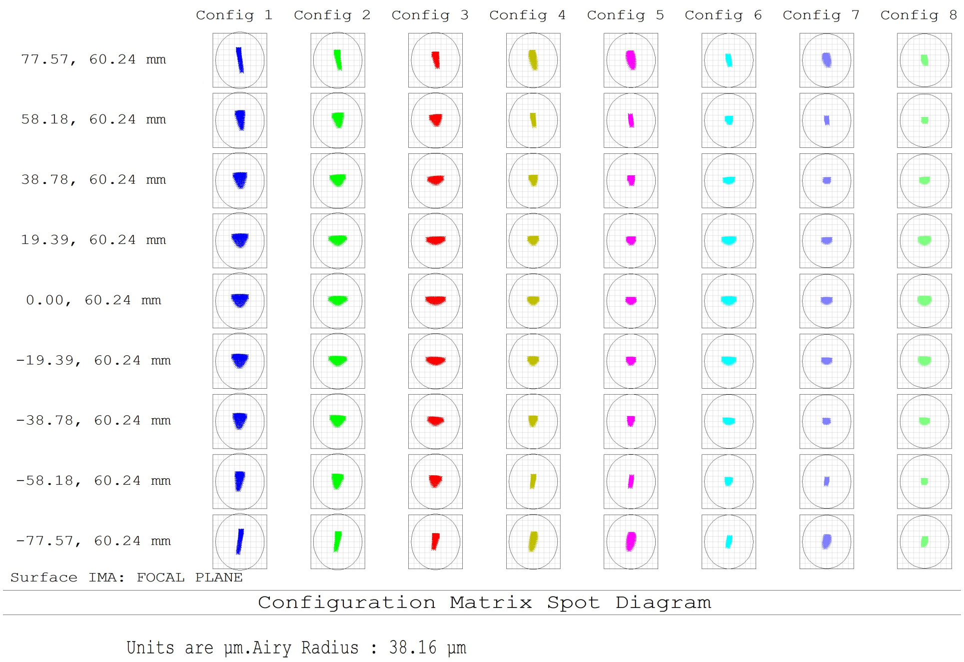

Figure 2.28: Spot diagram of the VIS-II spectrograph evaluated at 6563 Å for a focal-ratio F/45 and a focal length of 7 metres. The optical quality is at diffraction limit.

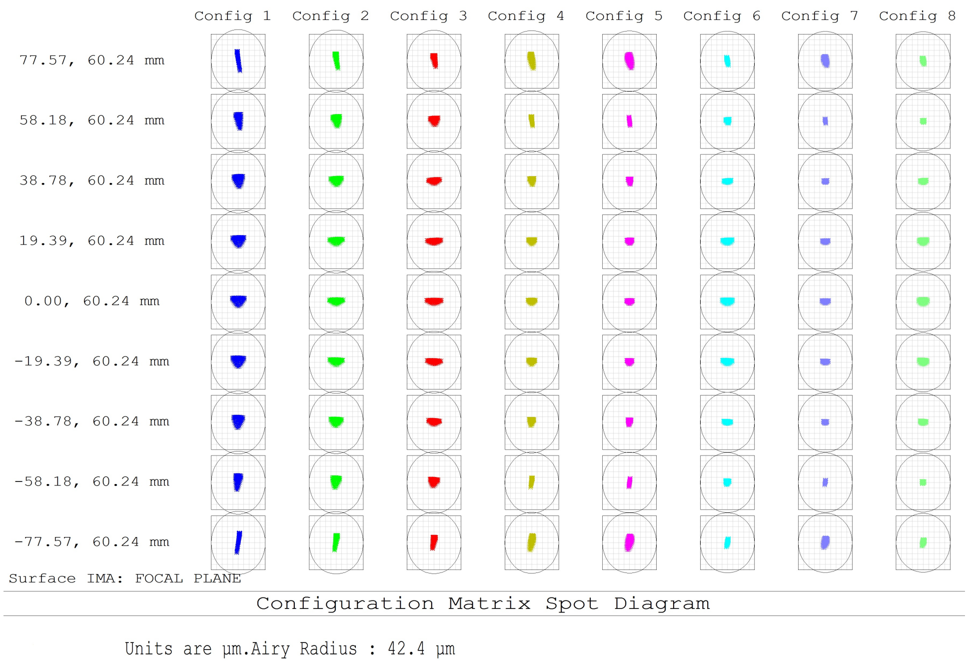

Figure 2.29: Spot diagram of the VIS-II spectrograph evaluated at 6563 Å for a focal-ratio F/50 and a focal length of 7 metres. The optical quality is at diffraction limit.

The following science programmes are assigned to the IR-I spectrograph: Flares and Hanle effect at 8542 Å, flux tube programme at 8542 Å, 15260 Å and 15650 Å, magnetic canopies with three wavelengths observed together, 8498 Å, 8542 Å and 15650 Å, and network elements at 15650 Å. The different combinations have been studied. The results for the magnetic canopies programme are presented in Figs. 2.30 for F/40, 2.31 for F/45 and 2.32 for F/50. The spot diagrams of these three figures have 24 configurations corresponding to the three eva-luated wavelengths (8498 Å, 8542 Å and 15650 Å). Eight configurations correspond to each wavelength and represent the image of the eight entrance slits evaluated at the spectrograph image focal plane at that specific wavelength. The larger the number of simultaneous wavelengths observed, it is more difficult to obtain an excellent optical quality for all of them. Since the wavelengths are observed in different detectors, they have to be separated at the image focal plane. Those wavelengths close to the optical axis will present the best optical quality and the aberrations increase with the off-axis distances. The magnetic canopies programme is one of the two programmes with the biggest number of simultaneous wavelengths, what makes it one of the most limiting programmes. The focal length of the proposed F/40 IR-I spectrograph, 8 metres, is the value considered for this study. This focal length is adequate to satisfy the specifications and separate the wavelengths. Also for IR-I, the spectrograph can operate using focal-ratios between F/40 and F/50 without modifying the system layout and with spectral resolutions always larger than 300,000.

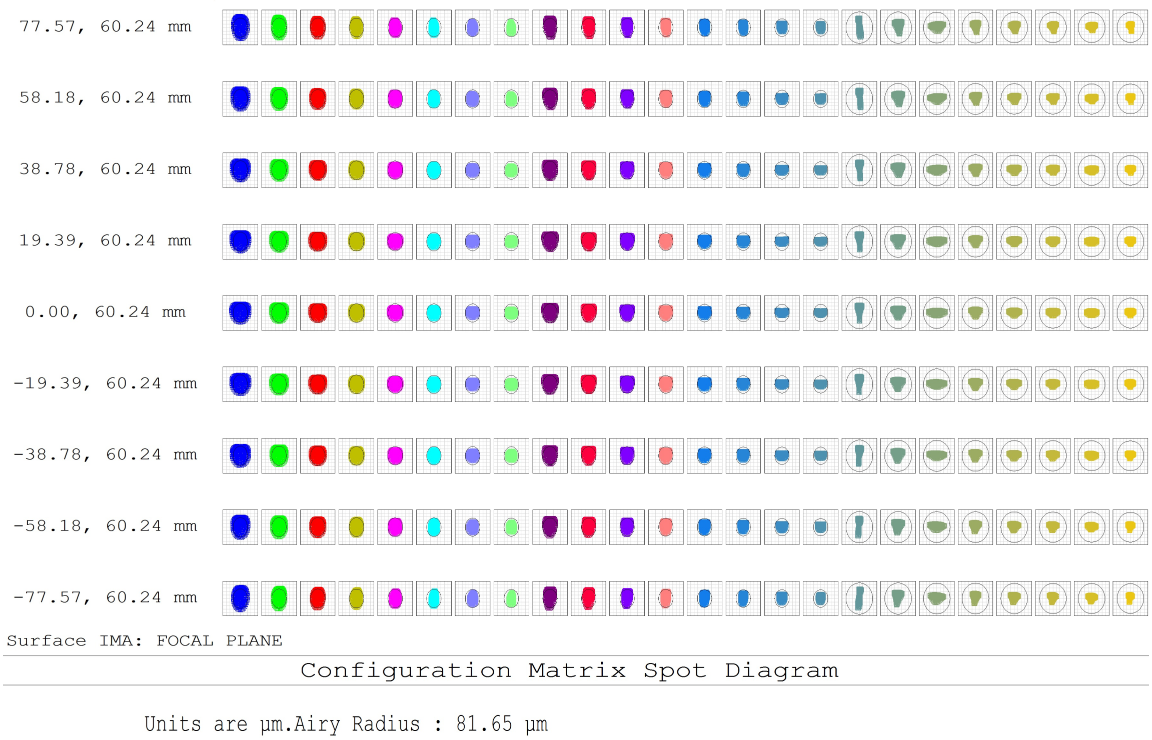

Figure 2.30: Spot diagram of the IR-I spectrograph evaluated at 8498 Å, 8542 Å and 15650 Å for the magnetic canopies science programme for a focal-ratio F/40 and 8 metres focal length.

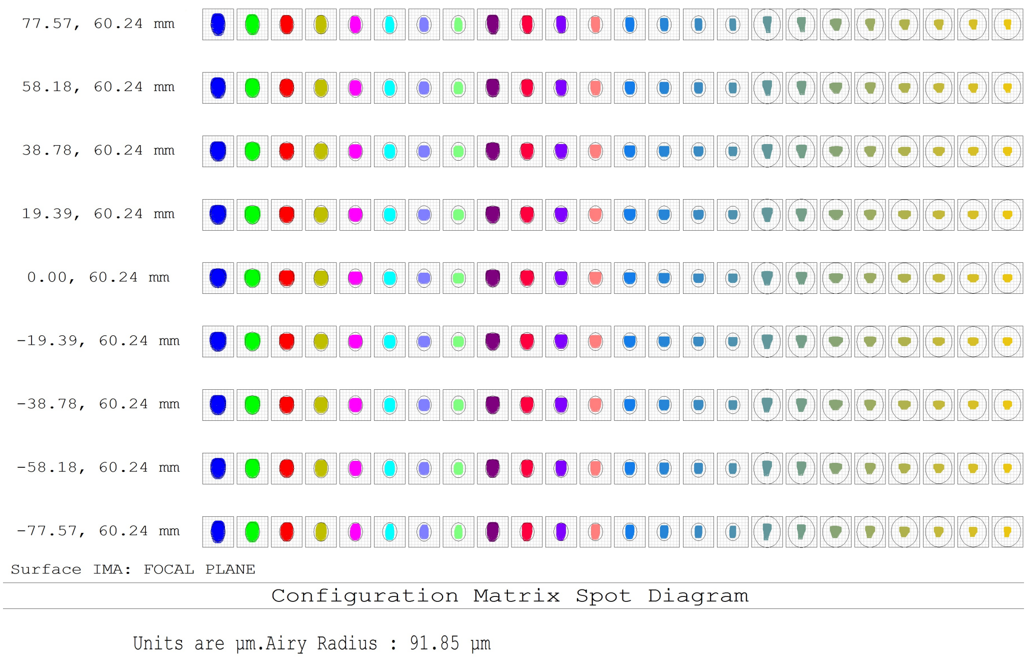

Figure 2.31: Spot diagram of the IR-I spectrograph evaluated at 8498 Å, 8542 Å and 15650 Å for the magnetic canopies science programme for a focal-ratio F/45 and 8 metres focal length.

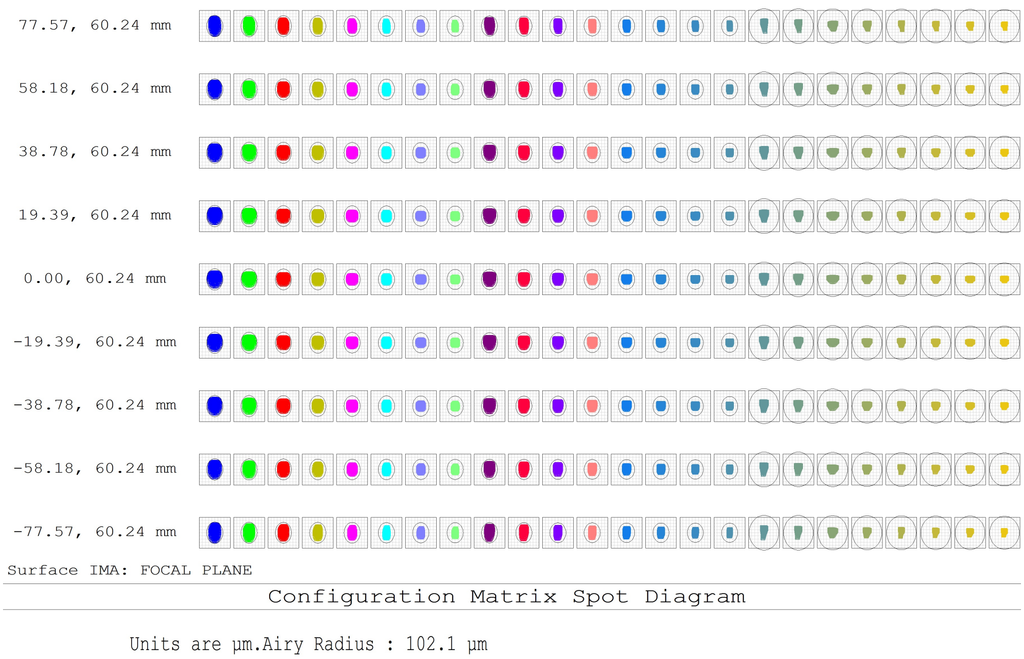

Figure 2.32: Spot diagram of the IR-I spectrograph evaluated at 8498 Å, 8542 Å and 15650 Å for the magnetic canopies science programme for a focal-ratio F/50 and 8 metres focal length.

The most conflictive wavelength for the IR-II spectrograph is the Ti I line at 22300 Å associated to sunspots, for which the spectral resolution is lower. So that it is a good candidate for this study. The spot diagrams associated to the optical designs for F/40, F/45 and F/50, keeping the focal length of 7 metres, are shown in Figs. 2.33, 2.34 and 2.35, respectively. The optical quality is excellent in all the cases and the critical parameter is the spectral resolution.

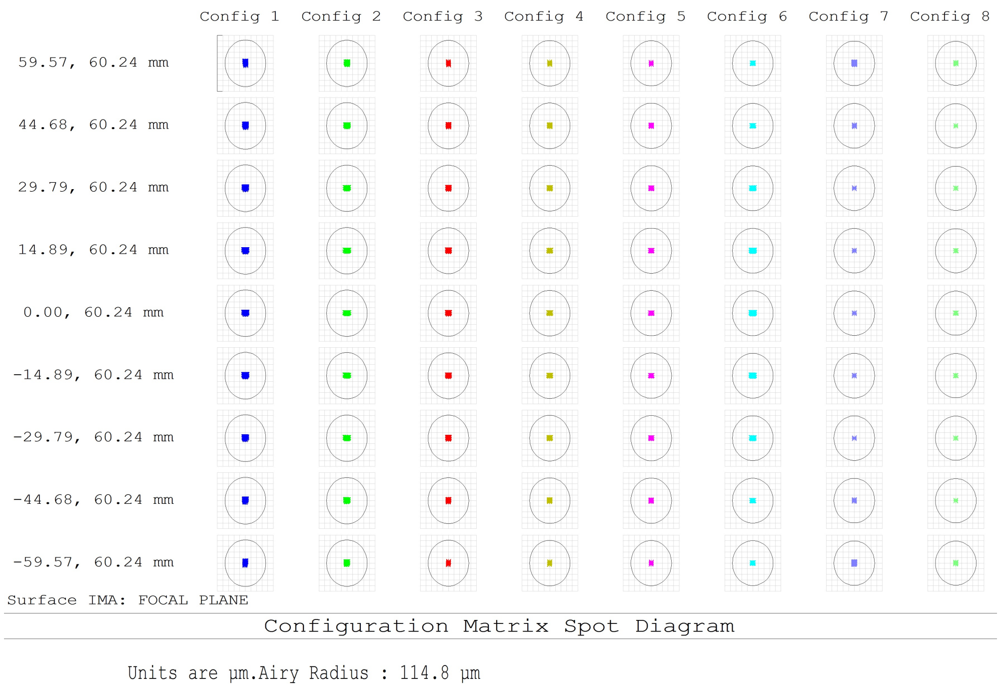

Figure 2.33: Spot diagrams at diffraction limit of the IR-II spectrograph evaluated at 22300 Å for a focal-ratio F/40 and 7 metres focal length.

Table 2.5: Calculated parameters for the IR-II spectrograph at 22300 Å for a focal length of 7 metres and three focal-ratios: F/40, F/45 and F/50. Focal means the collimator and camera focal lengths, efficiency is the grating efficiency and L^{-1} is the linear dispersion. The total spectral resolving power decrease too much for F/50 with respect to the requirement.

F/♯	focal(m)	pupil diam.(mm)	efficiency	L^{-1} (Å/mm)	R_g	R_T
40	7.00	175.00	1.00	0.85	291,610	260,520
45	7.00	155.56	1.00	0.85	259,220	236,650
50	7.00	140.00	1.00	0.85	233,290	216,430

The proposed F/40 IR-II spectrograph was selected as the best option according to the requirements, for which the spectral resolving power was higher. Anyway, the spectrograph can be illuminated with a range of focal-ratios between F/40 and F/50, nevertheless the spectral resolution decreases significantly for higher f-numbers.

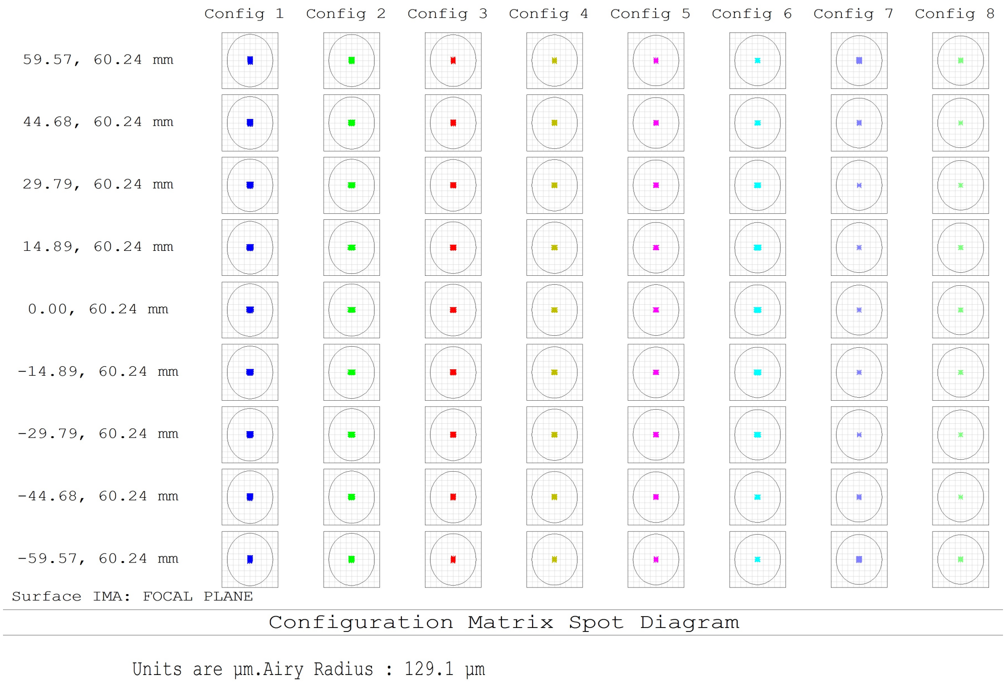

Figure 2.34: Spot diagrams at diffraction limit of the IR-II spectrograph evaluated at 22300 Å for a focal-ratio F/45 and 7 metres focal length.

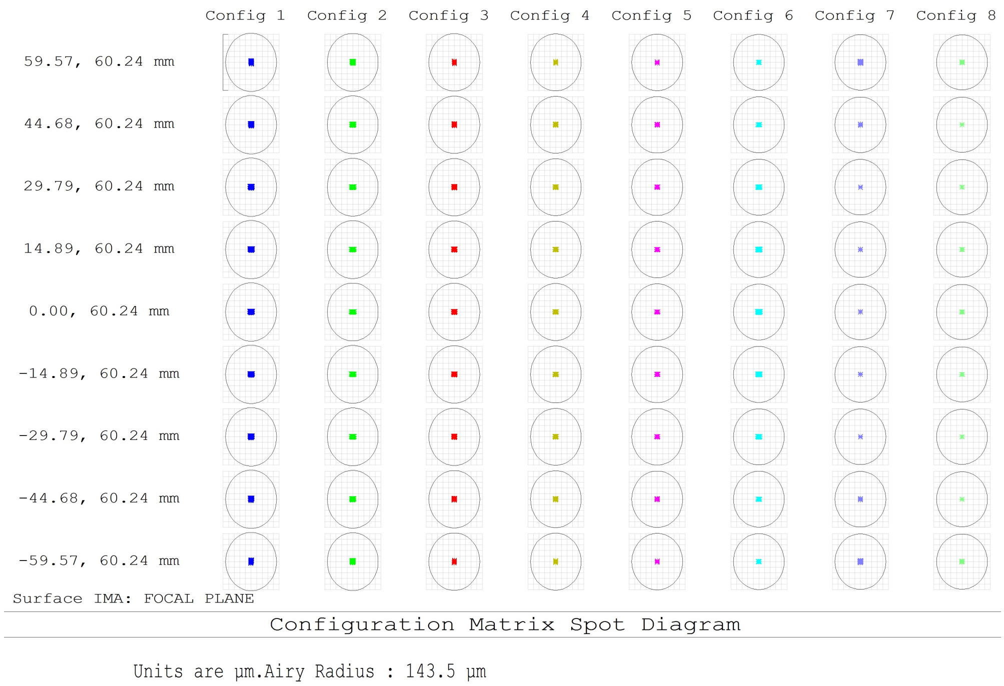

Figure 2.35: Spot diagrams at diffraction limit of the IR-II spectrograph evaluated at 22300 Å for a focal-ratio F/50 and 7 metres focal length.

3

Integral Field Unit

The integral field unit is the first of the subsystems that compose the proposed instrument. It is placed at the telescope image focal plane. An IFU based on the image slicer concept has been decided as the best choice. Image slicers solve some of the critical points of the other integral field unit alternatives (Fig. 1.14). The spectra are not overlapped, as in the case of using microlenses. The focal-ratio degradation of optical fibers does not occur in the case of image slicers, whose focal ratio can be preserved or a magnification can be produced using its own optical components without adding extra surfaces. In addition, the possible loss of transmission of some fibers in the infrared spectral range can be solved with an adequate coating in the case of image slicers. And, since this instrument also offers a polarimetric mode, the advantage of this option over the optical fibers is that these are depolarising elements. Two integral field units are currently considered, one to feed the VIS-I and VIS-II spectrographs and a second image slicer for the IR-I and IR-II spectrographs.

3.1 Requirements

The image slicer of the integral field spectrograph of EST has been designed to observe a bidimensional field of view of 80 arcsec^2 and reorganise it into eight slits, each one of them with 200 arcsec length by 0.05 arcsec width. The spectra of all the points of the field of view will be obtained simultaneously. The input focal ratio is the one offered by the telescope, $F/50$. The spatial sampling required for the instrument is 0.05 arcsec/slit width and, since the sampling is given by the width of the mirrors that cut the entrance field of view, for this specific focal ratio the value is 50 μm. Although this width implies the thinnest one ever proposed for an image slicer, its manufacturing feasibility has already been confirmed.

Although the spectrograph can be illuminated by a beam with a focal-ratio between F/40 and F/50, F/40 has been chosen as the best one to satisfy the requirements. The focal-ratio conversion from the telescope F/50 to the spectrograph F/40 is done by the last array of mirrors of the image slicer without any extra optical component and preserving the optical quality that, for the different presented proposals, is at diffraction limit. Table 3.1 shows the requirements that have driven the design.

Table 3.1: Requirements for the design of the multi-slit image slicer of EST.

Entrance FoV	80 arcsec^2
Number of output slits	8
Field of view of each slit	0.05 arcsec x 200 arcsec
Slices width	50 μm
Sampling per slice	0.05 *arcsec*
Input F-ratio	F/50
Output F-ratio	F/40
Output illumination	Telecentric

3.2 Alternatives of design

Three alternatives have been studied: two based on the concept of the image slicer of MUSE (Laurent et al., 2006) and FISICA (Glenn et al., 2004), which have been adapted to the EST requirements and implemented in ZEMAX during this work, and a new design that has been called MuSICa, which minimizes the number of optical elements for the multi-slit capability and that will be selected for EST. Different variations of each one have been designed considering different geometric distributions for the mirrors.

1. MUSE

   MUSE (Laurent et al., 2008) has been designed for the 8.2 metres VLT (Bacon et al., 2010). It presents an excellent image slicer which minimizes the number of optical elements used to reorganise a bidimensional field of view into a long slit. This is the reason why it is one of the concepts studied for EST. Its optical design is schematised in Fig. 3.1. An array of powered slicer mirrors with spherical curvature, called image dissector array (IDA), cuts the entrance bidimensional field of view decomposing the incoming beam into different sub-beams, one per slice. At the pupil position a mask is placed, which allows the pass of the light associated to the pupil of each sub-beam and avoids the contribution of scattered light. An array of powered mirrors, also spherical, focuses the sub-beams generating the output slit and sends the pupil to infinity verifying the condition of the telecentrism. For the study of an image slicer based on this concept, the optical path for one configuration, which corresponds to the path followed by a part of the entrance sliced field of view using one mirror of each array, can be described in two steps as it is shown in Fig. 3.2.

   Different design options were studied. The initial entrance focal-ratio for the IFU was F/100 to facilitate the slicer mirrors manufacturing, which in this case would present a width of 100 μm. A 1:2 reimaging system composed by two powered mirrors was considered for this option before the image slicer. The last array of mirrors makes the focal-ratio conversion, from F/100 to $F/40$ in the first studied designs and from F/50 to F/40 in the final ones, once the possibility to manufacture slices with 50 μm width was confirmed. In addition, the shape of the entrance field of view changed during the optical design study. Firstly, a square field of view of 9 $\times$ 9 arcsec^2 was considered. This shape is advisable if image reconstruction techniques were to be applied, however

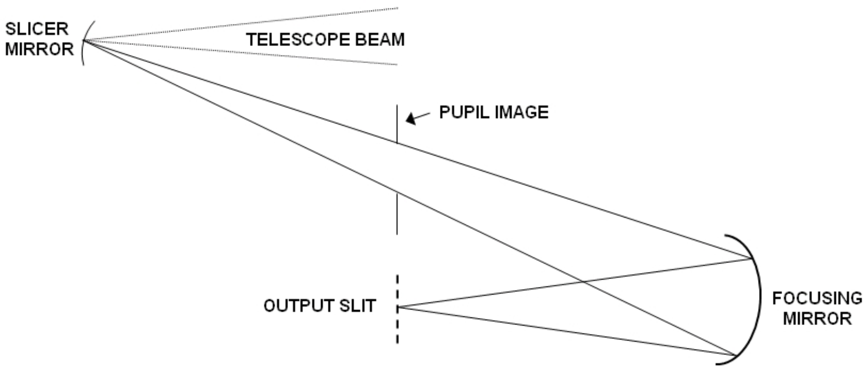

Figure 3.1: Scheme of the MUSE image slicer. An array of powered slicer mirrors with spherical curvature, called image dissector array, cuts the entrance bidimensional field of view decomposing the incoming beam into different sub-beams, one per slice. At the pupil position a mask is placed, which allows the pass of the light associated to the pupil of each sub-beam and avoids the contribution of scattered light. An array of powered mirrors, also spherical, focuses the sub-beams generating the output slit and sends the pupil to infinity verifying the condition of the telecentrism.

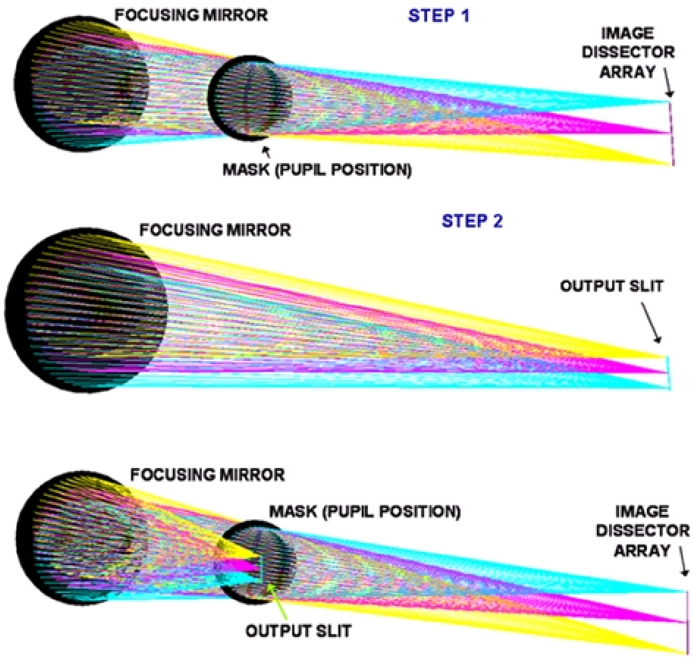

Figure 3.2: Step by step of the concept 1 layout for one configuration. Step 1: the image dissector array is placed at the telescope image focal plane. It is composed by spherical mirrors. Its function is to cut the input beam and send each sub-beam to a focusing mirror. Between them a pupil mask is placed to allow the pass of the pupil avoiding scattered light contribution. The step 2 shows how the focusing mirror makes the beam converge generating a piece of the output slit and sends the pupil to infinity. In the last picture all the steps are presented together.

the final shape of the field is rectangular, with 6.32 arcsec width $\times$ 12.66 arcsec length. The number of slicer mirrors in order to compensate the aberrations to improve the optical quality and to reduce the costs have been the reasons to modify the initial geometry.

The optical design of the adaptation of this concept is presented in Fig. 3.3, where the considered field of view is 9 $\times$ 9 arcsec^2, the initial focal-ratio is F/100 and the final one is F/40. The focal lengths and radius of curvature of the image dissector mirrors and the focusing ones are presented in Table 3.2. The mirrors of the two arrays of this concept are spherical. The optical quality of this design is diffraction limited, as shown in Fig. 3.4, where the rays are perfectly contained within the Airy disk for all the configurations.

Table 3.2: Focal length and radius of curvature of the spherical mirrors of the two arrays used in the image slicer based on the concept of MUSE.

ELEMENT	FOCAL LENGTH (mm)	RADIUS (mm)
Image dissector array	2000	4000
Focusing mirror	800	1600

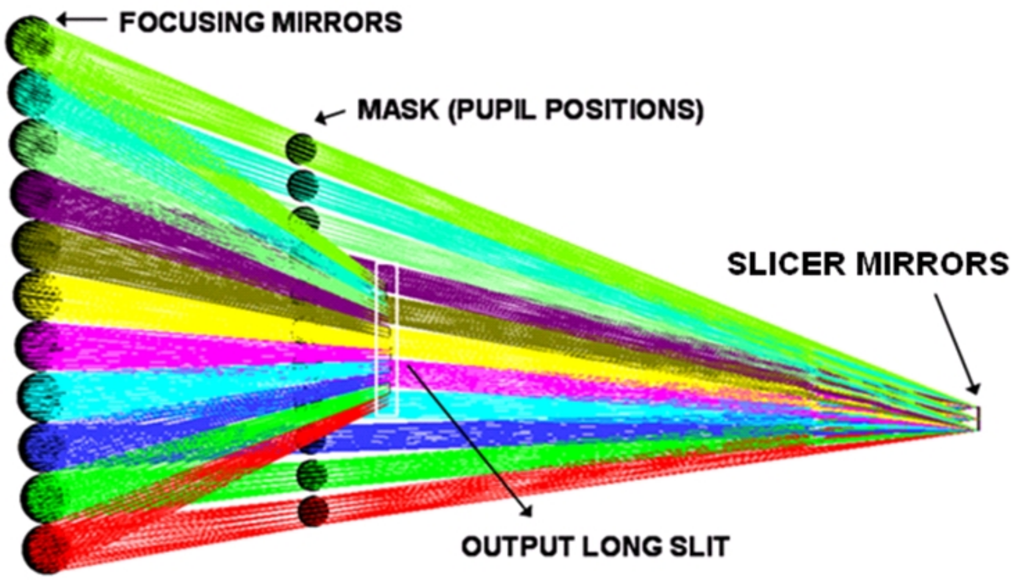

Figure 3.3: Optical design of the adaptation of the first concept studied, based on MUSE, for the integral field spectrograph of EST. The output slit is generated by the alignment of the focused beam of each configuration. This design shows the feasibility of the adaptation of this concept using 11 configurations, one half of the total number for a field of view of 9 $\times$ 9 arcsec^2 and 100 μm width of the mirrors that cut the entrance field of view.

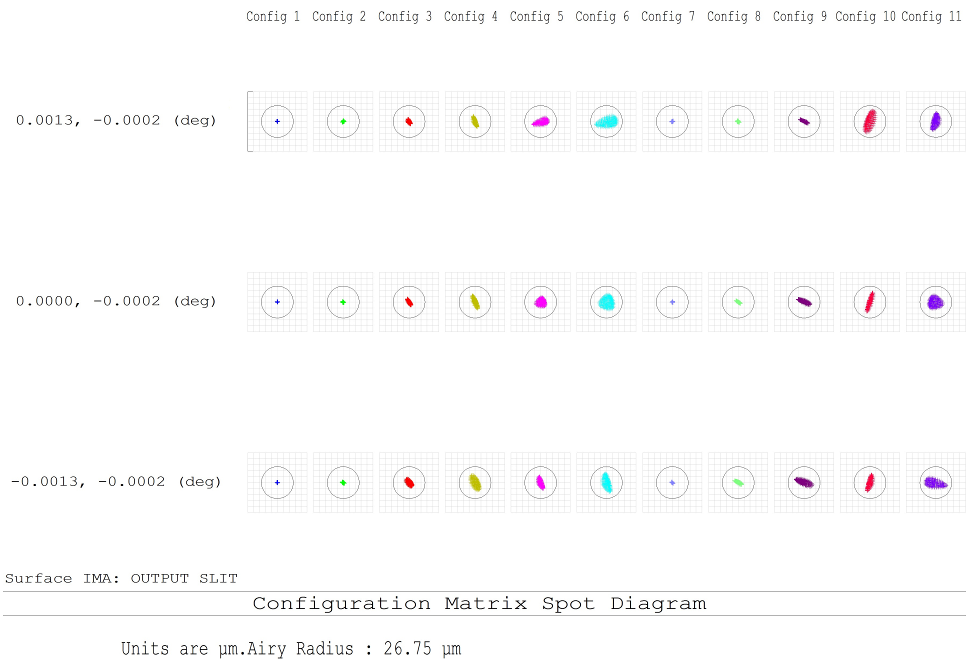

Figure 3.4: Diffraction limited spot diagram for the 11 configurations of the design of Fig. 3.3. Each column represents a piece of the generated output slit, which is really composed by 22 configurations. The spot diagram is also at diffraction limit for all of them.

In order to minimize the aberrations due to off-axis distances, some variations based on this concept have also been studied. These variations are made over F/50 to F/40 systems using 16 configurations. In one of them the focusing mirrors are reorganised in two columns (see Fig. 3.5) to minimize the off-axis distances and the angles of incidence. The output slit length in this case is comparable with the height of the columns in which the focusing mirrors are organised, what improves the optical quality. A different geometrical layout using four columns (Fig. 3.6) has also been analysed, where the improvement due to the decrease of the height over the optical axis is affected by lateral decentring. Comparing these optical designs, the one of Fig. 3.5 seems to be the best for this instrument.

There are some important points in the design of an image slicer. The organisation of the mirrors within an array is very important. The number of components, their location and their correspondence to elements of the other arrays are crucial to optimize the final optical quality. In addition, since the output slit is generated as the composition of each focused beam, all of them have to be perfectly aligned. The considered concepts for the image slicer of this instrument must verify the telecentricity condition. All these points have been meticulously analysed in all the design study process.

According to all these points, this first concept is applicable for EST.

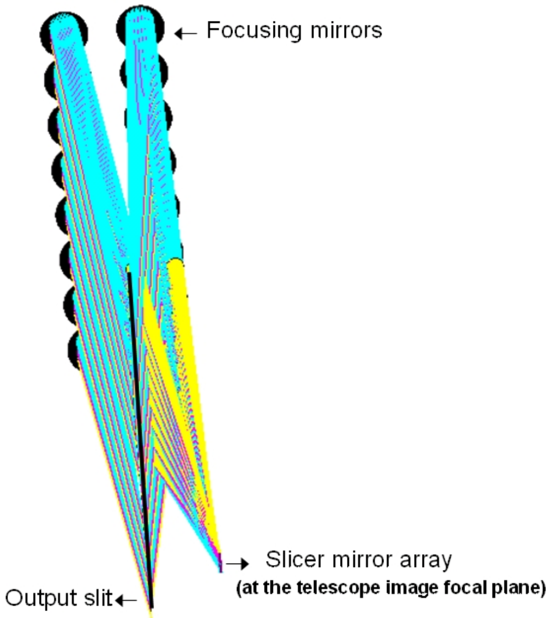

Figure 3.5: Optical design of the first studied concept reorganizing the focusing mirrors in two columns to minimize the off-axis distances and the angles of incidence. For this design the input f-number is 50 and the output one, 40. Sixteen configurations are used.

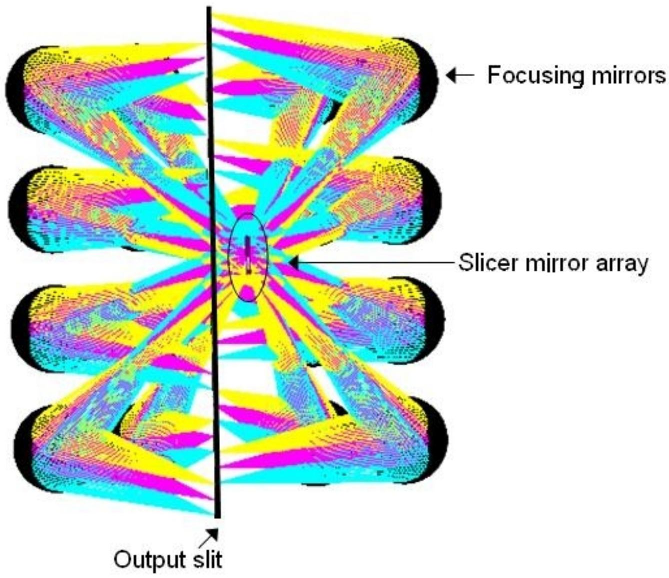

Figure 3.6: Optical design of the first studied concept reorganizing th focusing mirrors in four columns. An input f-number of 50 and an output one of 40 have been considered for this design. Sixteen configurations are used. Despite of presenting smaller off-axis distances, the increment in lateral displacement deteriorates the optical quality more than in the case of Fig. 3.5.

2. FISICA

   The second studied concept is FISICA (Eikenberry et al., 2006c), an excellent image slicer in which the IFU of other instruments like HRNIRS (Eikenberry et al., 2006b), FRIDA (Cuevas et al., 2008) or IRMOS (Eikenberry et al., 2006a) are also based on. FISICA is the image slicer of the instrument FLAMINGOS (Gorlova et al., 2010), for the 4-m Kitt Peak National Observatory (KPNO) and the 8-m Gemini-South Observatory in Chile. Its layout is schematised in Fig. 3.7. This option presents three powered optical components where each one is an array of spherical mirrors. The slicer mirror array cuts the entrance field of view at the telescope image focal plane in very thin slices and images the pupil of each sub-beam. The second array of mirrors is placed in the pupil position and, for that reason, it is called pupil mirror array. It collimates the beams for each configuration. These collimated beams are focused by the last optical component, whose name is field mirror array, composing the output slit. In addition it sends the pupil to the infinity verifying the telecentrism.

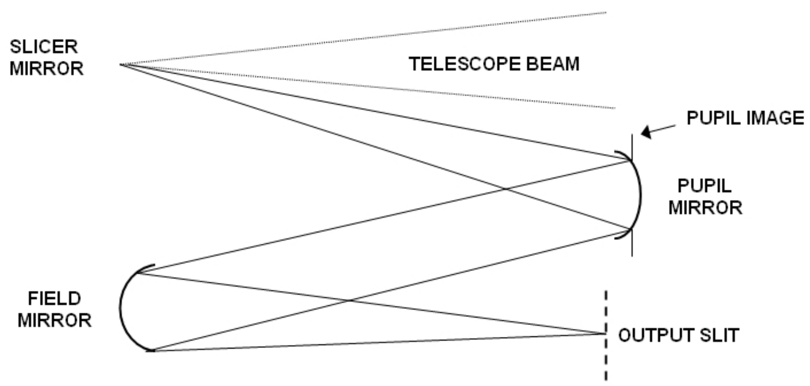

Figure 3.7: Layout of the second studied concept of image slicer based on FISICA. It uses three arrays of spherical mirrors. The first one (slicer mirror array) cuts the entrance field of view, the second one (pupil mirror array) is located at the pupil position and collimates the beams. These collimated beams are focused by the last array (field mirror array), composing the output slit. In addition it sends the pupil to the infinity verifying the telecentricity.

   As for the first alternative, the way in which the field of view is cut and reorganised into a piece of the output slit for one configuration is explained in the mosaic of Fig. 3.8. The same process realised for the first concept has been followed for this one, starting with the considerations of an F/100 to F/40 system using a 9 $\times$ 9 arcsec^2 until finishing with the final F/50 to F/40 system and a field of view of 6.32 arcsec width $\times$ 12.66 arcsec length.

   The focal length and radius of curvature of the different elements used for the first case are presented in Table 3.3. The number of configurations needed for the whole design depends on the size of the input field and the width in which it is cut, this is, the slicer mirrors width. In this case 22 configurations are required.

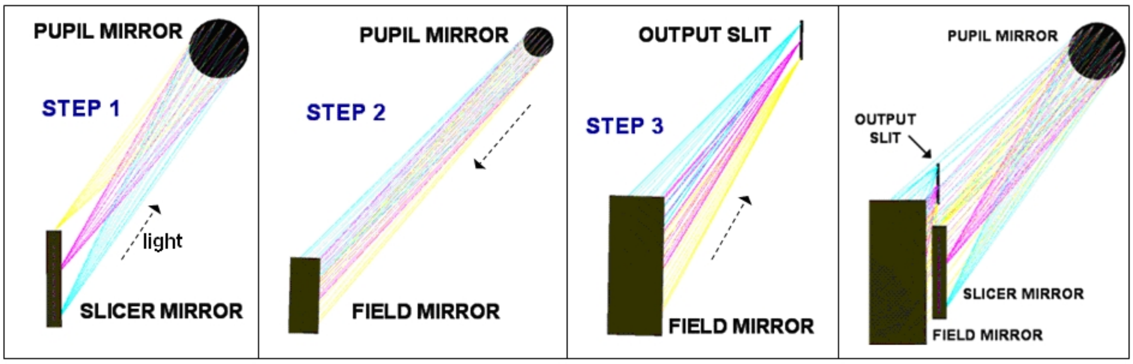

Figure 3.8: Mosaic of images of the step by step functionality of the image slicer based on concept 2 for one configuration defined by three field points. In the step 1 the slicer mirror cuts the entrance field and sends it, by X and Y-axis tilts, to its pupil position, where the pupil mirror is placed. In the step 2 the pupil mirror collimates the beam and sends it to the field mirror. The step 3 shows the field mirror that focuses the beam generating a piece of the output slit and sends the pupil to infinity. The fourth picture, on the right, shows all the steps together.

Table 3.3: Focal length and radius of curvature of the spherical mirrors of the three arrays used in the image slicer based on the concept of FISICA. The focal length of the field mirrors is shorter to make the focal-ratio conversion from F/100 to F/40.

ELEMENT	FOCAL LENGTH (mm)	RADIUS (mm)
Slicer mirror	1000	2000
Pupil mirror	1000	2000
Field mirror	400	800

This concept, as well as the first one based on MUSE, has been adapted because it is an excellent telecentric optical systems.

As in the first case, different alternatives have also been studied for this second concept, distributing the pupil and field mirrors in two columns to minimize off-axis aberrations (see the layout of Fig. 3.9 a) or combining the pupil mirrors arranged in two rows orthogonal to the two field mirrors columns (see Fig. 3.9 b). Although both of them present very good optical quality limited by diffraction (see the spot diagram of Fig. 3.10), the layout (a) uses smaller angles and the optical quality is more compensated.

Other options have also been studied, like the ones of Figs. 3.11 (a) and (b). In both cases the pupil mirrors are organised in four columns where two rows are placed over the incoming telescope beam and the other two under it. The field mirrors are arranged in two columns. The layout on the left (a) presents a design in which the pupil mirrors are separated to locate the output slit in the middle, parallel to the telescope image. The main difference of the layout (b) is that the output slit is decentred, generated on a side of the pupil mirror array.

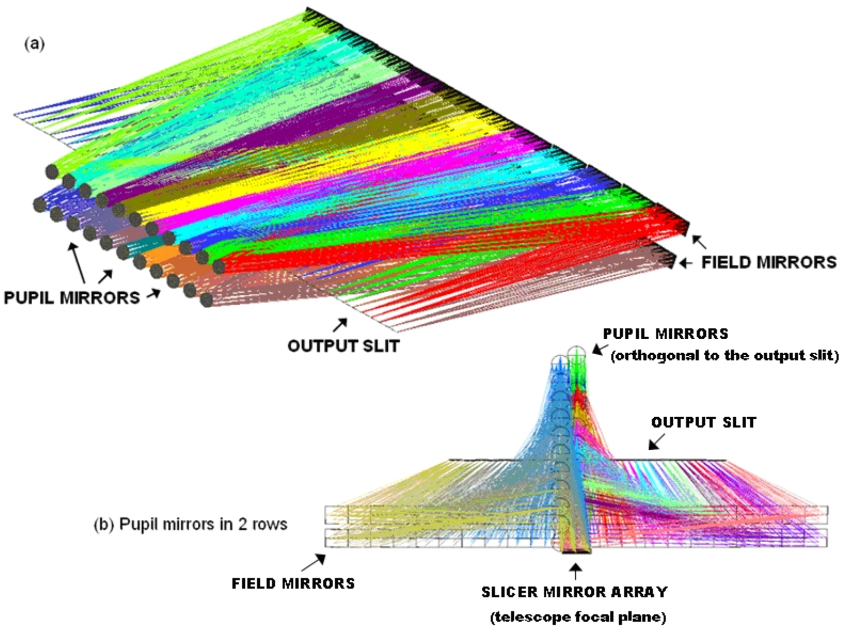

Figure 3.9: Two studied alternatives of the concept 2. The layout on the top (a) presents a geometrical distribution where pupil and field mirrors are arranged in two columns to reduce the angles due to the height of the elements with respect to the optical axis. The design (b) presents another alternative, where the pupil mirrors are distributed in two rows orthogonal to the field mirrors that are organised in two columns parallel to the output slit.

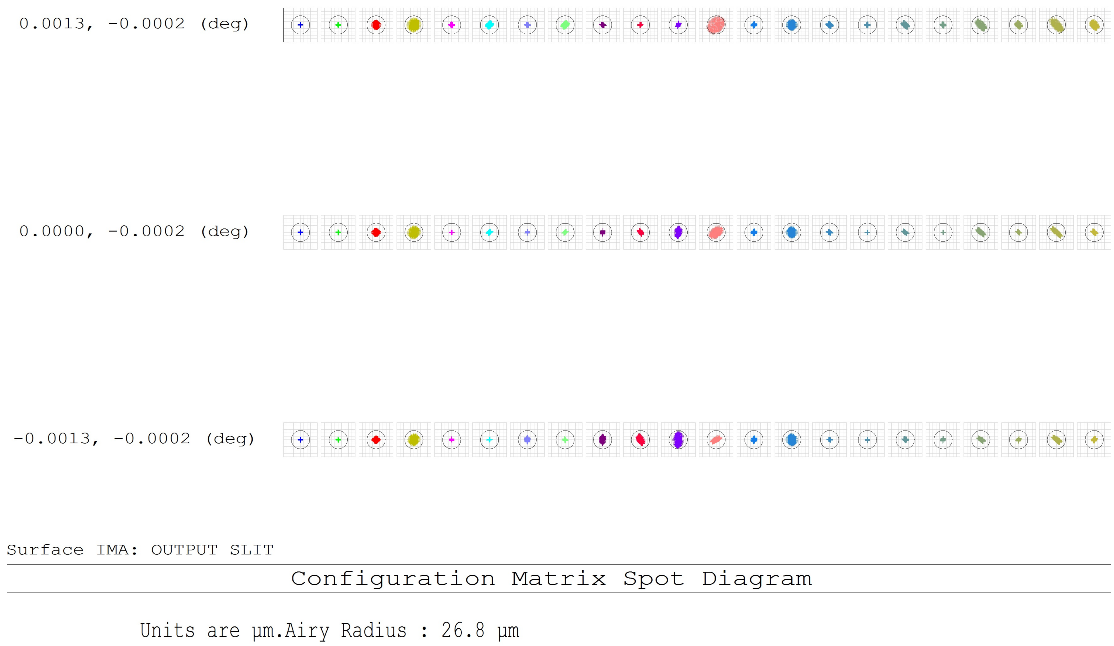

Figure 3.10: Spot diagram associated to the design of Fig. 3.9 b. The optical quality is diffraction limited.

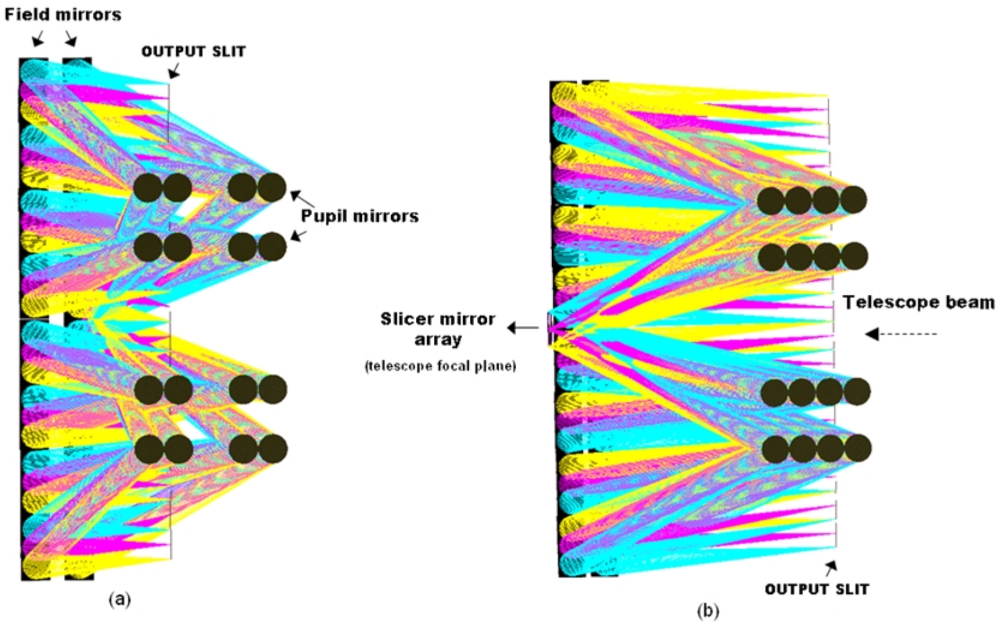

Figure 3.11: On the left, the layout (a) presents an alternative of optical design based on the second concept in which the pupil mirrors are distributed above and below the telescope beam. On the right (b), a variation of (a) is presented where the output slit is generated on a side of the pupil mirrors.

3. MuSICa

   In addition to the adaptation of the concepts based on MUSE and FISICA, a new design of image slicer has been developed with the purpose of minimizing the number of optical surfaces for the multi-slit capability (Calcines et al., 2012c). It has been called MuSICa (Multi-Slit Image slicer based on collimator-Camera). Its layout is presented in Fig. 3.12.

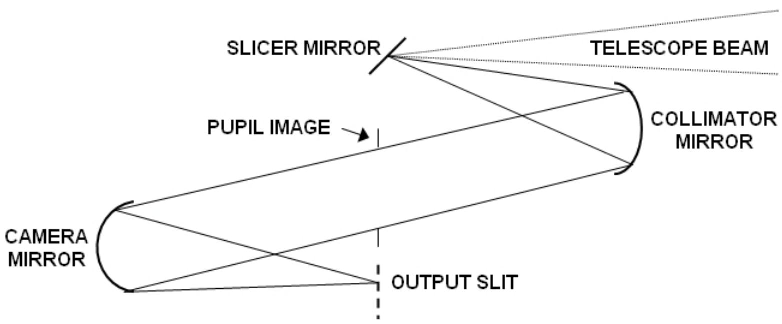

Figure 3.12: Schematised layout of the MuSICa concept.

   For one image slicer the number of components is three: slicer, collimator and camera mirror arrays. As a difference with the last concepts, in this case the slicer mirrors are flat and the pupil is produced by the collimator mirrors in a location between them and the camera mirrors. Both, collimator and camera mirrors, are spherical. A pupil mask is then placed to allow the pass of the pupils avoiding the contribution of scattered light. Attending to the studies of the other alternatives, collimator and camera mirrors are organised in two columns in front of each other and the output slit is generated between them. In every case in which more than one column of mirrors is used, the output slit is generated by alternating the image of a configuration from each column. This compensates the possible aberrations improving the optical quality. A sketch of the step by step of the MuSICa design is shown in Fig. 3.13.

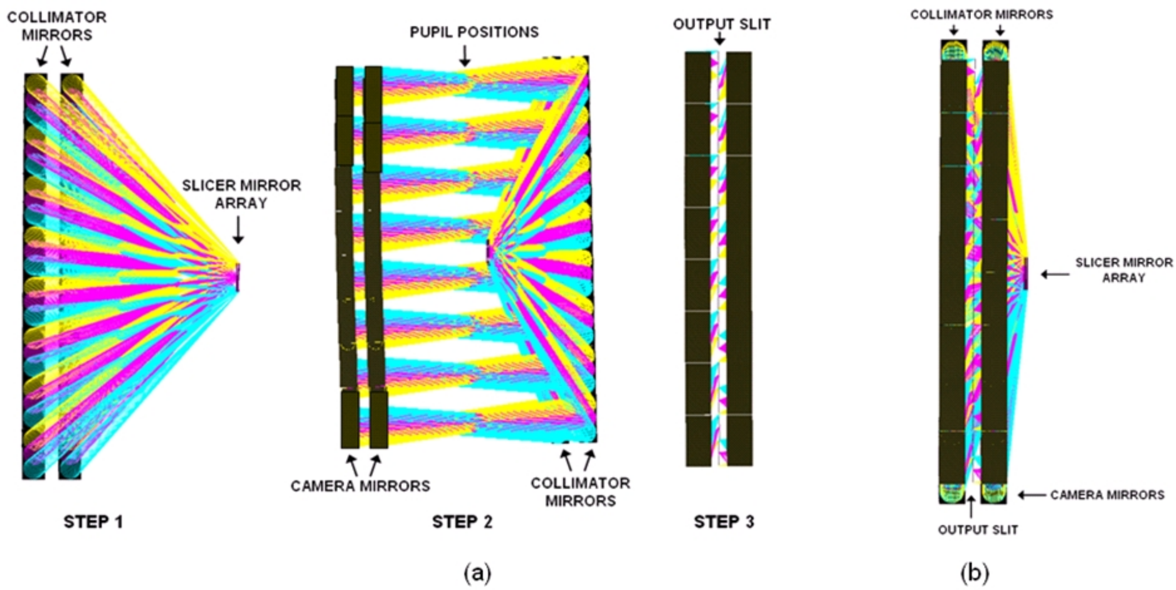

Figure 3.13: Step by step of the MuSICa concept. The step 1 shows how the slicer mirrors, after decomposing the field of view, send each sub-beam to a collimator mirror. These collimate the beams and send them to the camera mirrors, located each of them in front of a collimator mirror. The pupils are focused in an intermediate position between them. Finally the third step is done by the camera mirrors and consists in focusing each sub-beam, all of them aligned, composing the output slit and sending the pupil to infinity. The layout (b) presents all the steps together.

Another option has also been studied using only one circular aperture for all the pupil images which are overlapped (see Fig. 3.14 b). To overlap the pupils and make the mask easier to manufacture, the correspondence between collimator and camera mirrors are crossed, being then antisymmetric. The optical design, including all the components, is presented in Fig. 3.14 a.

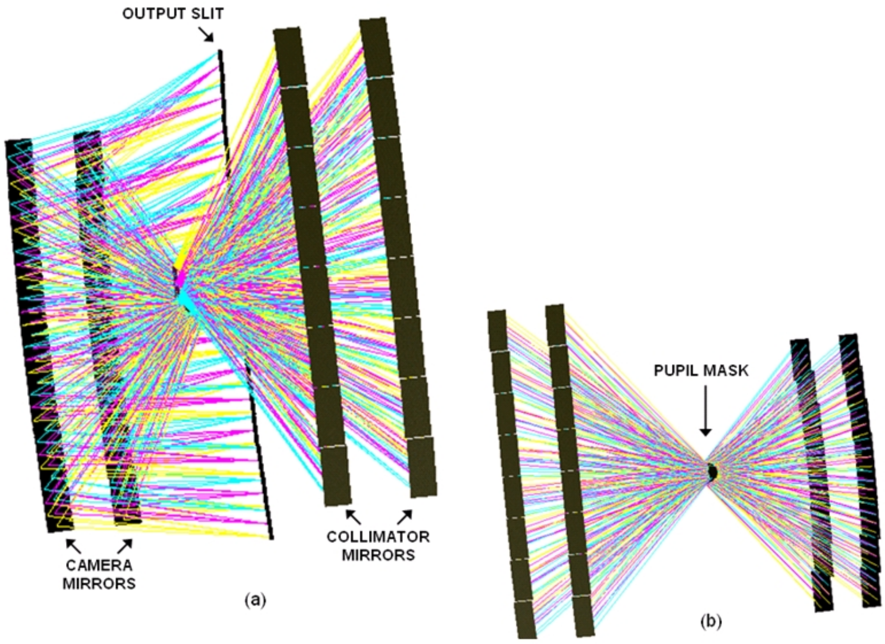

Figure 3.14: MuSICa optical design using a pupil mask with only one circular aperture. On the left (a), the layout, including all the components, is presented, while on the right (b) the detail of the symmetry with respect to the pupil mask is outstanding.

3.3 MuSICa technical characteristics

The 80 arcsec^2 entrance field of view has been selected in a rectangular shape with 6.32 arcsec width by 12.66 arcsec length. The macro-slicer, placed at the F/50 telescope image focal plane has the linear size of this field, 6.128 mm width by 12.275 mm length. It is composed by eight flat mirrors that cut the entrance field using different orientations, each one with a size of 0.766 mm by 12.275 mm that corresponds to a field eight times smaller in width and with the same length, 0.79 arcsec by 12.66 arcsec, respectively (see the sketch of Fig. 3.15). Each one of these eight sub-fields is the entrance of an image slicer (Fig. 3.16). The linear size of the sub-field is also the size of the slicer mirror array in each case. The slicer mirror array cuts its entrance sub-field into slices of 0.049 arcsec width. This value is given by the required spectrograph spatial sampling, 0.05 arcsec/slit width. Sixteen slicer mirrors imply $\sim$0.049 arcsec per slice and fifteen slicer mirrors, $\sim$0.053 arcsec per slice. In addition, a characteristic of MuSICa is the symmetry of its layout, in which the collimator and camera mirrors are arranged in two columns with the same number of mirrors. Thus, an even number of mirrors is considered, in this case, sixteen flat slicer mirrors with 0.049 mm width by 12.275 mm length. So every array of the image slicer presents sixteen elements, arranged in two columns to minimize the off-axis distances and angles. Collimator and camera mirrors are spherical. The field of each slicer mirror, $\sim$0.049 arcsec, multiplied by the number of slicer mirrors per sub-field, sixteen, and by the number of sub-fields, eight, is the width of the entrance IFU field of view, 6.32 arcsec.

For the design of a focal reducer image slicer, from the telescope focal ratio F/50 to the spectrograph F/40, a collimator with 220 mm focal length has been considered and a radius of curvature of 440 mm. This is the distance from the slicer mirror array to the collimator one and from this to the pupil mask. The pupil mask of MuSICa presents only a circular aperture with 5.00 mm diameter in which the pupil images of each configuration are perfectly overlapped. The camera mirror array is placed at 176 mm from the mask and equidistant to the output slit. Its radius of curvature is 352 mm. The ratio between camera and collimator focal lengths gives the magnification of the system, 0.8 in the case of this focal-ratio converter design. The technical characteristics of the image slicer components are presented in Table 3.4.

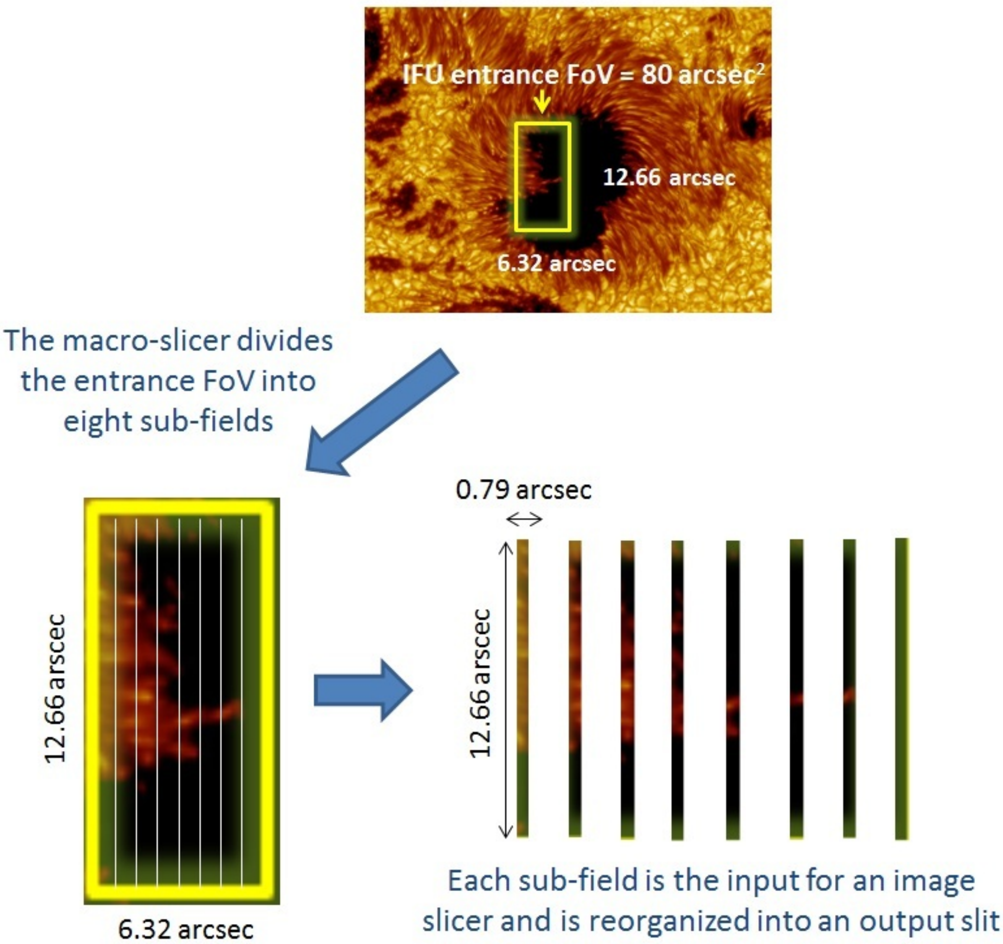

Figure 3.15: Sketch of the integral field unit field of view division into eight sub-fields. The input FoV, 6.32 arcsec width × 12.66 arcsec length, is divided at the telescope image focal plane by the macro-slicer, which, using eight flat mirrors, cuts the entrance field of view into eight sub-fields with 0.79 arcsec width × 12.66 arcsec length. Each sub-field is the entrance for an image slicer and is reorganised into an output slit.

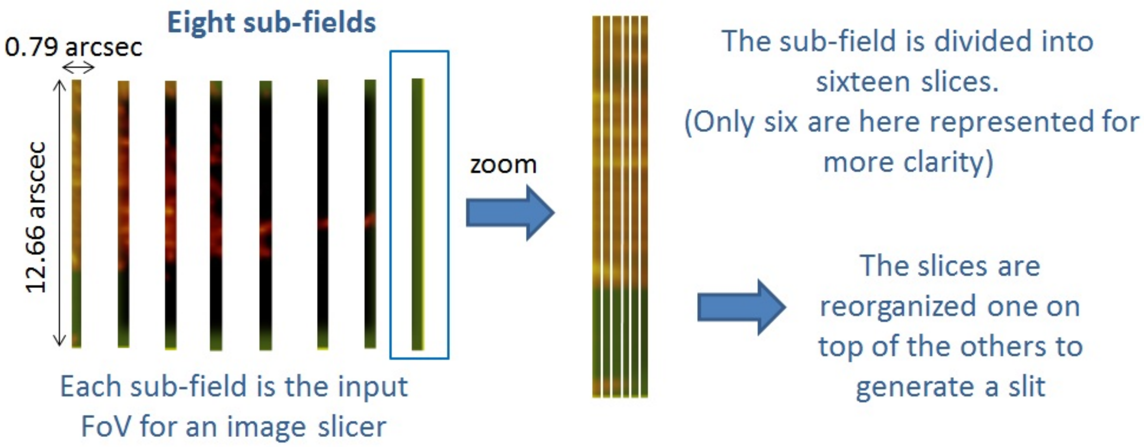

Figure 3.16: Sketch of the sub-field division. Each one of the eight sub-fields is the entrance field of view for an image slicer. It is divided by the slicer mirrors into sixteen slices of ∼0.049 arcsec. The slices are reorganised, one on top of the others, to generate an output slit.

Table 3.4: Technical characteristics of the image slicer of EST.

MACRO-SLICER	
Entrance FoV	$6.32 \times 12.66\,\text{arcsec}^2$
Linear size of the array	6.128 mm ×12.275 mm
Input focal-ratio	F/50
Number of mirrors of the array	8
Curvature	Flat
Linear size of each mirror	0.766 mm × 12.275 mm
FoV per image slicer	0.79×12.66 arcsec^2
SLICER MIRROR ARRAY	
Number of mirrors	16
Curvature	Flat
Size of each mirror	0.049 mm × 12.275 mm
COLLIMATOR MIRROR ARRAY	
Number of mirrors	16
Curvature	Spherical
Focal length	220 mm
CAMERA MIRROR ARRAY	
Number of mirrors	16
Curvature	Spherical
Output focal-ratio	F/40
Focal length	176 mm

3.4 Mathematical treatment

For the design of MuSICa, the coordinates of each optical element can be calculated using the following equations that have been obtained applying geometrical optics. The position of the slicer mirror array is at the telescope image focal plane, centred with respect to the optical axis. Each one of these mirrors presents a different X and Y axis tilts to send the light corresponding to the different parts of the field to their associated collimator mirrors. The position of each collimator mirror is defined by its cartesian coordinates $(X_{COL}, Y_{COL}, Z_{COL})$ that can be calculated using Eq. 3.1, Eq. 3.2 and Eq. 3.3.

$$X_{COLi} = dec_{Xsi} + (f_{COL} \pm sag_i) \cdot tan(ty_{si})\,, \tag{3.1}$$

$$Y_{COLi} = dec_{Ysi} + (f_{COL} \pm sag_i) \cdot tan(tx_{si})\,, \tag{3.2}$$

$$Z_{COLi} = f_{COL} \pm sag_i\,, \tag{3.3}$$

for $i = 1, ..., N$ and N: number of configurations.

The parameters dec_{Xsi} and dec_{Ysi} are the decentred distances in X and Y axis, ty_{si} is the tilt of the slicer mirror around the X axis, tx_{si} is the tilt over the y axis and sag is the saggita, which is taken into account because the collimator and camera mirrors define the surface with the curvature of a sphere (see Fig. 3.14 b). It can be calculated attending to the general Eq. 3.4.

$$sag = \frac{c \cdot s^2}{1 + (1 - (K+1) \cdot c^2 \cdot s^2)^{\frac{1}{2}}}\,. \tag{3.4}$$

In this equation, c is the inverse of the radius of curvature, s is the distance with respect to the optical axis and K is the conicity constant, which for a sphere is $K = 0$.

The pupil mask in this case presents only an aperture in which all the pupil images are overlapped. They verify, thus, that their coordinates, X_P, Y_P and Z_P, for each configuration, are the same (Eq. 3.5).

$$X_{Pi} = constant, Y_{Pi} = constant, Z_{Pi} = constant\,. \tag{3.5}$$

The pupil mask is centred in the optical axis and aligned with the slicer mirror array. Its position defines the collimator tilts (ty_{COLi}, tx_{COLi}) that are defined by Eqs. 3.6 and 3.7.

$$ty_{COLi} = \arctan\left(\frac{X_{COLi}}{Z_{COLi}}\right)\,, \tag{3.6}$$

$$tx_{COLi} = \arctan\left(\frac{Y_{COLi}}{Z_{COLi}}\right)\,. \tag{3.7}$$

Collimator and camera mirrors are antisymmetric, and their coordinates verify the Eqs. 3.8, 3.9 and 3.10.

$$X_{CAMi} = -X_{COLi}\,, \tag{3.8}$$

$$Y_{CAMi} = -Y_{COLi}\,, \tag{3.9}$$

$$Z_{CAMi} = -\Gamma_{IFU} \cdot Z_{COLi}\,. \tag{3.10}$$

In Eq. 3.10, Γ_{IFU} is the magnification of the IFU, calculated as the ratio between the camera and collimator focal lengths.

The coordinates of each piece of the output slit can be calculated using Eqs. 3.11, 3.12 and 3.13.

$$X_{Si} = decx_{CAMi} + (f_{CAMi} \pm sag_{xi}) \cdot tan(ty_{CAMi})\,, \tag{3.11}$$

$$Y_{Si} = decy_{CAMi} + (f_{CAMi} \pm sag_{yi}) \cdot tan(tx_{CAMi})\,, \tag{3.12}$$

$$Z_{Si} = f_{CAM}\,, \tag{3.13}$$

where ty_{CAMi} and tx_{CAMi} are the tilts over the X and Y axis respectively of each camera mirrors, sag_{xi} and sag_{yi} are the saggita of the X and Y axis and $decx_{CAMi}$, $decy_{CAMi}$ are the decentred distances of the camera mirrors with respect to the X and Y axis respectively.

3.5 2-modes image slicer

Since the science goals include polarimetric studies for the study of the magnetic fields, the structure and evolution of magnetic flux or the magnetic coupling of photosphere and chromosphere, the proposed instrument has been designed considering the possibility to couple a polarimeter and offer a second mode of operation. This increases the instrument performance and the science cases that can be observed with high resolution spectroscopy and with high resolution spectro-polarimetry.

For the spectroscopic mode, an entrance field of view of 80 arcsec^2 is reorganised into eight long slits of 200 arcsec length by 0.05 arcsec width. In the spectro-polarimetric mode, a field of view of 40 arcsec^2 is redistributed into eight slits of 100 arcsec length by 0.05 arcsec width. These slits will be later duplicated by the beam splitter of the polarimeter in two orthogonal linear polarisations, which are aligned one on top of the other obtaining a slit twice larger. Finally, eight long slits of 200 arcsec length are generated for this mode too, where 100 arcsec corresponds to a polarimetric state of the light and the rest to the orthogonal one (see the sketch of Fig. 3.17).

The polarimeter is composed by a modulator and a beam-splitter. These could be placed together or in different positions. In the case of the beam-splitter, it should be located after the image slicer to satisfy the science requirement for the polarimetric sensitivity of 10^{-4}.

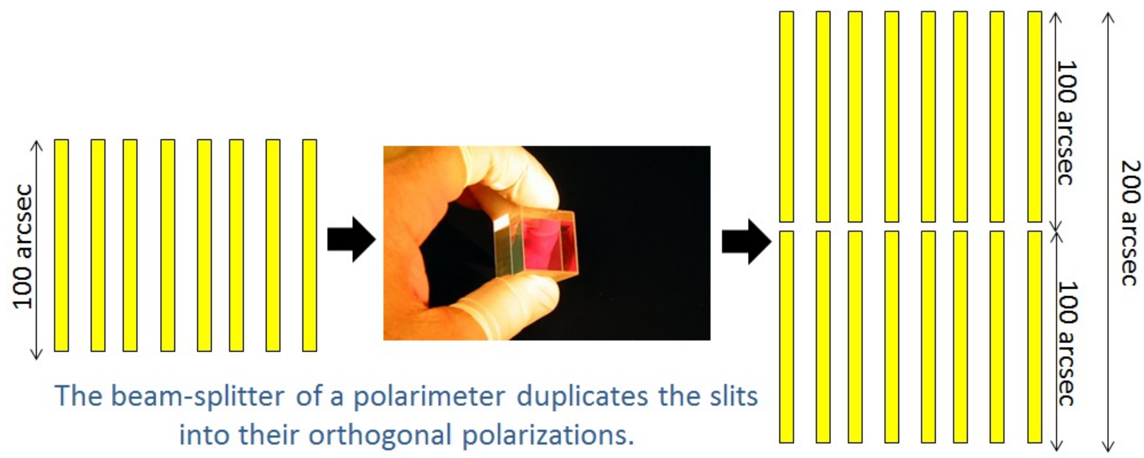

Figure 3.17: This sketch shows the steps followed to reorganise the bidimensional entrance field of view into the eight output slits for the spectro-polarimetric mode of observation. At the telescope image focal plane the field of view is sliced and reorganised into eight slits with 0.05 arcsec width by 100 arcsec length. These slits are duplicated by the beam-splitter of the polarimeter obtaining slits twice larger, composed by the two orthogonal linear polarisations.

If the beam-splitter were assembled before the image slicer, it would be very difficult to guarantee that, after cutting the field of view in 50 μm slices and reorganizing it into the slits, the same point would be strictly sampled by the image slicer at the two images produced by the beam-splitter.

The proposed image slicer concept is very versatile and can operate in the 2 different modes illuminating adequately the spectrograph in each case. Technically, these 2 modes can be compatible with the same integral field unit taking into account parameters like: the entrance field of view and its shape, the number of mirrors of each array and the way in which the configurations are organised to compose the final slits.

The entrance field of view can be considered in different shapes. A rectangular one with 6.32 arcsec by 12.66 arcsec has been assumed for this design proposal. It is advisable to use the smaller side along the cut direction, what implies a smaller number of slices and, as a consequence, each array presents less number of elements than doing it the other way.

The design of this double mode IFU uses the totality of the mirrors of each array for the spectroscopic mode. All the configurations are required to compose the 200 arcsec length slits. On the other hand, the spectro-polarimetric mode offers slits of 100 arcsec length, and only one half of the total number of mirrors, eight in this case, are required. The tilts of the mirrors of each array are fixed and common for both modes. The central configurations of the slicer mirror array, which are symmetrically distributed between the 2 columns of collimator and camera mirrors, generate a centred slit of 100 arcsec length that corresponds to the spectro-polarimetric mode. The rest of the configurations provide the other 100 arcsec, unused in the spectro-polarimetric mode, that are distributed symmetrically at both sides with respect to the optical axis to complete the 200 arcsec length for the spectroscopic slits. To optimise the optical quality and compensate the possible aberrations, the best alternative to design a 2-modes image slicer is obtained using an even number of slices (Eq. 3.14). Thus, an even number of configurations at both sides of the optical axis is then used. The symmetry of the design offers an IFU where the beams are very compensated and the optical quality is improved.

$$2^n,\ with\ n > 2\,. \tag{3.14}$$

This equation gives an even number of slices, which determines the number of mirrors of each array. And n is an integer number larger than 2.

Designs with other number of mirrors are also possible. For instance, there may be systems with an even number of elements that use an odd number of configurations at both sides of the optical axis to complete the spectroscopic mode. The number of mirrors for each case verifies the Eq. 3.15.

$$(2m+1)\cdot 2^n,\ with\ n = 2, m \geqslant 0, \tag{3.15}$$

where m and n are integer numbers.

The field of view for the spectro-polarimetric mode can be selected using a mask in front of the IFU entrance. This mask is simpler if the selected slicers are located together one adjacent to the other, instead of alternating them. This distribution also facilitates the scan of a bigger field of view with an external image scanner or with the telescope itself. In terms of aberrations, the best is to use the central mirrors and generate a middle-length slit, centred with respect to the optical axis. On the other hand, for the spectroscopic mode, these slicer mirrors also generate the central part of the long slit, while the others offer the contribution of the rest. This 2-modes capability for the IFU offers versatility to the instrument.

3.6 Multi-slit image slicer

In general, an image slicer generates a slit from a bidimensional field of view. For the multi-slit capability, eight image slicers, one per slit, are needed. In order to fulfil this multi-slit capability, the image generated by the telescope is cut into as many smaller sub-fields as the number of slits. This can be done using an array of flat mirrors called macro-slicer that, with different orientations, cuts the entrance field into eight sub-fields and sends them to different locations such that each sub-field feeds an image slicer.

Both macro-slicer and slicer mirror array must be placed at a focal plane. As a consequence, the macro-slicer would be placed at the telescope image focal plane and a 1:1 reimaging system between the macro-slicer and the slicer mirror array is then required, to generate a focus to locate this last component. A macro-slicer with eight flat mirrors, a 1:1 reimaging system and eight image slicers, with their corresponding components, are required to generate the multi-slit spectrograph entrance.

The slicer mirrors for the first two concepts are spherical. Nevertheless, in the case of MuSICa, both macro-slicer and slicer mirrors are flat and they can be combined to be integrated together. The macro-slicer has eight flat mirrors that cut the field of view into eight sub-fields and send them to a different image slicer using the appropriate orientation. As the slicer mirror array of each image slicer is also composed by flat mirrors, it can be integrated over its corresponding mirror of the macro-slicer. Doing it this way, the field of view is cut into sub-fields using appropriate orientations of the different mirrors of the macro-slicer. Each sub-field is itself divided into thin slices by the slicer mirrors integrated over the surfaces of the macro-slicer. The joint combination of these elements does not require any reimaging system, so that, the number of elements necessary to get the multi-slit capability is smaller in the case of this design. Because of the arrangement of macro-slicer and slicer mirrors, the final number of optical elements needed to generate, either one slit or, in this case, eight, is the same: three optical elements (macro-slicer + slicer mirror array, collimator mirror array and camera mirror array). In the cases of concepts 1 and 2, considering two optical elements for the reimaging system, the number of total components are five and six, respectively. The number of optical components needed for the three studied concepts to satisfy the multi-slit capability is presented in Table 3.5.

Table 3.5: Number of optical elements associated to each alternative for the multi-slit capability.

ELEMENT	Number of mirrors or arrays
CONCEPT 1 BASED ON MUSE	
Macro-slicer	1
Reimaging system	2
Image dissector array	1
Focusing mirror array	1
Total number of surfaces	**5**
CONCEPT 2 BASED ON FISICA	
Macro-slicer	1
Reimaging system	2
Slicer mirror array	1
Pupil mirror array	1
Field mirror array	1
Total number of surfaces	**6**
CONCEPT 3: MuSICa	
Macro-slicer+Slicer mirror array	1
Collimator mirror array	1
Camera mirror array	1
Total number of surfaces	**3**

For the purpose of maximizing the total throughput of the instrument the number of optical elements should be minimised. Attending to Table 3.5, MuSICa is the alternative with the minimum number of surfaces in order to get the multi-slit capability, due to the macro-slicer and the slicer mirror array can be integrated together avoiding the necessity of a reimaging system. This is the concept proposed and developed for the integral field spectrograph of EST.

In order to demonstrate the manufacturing feasibility of the image slicer components and to get an idea of how the system will be, Figs. 3.18 and 3.19 show some examples of image slicer components developed for MUSE by Winlight Optics, the company that will manufacture the prototype of image slicer for EST. These images are shown freely on their website.

Fig. 3.18 helps to get an idea about the combination of macro-slicer and the slicer mirrors of EST. This combination will present a similar appearance where, instead of four sets of mirrors, the macro-slicer will have eight, each one of them with a different orientation. The slicer mirrors associated to each one of the macro-slicer faces, here presented horizontally, would be located vertically. This optical component is also shown in Fig. 3.19, as well as an example of an array of spherical mirrors. The collimator and camera arrays of mirrors of MuSICa will present a similar aspect, using this array in vertical position. The mirrors, then, are distributed in two columns, as considered in the optical design alternatives studied for EST.

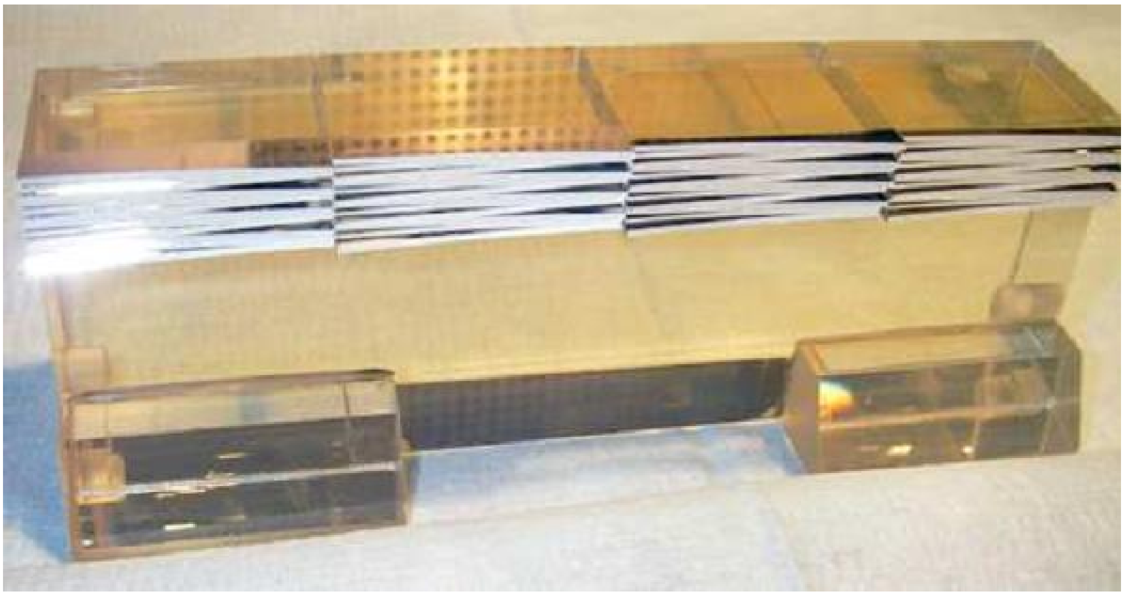

Figure 3.18: Example of the slicer mirrors of MUSE. This figure helps to get an idea about the combination of the macro-slicer and the slicer mirrors of EST, in which instead of four sets of mirrors, the macro-slicer presents eight, each one with a different orientation. The slicer mirrors, placed here horizontally, would be located vertically. Figure obtained from the Winlight Optics webpage.

3.7 Telecentricity

Telecentricity is a very important condition for both the integral field unit and the spectrograph. A telecentric system keeps the final plate scale and, in the detector, every pixel has the same energetic charge. Using an image slicer, the entrance field is sliced into several subbeams and a pupil image is generated for each one of them. After the reorganisation of the field into the slit, all these pupil images are again recomposed into one over the diffraction grating. Finally, the pupil is sent to infinity and, at the spectrograph image focal plane, the detectors are illuminated homogenously.

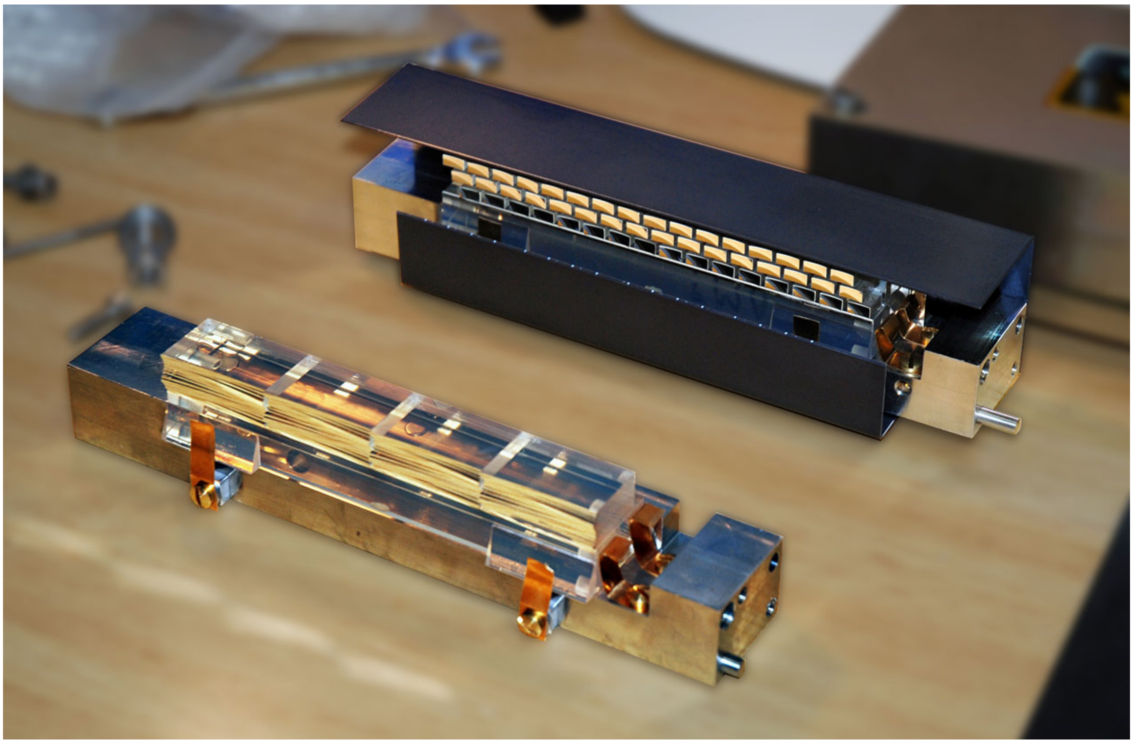

Figure 3.19: Example of image slicer components manufactured by Winlight Optics for MUSE. Figure obtained from the Winlight Optics webpage.

There are different types of telecentric systems:

1. Object-side telecentric system
2. Image-side telecentric system
3. Both-sides telecentric system

An object-side, also called object-space telecentric system has its entrance pupil at infinity. The chief rays that are oblique rays which pass through the centre of the aperture stop are, in this case, parallel to the optical axis, as shown in Fig. 3.20.

An image-side telecentric system has its exit pupil at infinity. If the system has its entrance and exit pupils at infinity the telecentricity occurs simultaneously in the object and the image space. A system with these characteristics is called both-sides telecentric system (Fig. 3.21).

The current design of the European Solar Telescope does not offer an exit pupil at infinity. The image slicer, coupled to the telescope, works as an image-side telecentric system, however it has been designed as a both-sides telecentric system. The spectrograph is a both-sides telecentric system in which the entrance pupil is sent to infinity by the image slicer and the exit pupil is sent to infinity by itself.

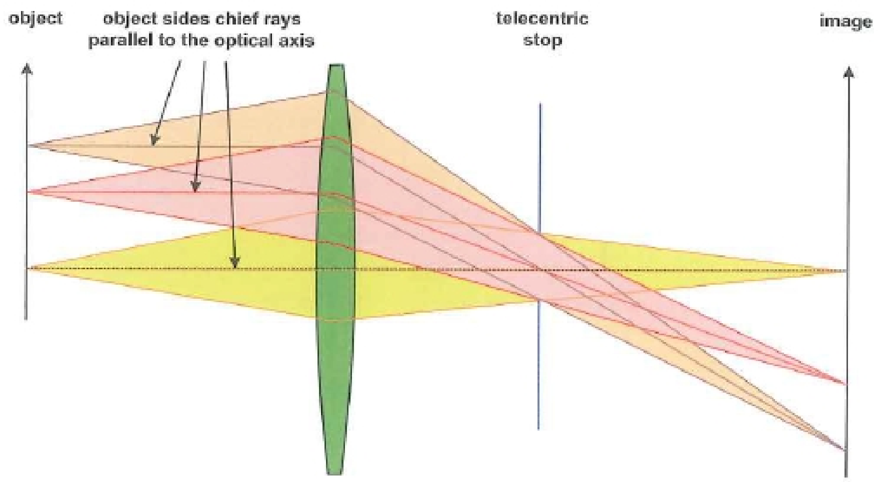

Figure 3.20: Principle of an object-side telecentric ray tracing. This image belongs to the Handbook of Optical Systems, vol.1.

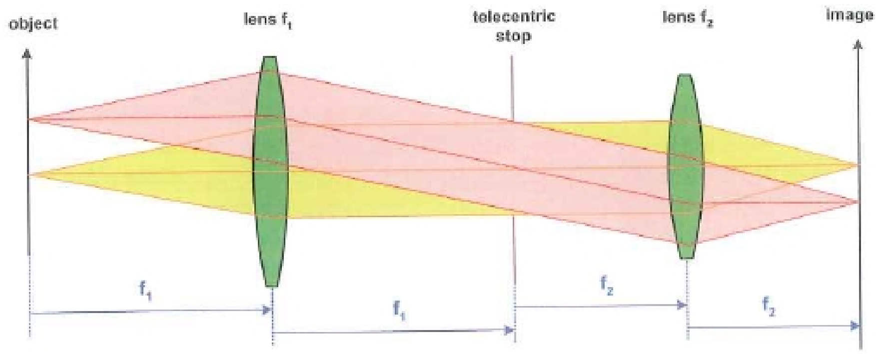

Figure 3.21: Ray tracing of a both-sides telecentric system with a stop in the common focal plane of the two subsystems. This image belongs to the Handbook of Optical Systems, vol.1.

The pupil position of the image slicer (s'), coupled to the telescope can be calculated with Eq. 3.16, considering the telescope exit pupil using Eq. 4.1, with $f = f_{COL_{IFU}}$ and $s = f_{COL_{IFU}} + d$, attending to the sketch of Fig. 3.22, where d is the position of the telescope exit pupil with respect to the focus.

$$s' = \frac{f_{COL_{IFU}} \cdot s}{s - f_{COL_{IFU}}} = \frac{f^2_{COL_{IFU}} + d \cdot f_{COL_{IFU}}}{d} \tag{3.16}$$

If the telescope sends the pupil to infinity, then: $s \to \infty$ due to $d \to \infty$ and s'$\simeq f_{COL_{IFU}}$. For this instrument, $f_{COL_{IFU}} = 220$ mm and the telescope exit pupil is located at 16710.90 mm with respect to the image focus. The IFU pupil position is placed at 222.90 mm from the collimator mirror array. This value is approximately the image slicer collimator focal length with an increment of 2.90 mm, what represents 1.32% of the focal length value.

To reorganise the pupils and verify the telecentricity condition is a hard point in the

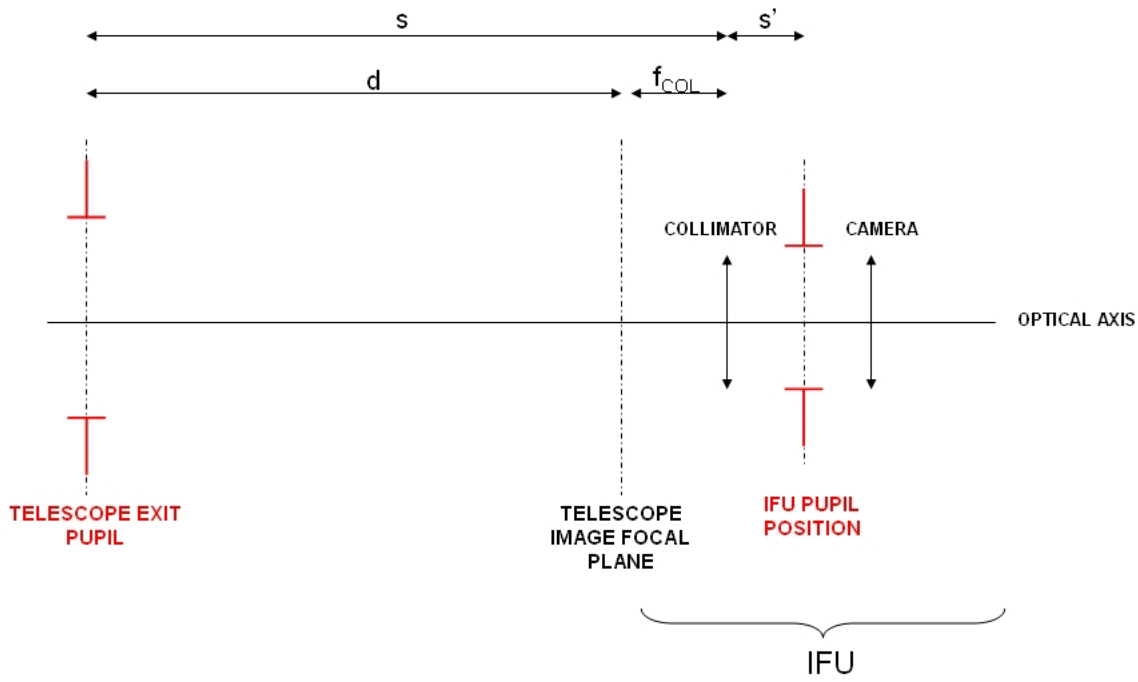

Figure 3.22: Sketch for the calculation of the pupil position in the IFU as a function of the telescope exit pupil location at a distance d with respect to the image focus.

image slicer design process. Even more when using a geometric distribution of the mirrors in two (or more) columns. Initially the orientations of the beams would lead to two separated pupil images over the gratings. Eqs. 3.17 to 3.19 help to solve the problem analytically and make all the images converge over a single one, implying an adjustment of the collimator and camera mirrors. Since MuSICa overlaps the pupil images inside the image slicer itself, the reunification process is greatly simplified.

Before the single pupil design of MuSICa, another layout using different locations for the pupil images of each configuration was also studied. This design, coupled to the predisperser and spectrograph of EST (see Fig. 3.23) has been chosen to show how the telecentricity condition is fulfilled and the pupil, as shown in the footprints on the diffraction gratings, is perfectly reconstructed, even with this layout of image slicer that presents sixteen separated pupil images. The footprint diagram, obtained from the ZEMAX file, shows the incidence of the beam in a specific plane of the optical system. This result is very important, since it demonstrates that the use of an image slicer has no impact in terms of loss of information. The initial beam can be sliced and recomposed to illuminate the spectrograph with a telecentric beam. As can be seen in Fig. 3.23, the pupil of each configuration is reconstructed into a single one over the predisperser and spectrograph gratings. All pupils are coincident and their coordinates $(X_{pgi}, Y_{pgi}, Z_{pgi})$ over the grating are the same and centred with respect to the optical axis.

The coordinates of the pupil for all the configurations is defined by Eqs. 3.17, 3.18 and 3.19, where f_{COLpd} is the collimator focal length of the predisperser coupled to the IFU.

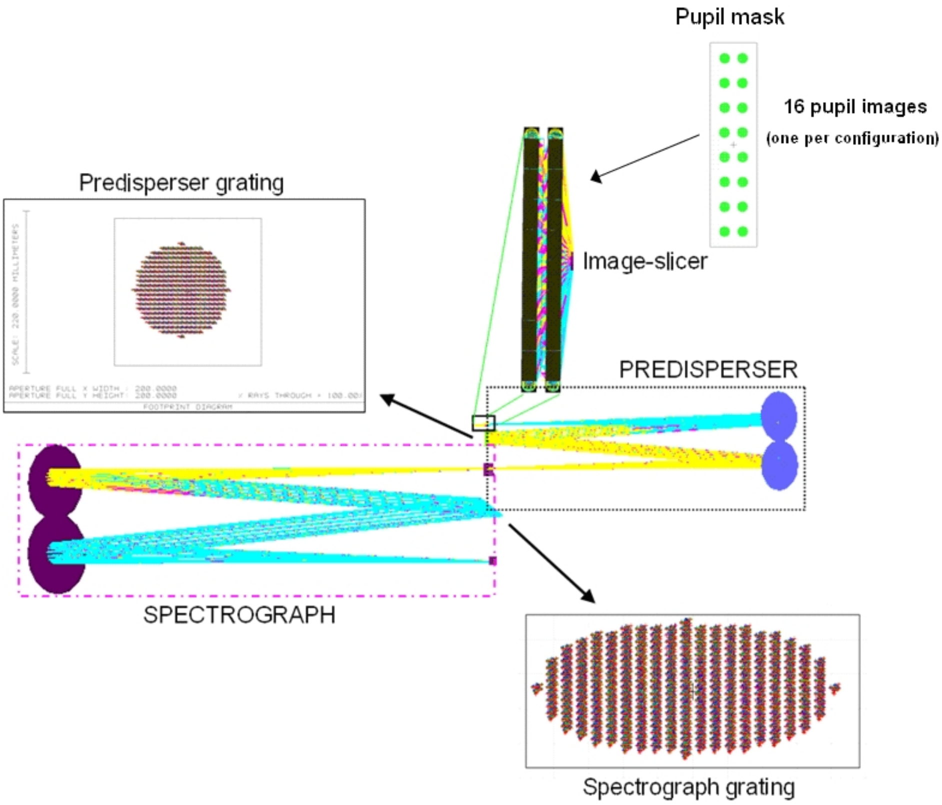

Figure 3.23: Confirmation of the telecentricity condition. This figure shows the coupling of an image slicer to the predisperser and spectrograph of EST. The design of the image slicer considered for this example presents 16 separated pupil images that are reorganised into one over the gratings.

$$X_{pgi} = f_{COLpd} \cdot tan(ty_{CAMi}) \, , \tag{3.17}$$

$$Y_{pgi} = f_{COLpd} \cdot tan(tx_{CAMi}) \, , \tag{3.18}$$

$$Z_{pgi} = f_{COLpd}, \tag{3.19}$$

for $i = 1, ..., N$ and N the number of configurations.

3.8 Materials

Another important point is the material with which the mirrors of the image slicers are fabricated, either for substrates or coatings.

3.8.1 Substrates

Some image slicers have used aluminium for the substrates, as it is the case of FISICA. Aluminium is the most widely used non-ferrous metal. It is a light material, what makes it a good candidate because it can be easily moldable. Nevertheless, its coefficient of thermal expansion is considerably greater than for other materials, like zerodur. The thermal expansion is the tendency of matter to change in volume in response to a change in temperature. The degree of expansion divided by the change in temperature is called the material's coefficient of thermal expansion. It measures the fractional change in size per degree change in temperature at a constant pressure and generally varies with temperature. For aluminium this coefficient has a value of $23.5 \pm 0.10 \times 10^{-6}$ °C^{-1} for a temperature of 20°C, while the value for zerodur is $\simeq 0.02 \times 10^{-6}$ °C^{-1}. The election of aluminium as the substrate imposes that at least the IFU has to be cooled to control the temperature. Zerodur is a glass-ceramic with a very low thermal expansion coefficient nearly zero, what allows 3D homogeneity. It presents other kind of characteristics that can be assumed as advantages. It can be po-lished to a very high accuracy, it can be coated easily, it presents good chemical stability, non-porous, high internal quality and good processing behaviour. There is a type of zerodur called zerodur zero expansion glass ceramic that is an inorganic, non-porous glass ceramic with a completely non-directional, isotropic structure whose thermal expansion coefficient is also nearly zero. Typical values for the homogeneity of the linear thermal expansion coefficient are between 0.01 and 0.02×10^{-6} °C^{-1}, however values lower than 0.01×10^{-6} °C^{-1} are possible. The final decision about the material used for the image slicer mirrors is conditioned by the manufacturing limits. Very thin mirrors, with a width on the order of 100-50 μm are not possible to be fabricated with all materials and it is important to control a good edges quality. The company that will fabricate the image slicer prototype has recommended zerodur as the best material and fused silica as the second one.

3.8.2 Coatings

For the studied optical designs all the elements work in reflection. Reflectivity is defined as the fraction of incident radiation reflected by a surface. To improve the reflectivity several coatings have been studied to be located over the substrate. An optical coating is a thin layer of material placed on an optical component such as a lens or mirror which alters the way in which the light is reflected or transmitted. There are different types but we are interested in high reflective coatings. The simplest optical coatings are thin polished layers of metals, such as aluminium, which are deposited on glass substrates to make mirror surfaces. The used metal determines the reflection characteristics of the mirror. In general, the best high reflective coatings are: aluminium, silver, protected silver and gold. The reflectance against wavelength for aluminium, silver and gold are presented in Fig. 3.24. Aluminium film serves as a good reflector (approximately 92%) for visible wavelengths and an excellent reflector (as much as 98%) of medium and far infrared radiation. But, as can be seen in Fig. 3.24, silver and gold are better in the infrared spectral range.

Aluminium is the cheapest and most common coating, and yields a reflectivity of around 88%-92% over the visible wavelength range. More expensive is silver, which has a reflectivity of 95%-99%, even into the far infrared, but suffers from decreasing reflectivity (<90%) in the blue and ultraviolet spectral regions. Silver can oxidize, for this reason is better to use protected silver in which the reflectivity is even higher. Protected silver (commonly named PAG) has the highest reflectance of any protected metal coating in the visible, near IR and mid IR regions. As an external reflector, silver is overcoated with one of several transmissive materials, depending on the wavelength region of interest. As an internal reflector, silver is overcoated with a black epoxy paint. Protected silver is not sensitive to wavelength and angle of incidence. The curves of reflectance against wavelength for protected silver are shown in Figs. 3.25 (a) and (b). Most expensive is gold, which gives excellent (98%-99%) reflectivity in the infrared range, but too low reflectivity for visible wavelengths. As a compromise between the reflectivity and the price, protected silver coatings have been selected.

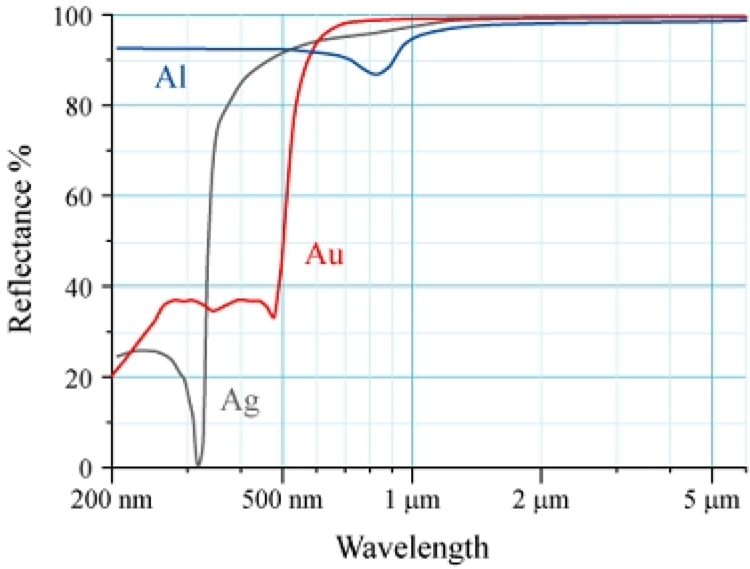

Figure 3.24: Reflectance against wavelength for: aluminium (Al), silver (Ag) and gold (Au). Aluminium film serves as a good reflector (approximately 92%) for visible wavelengths and an excellent reflector (as much as 98%) of medium and far infrared radiation. But, as can be seen in the figure, silver and gold are better in the infrared spectral range. Figure obtained from Wikipedia.

The coupling of an integral field unit based on the image slicer concept to the spectrograph of EST, and, especially an IFU like MuSICa, with all its characteristics and capabilities, significantly increases its performance. No doubt, specifically this subsystem is its main attractive feature and its greater innovation. The design of MuSICa is completely new, and can be situated within the state-of-the-art of the image slicers. It has been designed for the requirements of this spectrograph to make it an avant-grade instrument.

3.9 FoV Scanning System

The telescope delivers a corrected field of view of 2 $\times$ 2 arcmin^2. Although the image slicer entrance field of view is 80 arcsec^2 for the spectroscopic mode and 40 arcsec^2 for the spectropolarimetric mode, the full field of view can be observed in sequential observations using

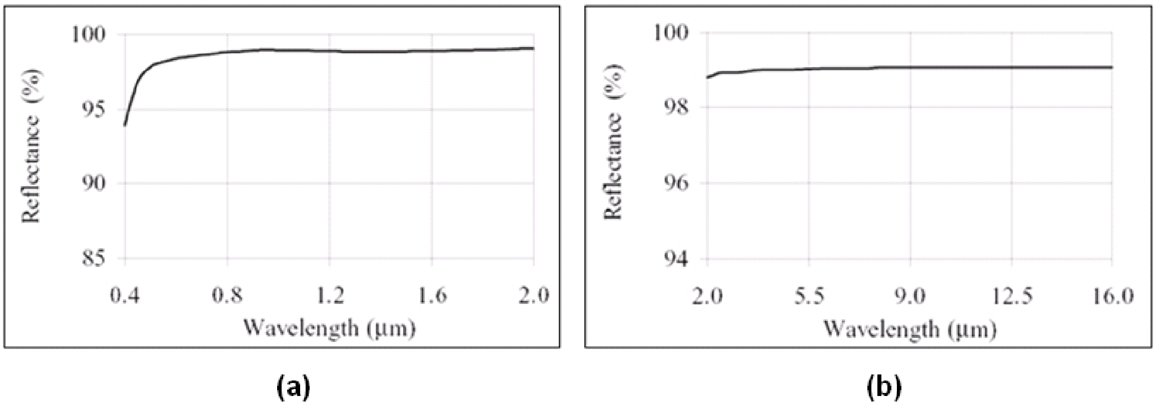

Figure 3.25: On the left, (a) shows the protected silver coating reflectance sample curve in the visible and near-infrared spectral range, while (b) shows the curve for the infrared wavelengths. Figures obtained from the Rocky Mountain Instruments' webpage.

a scanning system before the integral field unit. In the special case of this integral field spectrograph, a bidimensional field of view scanning system, able to scan along X and Y axis, is needed.

3.9.1 Alternatives of scanning system

There are different alternatives of scanning system. Four of them are presented in Fig. 3.26.

The simplest scanning system is known as tip-tilt scanning. It is shown in Fig. 3.26a. This layout controls the pupil using a scan mirror that is located in a pupil image. The scanning step has to be small since the movement at the pupil position implies decentring of the beam in the focusing mirror, what can introduce aberrations. Considering the entrance field of view for the image slicer and the full field of view delivered by the telescope, this is not a good alternative.

The second concept, presented in Fig. 3.26b, is the prism scanning. The scan is here done immediately in front of the spectrograph entrance slit. This prism is rotated to focus different parts of the sun over the slit. This layout has not been considered due to the chromatism of the prism and the aberrations that it introduces.

The sketch of Fig. 3.26(c) shows the concept integrated at the Advanced Technology Solar Telescope, ATST. Slit and collimator element can move along the horizontal axis. Their movements are coupled and simultaneous. This concept is advisable for compact systems but not for large focal lengths like those of the spectrographs of EST, of the order of 8 metres.

The quad-mirror scanning solution of Fig. 3.26d uses four flat mirrors orthogonal to each other and tilted 45° with respect to the incoming beam. The orientation of the mirrors is fixed and they have a translation degree of freedom. This system makes the scanning along one axis using the first pair of mirrors and scans the orthogonal direction using the second pair. It can be also used as a focusing mechanism by varying the distance between the two pairs of mirrors. An important advantage to be pointed out is that this system is polarimetrically compensated. This is the current concept adopted for the spectrographs of EST.

3.9.2 Technical characteristics

The quad-mirror concept is composed by four flat mirrors organised in two pairs orthogonal to each other. The mirrors are tilted 45° with respect to the incoming beam. Each pair of mirrors scans along one axis. For this purpose, each mirror presents two degrees of freedom: Z and Y axis, for the first two, and Z and X axis, for the other two. The orientation is fixed. The movements over the X and Y axis make possible the scan of the field of view in those directions, and the ones over the Z axis allow to adjust the focus. The interval of translation assigned to each pair of mirrors is ± 10 mm.

The described instrument is one of the spectrograph proposals for EST (Calcines et al., 2012a) and, since the field of view scanning system is common for all of them, this determines the size of the mirrors of the scanning system. The calculated size for each mirror in order to observe a field of view of 2×2 arcmin^2 is 200 mm $\times$ 300 mm. This allows the direct observation of the full field of view. In addition, the proposed system offers the possibility to scan along one axis. In this case, the mirrors associated to the scan along this axis are mobile, while the others, which can use translation movements to adjust the focus, works only as a folding mirror.

A sketch of the quad-mirror concept of Fig. 3.26 adapted for the spectrograph described in this thesis is shown in Fig. 3.27 and the optical design is presented in Fig. 3.28.

Since the beam is divided by a dichroic (D1) in the visible and infrared spectral ranges before the scanning system, as shown in the sketch of Fig. 3.29, two field of view scanning systems are required, whose concepts are the same. Both should observe the same area over the Sun.

3.9.3 Scanning steps and exposure time

For an IFU field of view of 6.32×12.66 arcsec^2, 19 scanning steps along the horizontal axis and 10 along the vertical ones are needed in the spectroscopic mode to cover the telescope 2×2 arcmin^2, in a total of 190 scanning positions.

For the spectro-polarimetric mode, for which the entrance field of view is half that of the spectroscopic mode, 6.32×6.32 arcsec^2, 380 scanning positions are needed to scan a 2 $\times$ 2 arcmin^2 field of view.

The science requirement establishes that the total throughput shall be sufficient to reach a signal-to-noise ratio of 1,000 in spectro-polarimetric observations with 1 sec integration time, at a spatial resolution of 0.04 arcsec and spectral resolution of 150,000. For a signal-to-noise ratio of 1,000 4×10^6 photons are needed. If this requirement is fulfilled, then this

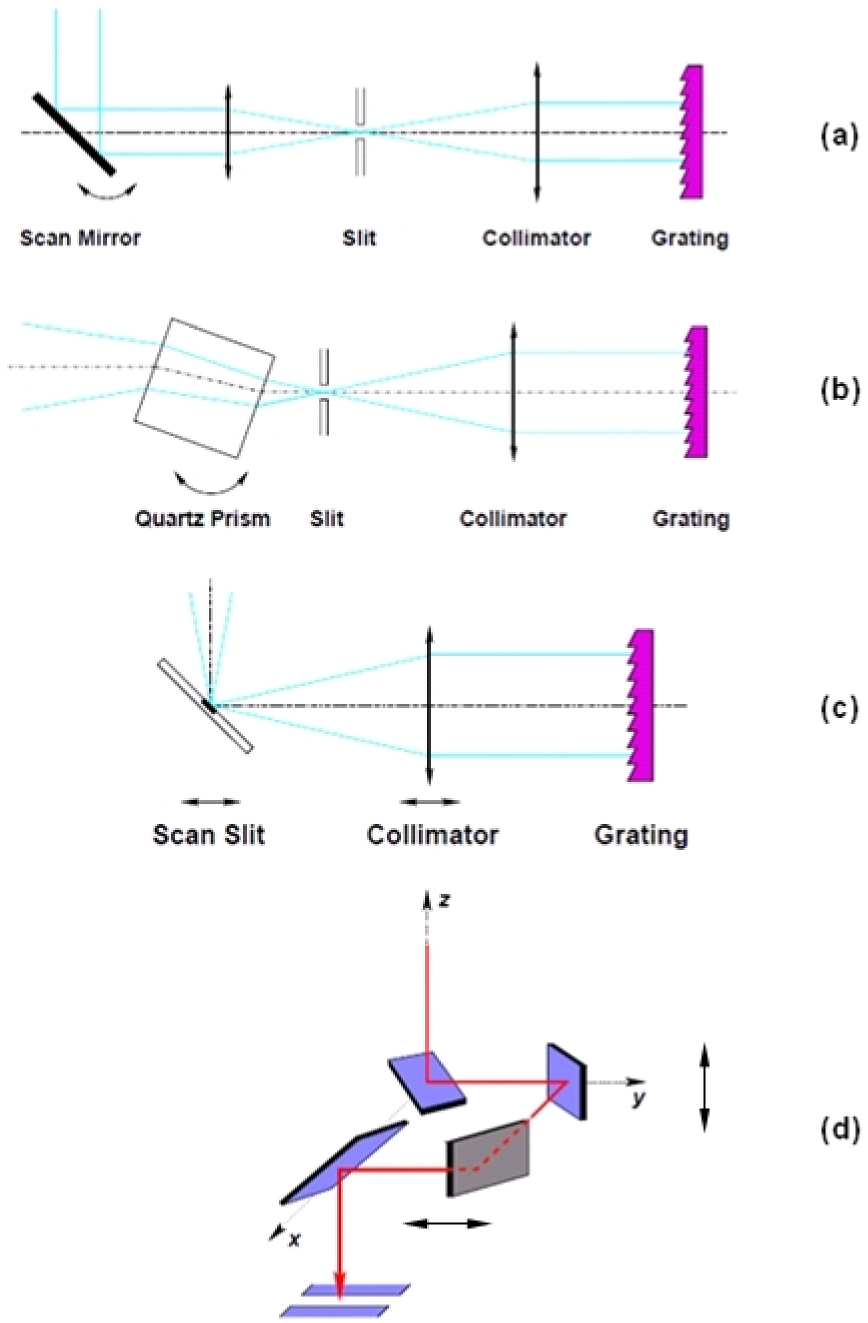

Figure 3.26: Four scanning system layouts. Figure (a) presents the concept of the tip-tilt scanning, using a scan mirror in a pupil image. The second alternative (b) shows the prism scanning mechanism, in which a rotating prism focuses different solar regions over the spectrograph slit. The third layout (c) is based on the scanning used at ATST, in which slit and collimator element present coupled and simultaneous movements. The fourth layout corresponds to the quad-mirror scanning solution that uses 4 flat mirrors orthogonal to each other and tilted 45° with respect to the incoming beam to make bidimensional scanning. This is the current concept adopted for the spectrographs of EST.

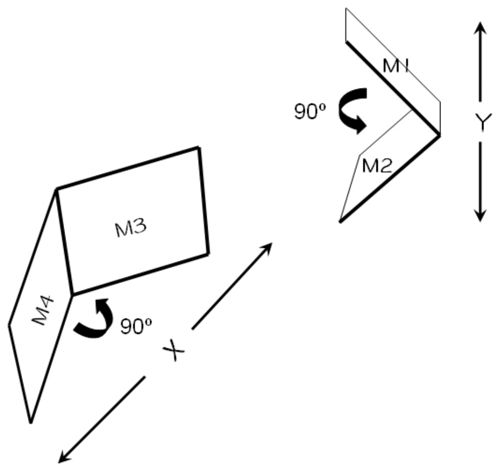

Figure 3.27: Sketch of the proposed scanning system based on the layout of Fig. 3.26 d. Four flat mirrors are used: M1, M2, M3 and M4. For the adaptation of this concept for the spectrograph of EST, the first two mirrors present vertical movements so they scan different columns of the bidimensional field of view, while the last two mirrors scan along the X-axis.

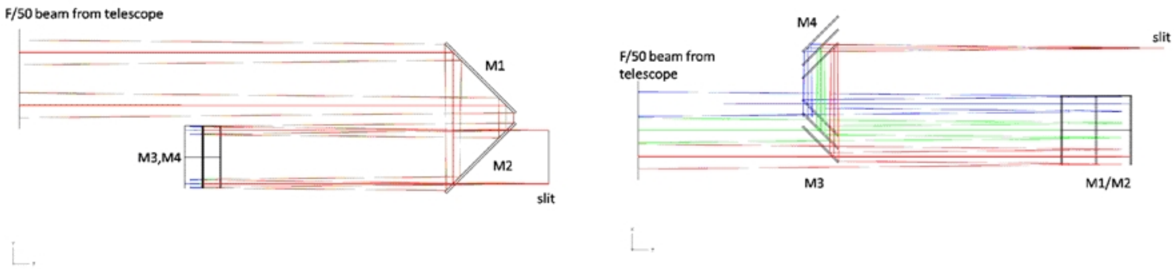

Figure 3.28: Optical design of the proposed 2D field of view scanning system. The side view is shown on the left and the top view on the right. Each mirror is 45° tilted with respect to the input beam.

signal-to-noise is reached with a sampling of 0.02 sec. At the spectrograph, the sampling is 0.05 arcsec, which is a factor of 2.5 more. Since this factor is related to the surface, it is the square of this value what gives the increase factor in intensity, 6.25. In addition, this requirement has been defined for a resolution of 150,000, nevertheless the spectrograph resolution is 300,000. Because the resolution is twice higher, there is a factor of two of loss in detected light. So the final gain factor is the ratio between the increase and loss factors, $\frac{6.25}{2} \simeq 3$. This implies that the same number of photons can be detected in a time three times lower than the considered 1 sec, leading to approximately 0.30 sec. This is the time estimated for the integration at a scanning position. Attending to this number, the corrected field of view offered by the telescope, 2×2 arcmin^2 is covered in the spectroscopic mode in 190 scanning positions, what makes a total of 57 sec, while for the spectro-polarimetric mode 380 scanning positions are needed and the total time is 114 sec. If a better/worse signal-to-noise ratio is valid for the observer, the exposure time can be increased/decreased. Since the noise is related with the square root of the detected photons, to improve the signal-to-noise ratio by a factor of two, an exposure time 4 times larger is required.

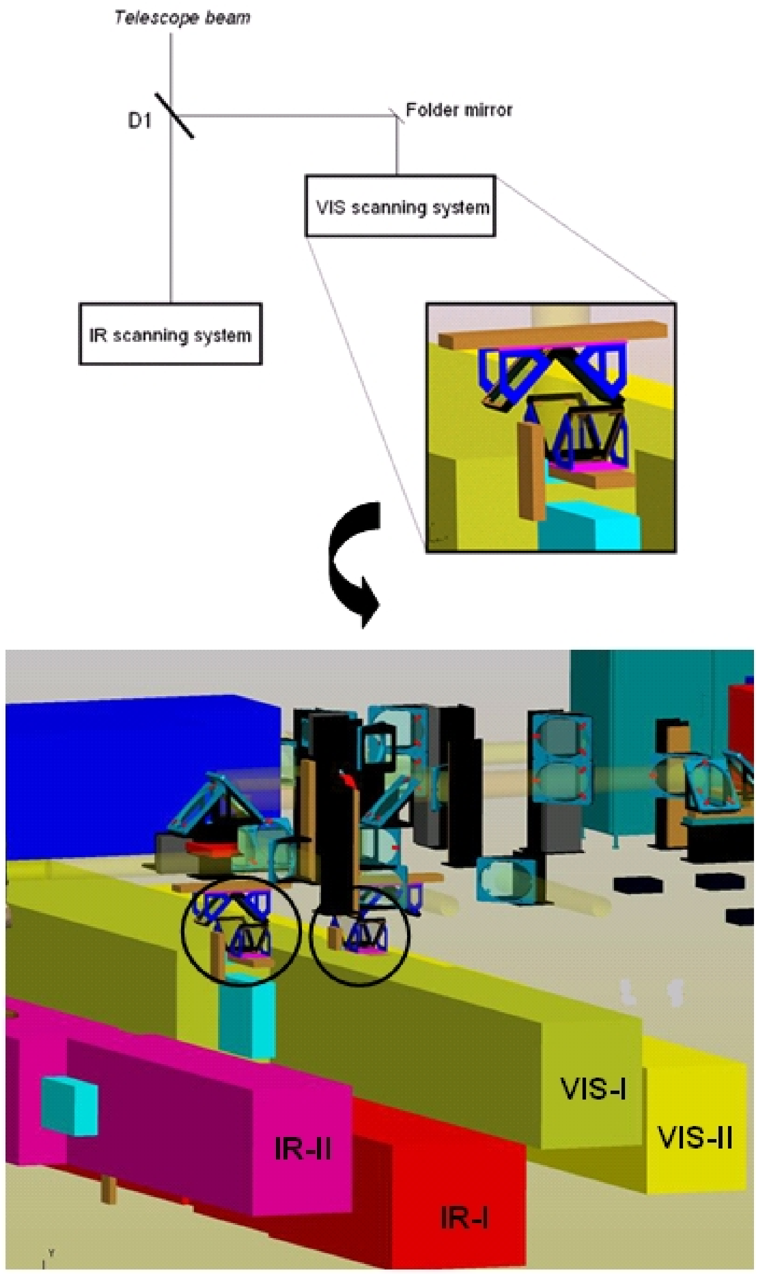

Figure 3.29: Top: sketch of the first division of the beam into the infrared and visible spectral ranges using a dichroic (D1). Two field of view scanning systems are used, whose concepts are exactly the same. They use two pairs of flat mirrors orthogonal to each other and tilted 45° with respect to the incoming beam. The systems are polarimetrically compensated and both should observe the same area over the sun. At the bottom, the 3-D mechanical design of the four spectrographs fed by the two scanning systems is shown.

3.10 Prototype at GREGOR

A prototype image slicer is designed for the 1.5 m GREGOR solar telescope at the Observatory of El Teide (Schmidt et al., 2012), (Volkmer et al., 2010). It will constitute a feasibility study for the image slicer of EST and will improve the performances of the GREGOR Infrared Spectrograph, GRIS (Collados et al., 2012). Like EST, GREGOR is specially designed for high resolution spectropolarimetry of solar fine structures and it is an ideal telescope to test a reduced version of MusICa.

3.10.1 Requirements

The design of MuSICa for GRIS has an entrance field of view of 24.5 arcsec^2 and reorganises it in a long slit. The entrance field of view of $2.93 \times 8.35\,\mathrm{arcsec}^2$ width is divided into eight slices of $0.367 \times 8.35\,\mathrm{arcsec}^2$ each. MuSICa reorganises them into a slit of $0.367 \times 66.8\,\mathrm{arcsec}^2$. This corresponds to the spectro-polarimetric mode. Although MuSICa was designed for EST compatible with two modes of operation and the spectrograph GRIS (Collados et al., 2008b) can also work in both, only the spectro-polarimetric mode has been designed for GREGOR. The output slit, resulting from the redistribution of the entrance field of view, will be later duplicated by a polarising beam-splitter located after the slits generated by the IFU. Once the slit is duplicated, its size is $100\,\mu$m $\times$ $36.4\,mm$, corresponding to 0.367 arcsec $\times$ 133.6 arcsec.

The specifications, requirements and technical characteristics of the design of the prototype are shown in Table 3.6.

Table 3.6: Specifications and requirements for the design of the image slicer prototype at GREGOR telescope.

Input focal-ratio	F/37.5
FoV	24.5 arcsec^2= 2.93 $\times$ 8.35 arcsec^2
Number of slices	8
Slices width	100 μm
Number of output slits	1
Magnificaton	1
Output focal-ratio	F/37.5
Optimum illumination	telecentric

MuSICa for GRIS is a 1:1 telecentric system in which the input and output focal-ratios are the same, F/37.5. This prototype has less slices than the design for EST. And the width of the slices is twice larger. The number of slicer mirrors, which defines in how many slices the image of the field of view is divided at the telescope image focal plane, also determines the number of mirrors of each array. The optical path of each sub-beam, resulting from the decomposition of the telescope beam by the slicer mirrors, is such that the light is reflected using only one mirror of each array, starting with a part of the image, at the telescope focal plane, and finishing as a part of the output slit, at the spectrograph object focal plane.

Table 3.7: Technical charecteristics of the image slicer designed for GRIS.

SLICER MIRROR ARRAY	
Size	0.8 mm width $\times$ 2.28 mm length
Curvature	Flat
Size of each mirror	0.1 mm width $\times$ 2.28 mm length
Field per slice	0.37 $\times$ 8.35 arcsec^2
COLLIMATOR AND CAMERA MIRROR ARRAYS	
Curvature	Spherical
Distribution	2 columns of 4 mirrors
Size of each mirror	4.8 mm width $\times$ 8.0 mm length
PUPIL MASK	
Number of apertures	1
Aperture diameter	5.0 mm

3.10.2 Optical design

The adapted design of MuSICa to the specifications for GREGOR is presented in Fig. 3.30, as well as some details of the layout that are pointed out. The optical quality of this design is diffraction limited. The spot diagram at the image slicer image focal plane is shown in Fig. 3.31, where, for every configuration, the rays are contained within the Airy disk and the spots are very small, showing a perfectly compensated optical design. Each of the columns represents a piece of the output slit associated to a configuration, which is defined by three field points. The smallest spots correspond to the most centred slicer mirrors whose optical paths present the smallest off-axis distances. The larger the off-axis distance, the larger the spot size, what can be translated into an increment of the aberrations. The possible aberrations under the Airy disk do not affect the optical quality performances of the design.

Since the decision to couple an image slicer to the spectrograph GRIS was made later than the design of the instrument itself, the IFU has to be adapted to the available space. The general assembly of the spectrograph is shown in Fig. 3.32. The instrument is distributed in two floors. In the upper one the slit and the polarimeter (placed within the green box) are placed. The light is driven until the lower floor where the rest of the optical elements are found. At the telescope image focal plane the slit is positioned, with an slit jaw at 30°. The implementation of the image slicer will keep the slit jaw imaging system with the difference that the spectrograph field of view will be bidimensional in this case. The slit generated by the IFU is placed at the telescope image focal plane, which is located at 823.00 mm to the first folder mirror (FM1) (see Fig. 3.34). The idea to adapt the MuSICa concept to the available space is to place the slicer mirror array at the telescope focal plane and then, tilting these mirrors, generate a plane parallel to the optical axis at a height of 50 mm. Collimator and camera mirrors and the pupil mask are integrated in this plane. The camera mirrors will orient the beams, using X and Y axis tilts to focus them over the optical axis, very close to the slit position, within the tolerances range ($\pm$50 mm). This is a very symmetric design that has been chosen, between several studied alternatives, because it minimizes the number of extra optical components needed to be adapted, only one flat mirror. A sketch of this layout is presented in Fig. 3.34.

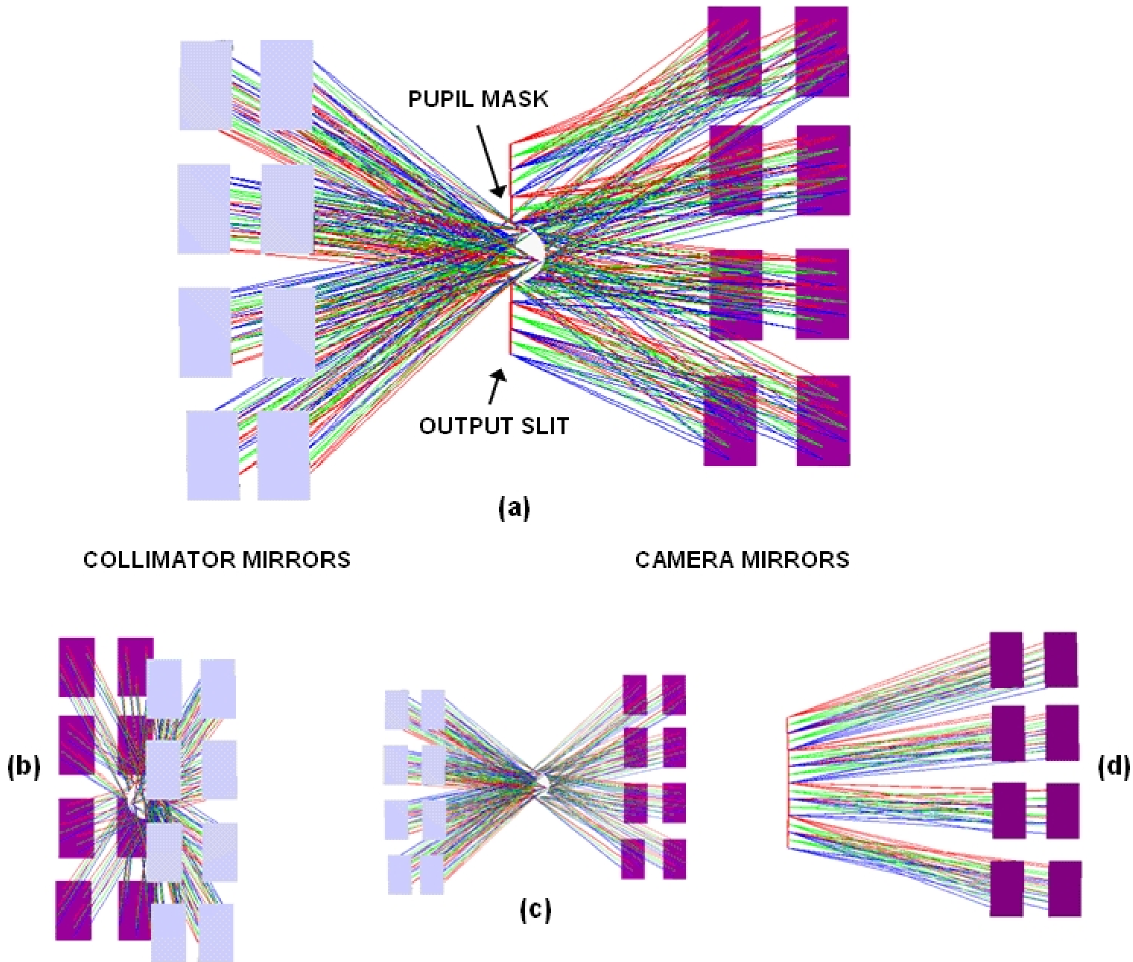

Figure 3.30: Top: (a) ZEMAX optical design of the EST image slicer prototype designed for the GREGOR telescope. Bottom: (b) distribution of collimator and camera mirror arrays, placed one in front of the other, with crossed correspondence. The symmetry of the layout is pointed out in (c). Collimator and camera mirrors are antisymmetric with respect to the pupil mask that is located between them. On the right, the detail (d) shows how the output slit is composed by the alignment of the focused sub-beams.

The ZEMAX optical design associated to the solution adopted to integrate MuSICa in GRIS is presented in Fig. 3.33.

The entrance slit of the GREGOR spectrograph is horizontal, however the combination of two folder mirrors (FM1 and FM2) orient it vertically before the collimator mirror. The design of Fig. 3.33 shows how the IFU generates a horizontal slit. Collimator and camera mirrors are distributed in two rows.

The prototype image slicer will be manufactured by Winlight Optics. The fabrication is expected to start during the end of this year, after a final optimisation of the optical design presented in Fig. 3.33.

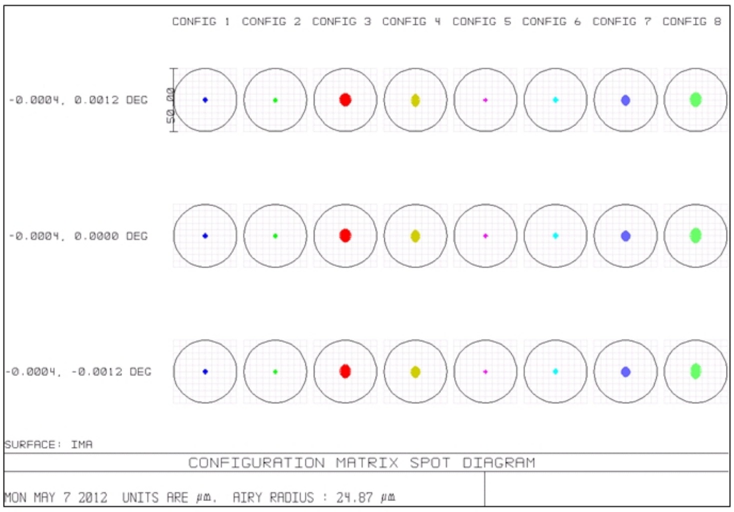

Figure 3.31: Diffraction limited spot diagram corresponding to the design of Fig. 3.30. The spot diagram is evaluated at the IFU image focal plane. Each column represents a part of the field of view, defined by three field points, which corresponds to a part of the output slit. The rays are contained within the Airy disk presenting an excellent optical quality.

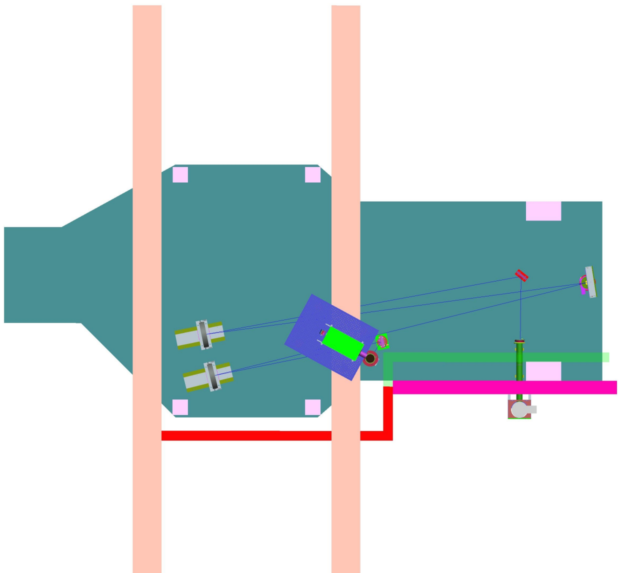

Figure 3.32: General assembly of the spectrograph GRIS distributed in two floors. In the upper one the slit and the polarimeter are placed. The light is driven using folder mirrors until the lower floor, where the rest of the optical elements are located.

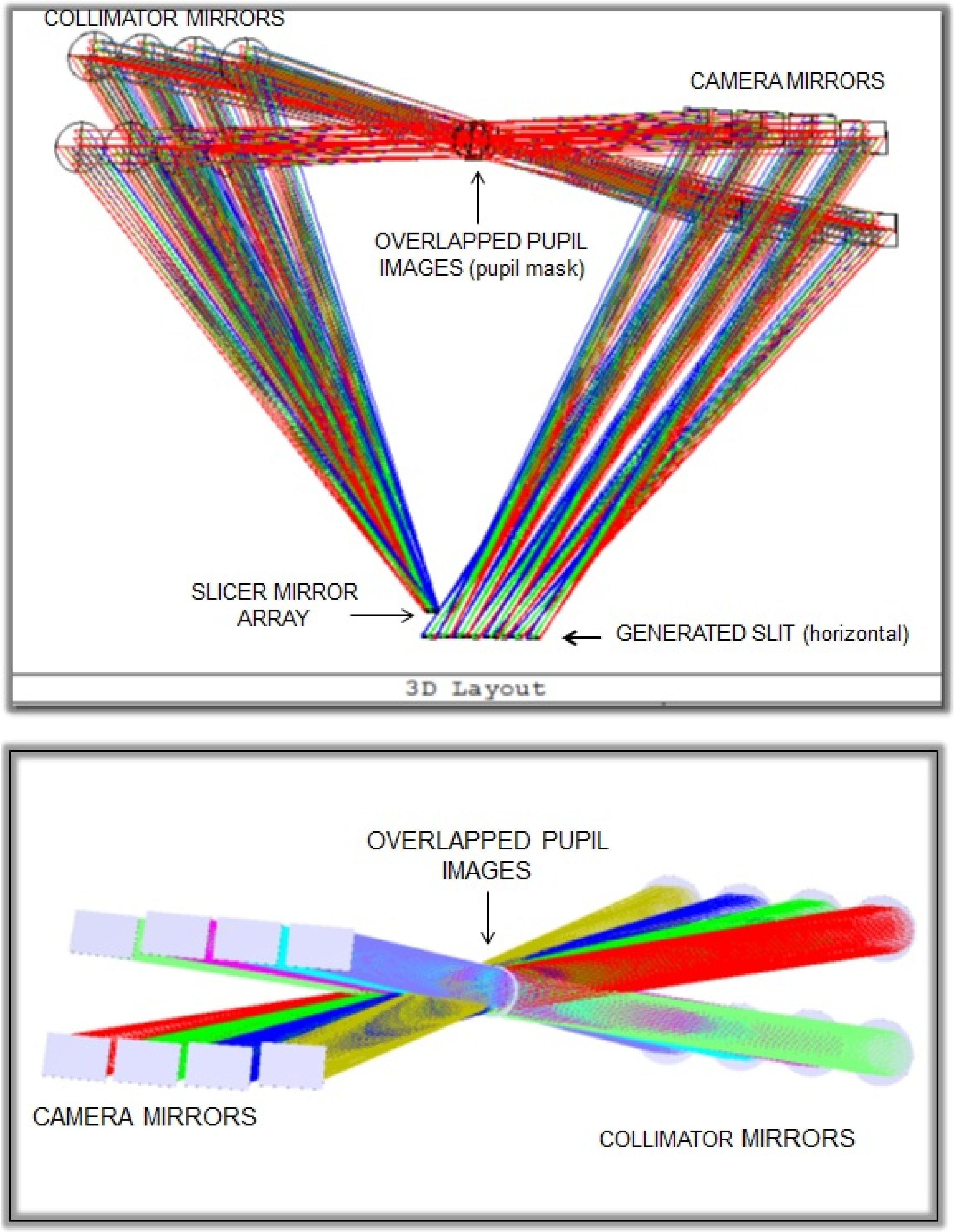

Figure 3.33: Top: ZEMAX optical design corresponding to the sketch of Fig. 3.34. At the bottom, the detail of the overlapping of the pupil images is pointed out.

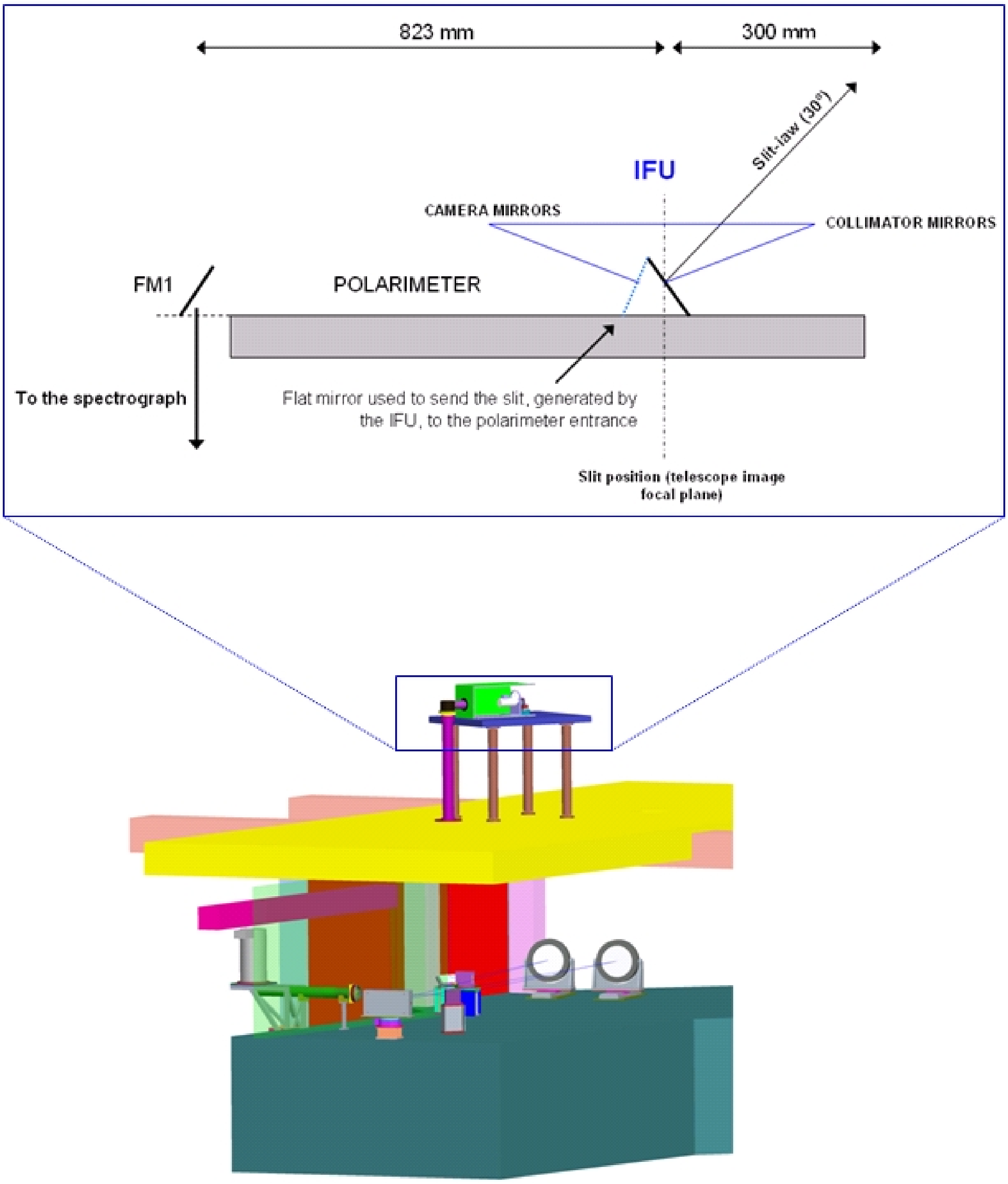

Figure 3.34: Sketch for the integration of an image slicer based on the MuSICa concept at GREGOR. Only one extra flat mirror is needed adopting this solution that distribute collimator and camera mirrors, as well as the pupil mask in a different plane, parallel to the optical axis.

4

Predisperser and Spectrograph

Following the light optical path direction, the subsystems after the IFU are predisperser and spectrograph. Both are described in this chapter.

4.1 Predisperser

The eight slits of 200 arcsec length by 0.05 arcsec width generated by the integral field unit are the entrance slits for the predisperser. Each spectrograph is preceded by a predisperser which acts like a prefilter. Thus, four predispersers are used, VIS-I, VIS-II, IR-I and IR-II, covering the spectral ranges defined in Table 2.3.

4.1.1 Predisperser calculation

The selected design for the predispersers is based on the Ebert-Fastie configuration, as a special case of the Czerny-Turner one, where collimator and camera mirrors belong to the same concave surface. Collimator and camera mirrors are, in each case, off-axis parabolic mirrors that belong to the same on-axis global parabola. The predispersers focal-ratio is F/40.

Diffraction gratings

Commercial diffraction gratings have been considered for predispersers and spectrographs. All the gratings of the Newport catalogue have been studied attending to different parameters: size, efficiency, separation between those wavelengths that are observed simultaneously and spectral resolution.

The grating physical size limits the maximum pupil diameter, since a pupil image is located at the diffraction grating. The pupil position and diameter can be calculated with the Lens Equation (Eq. 4.1) and trigonometry, simplifying the system as if it works in transmission, in accordance with the schemes of Figs. 4.1 and 4.2, respectively. These sketches can be used for both predisperser and spectrograph. The telescope entrance pupil has been taken into account for these calculations. Only the marginal rays are traced in the sketches. These rays correspond to the farthest points of the field of view and, since the pupil is defined as the geometrical location through which all the rays of the field pass, its diameter can be defined using them.

If F_T is the telescope effective focal length, f_{COL} and f_{CAM} are the collimator and camera mirrors focal lengths, s is the object distance and s' is the image distance, using the Lens Equation (Eq. 4.1), an estimation of the pupil location (s') is obtained.

$$\frac{1}{s} + \frac{1}{s'} = \frac{1}{f}\,, \tag{4.1}$$

where $f = f_{COL}$ and $s = F_T + f_{COL}$. The pupil location can be calculated as shown in Eq. 4.2.

$$s' = \frac{F_T \cdot f_{COL} + f_{COL}^2}{F_T} \tag{4.2}$$

Solar telescopes have a very large effective focal length, so $F_T \gg f_{COL}$ and s'$\simeq f_{COL}$. At this position is placed the diffraction grating. The grating is equidistant to the collimator and camera elements in 1:1 systems, for which their focal lengths present the same value. However, this does not happen for optical systems with a magnification.

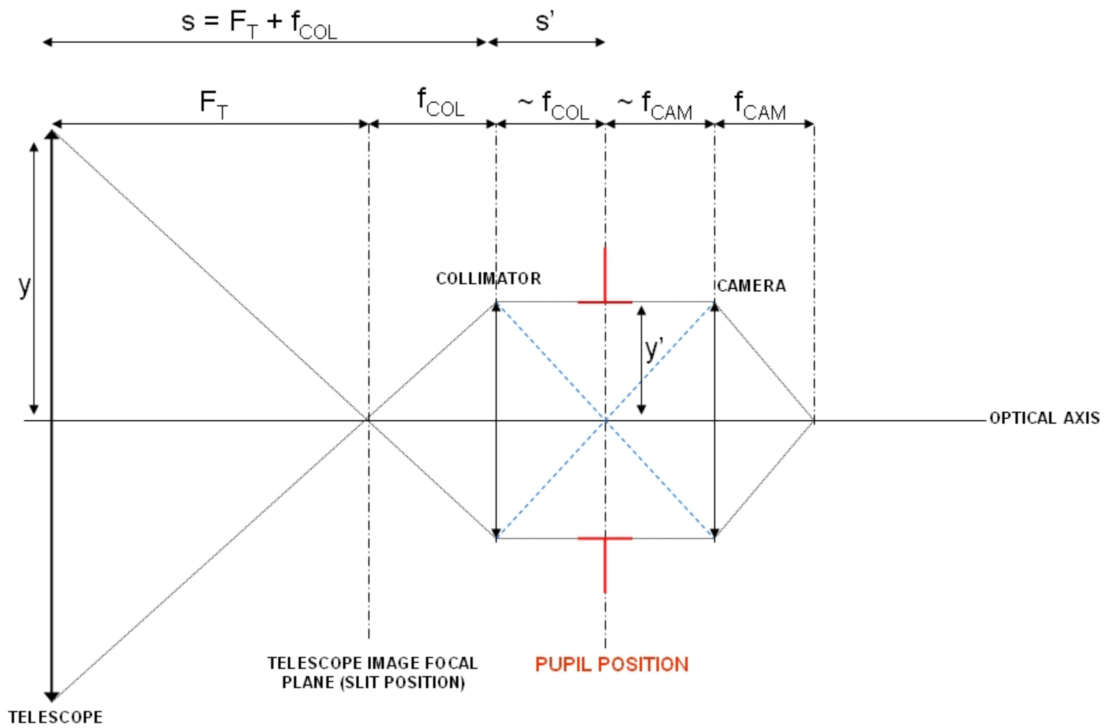

Figure 4.1: Sketch for the pupil position calculation. F_T is the telescope effective focal length, f_{COL} and f_{CAM} are the collimator and camera focal lengths. For telecentric systems, the position of the pupil (s'), with respect to the collimator surface is approximately its focal length.

The pupil diameter, 2y', is calculated mathematically using trigonometry and the triangles defined in Fig. 4.2, where $D_T/2$ is the semidiameter of the telescope primary mirror aperture, which can be denoted by y. By similarity of triangles 1 and 2, which are defined by the same lines and present, then, the same angle, α, the Eq. 4.3 is obtained for the calculation of the pupil semidiameter, y'.

$$y' = \frac{s' \cdot y}{s}, \tag{4.3}$$

where s is the sum of the telescope effective focal length and that of the collimator and s' has been defined in Eq. 4.2. Finally, substituting these expressions, the pupil semidiameter is obtained using Eq. 4.4.

$$y' = \frac{y \cdot (\frac{F_T \cdot f_{COL} + f_{COL}^2}{F_T})}{F_T + f_{COL}} \approx y \cdot \frac{f_{COL}}{F_T} \tag{4.4}$$

In the particular case of the European Solar Telescope, the effective focal length is 200 m and the primary mirror diameter is 4 m.

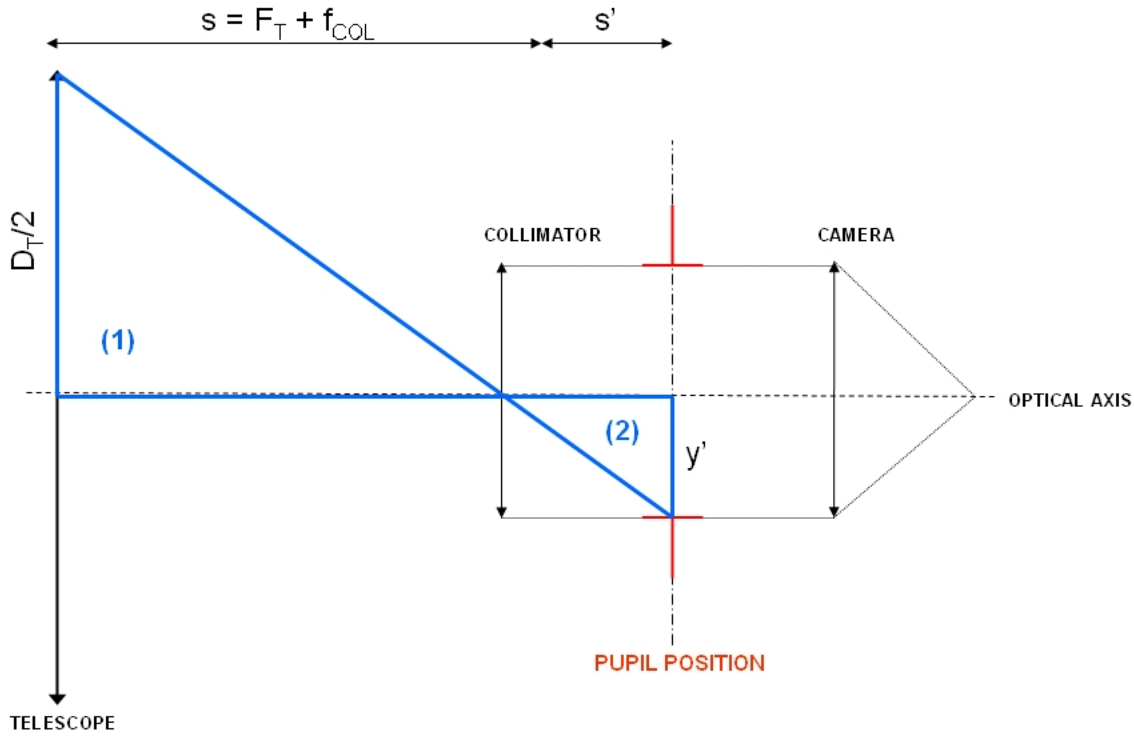

Figure 4.2: Trigonometric scheme for the pupil diameter calculation.

These expressions to calculate the pupil size and position are applied once the collimator mirror focal length is known. For the design of this instrument, the biggest pupil diameters have been limited by the size of the commercial gratings and conditioned by a compromise with the focal-ratio, the optical quality and the spectral resolution. The pupil diameters for the four predispersers are presented in Table 4.1.

Table 4.1: Predisperser pupil diameters.

PD	PUPIL DIAMETER (mm)
VIS-I	125.00
VIS-II	125.00
IR-I	100.00
IR-II	82.50

With the knowledge of the focal-ratio and using these values for the pupil diameters, the focal lengths of collimator and camera mirrors have been calculated using Eq. 4.5.

$$f_{COL} = \phi_{pup} \cdot f/\sharp\,, \tag{4.5}$$

where ϕ_{pup} is the pupil diameter and $f/\sharp$ is the f-number.

The predispersers work generally at first diffraction order, however for some wavelengths the second order is the most appropriate in terms of efficiency and linear dispersion. The separation between the wavelengths that are observed simultaneously and, consequently, the separation of their associated slits at the predisperser mask, is a function of the linear dispersion. The blaze wavelength of the gratings considered for the predispersers are, generally, specified for first order in Littrow configuration. In this case, Eq. 1.14 is transformed into Eq. 4.6.

$$m \cdot \lambda_B = 2 \cdot d \cdot \sin\varphi_B \tag{4.6}$$

According to this expression, the blaze wavelength is defined in Eq. 4.7.

$$\lambda_B = 2 \cdot d \cdot \sin\varphi_B \tag{4.7}$$

The blaze wavelength for other general diffraction order, m_g, can be calculated from the value obtained for first order, as shown by Eq. 4.8.

$$\lambda_B(m = m_g) = \frac{\lambda_B(m = 1)}{m_g} \tag{4.8}$$

The visible spectral range covers from 3900 Å to 11000 Å and the infrared interval from 7000 Å to 23000 Å. The overlapping region from 7000 to 11000 Å gives the versatility to observe spectral lines in this region in the visible or the near-infrared channels.

The first studied option was the division of the spectral range in these two spectral intervals, what leads to two spectrographs. The commercial gratings were analysed. As an example of the results, the Fig. 4.3 presents the theoretical efficiency curves , defined by Eq. 1.15, of different gratings for visible wavelenghts associated to the main science programmes. Finally, it was not possible to find only one grating with high efficiency for all the wavelengths of the interval.

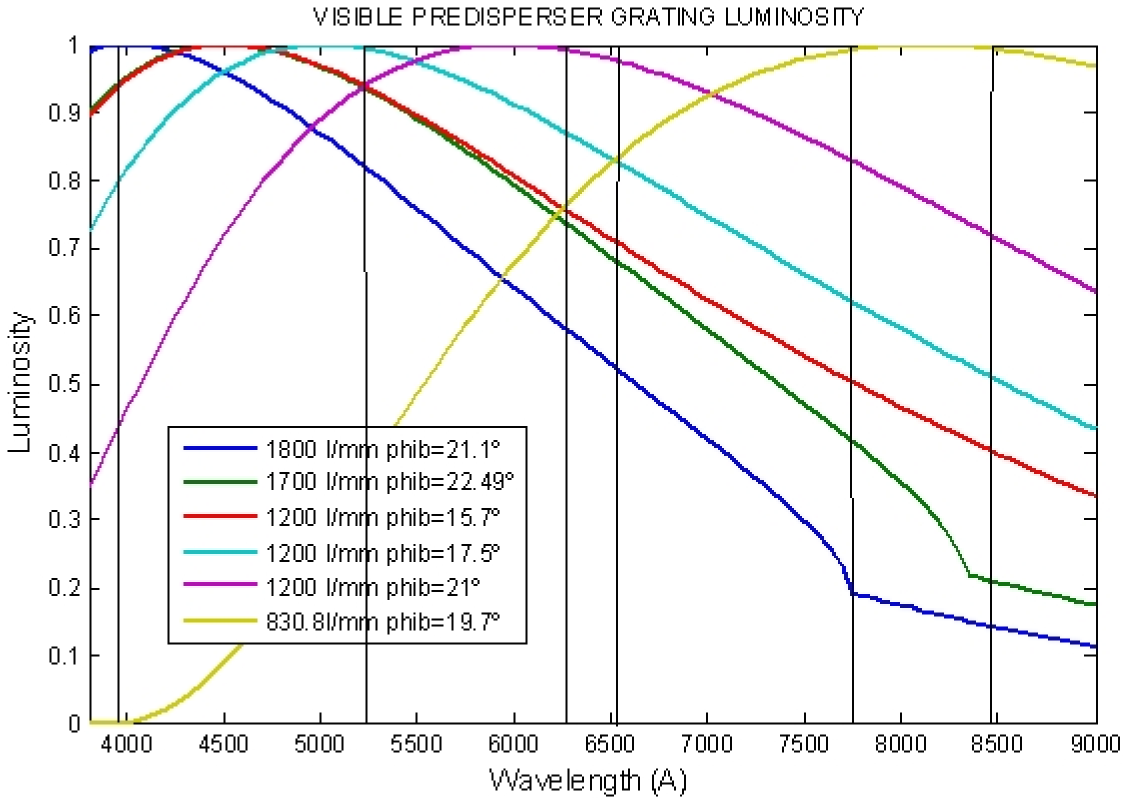

Figure 4.3: Curves of theoretical grating efficiency of different plane ruled reflectance gratings from the Newport catalogue studied for the visible wavelengths associated to the main science programmes. The luminosity means the grating efficiency at first order, represented as a function of wavelength. Each curve corresponds to a different grating, whose main characteristics are defined in the legend.

The gratings for each predisperser have been especially analysed to choose the optimum option for all their wavelengths, or at least most of them, in terms of efficiency. The main characteristics of the selected predisperser gratings are presented in Table 4.2.

Table 4.2: Characteristics of the selected predisperser gratings.

PD	σ (grooves/mm)	φ_B (°)	$\lambda_B(m=1)$(Å)	Size (mm^2)
VIS-I	300.00	3.60	4220	154×206
VIS-II	36.15	1.40	13000	135×168
IR-I	200.00	8.95	15500	154×206
IR-II	85.00	5.10	21400	84×84

Optical components

Technically, the four predispersers are conceptually identical. They are 1:1 systems and the focal lengths of collimator and camera mirrors are the same.

A first estimation of the diameter of the optical components (collimator and camera mirrors) can be obtained using Eq. 4.9, as the ratio between the focal length and the beam focal-ratio.

$$\phi_{COL} = \frac{f_{COL}}{(f/\sharp)_{COL}} \tag{4.9}$$

Nevertheless, the real collimator diameter is bigger than this first estimation, due to the aperture of the focal-ratio for the 8 entrance slits. Although the focal lengths and the f-number are the same for collimator and camera mirrors, the camera mirror is bigger than the collimator one, because of the dispersion. The diffraction grating disperses the constituent wavelengths of the input white light beam in different directions, producing a spectral decomposition of the beam. The camera mirror has to collect those wavelengths that are observed together, in the selected diffraction orders, what implies an increment in the diameter. In addition, both, collimator and camera mirrors are off-axis parabolic apertures of the same global parabola, which is centred in the optical axis. The collimator and camera mirrors apertures and their decentred distance are calculated using the design programme, ZEMAX. Every combination of simultaneous wavelengths associated to the science programmes of Table 1.1 has been studied and, the maximum sizes and decentred distances have fixed the final values for these parameters. These values are presented in Table 4.3.

Table 4.3: Technical characteristics of the predisperser collimator and camera mirrors. The values are given in millimetres.

PD	ϕ_{COL}	ϕ_{CAM}	FOCAL LENGTH
VIS-I	340	540	5000
VIS-II	330	360	5000
IR-I	340	460	4000
IR-II	300	400	3300

4.1.2 Predisperser Mask

At the predisperser image focal plane, the spectra associated to the eight entrance slits are obtained for each wavelength and each diffraction order. A multi-slit mask is placed to select the combination of wavelengths, at the appropriate order, which will be observed simultaneously with the spectrograph, blocking the others. The predisperser mask presents eight slits per wavelength, associated to the image of the eight entrance slits and a mask per combination of wavelengths is needed.

The slits of the mask are generated by the predisperser and represent the input slits for the spectrograph (see Fig. 4.4).

The spectra corresponding to the eight slits centred at a given wavelength are observed in the same detector. The slits width and the grating linear dispersion limit the spectral range centred in the wavelength of interest and whose image, once dispersed by the spectrograph, presents a spectral width, $\Delta\lambda$, which is a function of the wavelength.

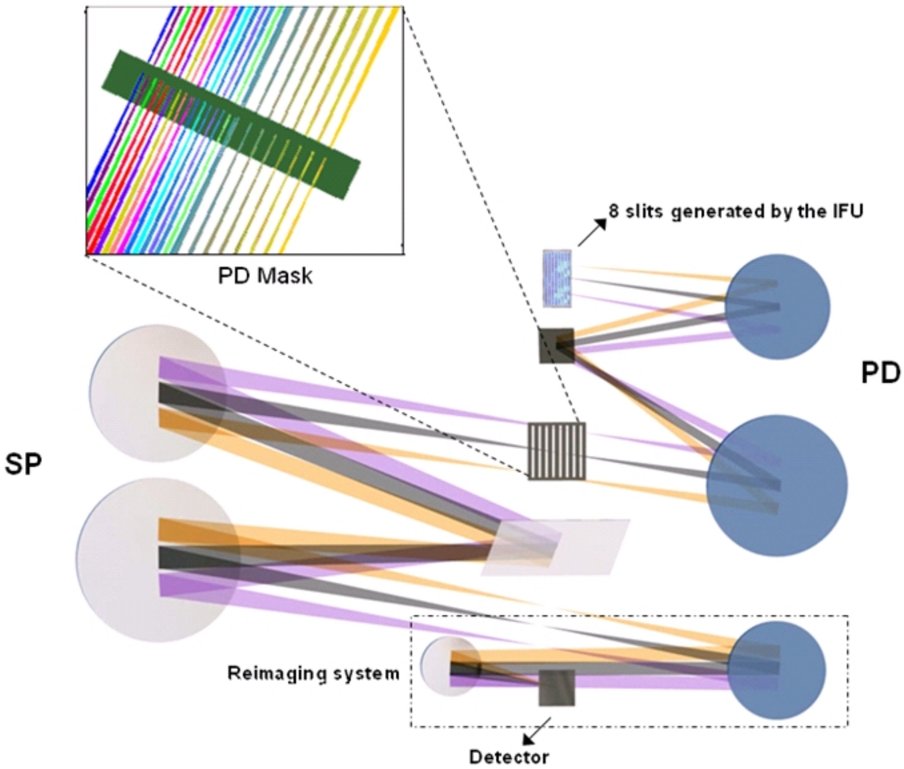

Figure 4.4: Layout of the spectrograph. The integral field unit reorganises a bidimensional field of view into the eight input slits for the predisperser. At the predisperser image focal plane, a mask is placed, which selects the combinations of wavelengths, at the appropriate orders, to be observed simultaneously with the spectrograph. The mask presents eight slits per wavelength, associated to the images of the input slits. These mask slits are the entrance for the spectrograph. At the spectrograph image focal plane a reimaging system makes the focal-ratio conversion. A detector per wavelength is used, in which the spectra corresponding to the eight slits centred at each wavelength are measured.

A mask per combination of wavelengths observed simultaneously is needed. In some cases, a same slit can be shared by two wavelengths that are later dispersed by the spectrograph grating. Three different examples are shown in Fig. 4.5, which represents the predisperser image focal plane. Each column represents a slit, defined by nine field points. The first case corresponds to the observation of 4102 Å with the VIS-I predisperser. The second case considers two wavelength intervals around 15260 Å (on the left) and 8542 Å (on the right), which are observed simultaneously with the IR-I predisperser. In the third example three wavelength intervals are studied together, 15260 Å, 15650 Å and 8542 Å. For this combination six slits of the mask are shared for the intervals centred at 15260 Å and 15650 Å.

In addition, in other cases, undesiderable wavelengths could coincide with the one of interest because their locations, at different orders, are found within the same spectral width. In those cases an interferential filter is used before the detectors to eliminate their contributions.

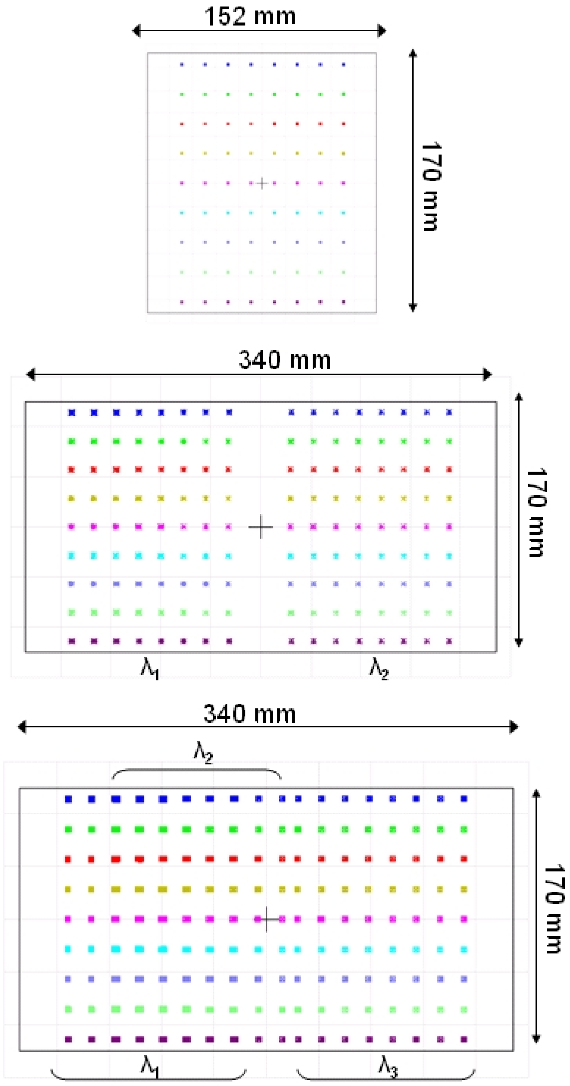

Figure 4.5: ZEMAX footprints associated to three examples of masks. The footprint shows the beams at the predisperser image focal plane. Each column represents a slit, defined by nine field points. The first case corresponds to the observation of a wavelength interval centred around 4102 Å with the VIS-I predisperser. The second case considers two wavelength ranges around 15260 Å (on the left) and 8542 Å (on the right), which are observed simultaneously with the IR-I predisperser. The third example, at the bottom, is an extension of the second one, in which three wavelengths are studied together qround 15260 Å, 15650 Å and 8542 Å. For this combination six slits of the mask are shared by 15260 Å and 15650 Å.

The number of slits of the mask is the number of entrance slits multiplied by the number of wavelengths observed simultaneously. For one entrance slit, the input angle of the beam over the predisperser grating, $\Theta_{i_{pd}}$, as well as the order, m, and the wavelength, λ, are known. The output grating angle, $\Theta_{o_{pd}}$, is obtained from Eq. 1.12. The position of the slit in the mask, at the predisperser image focal plane, z, is calculated with the values of the grating output angle and the predisperser camera focal length, $f_{cam_{pd}}$, as shown in Eq. 4.10.

$$z = f_{cam_{pd}} \cdot \tan \Theta_{o_{pd}} \tag{4.10}$$

For 1:1 systems, the separation between the slits of the mask is the same that the separation between the entrance slits. This value depends on the separation of the images of the entrance slits on the detector. The detectors have 4096 pixels, 512 pixels for the image of each slit associated to the same wavelength. For the visible spectral ranges the assumed pixel size is 10 μm. The separation between the images of the slits on the detector is 5.12 mm for a focal-ratio F/10.3, what implies that the separation between the slits of the mask and the predisperser entrance slits generated by the IFU is 19.88 mm for F/40. The pixel size considered for the infrared spectral ranges is 20 μm and the separation between the slits is 10.24 mm for F/20.6 and 19.88 mm for F/40. The separation between the slits generated by the IFU is independent on the wavelength.

The width of the slits of the predisperser mask depends on the wavelength interval, the linear dispersion and the spectral range for the image of each slit on the detector.

The spectral range, $\Delta\lambda_{pd}(\text{Å})$, associated to the slit width of the predisperser mask, can be calculated multiplying the sampling, defined in Eq. 1.31, by the number of pixels associated to the image of the slit on the detector. The linear size of the predisperser mask slits is obtained dividing $\Delta\lambda_{pd}$, by the reciprocal linear dispersion (Eq. 1.23). Some examples of the calculated slit width are presented in Table 4.4. According to the calculated values, an estimation of the spectral range can be obtained as $\Delta\lambda(\text{Å}) \simeq 8 \cdot \lambda(\mu\text{m})$.

Table 4.4: Calculated values for the predisperser mask slit width for some wavelengths and their corresponding spectral ranges.

λ (Å)	Slit width (mm)	$\Delta\lambda_{pd}$ (Å)
3933	0.49	3.26
8498	1.03	6.32
8542	0.99	6.08
15650	0.99	12.22
22300	0.50	17.74

The calculation of the predisperser mask for the multi-slit case is done following the steps shown in Fig. 4.6. For a same wavelength, the steps of the diagram are repeated as many times as the number of the predisperser entrance slits (at F2).

Tests at THEMIS telescope

The THEMIS telescope (Gelly, 2007) has been used as a testbed for the manufacturing and design of spectral masks in an existing solar facility, whose spectrograph is also preceded by a predisperser with a mask at its focal plane. The goal of these tests is the study of the mask for different cases (one slit and one observed wavelength, one slit and multi-wavelength capability or even more than one entrance slit, as well as the result obtained the detector) and the analysis of the most restrictive parameters in the design, fabrication and in practice, the use of the masks.

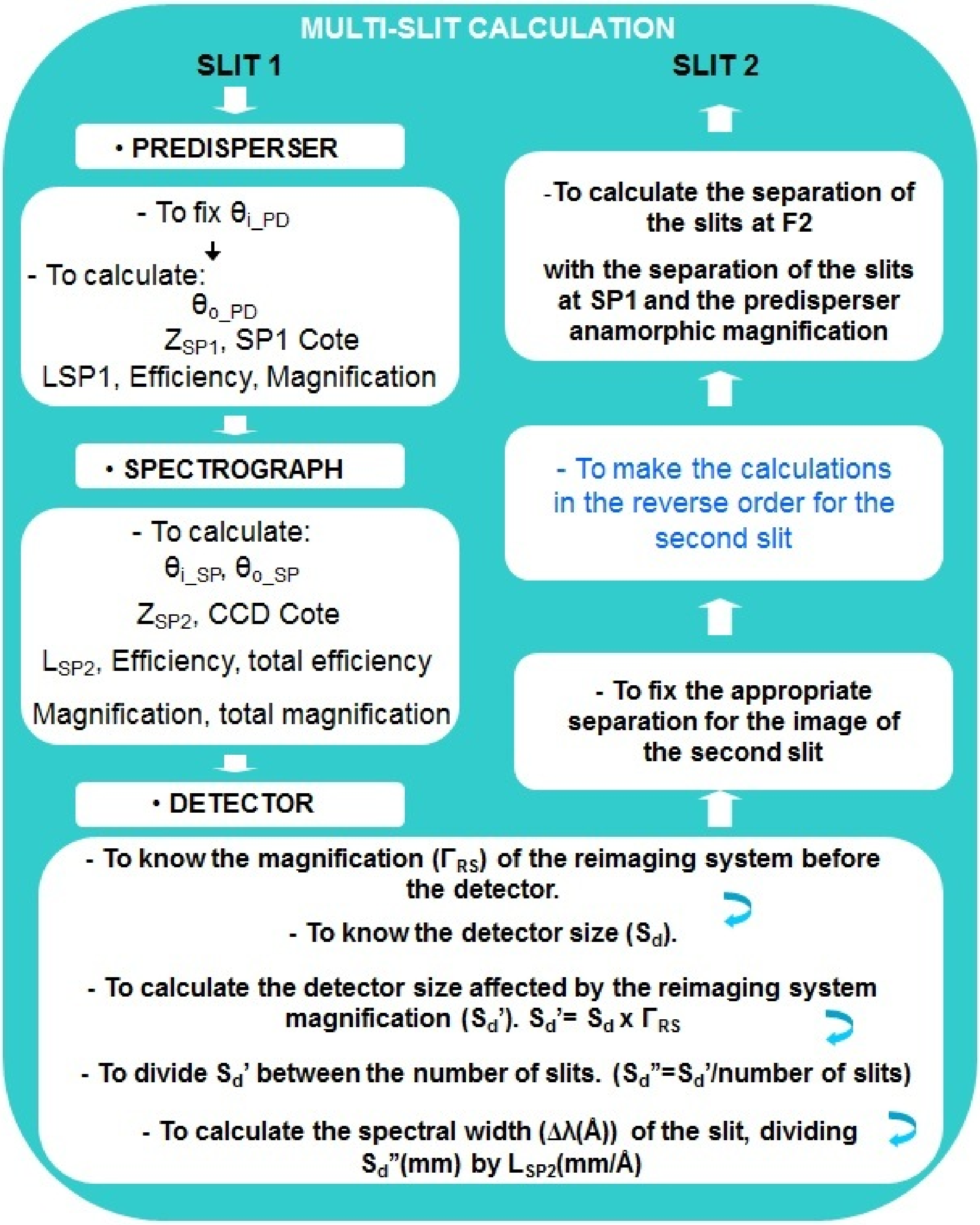

Figure 4.6: Calculation steps for the multi-slit case. The steps consist in applying Eqs. 4.11 to 4.17, as well as Eqs. 1.15 and 1.23, for predisperser and spectrograph. In addition, the detector and the reimaging system located before it are also taken into account to calculate the spectral range associated to each slit on the detector. Once these values are obtained for the first slit, the next step is to fix the appropriate separation between the image of the slits at SP2, what gives the position of the image of the second slit at the spectrograph image focal plane. From here, the calculation is reversed and the parameters associated to the second slit are obtained from the detector back to the predisperser entrance.

A side view of the optical design of the THEMIS spectrograph is presented in Fig. 4.7.

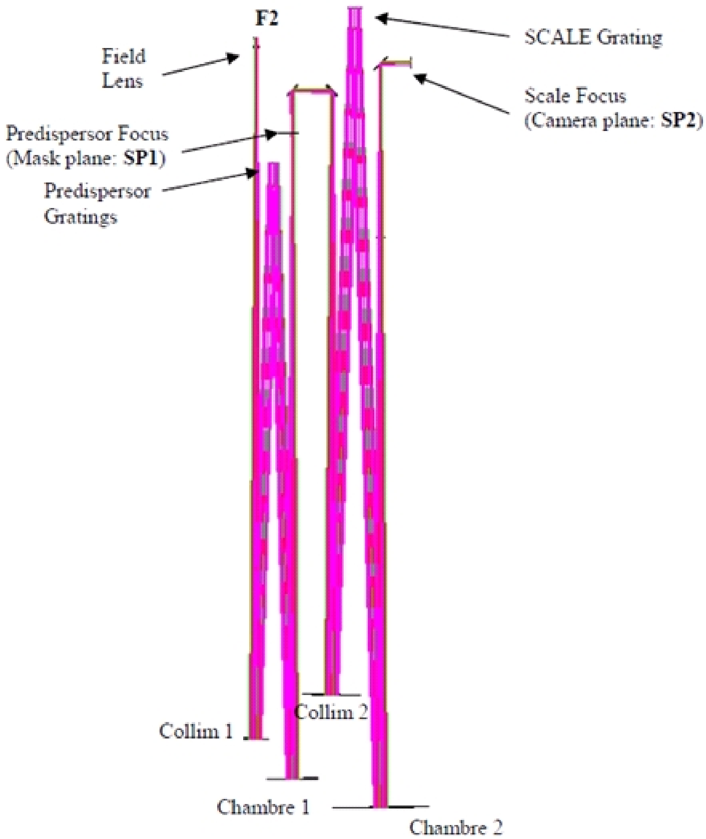

Figure 4.7: THEMIS spectrograph side view. F2 is the telescope image focal plane. The mask is located at the predisperser focus, in SP1 position. Two folding mirrors bend the light to compact the system and drive the beam to the spectrograph. The detector is placed at SP2.

Table 4.5: Characteristics of THEMIS predisperser and spectrograph. Where: F_{col} and F_{ch} are the focal lengths of collimator and camera mirrors, respectively. φ_B is the blaze angle, σ the grooves density and d the grating constant, inverse of the grooves density.

Parameter	PD	SP
F_{col}	7618 mm	7490 mm
F_{ch}	7011 mm	8437 mm
	GRATINGS	
φ_B	2.151°	63.433°
σ	150 grooves/mm	79 grooves/mm
d	0.0067 mm	0.0127 mm

The characteristics of predisperser and spectrograph are presented in Table 4.5.

The easiest case consists in the use of an entrance slit at F2 (Fig. 4.7) and one observed wavelength. In this case the predisperser mask presents a slit (see Fig. 4.18 a), for the observed wavelength with the predisperser at first diffraction order. The mask also acts as a prefilter to avoid the contribution of other wavelengths.

Before the observations at the telescope, the calculations have been made, as well as the design of the mask used for the tests.

The predisperser grating input angle is selected in order to work with the wavelength of interest as centred as possible at the predisperser image focal plane (SP1). In this case, this angle is $\Theta_i = 2.4554°$, which is close to the blaze angle. The predisperser grating output angle, Θ_o, can be calculated finding its value from Eq. 1.12, as shown in Eq. 4.11.

$$\Theta_o = \arcsin(\frac{m \cdot \lambda}{d} - \sin \Theta_i) \tag{4.11}$$

The location of the slit (Z_{SP1}) in the predisperser mask at SP1 is obtained with Eq. 4.12.

$$Z_{SP1} = F_{ch} \cdot \tan(\Theta_o - \Theta_i)\,, \tag{4.12}$$

where F_{ch} is the predisperser camera focal length.

The predisperser mask mount has a width of 300 mm. This is the size of the mask mount independently on the number of slits. In this particular case, the associated predisperser mask has only one slit. In order to centre this slit in the mask, an offset is considered, 150 mm, which is half of the mask width. A mechanical reference is used and the slit centred position, denoted by SP1 Cote, is calculated using Eq. 4.13.

$$SP1Cote = 150 - Z_{SP1} \tag{4.13}$$

The spectrograph grating input angle, $\Theta_{i_{sp}}$, depends on the slit position at SP1, which is itself a function of the predisperser grating output angle, Θ_o, and the predisperser camera focal length, and the spectrograph collimator focal length, $f_{col_{sp}}$, as shown in Eq. 4.14.

$$\Theta_{i_{sp}} = f(Z_{SP1}(\Theta_o, f_{cam_{pd}}), f_{col_{sp}}) \tag{4.14}$$

The spectrograph grating input angle can be calculated with Eq. 4.15.

$$\Theta_{i_{sp}} = \chi - \arctan(\frac{Z_{SP1}}{F_{col}})\,, \tag{4.15}$$

where χ is the grating rotation angle, which, for these tests has a value of $\chi = 62.9378°$. Once the incident angle over the spectrograph grating is known, the output angle, $\Theta_{o_{sp}}$ is obtained applying the grating equation defined in Eq. 1.12. The diffraction order in which the wavelength is observed is calculated using the grating equation (Eq. 1.14), as the integer value closest to the obtained value.

The wavelength position, Z_{SP2}, at the spectrograph image focal plane, SP2, is given by Eq. 4.16.

$$Z_{SP2} = F_{ch_{sp}} \cdot \tan(\chi - \Theta_{o_{sp}}) \tag{4.16}$$

Analogously to the predisperser calculation, an offset (502 mm) is considered to centre the observed wavelength at the spectrograph image focal plane, SP2. The detector position (SP2 Cote) is then obtained using Eq. 4.17.

$$SP2\ Cote = 502 - Z_{SP2} \tag{4.17}$$

Using these equations, the values of Table 4.6 have been obtained.

Table 4.6: Calculated values for the observation of 6302 Å using one slit at F2 and a predisperser mask with one slit.

PREDISPERSER VALUES	
Θ_i	2.7091°
Order	1
Θ_o	2.7091°
Z_{SP1}	0.00 mm
SP1 Cote	150.00 mm
L	0.1053 $mm/$Å
Efficiency	0.72
$\mathit{\Gamma}_{PD}$	0.92
γ_{an}	1.00
SPECTROGRAPH VALUES	
Θ_i	63.3873°
Order	36
Θ_o	63.9268°
Z_{SP2}	-79.40 mm
SP2 Cote	581.40 mm
Efficiency	0.79
Total efficiency	0.57
L_{SP2}	5.46 $mm/$Å

A layout of the associated predisperser mask, at SP1, is presented in Fig. 4.8, where the real size of the mask has been considered. The slit is located at 150 mm, with an inclination of 8.5° due to the inclination of the spectrum at the predisperser image focal plane. This inclination is given by the instrument optical design.

Before the tests at the telescope, the calculated values have been verified using the THEMIS spectrograph simulator, whose results are shown in Fig. 4.9.

Once at the telescope, the sunspot NOAA 11532 has been observed with a slit width of 0.50 arcsec and an exposure time of 70 msec. In addition, 40 flat and 40 dark images of 70 msec have also been taken. They have been combined in order to use average flat and dark

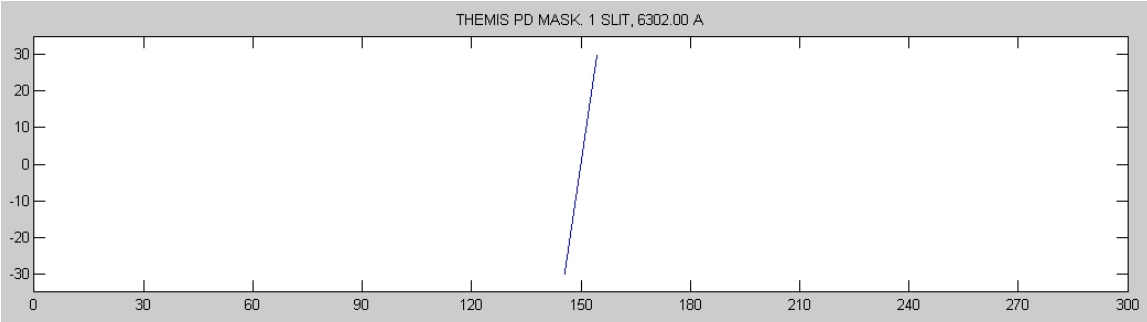

Figure 4.8: Layout of the calculated predisperser mask, associated to the first studied case at THEMIS spectrograph, using one entrance slit at F2 and a predisperser mask with one slit for the observation of 6302 Å at orders 1 and 36 for predisperser and spectrograph, respectively. The mask has been represented considering its real size (300 mm width by 70 mm length). The slit is centred in the mask and presents an inclination of 8.5° given by the instrument optical design.

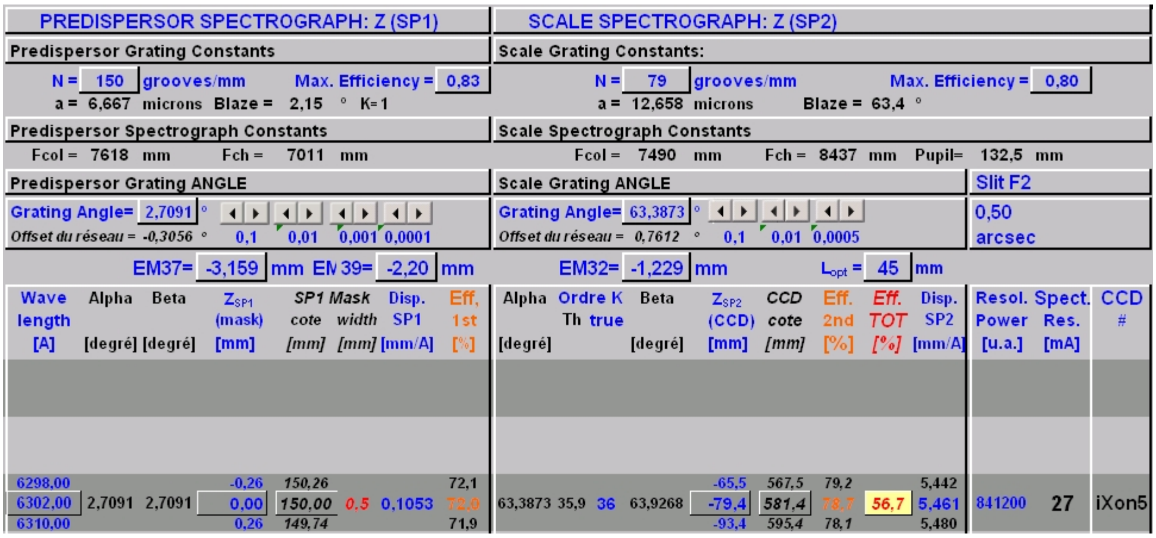

Figure 4.9: Values obtained using the THEMIS spectrograph simulator for one slit at 6302 Å. These values coincide with those of Table 4.6. The data on the top show the gratings characteristics and the collimator and camera focal lengths. The values on the left are associated to the predisperser and those on the right correspond to the spectrograph.

images. A slit-jaw image has also been taken to identify the slit position over the field of view.

The spectrum obtained is shown in Fig. 4.10. An interval of ∼6 Å centred at a wavelength of ∼ 6302 Å is observed. The telluric lines are superimposed to the solar spectrum. The solar spectral lines show a widening produced by the Zeeman effect.

This first case can be improved adding multi-wavelength capability. If two wavelengths are observed using one slit at F2, the predisperser mask, at SP1, has 2 slits, one per wavelength. The values obtained with the simulator for 6302 Å and 5250 Å are presented in Fig. 4.11. These values are consistent with the calculated ones. The same input angle for the predisperser grating than in the previous case has been used. The wavelengths are observed

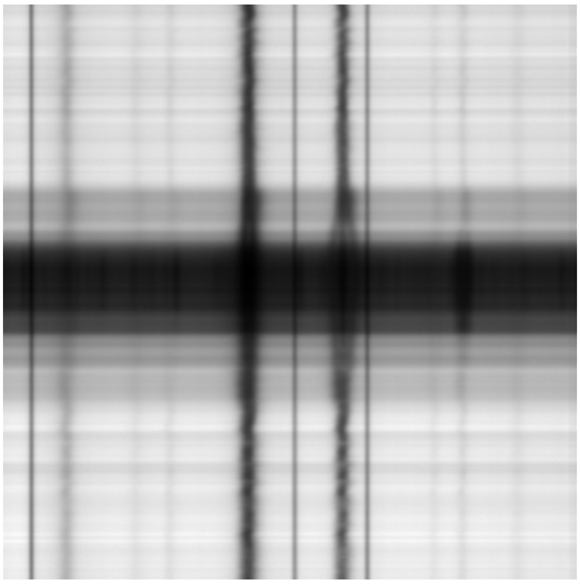

Figure 4.10: Spectrum obtained for 6302 Å (on the right) for the first studied case, using an entrance slit at F2 and a predisperser mask with one slit at SP1. Since the spectral range over the detector is ∼6 Å, the spectral line associated to 6301 Å is also observed (on the left).

at first order in the predisperser and at order 36 and 43, respectively, in the spectrograph. Each one is observed in a different detector. The data on the top correspond to the gratings parameters and collimator and camera focal lengths. The values at the bottom show the calculated results. The values for the predisperser are presented on the left and those for the spectrograph are shown on the right.

The number of simultaneous wavelengths can be increased. As a third step, four wavelengths have been evaluated together: 4861 Å, 5875 Å, 6302 Å and 6563 Å. At F2, one slit is used, which is illuminated by the white light beam of the telescope (see Fig. 4.12). For this reason, all the wavelengths present the same input angle over the predisperser grating, 2.45°. The predisperser grating decomposes the beam in its constituent wavelengths and separates them. The spectrum is formed at the predisperser image focal plane, at SP1, where the mask selects these wavelengths, at first diffraction order, elliminating the contribution of the others. The values for the predisperser calculated for this multi-wavelength case are presented in Table 4.7.

Table 4.7: Calculated values for four wavelengths: 4861 Å, 5875 Å, 6302 Å and 6563 Å, using one entrance slit at F2. The input angle over the predisperser grating is 2.45°.

λ (Å)	$\Theta_o(°)$	Z_{SP1}	L (mm/Å)	SP1 Cote	Efficiency	Γ_{PD}
4861	1.72	-89.55	0.10	239.55	0.80	0.92
5875	2.60	17.21	0.10	132.79	0.81	0.92
6302	2.96	62.09	0.10	87.90	0.77	0.92
6563	3.19	89.56	0.10	60.43	0.74	0.92

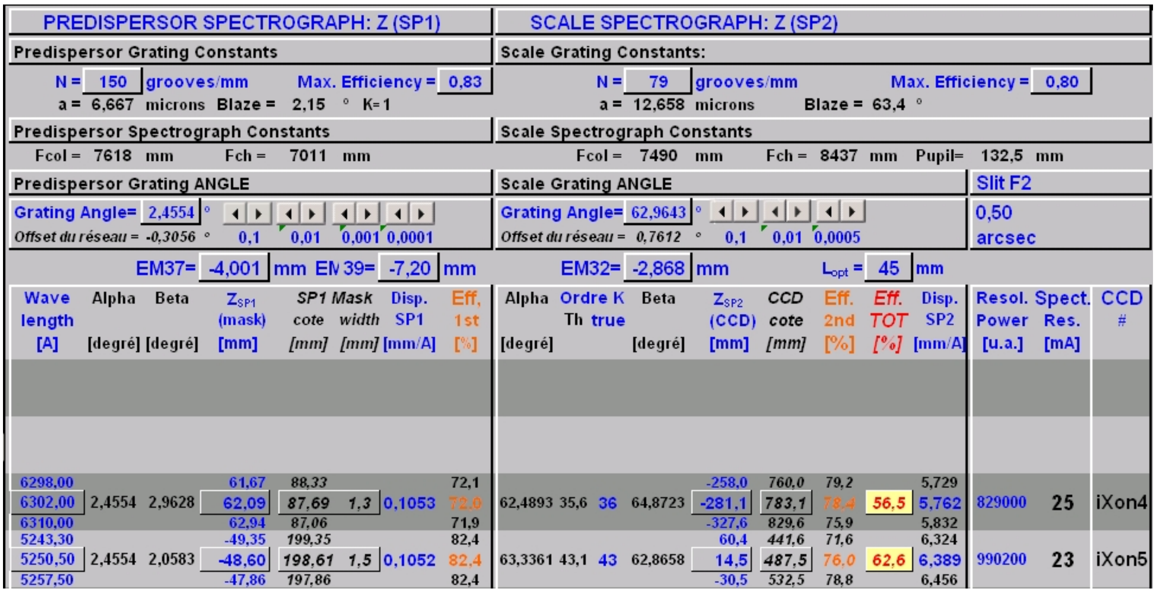

Figure 4.11: Values calculated with the THEMIS spectrograph simulator for one entrance slit at F2 and two observed wavelengths: 6302 Å and 5250 Å at order one in the predisperser and 36 and 43, respectively, in the spectrograph. Each wavelength is observed in a different detector. The data on the top correspond to the gratings parameters and collimator and camera focal lengths. The values at the bottom show the calculated results. The values for the predisperser are presented on the left and those for the spectrograph are shown on the right.

Each wavelength presents a different location at the predisperser image focal plane, this means, in the mask. As a difference with respect to the predisperser, they illuminate the spectrograph with different angles given by their positions. These angles, as well as the other calculated parameters for the spectrograph are shown in Table 4.8. The values obtained for these wavelengths using the spectrograph simulator are presented in Fig. 4.13.

Table 4.8: Calculated spectrograph values for the multi-wavelength case. One entrance slit at F2 and four at SP1, one per wavelength are used.

λ (Å)	$\Theta_o(°)$	$\Theta_o(°)$	Z_{SP2}	L	SP2 Cote	Efficiency	Total efficiency	Γ_{SP}
4861.30	63.62	65.38	-360.27	7.63	862.27	0.69	0.57	1.20
5875.70	62.81	60.98	288.94	5.33	213.06	0.68	0.53	1.06
6302.00	62.46	64.90	-289.23	5.76	791.23	0.76	0.55	1.23
6562.80	62.25	61.37	230.46	4.83	271.54	0.73	0.50	1.09

The calculated mask in this case presents four slits, one per wavelength. The layout is presented in Fig. 4.14. The mechanical drawing for the fabrication of this mask is shown in Fig. 4.15.

More than one slit can be used at the predisperser entrance (F2), increasing the field of view observed in an exposure time. In this case and, because of the separation between the slits, a different input angle over the predisperser grating corresponds to each slit. The

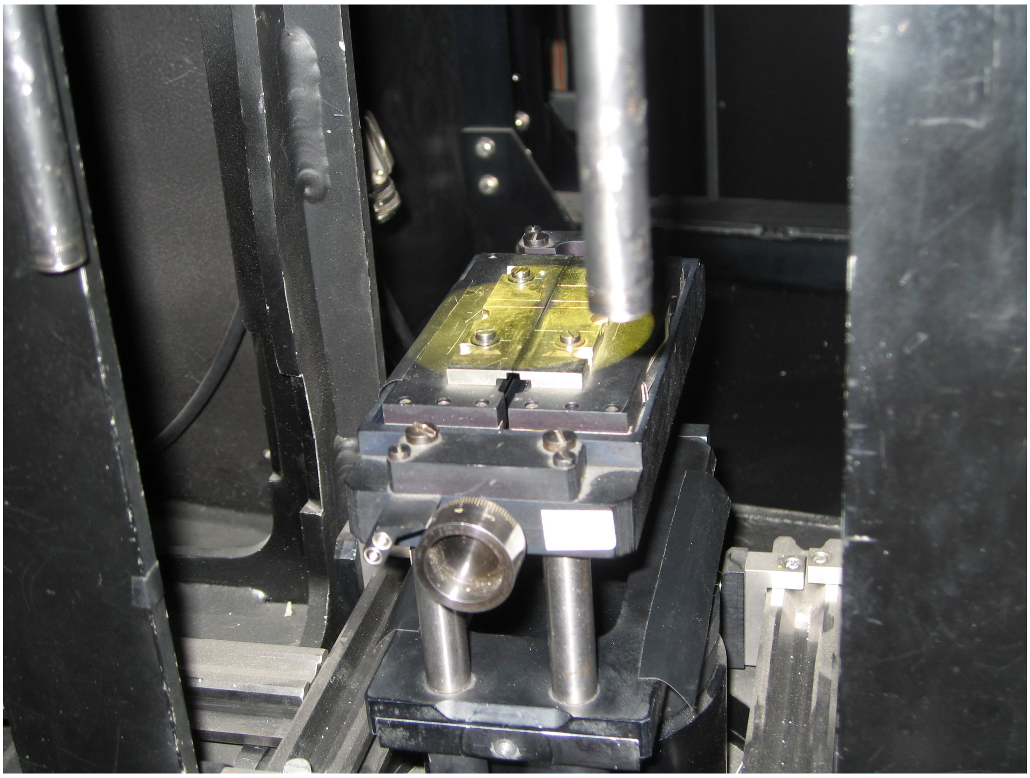

Figure 4.12: THEMIS entrance predisperser slit at F2 illuminated by the white light beam of the telescope.

PREDISPERSOR SPECTROGRAPH: Z (SP1)

Predispersor Grating Constants

N = 150 grooves/mm Max. Efficiency = 0,83
a = 6,667 microns Blaze = 2,15 ° K=1

Predispersor Spectrograph Constants

Fcol = 7618 mm Fch = 7011 mm

Predispersor Grating ANGLE

Grating Angle= 2,4554 ° 0,1 0,01 0,001 0,0001
Offset du réseau = -0,3056 °

EM37= -4,001 mm EM 39= -7,20 mm

SCALE SPECTROGRAPH: Z (SP2)

Scale Grating Constants:

N = 79 grooves/mm Max. Efficiency = 0,80
a = 12,658 microns Blaze = 63,4 °

Scale Spectrograph Constants

Fcol = 7490 mm Fch = 8437 mm Pupil= 132,5 mm

Scale Grating ANGLE

Grating Angle= 62,9643 ° 0,1 0,01 0,0005
Offset du réseau = 0,7612 °

EM32= -2,868 mm L_{opt} = 45 mm

Slit F2

0,50 arcsec

Wave length [A]	Alpha [degré]	Beta [degré]	Z_{SP1} (mask) [mm]	SP1 Mask cote [mm]	SP1 Mask width [mm]	Disp. SP1 [mm/A]	Eff, 1st [%]	Alpha [degré]	Ordre K Th	Ordre K true	Beta [degré]	Z_{SP2} (CCD) [mm]	CCD cote [mm]	Eff. 2nd [%]	Eff. TOT [%]	Disp. SP2 [mm/A]	Resol. Power [u.a.]	Spect. Res. [mA]	CCD #
4856,40			-90,07	240,07			82,8					-314,9	816,9	48,0		7,556			
4861,30	2,4554	1,7236	-89,55	239,55	1,0	0,1052	82,8	63,6493	46,7	47	65,3547	-352,2	854,2	41,2	34,1	7,631	######	19	iXon2
4866,20			-89,04	239,04			82,8					-389,9	891,9	34,4		7,708			
5867,70			16,37	133,63			77,2					339,0	163,0	24,2		5,283			
5875,70	2,4554	2,5960	17,21	132,90	1,5	0,1053	77,1	62,8327	38,3	38	60,9514	296,5	205,5	30,1	23,2	5,328	875100	27	iXon3
5881,70			17,84	132,16			77,1					264,4	237,6	34,8		5,363			
6298,00			61,67	88,33			72,1					-258,0	760,0	79,2		5,729			
6302,00	2,4554	2,9628	62,09	87,69	1,3	0,1053	72,0	62,4893	35,6	36	64,8723	-281,1	783,1	78,4	56,5	5,762	829000	25	iXon4
6310,00			62,94	87,06			71,9					-327,6	829,6	75,9		5,832			
6555,60			88,81	61,19			68,7					272,9	229,1	29,5		4,801			
6562,80	2,4554	3,1873	89,56	60,45	1,5	0,1053	68,7	62,2792	34,1	34	61,3474	238,2	263,8	34,0	23,4	4,835	783000	30	iXon5
6569,80			90,30	59,70			68,6					204,1	297,9	38,6		4,869			

Figure 4.13: Values obtained using the THEMIS spectrograph simulator for one entrance slit and four wavelengths: 4861 Å, 5875 Å, 6302 Å and 6563 Å.

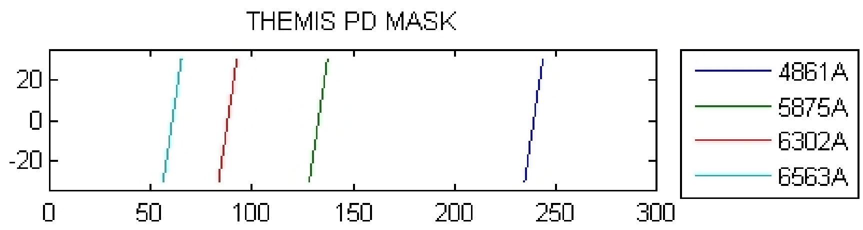

Figure 4.14: Multi-wavelength predisperser mask for: 4861 Å, 5875 Å, 6302 Å and 6563 Å at first diffraction order with an input angle over the diffraction grating of 2.5°. The slits present an inclination of 8.5°.

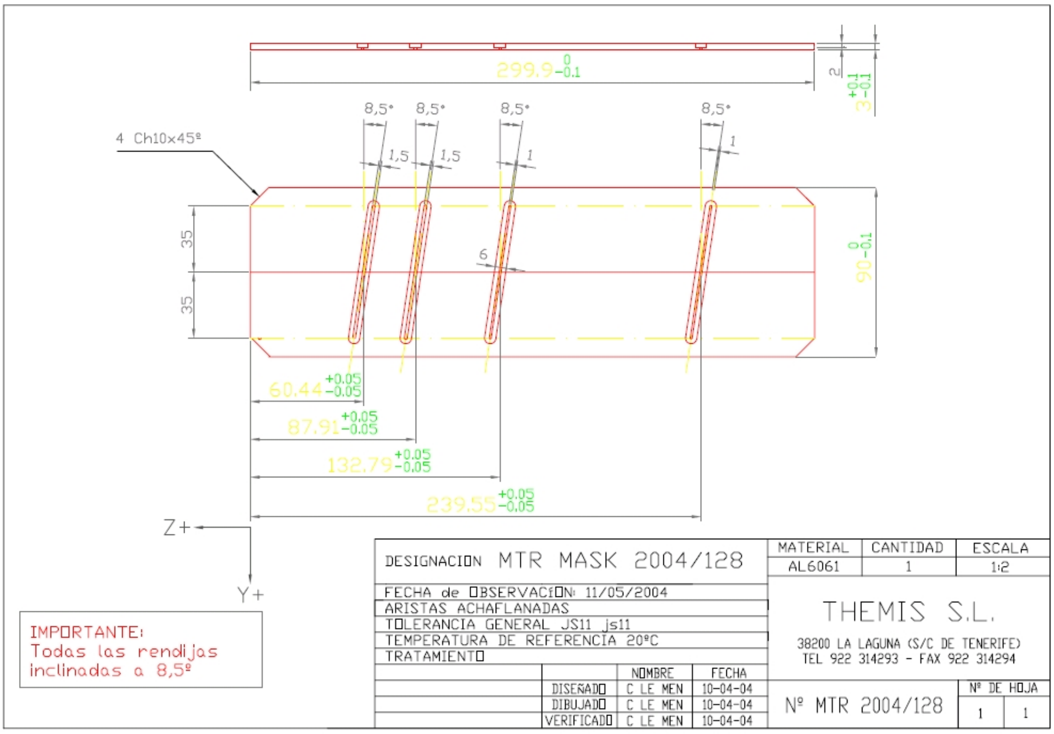

Figure 4.15: THEMIS mechanical drawing of the predisperser mask, designed for the simultaneous observation of 4861 Å, 5875 Å, 6302 Å and 6563 Å at first diffraction order, with an input angle over the diffraction grating of 2.5° and using one slit at F2. The slits are centred in the SP1 Cote values of Table 4.7 and present an inclination of 8.5°.

separation between the entrance slits and the input angles for predispersers are conditioned by the separation of the spectra in the detector. Two different parts of the field are observed simultaneously at the same wavelength.

For the tests at telescope, a double slit to be located at F2 has been calculated, designed and manufactured. The mechanical drawing is presented in Fig. 4.16. Once they are placed at F2 they are oriented at 8.5° using a calibrated rotator, which is shown in Fig. 4.17.

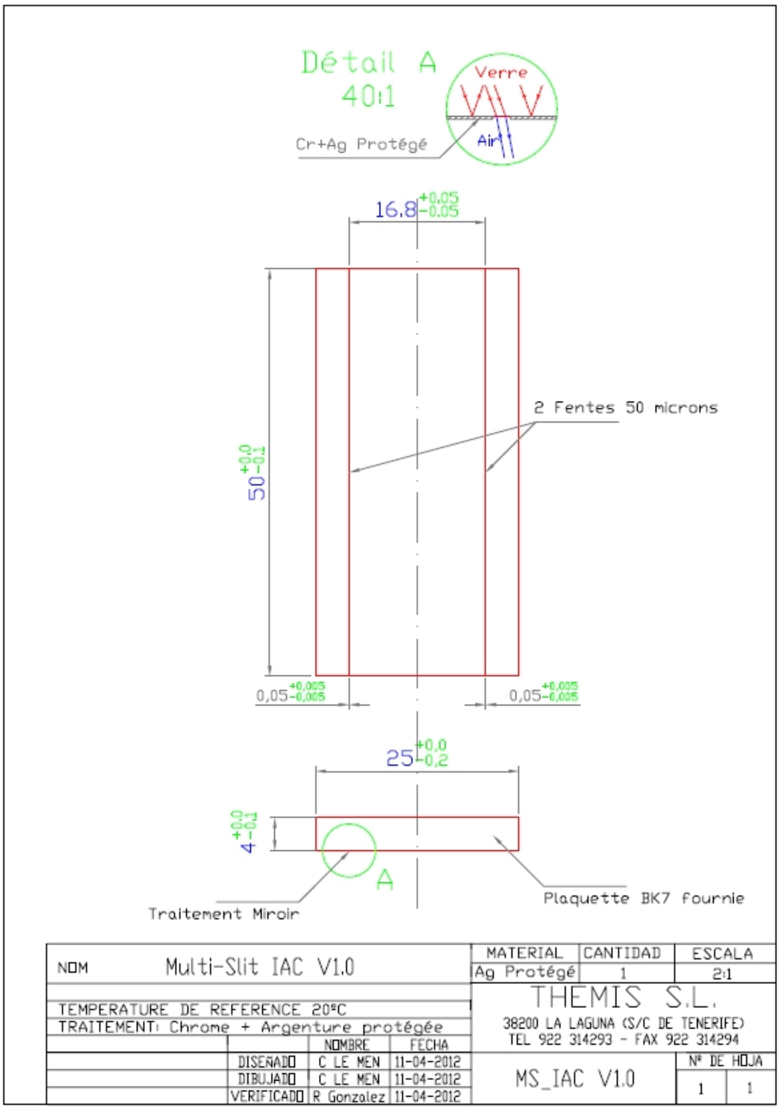

Figure 4.16: Mechanical drawing for the double slit of F2. The slits are oriented at F2 using a calibrated rotator (see Fig. 4.17).

If two input slits and one wavelength are considered, the mask has two slits, associated to the image of the entrance slits at the predisperser image focal plane. The predisperser mask for the case of two slits at F2 and one wavelength, is shown in Fig. 4.18 (b). The slits, either at F2 or at SP1, are centred. And, since predisperser and spectrographs are $\sim$ 1:1 systems, the separation of the slits at SP1 is nearly the same than at F2, independently on the considered wavelength. The values for the multi-slit case can be calculated according to the diagram of Fig. 4.6. The process starts by choosing an input angle for slit 1 over the predisperser grating. The following steps consist in applying Eq. 4.11 and to calculate the total magnification for predisperser and spectrograph. In addition, the detector and, the reimaging system located before it are also taken into account to calculate the spectral

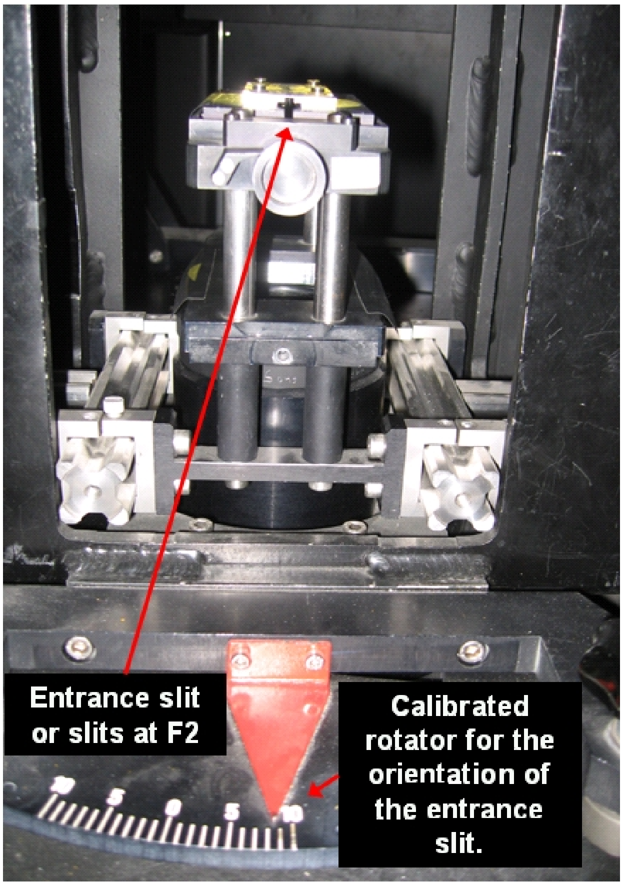

Figure 4.17: Calibrated rotator mechanism for the orientation of the entrance slits at F2.

interval associated to each slit on the detector. Once these values are obtained for the first slit, the next step is to fix the appropriate separation between the image of the slits at SP2 to get the position of the image of the second slit at the spectrograph image focal plane. From here, the calculation is reversed and the parameters associated to the second slit are obtained from the detector back to the predisperser entrance.

The wavelength considered for this test is 6302 Å. The spectra associated to the two slits are observed within the spectral range covered by the detector, ~ 6 Å. The spectral width for each one is ~ 3 Å. Thus, the two Fe I lines at 6302 Å and 6301 Å are observed together, as well as the telluric lines, due to the Earth's atmosphere. The observed image is presented in Fig. 4.19, where two different fields are observed at the same wavelength and the same time. This image can be compared with Fig. 4.10.

The spectrograph performances can be improved by combining multi-slit and multi-wavelength capabilities. Each wavelength range is then observed in a different detector. The number of slits in the mask corresponds to the product of the number of the predisperser entrance slits by the number of wavelengths observed at the same time.

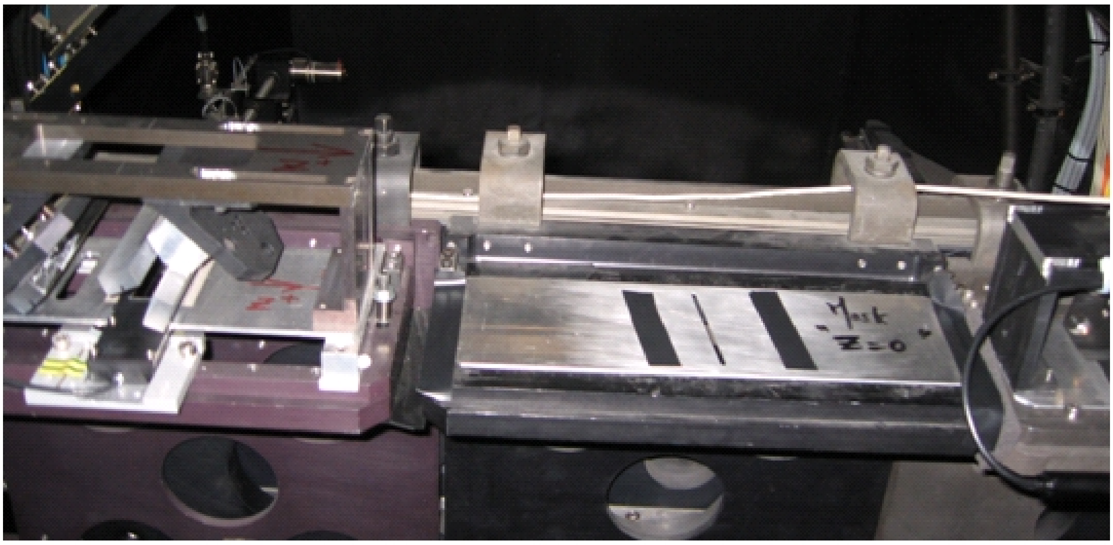

(a)

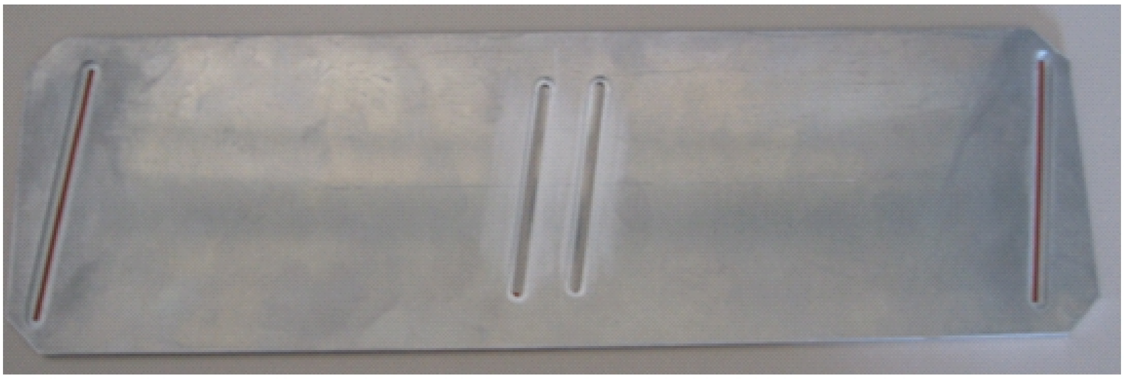

(b)

Figure 4.18: On top, figure (a) presents the predisperser mask location. In this case the mask shown is the associated to the first case studied, using one slit at F2 for one observed wavelength and a predisperser mask at SP1 with one slit. At the bottom, the figure (b) presents the mask used for two entrance slits at F2 and one observed wavelength, 6302.00 Å. The predisperser mask has two slits associated to the image of the input ones.

The same calculation as in the previous case is made following the steps of the diagram of Fig. 4.6 and repeating the process as many times as the number of considered wavelengths. The predisperser input angles do not vary with wavelength but with the slit. Nevertheless the spectrograph input angles depend on wavelength, since the predisperser output angle is different too.

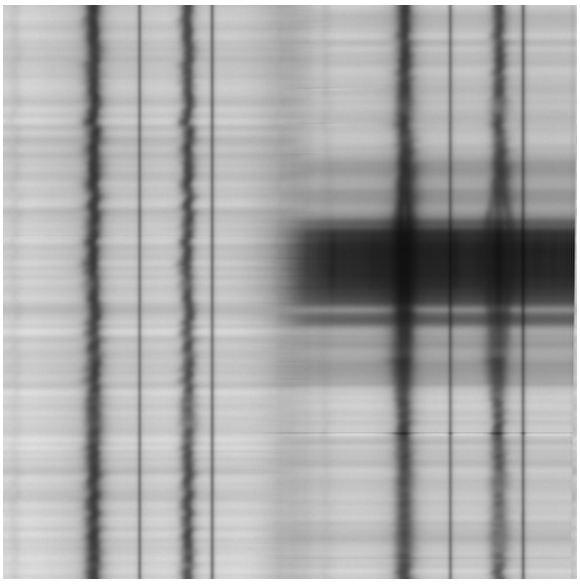

Figure 4.19: Observed spectral range centred around 6302 Å, using two predisperser entrance slits. Two different fields over the Sun are observed simultaneously. The first slit (left) offers the spectrum of the quiet sun while the second one (right) corresponds to a sunspot.

Manufacturing points to be considered

The tests at THEMIS telescope have been useful to detect the manufacturing points that must be considered in the design and the technical specifications for the mask fabrication.

An important point is the homogeneity of the slit edges. In addition, the spectrum does not present an abrupt jump like the one corresponding to a step function at the slit edges. The spectrum decays smoothly. This effect is produced by the convolution of the predisperser entrance slit at F2 with the slit of the predisperser mask. This effect is smaller the thinner the entrance slit.

Another aspect to consider in the fabrication process is the accuracy in the parallelism of the slits of the mask. If the slits of the predisperser mask were strictly parallel, the image associated to the space between the predisperser mask slits would be seen on the detector as a rectangular obscuration. Nevertheless, a small variation of this parallelism leads to the effect shown in the central part of Fig. 4.20.

These two mentioned problems depend on the way in which the slits of the mask are fabricated, on the tolerances. The mask slits like the ones of Fig. 4.18 (b) are made mechanically using a milling machine. The typical tolerance in the homogeneity of the slits edge is 20 μm. The best technique to manufacture very thin slits with high precision is photodeposition. This technique has been applied for the fabrication of the double slit of F2, whose mechanical drawing is shown in Fig. 4.16 and consists of the deposit of protected silver over glass.

If the polishing quality with which the predisperser mask slits are fabricated is not very high, the small uniformities along the different points of the edges of these slits are translated

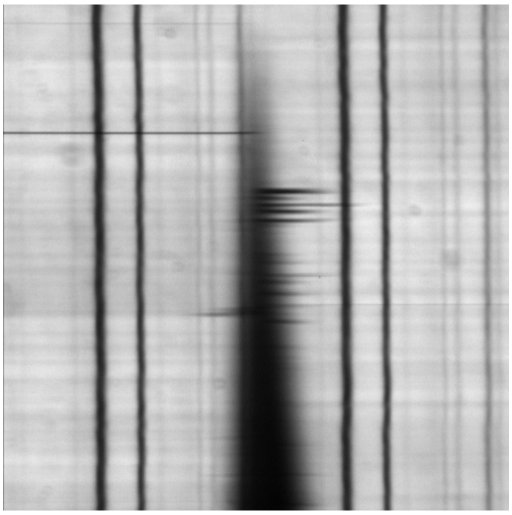

Figure 4.20: Effect of a small deviation in the mask slit parallelism using a predisperser mask with two slits for the observation of two different parts of the field of view at the same wavelength. If the slits of the predisperser mask were strictly parallel, the image associated to the space between the predisperser mask slits would be seen on the detector as a rectangular obscuration. Nonetheless, a small deviation in the parallelism of the predisperser mask slit on the right leads to a shape like the central one shown in this figure.

into a rugosity and produce effects like the ones observed horizontally in the centre of Fig. 4.20. The result of this effect that is observed as horizontal peaks accross the image decreases if the width of the predisperser entrance slit is reduced.

A different test was done using a slit width of 0.50 arcsec at F2 and moving the predisperser mask with a step of 0.10 mm, equivalent to $\sim$1.00 Å. The mask translation at SP1 implies a spectral scanning. A sequence of three images was obtained (Fig. 4.21), where the irregularities in the edge of the slit of the mask are evident.

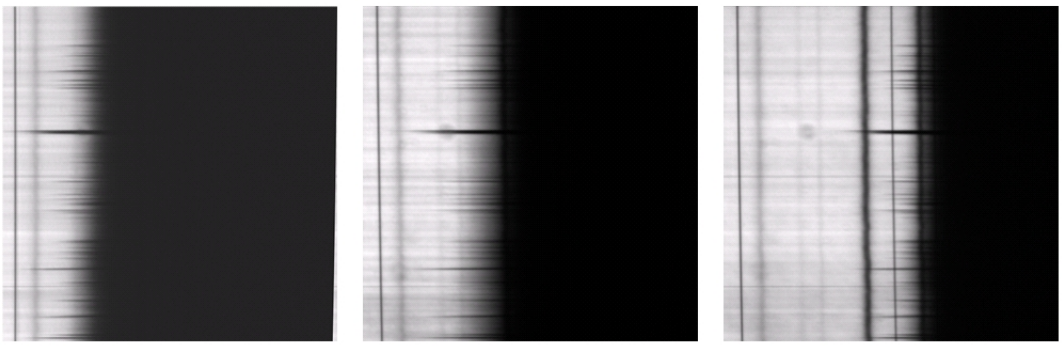

Figure 4.21: The sequence of images corresponds to three different positions of the predisperser mask at SP1 with a step between them of 0.10 mm, equivalent to $\sim$1.00 Å. The mask translation at SP1 implies a spectral scanning. The effect of the irregularities in the slits edges polishing is visible in each image.

Degrees of freedom of the predisperser mask

The predisperser mask must have mechanical degrees of freedom. The mask must be integrated over a rail with translation in both directions. Since the different optical elements are aligned in the optical axis, vertical movements are not required. Orientation is also needed, for a high-precision assembly of the mask. For this purpose, the mask is integrated on a calibrated rotator.

4.2 Spectrograph

The slits of the predisperser mask are the spectrograph entrance slits.

4.2.1 Spectrograph calculation

The four spectrographs (VIS-I, VIS-II, IR-I, IR-II) have also been designed as 1:1 F/40 systems with Ebert-Fastie configuration using parabolic mirrors for collimator and camera elements, which are two sub-apertures of the same on-axis global parabola.

The selection of the commercial gratings, as well as the optical components parameters are calculated analogously than for the predispersers.

Diffraction gratings

For the spectrographs, as for the predispersers, a pupil image is placed at the diffraction grating. The pupil diameters are shown in Table 4.9.

Table 4.9: Spectrographs pupil diameters.

SP	PUPIL DIAMETER (mm)
VIS-I	187.5
VIS-II	175.0
IR-I	200.0
IR-II	175.0

And the selected diffraction gratings are presented in Table 4.10.

Table 4.10: Characteristics of the selected spectrograph gratings.

SP	σ (grooves/mm)	φ_B (°)	Size (mm^2)
VIS-I	316	63	204×408
VIS-II	110	64	310×413
IR-I	79	62	210×411
IR-II	79	62	210×411

Optical components

The main characteristics of the spectrograph collimator and camera mirrors are presented in Table 4.11.

Table 4.11: Technical characteristics of the spectrograph collimator and camera mirrors. The values are given in millimetres. The focal length is calculated with Eq. 4.5 and the collimator and camera mirror diameter, ϕ_{COL} and ϕ_{CAM}, respectively, applying Eq. 4.9 in both cases.

SP	ϕ_{COL}	dec_{COL}	ϕ_{CAM}	dec_{CAM}	FOCAL LENGTH
VIS-I	600	210	820	420	7500
VIS-II	600	200	400	200	7000
IR-I	700	300	660	350	8000
IR-II	500	200	380	240	7000

The angles between collimator and camera mirrors for each spectrograph are: 4.80°, 3.27°, 4.64° and 3.60° for VIS-I, VIS-II, IR-I and IR-II respectively.

4.2.2 Effect of blaze angle in the efficiency curve

The blaze angle for the spectrographs gratings is much bigger than that of the predispersers. Echelle gratings have been chosen for the spectrographs in order to reach high spectral resolution and a larger dispersion than the one obtained in the first step with the predispersers. Another difference is that the plane ruled reflectance gratings for predispersers are optimised to work at low order, generally at first one, while the echelle spectrographs gratings work at high orders. The blaze angle affects the efficiency curve, since it is one of the factors involved in its calculation. Using Eq. 1.15 and replacing the expressions of Eqs. 1.16, 1.17, 1.18 and 1.19, the grating efficiency is then a function of the grating grooves size, the input and output angles of the light with respect to the grating, the wavelength and, also, the blaze angle. The Eq. 4.18 shows the implicated parameters.

$$Eff = \left[\frac{\sin\left(\frac{\pi \cdot d \cdot \cos\varphi_B \cdot (\sin\alpha + \sin\beta)}{\lambda}\right)}{\left(\frac{\pi \cdot d \cdot \cos\varphi_B \cdot (\sin\alpha + \sin\beta)}{\lambda}\right)} \right]^2 \tag{4.18}$$

The theoretical efficiency curve of the diffraction grating is narrower for large blaze angles, of the order of 60°, corresponding to echelle gratings. The efficiency value for the optimum order decreases rapidly for one order higher or lower. This is shown in the example of Fig. 4.22, in which the blaze angle is 62°. This curve, obtained for the IR-I spectrograph grating and evaluated at 8500 Å, shows how for an order higher or lower than the optimum one, the value of the efficiency is much lower. This effect difficults the instrument calculation and optimisation for the multi-wavelength capability. As well as the list of requirements, other considerations have also been taken into account as obtaining the highest efficiency possible for all the spectral range and avoiding the wavelengths overlapping at the spectrograph image focal plane in order to allow the observation of each wavelength in a different detector. In those cases in which two wavelengths were too close to each other it has not been possible to vary the diffraction order. This has implied a hard calculation restriction.

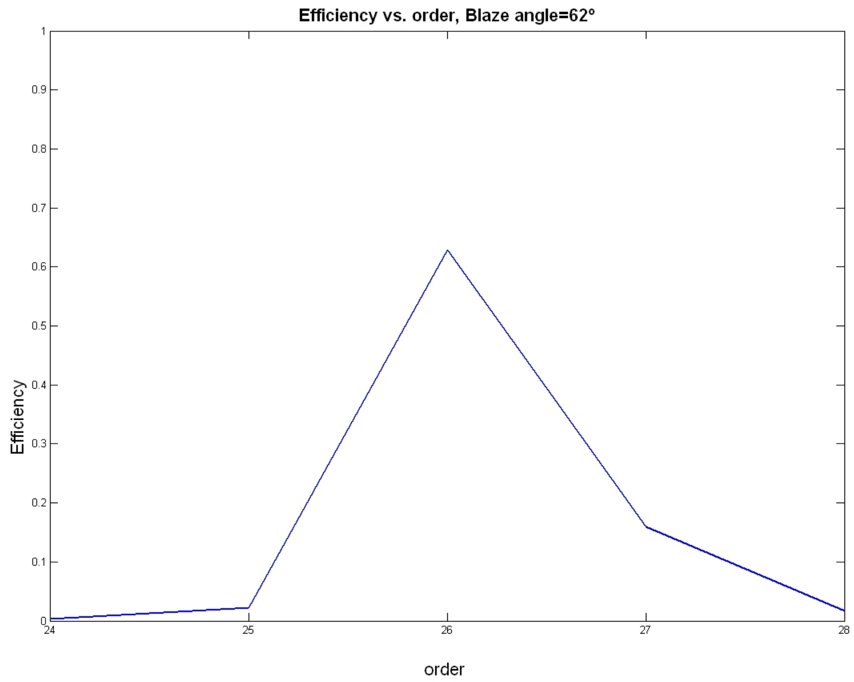

Figure 4.22: Grating efficiency curve versus diffraction order for the IR-I spectrograph grating, whose main characteristics are: 79 grooves/mm and a blaze angle equal to 62°, evaluated at 8500 Å. The curve shows how, for an order larger or smaller than the optimum one for that wavelength, the value of the efficiency is much lower.

4.3 Predisperser and Spectrograph Coupling

Predispersers and spectrographs are F/40 systems perfectly coupled to each other. There is no loss of light in their coupling. Predisperser and spectrograph are coupled by the predisperser mask, placed at the predisperser image focal plane, which is also the spectrograph object focal plane.

An example of the coupling between the predisperser and the spectrograph for the IR-I spectral range is shown in Fig. 4.23. This figure presents the ZEMAX optical design for the simultaneous observation of two wavelengths, 8542 Å and 15650 Å. At the spectrograph image focal plane the images of the 8 entrance slits are obtained for each wavelength that would be observed in two different detectors. The designs of the other spectrographs are conceptually identical. The layouts of the 4 systems are presented in Fig. 4.24.

The coupling, in each case, has been designed trying to satisfy the technical requirements. The optical quality offered by the designs, for the different combinations of wavelengths is diffraction limited. As examples of this, Figs. 4.25 and 4.27 show the optical designs of a visible (VIS-I) and an infrared (IR-II) systems and Figs. 4.26 and 4.28 present their spot diagrams. The VIS-I layout is evaluated at 3933 Å.

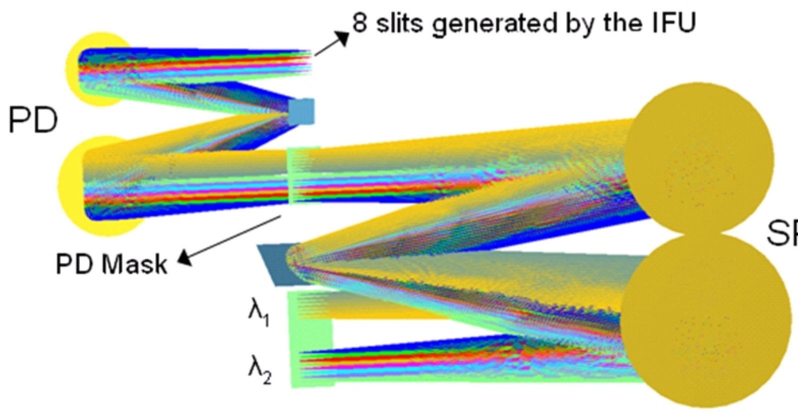

Figure 4.23: Optical design of the coupling between the IR-I predisperser and spectrograph, evaluated for two simultaneous wavelengths, 8542 Å and 15650 Å. The eight slits generated by the integral field unit represent the entrance of the predisperser (PD). At the predisperser image focal plane the mask selects the wavelengths that illuminate the spectrograph (SP) at the appropriate diffraction order. At the spectrograph image focal plane the images of the eight entrance slits are obtained for each wavelength, which would be observed in two different detectors.

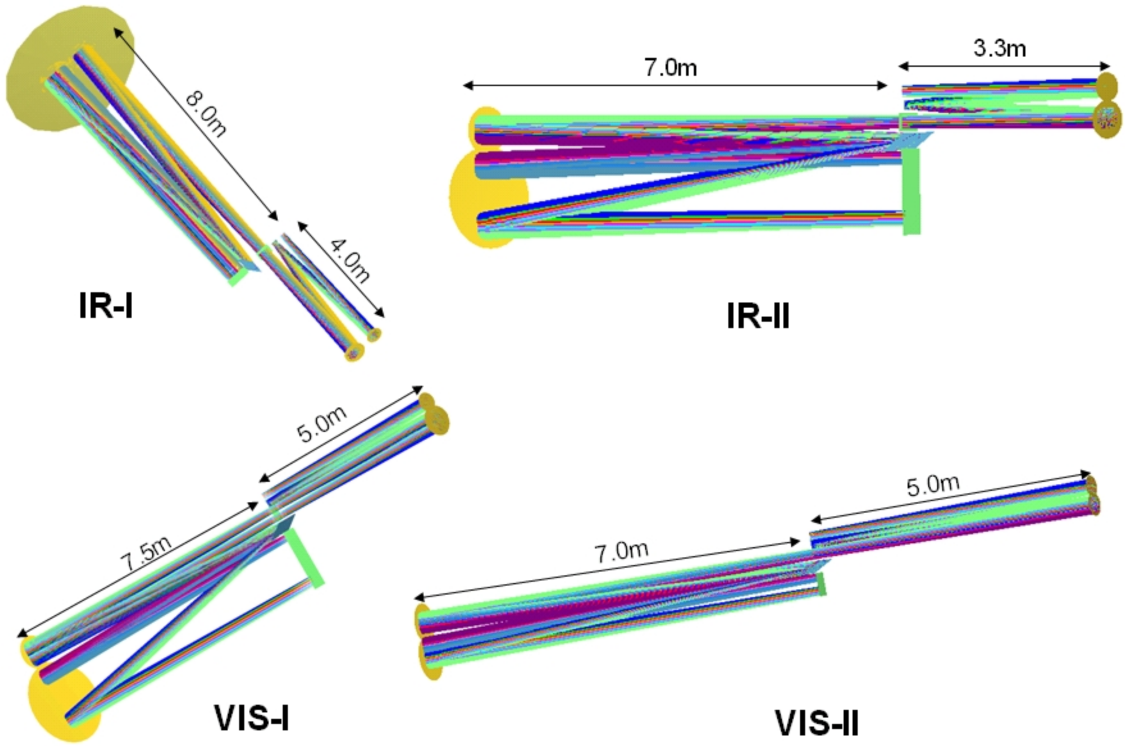

Figure 4.24: Optical designs of the four systems composed by predisperser and spectrograph. The big parabolic surface presented in some of the designs are the global parabolas. They have been added to show that collimator and camera mirrors are two sub-apertures of the global parabolic mirror.

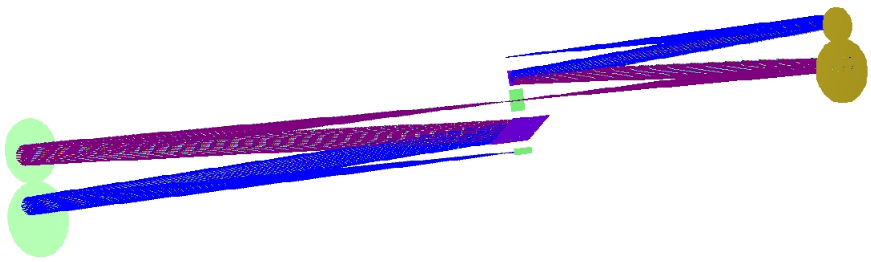

Figure 4.25: VIS-I predisperser and spectrograph coupling.

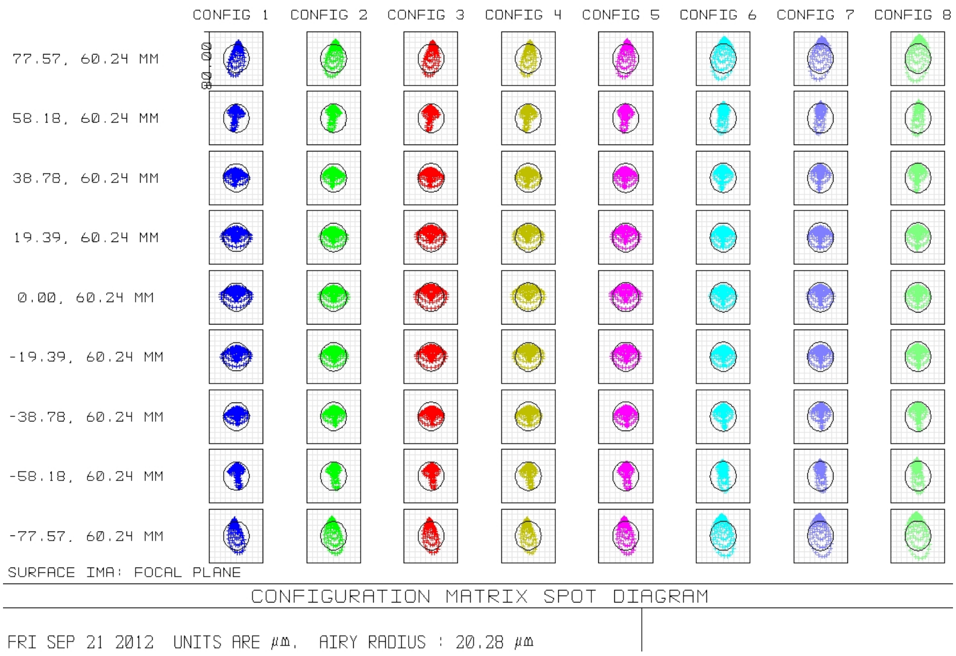

Figure 4.26: Spot diagram near the diffraction limit of the VIS-I predisperser and spectrograph coupling evaluated at 3933 Å.

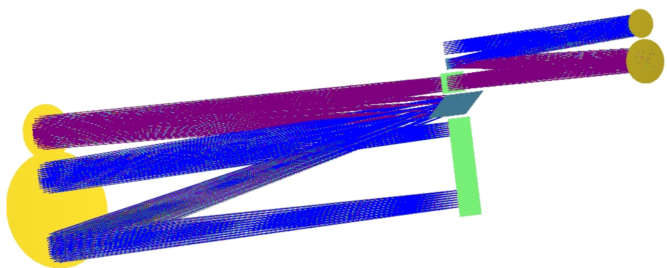

Figure 4.27: ZEMAX optical design of the IR-II system composed by predisperser and spectrograph. The design is evaluated for two simultaneous wavelengths, 10830 Å and 22300 Å.

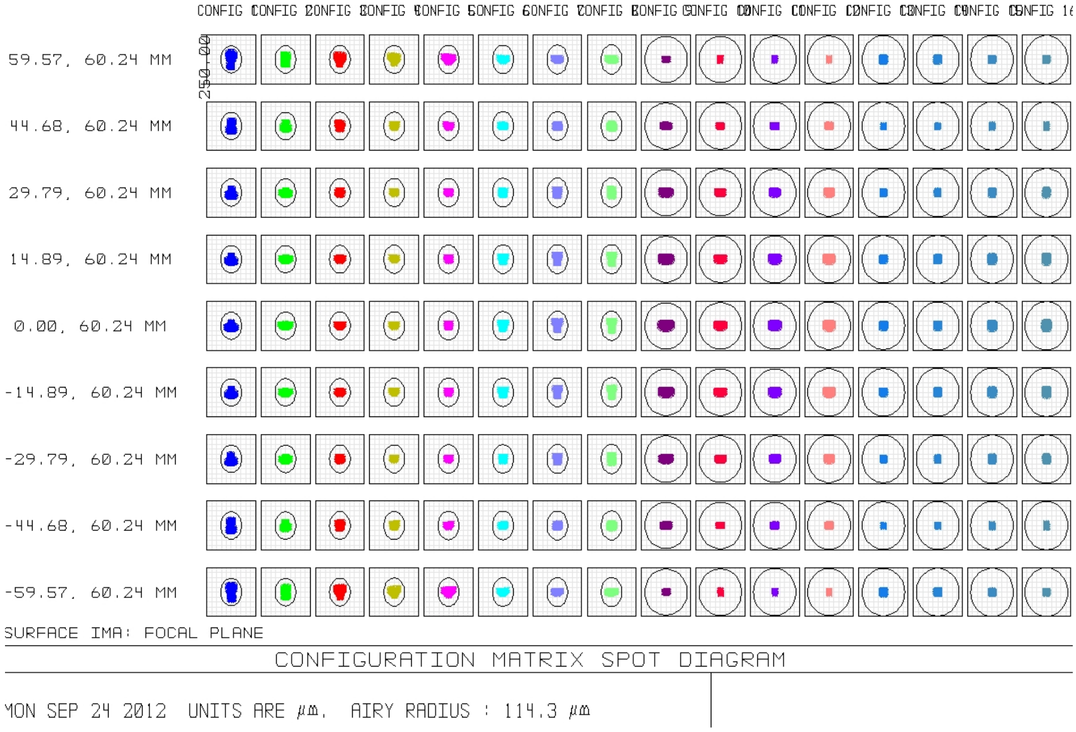

Figure 4.28: Spot diagram of the IR-II coupling between predisperser and spectrograph, evaluated for two wavelengths simultaneously. The first eight columns correspond to the image of the eight entrance slits at 10830 Å, while the others are evaluated at 22300 Å. For all of them, the rays are contained within the Airy disk, presenting an optical quality at diffraction limit. In addition these spots show how, the larger the wavelength, the bigger the Airy disk.

4.4 Reimaging System

In order to have the appropriate scale on the detector, a focal-ratio conversion, from the spectrograph F/40 to F/10.3 for the visible wavelengths and F/20.6 for the near-infrared ones, is needed. This is done using a reimaging system per wavelength before the detectors. Thus, eight reimaging systems are needed. The magnification of the reimaging systems is 0.2575 for VIS-I and VIS-II and 0.515 for IR-I and IR-II.

Because of the size of the beam (eight slits of 200 arcseconds length) reflective solutions have been considered. Commercial lenses are not big enough. In addition, lenses have chromatic problems. Although it can be solved using achromatic systems, the mirrors focal lengths do not have wavelength dependence. So each designed solution for the reflective reimaging system is versatile enough to be used for different wavelengths within the same spectral division.

For the design of the reimaging systems, several options have been studied using ZEMAX. Once a merit function (a function that measures the agreement between the data and the used fitting model according to the parameters and the specific design conditions) has been defined for all the configurations, an optimisation process varying the conic surface conditioned by the optical quality result, was performed. Different options were valid under

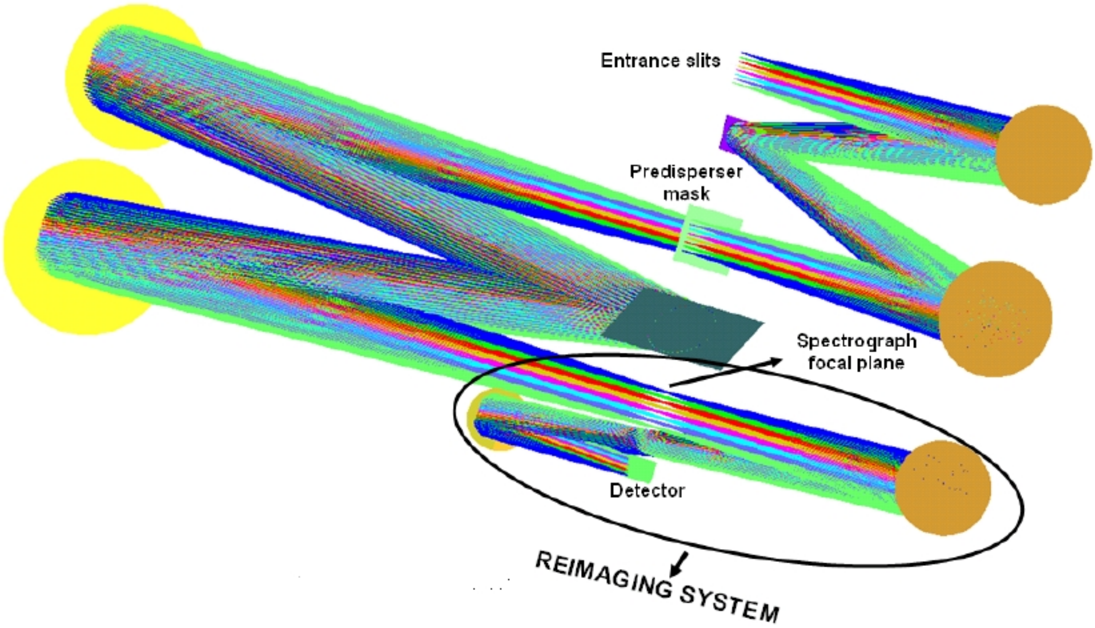

Figure 4.29: Optical design of the IR-I coupling between predisperser, spectrograph and reimaging system, at 8662 Å.

this criterion. For the infrared systems, two surfaces were considered, working as collimator and camera. In the case of the visible systems, the studied cases using two surfaces did not offer an optical quality as good as using four. The best alternative is using a system similar than the infrared one, twice. The demagnification is then done in two stages, each one with one half of the final demagnification. The change is then softer, what minimizes the aberrations leading to better optical performances. Some of these studied combinations of concave surfaces for the IR-I spectrograph are presented in Fig. 4.30, where K_1 is the collimator mirror conic constant and K_2 that of the camera mirror.

An example of the coupling of predisperser, spectrograph and reimaging system (this last one at the spectrograph image focal plane), for IR-I at 8662 Å is shown in Fig. 4.29.

After the reimaging system and before each detector an interferential filter is used to avoid the contribution of other wavelengths that, for specific orders, coincide with the ones of interest.

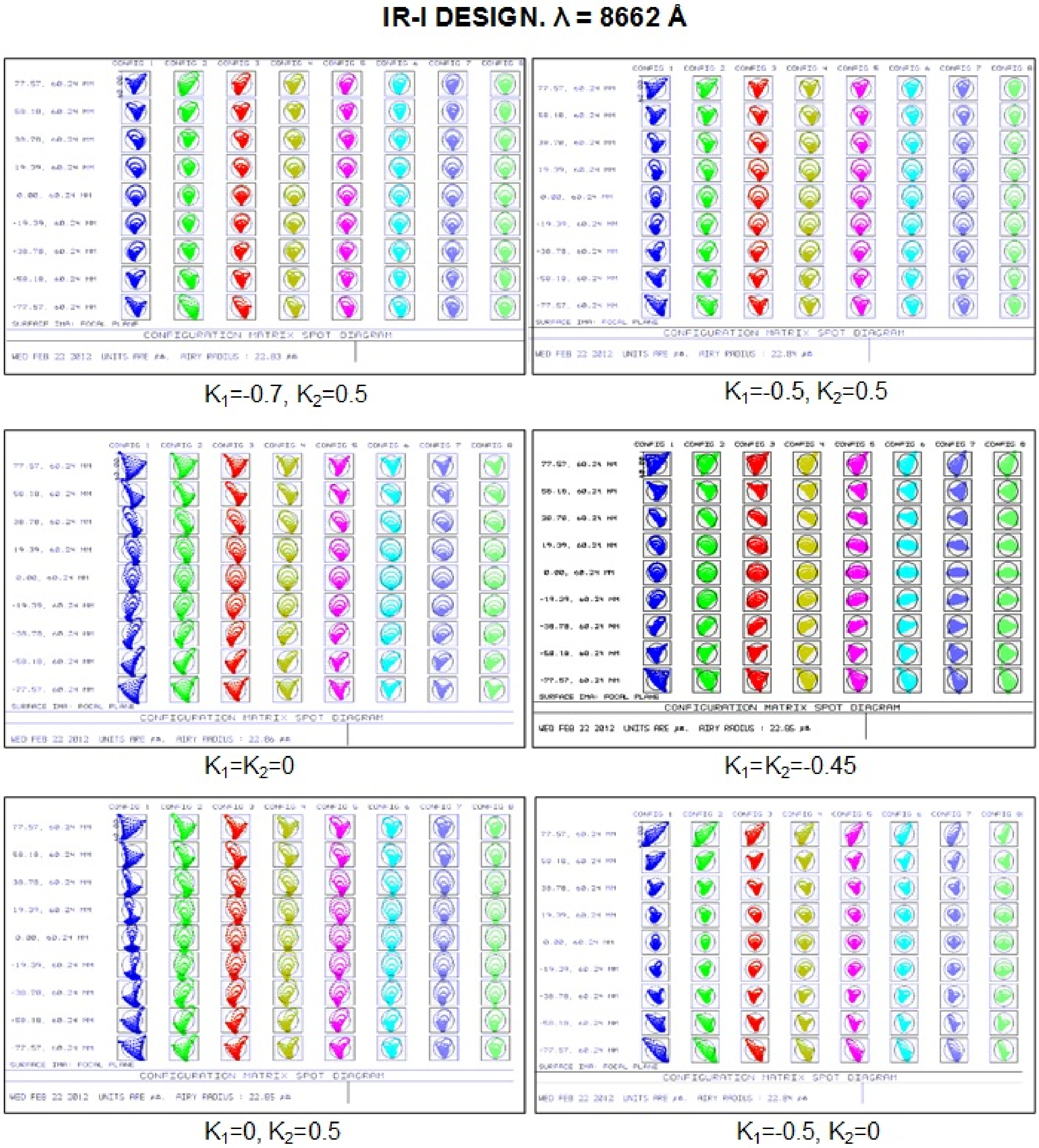

Figure 4.30: Mosaic of different solutions for the IR-I reimaging system at 8662 Å obtained after an optimisation process using ZEMAX. Although these examples present a spot diagram close to the Airy disk, the best obtained solutions correspond to the conic constant combinations: -0.7, 0.5 and -0.5, 0.5, for collimator (K_1) and camera (K_2) mirrors, respectively. The demagnification is 0.515.

5

Final Design Performance

This chapter presents the instrument final design performance.

5.1 Design studies and Optical quality

5.1.1 Optical quality interpretation

In paraxial optics, the image of a point is another point. In real optical systems that image is a spot, whose size increases with aberrations.

There are two types of aberrations, chromatic and monochromatic. The chromatic ones are due to the index of refraction dependence on wavelength. Since the proposed instrument has been designed as a completely reflective system, this kind of aberration does not appear. Nevertheless, mirrors, except for flat ones, also suffer the effects of monochromatic aberrations. This type of aberrations is presented as the difference between the third order theory, in which the two first terms of the Taylor's sinus development are included, and the paraxial approximation that only considers rays close to the optical axis. Aberrations like: spherical, coma or astigmatism deteriorate the image, while others like field curvature or distortion deform it.

Some reasons for the presence of aberrations in an optical system are the off-axis distances, for example the off-axis incidence of rays with large angles because of the object size. Another reason is an abrupt change in the focal-ratio, for example using optical elements with large apertures and small focal lengths.

The optical quality study shows the size of the image obtained through the system and how good the design is. This is evaluated with the spot diagram, which can be obtained using an optical ray tracing software, as ZEMAX. The footprint is a cut in any of the planes of the layout selected by the designer. To obtain the final optical quality, the footprint is got at the image focal plane. It presents the incidence of the rays in that plane. The design of this spectrograph, including its subsystems, has been done as a multi-configuration file using the ZEMAX sequential mode. Eight configurations have been defined for each wavelength. For every configuration nine pairs of field points (x-field, y-field) are used to define the slit. The total number of configurations is the number of slits, eight, multiplied by the number of wavelengths that are evaluated together. Thus, in the spot diagrams, each column represents a slit and each group of eight slits are associated to the same wavelength. The spot is given for every field point of the configuration.

The Airy disk is also shown in the spot diagram, to have a reference of how far, or close to, the optical quality is with respect to the diffraction limit. If the design of the system is well compensated the existing aberrations are contained within the Airy disk. In that case they do not affect the final optical quality and the system does not limit the optical performance. This is the case of the design of this instrument, even considering that the object is, in this case, eight slits of 200 arcsec length.

The optical design and optical quality have been studied for all the combinations of wavelengths associated to the science programmes of Table 1.1 (Calcines, 2011a). The results are presented below. Although the requirement in optical quality (EST Science Group, 2011) is not the diffraction limit, the proposed designs present spot diagrams limited by diffraction or near the Airy disk.

5.1.2 Optical designs and spot diagrams of the main science programmes

1. Flux tube programme:

   The wavelength intervals for this programme are centred around: 5177 Å, 5250 Å and 6302 Å for the visible spectral range, and 8542 Å, 10829 Å, 15260 Å and 15650 Å for NIR.

   The distribution of these wavelength intervals in the four spectrographs is: 5177 Å and 5250 Å are observed with VIS-I; 6302 Å with VIS-II; 8542 Å, 15260 Å and 15650 Å with IR-I and 10829 Å with IR-II.

   The layout of the VIS-I spectrograph is presented in Fig. 5.1.

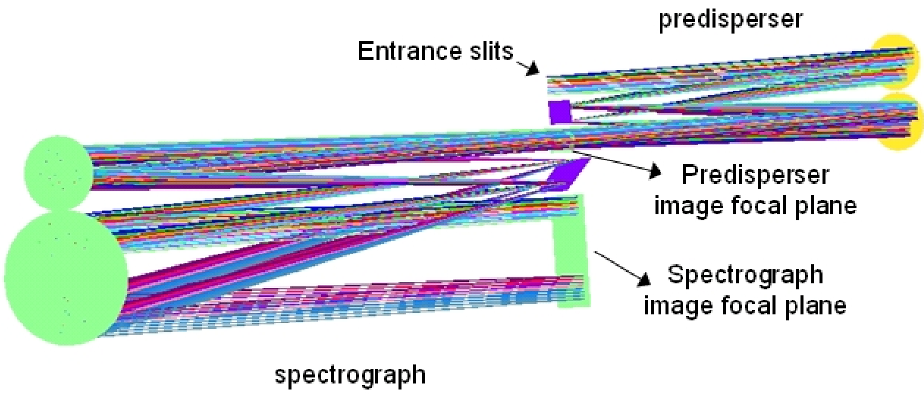

Figure 5.1: ZEMAX optical design of 5177 Å and 5250 Å evaluated for the VIS-I spectrograph.

   The spot diagram of this design, which does not include the reimaging system, is presented in Fig. 5.2, showing a diffraction limited optical quality.

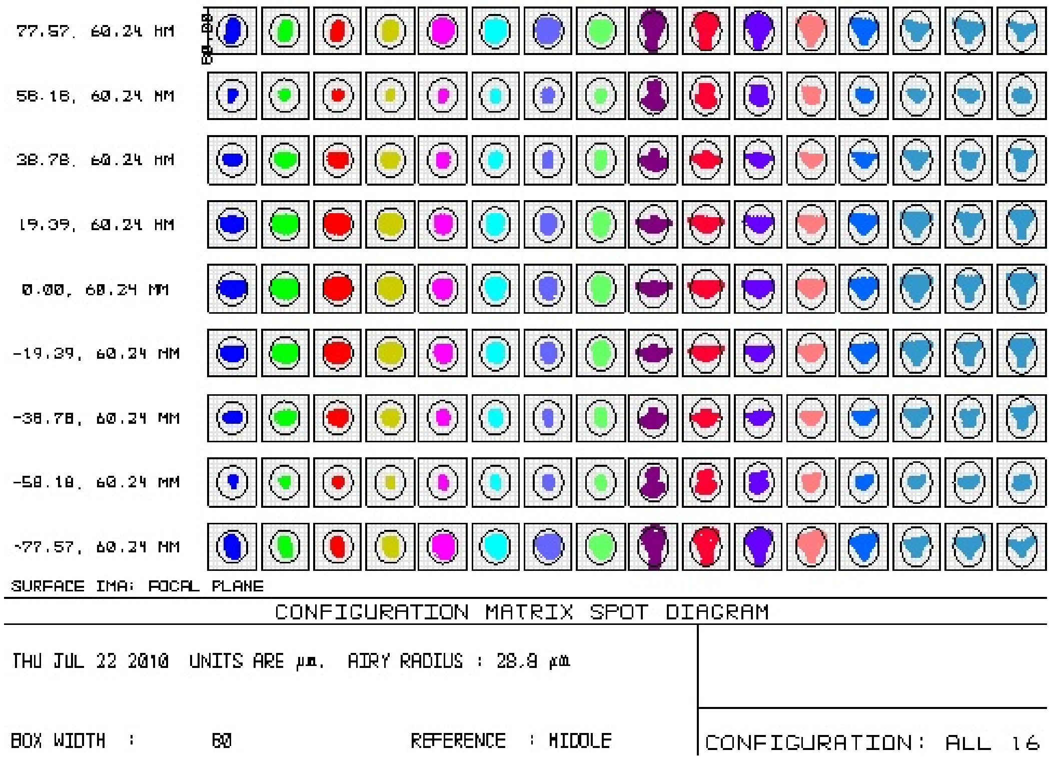

Figure 5.2: Multi-configuration spot diagram associated to the design of Fig. 5.1 and evaluated at 5177 Å and 5250 Å with the VIS-I spectrograph. Each column represents a slit of 200 arcsec length and each group of eight slits corresponds to a wavelength. The rays are contained within the Airy disk, showing very good optical quality at diffraction limit.

The VIS-II spectrograph is evaluated at 6302 Å. The design and spot diagram are presented in Figs. 5.3 and 5.4, respectively.

The spectral lines Ca II 8542 Å, Mn I 15260 Å and Fe I 15650 Å are observed simultaneously with the IR-I spectrograph. Its design (Fig. 5.5) shows a larger separation between the wavelengths in the camera mirror and at the image focal plane compared with the previous designs, however its optical quality continues being diffraction limited, as shown in Fig. 5.6. The largest separation belongs to the wavelength 15260 Å. The simultaneous observation of 8542 Å, 15260 Å and 15650 Å implies a camera mirror of 2.10 m diameter, that is too big. If 15260 Å is observed sequentially, this diameter decreases to 660 mm and the optical quality continues being diffraction limited. The design of 8542 Å and 15650 Å is presented in Fig. 5.7. The diameter of the camera mirrors can be compared in the footprints of Fig. 5.8.

The spectral lines Si I 10827 Å and the He I triplet 10830 Å are observed together with the IR-II spectrograph, using the same detector. For their evaluation, the average wavelength, ∼10828 Å has been considered. The ZEMAX optical design is presented in Fig. 5.9, while its optical quality is shown in Fig. 5.10.

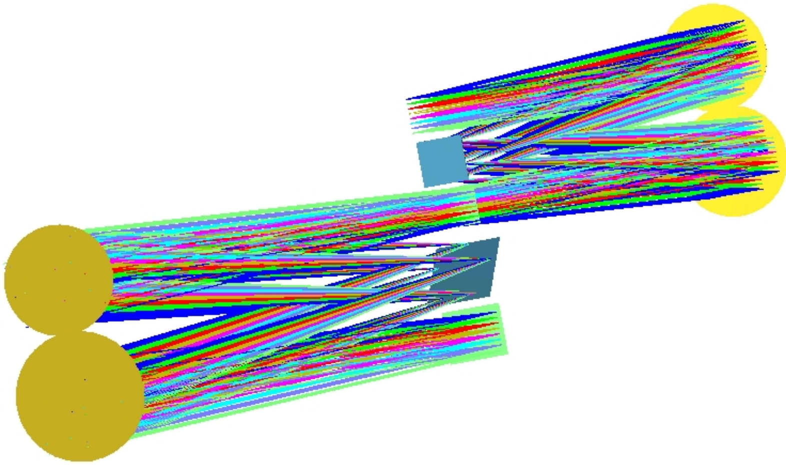

Figure 5.3: Layout of the VIS-II spectrograph for 6302 Å.

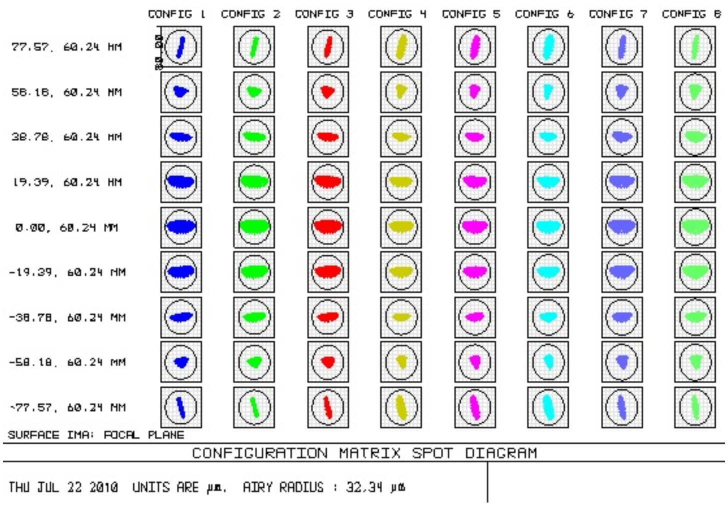

Figure 5.4: Spot diagram matrix of the VIS-II spectrograph evaluated at 6302 Å. All the rays are perfectly contained within the Airy disk.

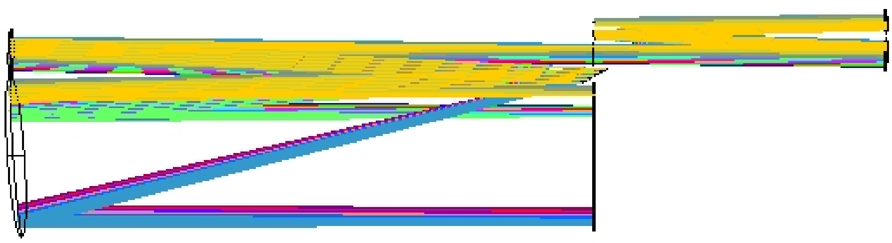

Figure 5.5: ZEMAX layout for 8542 Å, 15260 Å and 15650 Å evaluated with the IR-I spectrograph.

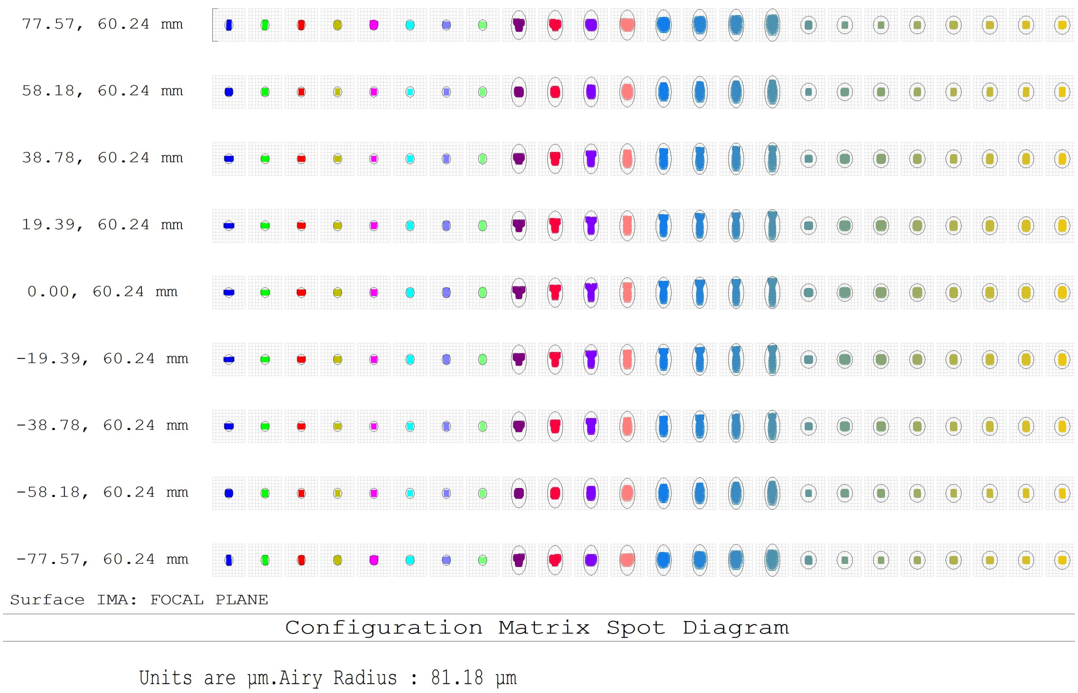

Figure 5.6: Spot diagram of the design of Fig. 5.5 for 8542 Å, 15260 Å and 15650 Å. Even with such a separation between the evaluated wavelengths at the spectrograph image focal plane, the system is perfectly compensated, showing a spot diagram matrix with the rays within the airy disk in all cases.

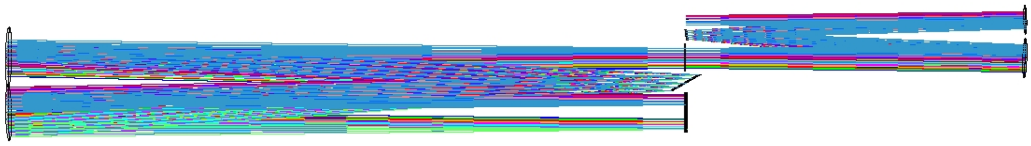

Figure 5.7: ZEMAX layout of the IR-I spectrograph at 8542 Å and 15650 Å. The size of the spectrograph image focal plane is clearly reduced if this design is compared with that of Fig. 5.5.

2. Network elements programme:

   The wavelengths observed in the network elements programme are Fe I 5576 Å with VIS-I, Fe I 6301.5 Å and 6302.5 Åwith VIS-II and Fe I 15650 Å with the IR-I spectrograph.

   The optical design of the VIS-I spectrograph evaluated at 5576 Å is presented in Fig. 5.11.

   When only one wavelength is observed it is easier to get a good optical quality, since the grating can be rotated to place the image close to the optical axis. The spot diagram of Fig. 5.12 shows how, for all the fields, the rays are contained within the Airy disk.

   As in the last science programme, the spectral lines observed together with the VIS-II spectrograph are 6301 Å and 6302 Å. The layout and optical quality result are already

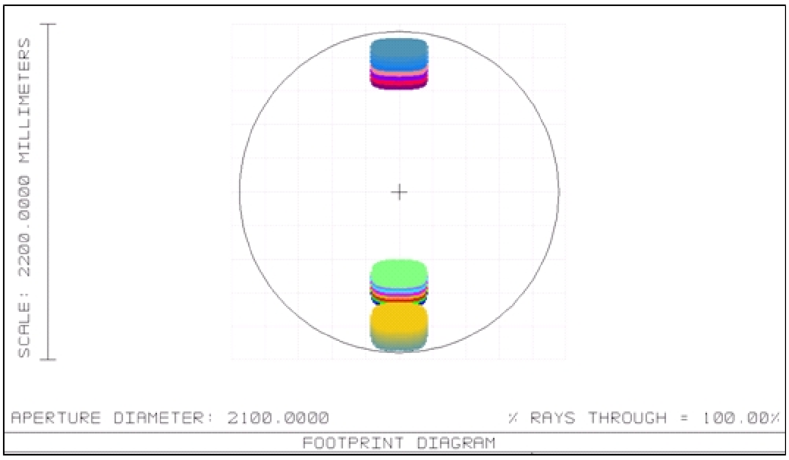

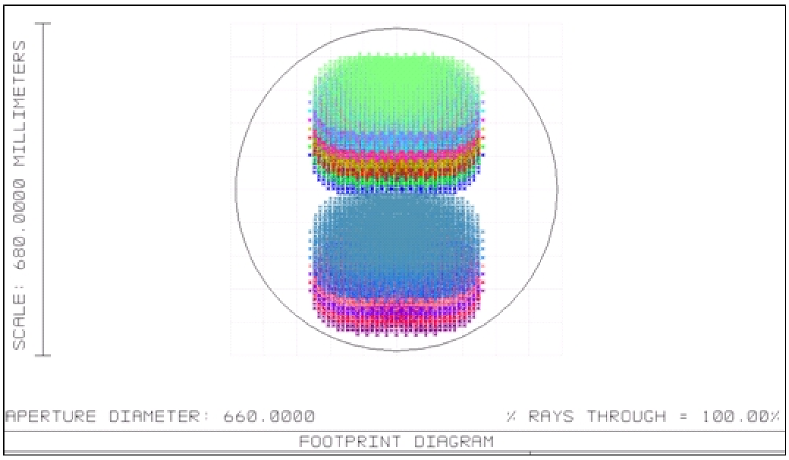

Figure 5.8: Footprints of the camera mirror diameter for the studied cases. On the top, the observation of 8542 Å, 15260 Å and 15650 Å together using a commercial diffraction grating requires a camera size of 2.10 m. At the bottom, the camera diameter is reduced to 660 mm if only 8542 Å and 15650 Å are observed together and 15260 Å is observed sequentially.

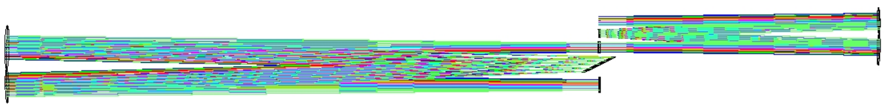

Figure 5.9: Optical design of the IR-II spectrograph for 10828 Å.

presented in Figs. 5.3 and 5.4.

The visible wavelengths required in the network elements programme, 5576 Å and 6302 Å, were firstly evaluated together with the VIS-I spectrograph and the optical performance was excellent, also diffraction limited. But, in order to optimise the optical quality of the flux tubes programme, the wavelength 6302 Å was finally evaluated with the VIS-II spectrograph, improving the aberrations. As the separations of the spectral ranges, done by the dichroics, have to be the same for all the programmes, this

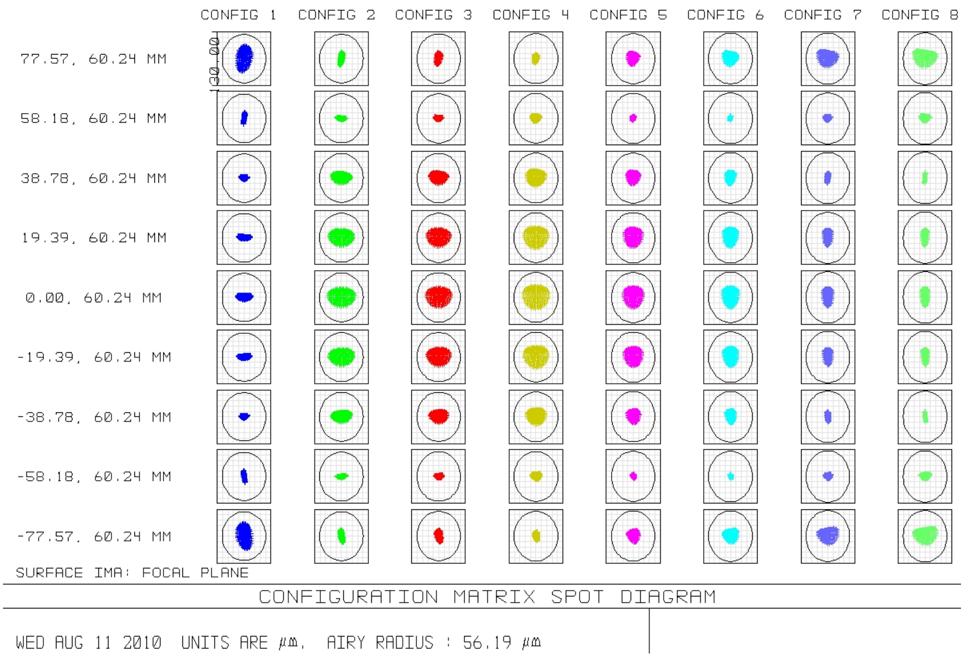

Figure 5.10: Spot diagram contained within the diffraction limit for 10828 Å.

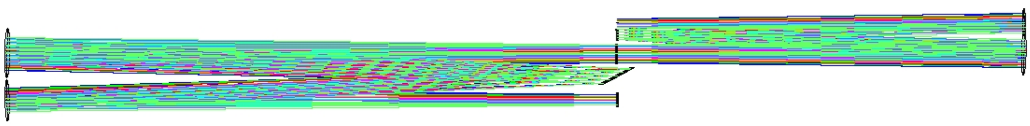

Figure 5.11: ZEMAX layout of the VIS-I spectrograph evaluated at 5576 Å.

wavelength has been finally studied in the VIS-II spectrograph for this programme too.

The wavelength 15650 Å is observed with the IR-I spectrograph for this programme, whose design is shown in Fig. 5.13. This design presents an excellent optical quality at diffraction limit (see Fig. 5.14).

3. Magnetic canopies programme:

   This programme requires a visible spectral line, Na I 5896 Å, observed with the VIS-II spectrograph, and 3 infrared spectral lines: Ca II 8498 Å, Ca II 8542 Å and Fe I 15650 Å, with the IR-I spectrograph. Figs. 5.15 and 5.17 show the optical designs and Figs. 5.16 and 5.18 the evaluation of their optical quality.

4. Hanle effect programme:

   The Hanle effect programme uses three spectrographs for the observation of Ca II 3933 Å and 3968 Å together with VIS-I, O I 7770 Å with VIS-II and Ca II 8542 Å with

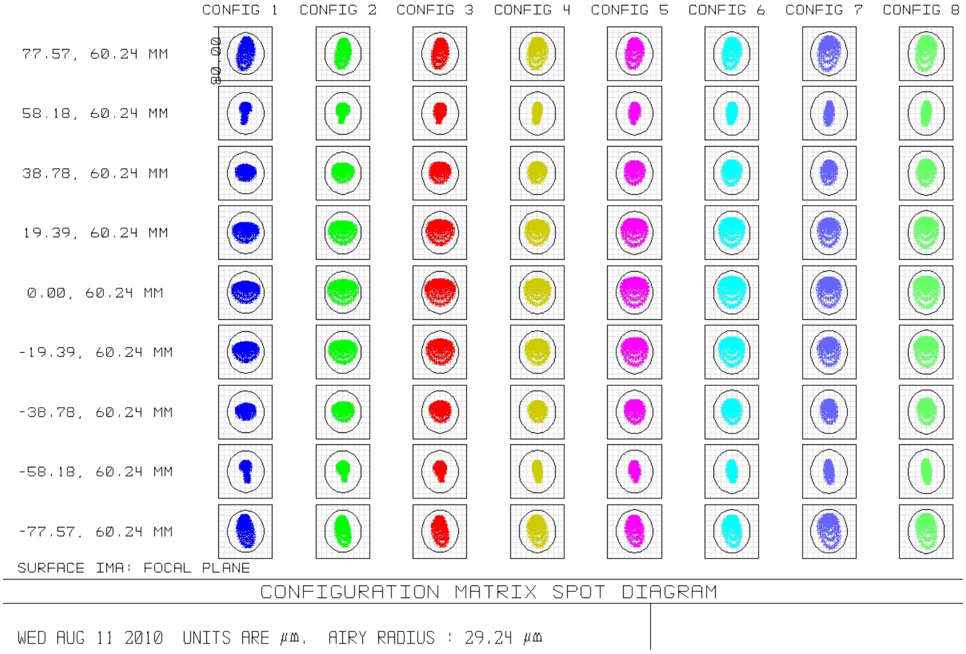

Figure 5.12: Spot diagram at diffraction limit of the VIS-I spectrograph at 5576 Å.

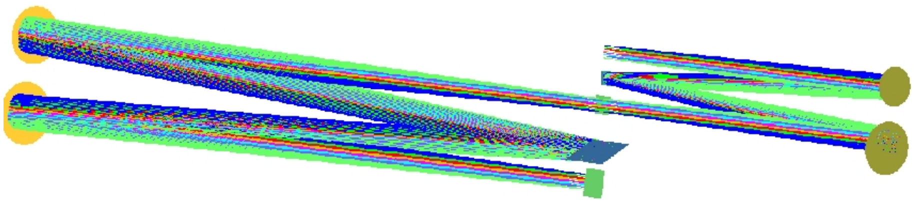

Figure 5.13: Optical design of the IR-I spectrograph for 15650 Å.

the IR-I spectrograph.

In the design of Fig. 5.19, corresponding to the VIS-I spectrograph at 3933 Å and 3968 Å, the spectrograph focal plane is pointed out. Two detectors, one per wavelength, are used in this case, where each one is used for the observation of the images of the eight input slits. The size corresponds to the spectrograph image focal plane without the reimaging systems. The optical quality of the design of Fig. 5.19 is presented in the spot diagram of Fig. 5.20.

In addition, the VIS-II spectrograph has been evaluated at 7770 Å. The layout and spot diagram are presented in Figs. 5.21 and 5.22, respectively.

The last wavelength for this science programme is 8542 Å, which is observed with the IR-I spectrograph (see Fig. 5.23). It also presents an optical quality limited by diffraction, as shown in Fig. 5.24.

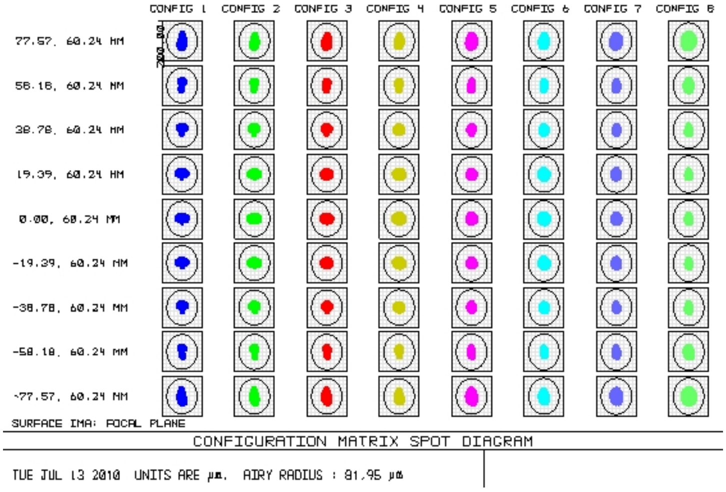

Figure 5.14: Diffraction limited spot diagram of the IR-I spectrograph evaluated at 15650 Å for the network elements science program.

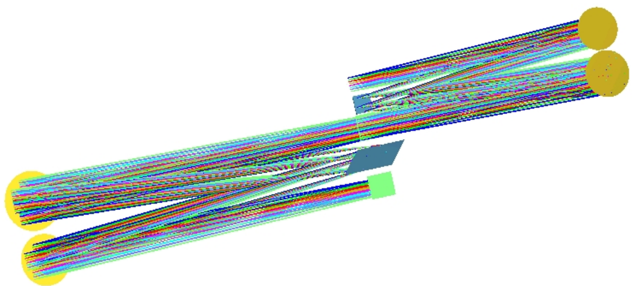

Figure 5.15: Layout of the VIS-II spectrograph for 5896 Å.

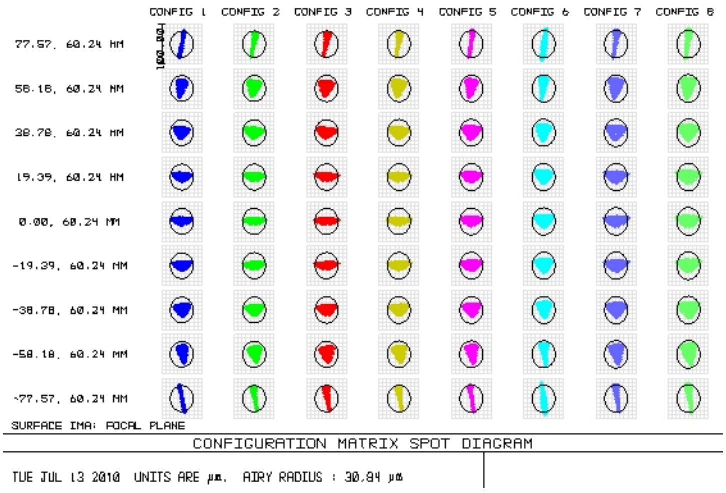

Figure 5.16: Spot diagram of the VIS-II spectrograph at 5896 Å, associated to the magnetic canopies science programme.

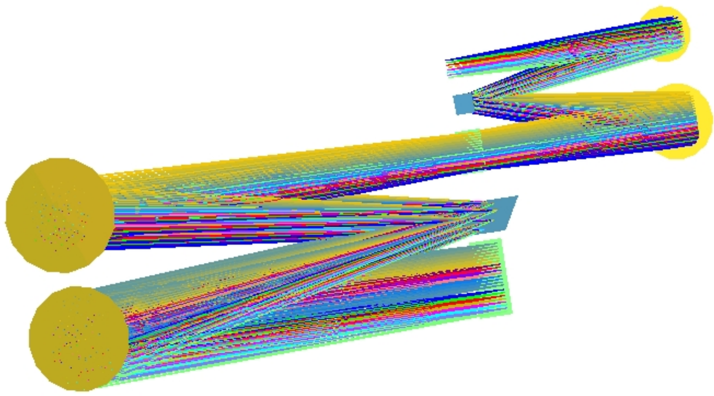

Figure 5.17: Optical design of the IR-I spectrograph evaluated at 8498 Å, 8542 Å and 15650 Å for the magnetic canopies science programme.

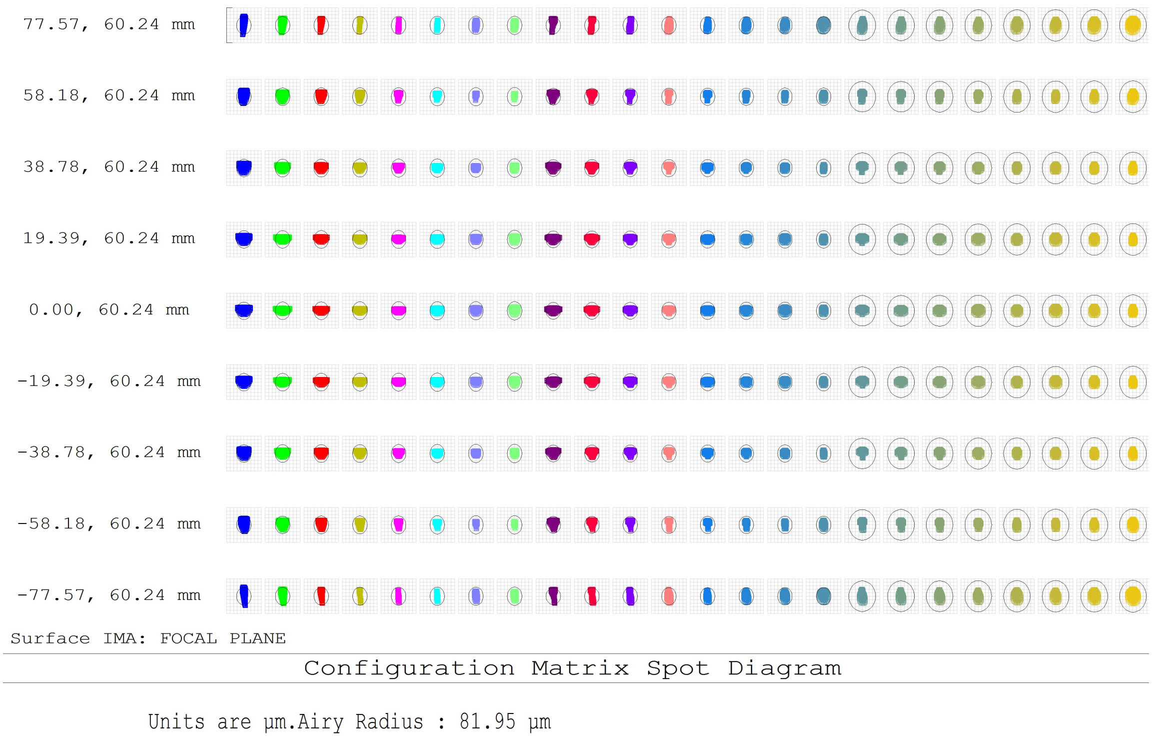

Figure 5.18: Spot diagram matrix for the evaluation of the optical quality of the IR-I spectrograph at 8498 Å, 8542 Å and 15650 Å.

5. Flares programme:

   The next programme presents a combination of seven spectral lines, distributed on the following way: Ca II 3933 Å, Ca II 3968 Å, observed simultaneously with VIS-I and Hδ 4102 Å, also observed with VIS-I but sequentially, in order to improve the optical

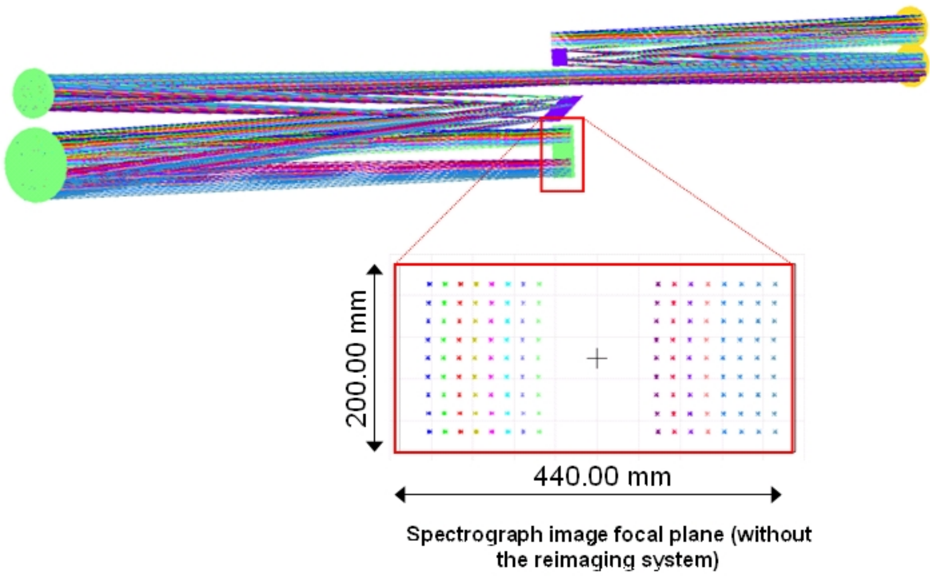

Figure 5.19: ZEMAX optical design of the VIS-I spectrograph for 3933 Å and 3968 Å. Two detectors are used in this case, one per wavelength. Each one is used for the observation of the images of the eight input slits. The spectrograph image focal plane is pointed out, however this size does not consider the reimaging systems.

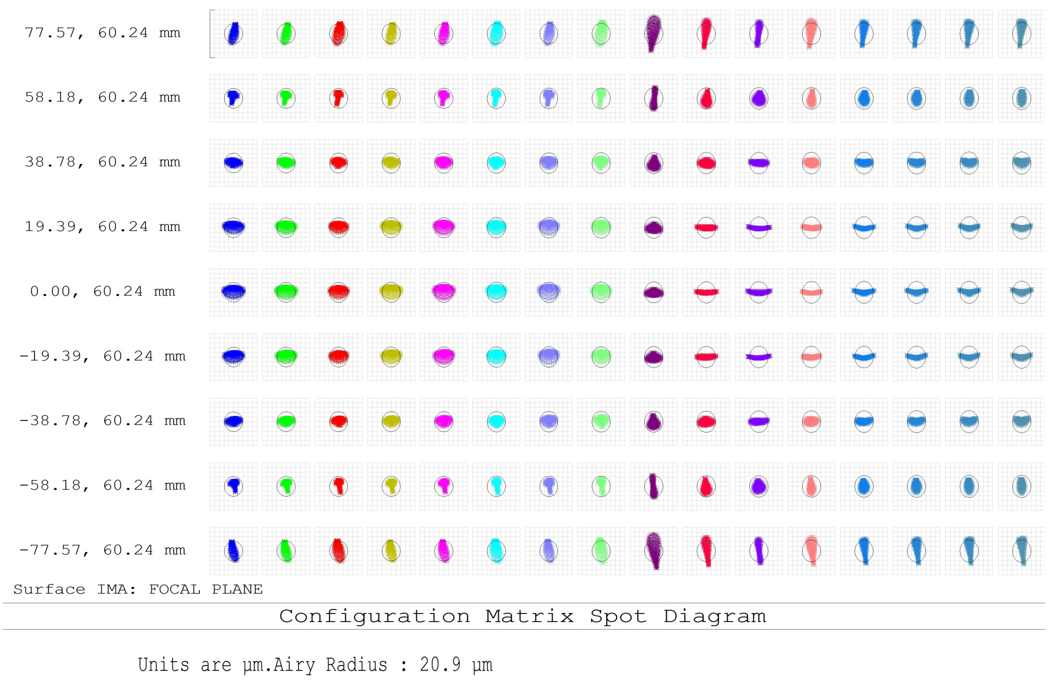

Figure 5.20: Configuration matrix spot diagram of the VIS-I spectrograph for 3933 Å and 3968 Å.

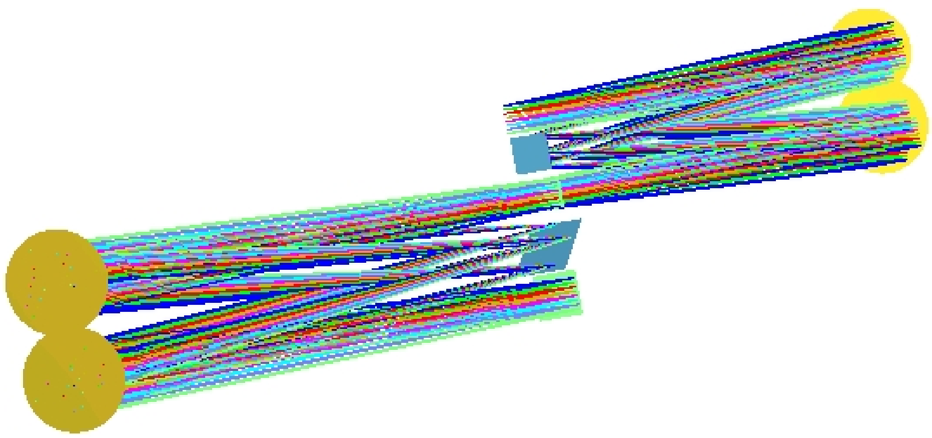

Figure 5.21: Optical design of the VIS-II spectrograph evaluated at 7770 Å for the Hanle effect science programme.

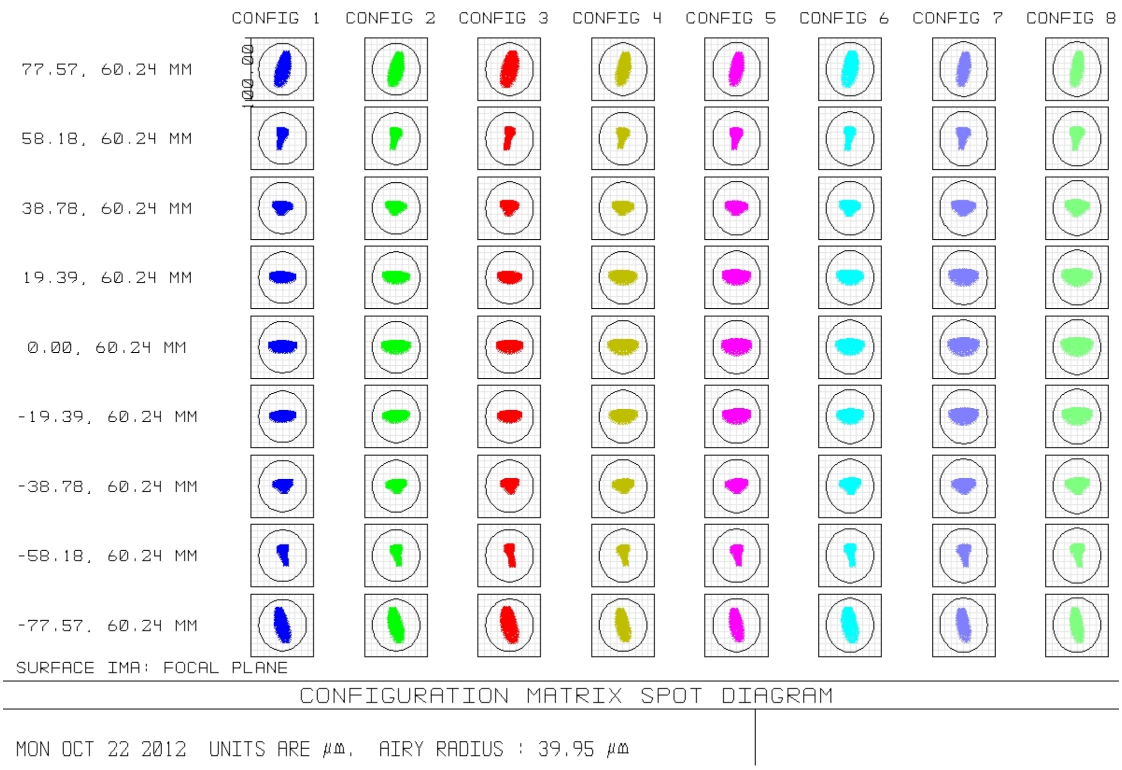

Figure 5.22: Spot diagram at diffraction limit associated to the design of Fig. 5.21.

quality. Hα 6563 Å with VIS-II, Ca II 8542 Å with IR-I and Si I 10827 Å with IR-II.

Some of these combinations have already been presented in previous designs like 3933 Å and 3968 Å with VIS-I (see Fig. 5.19). These two last wavelengths are observed together

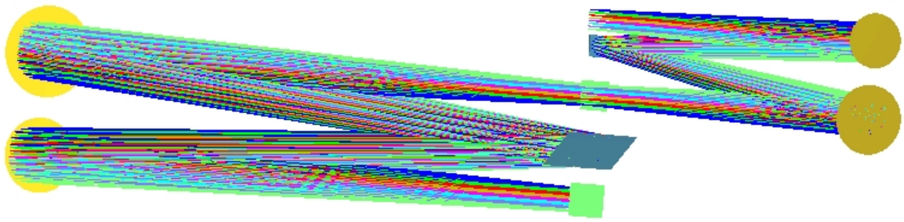

Figure 5.23: Layout of the IR-I spectrograph at 8542 Å.

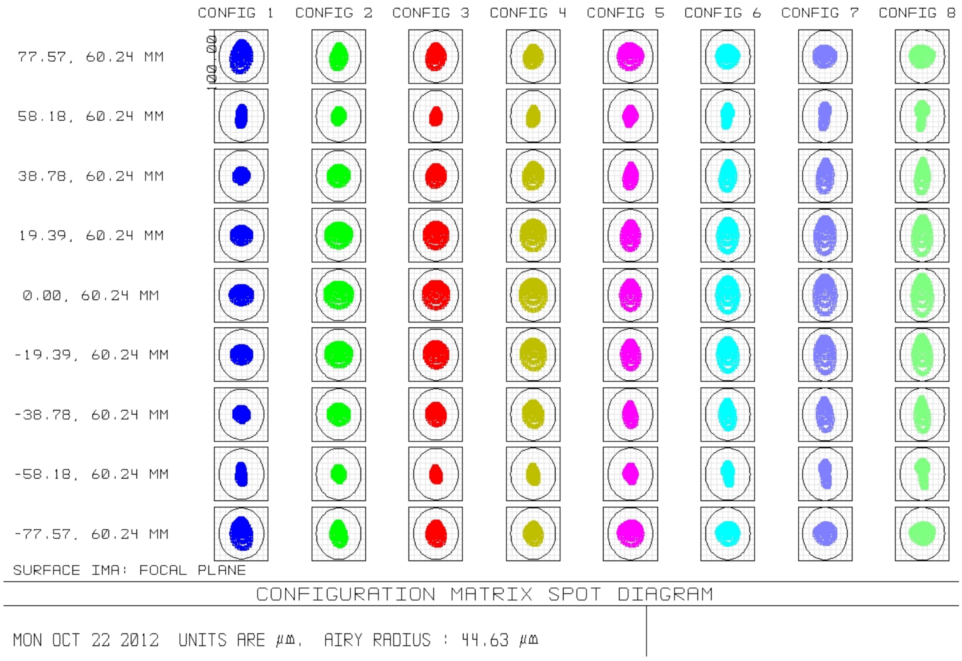

Figure 5.24: Spot diagram associated to the IR-I spectrograph evaluated at 8542 Å, whose ZEMAX design is shown in Fig. 5.23. The optical quality of this design is under the diffraction limit, with the rays contained within the Airy disk for all the defined fields.

in the same detector. 8542 Å was also studied for the Hanle effect (Fig. 5.23).

If 4102 Å were observed simultaneously with 3933 Å and 3968 Å, it would present such an off-axis distance that its optical quality would not be acceptable (see Fig. 5.25). In addition, when the three wavelengths are observed simultaneously, the spectrograph image focal plane increases up to 1.80 m, as well as the camera mirror diameter that also increases until 1.82 m (see Fig. 5.26). If this wavelength is observed sequentially (see the optical design of Fig. 5.27), its optical quality improves, as shown in Fig. 5.28.

The layout of the VIS-II spectrograph at Hα 6563 Å for the Flares science programme, as well as its optical quality, are presented in Figs. 5.29 and 5.30.

The results of the evaluation of Si I 10827 Å with the IR-II spectrograph are presented

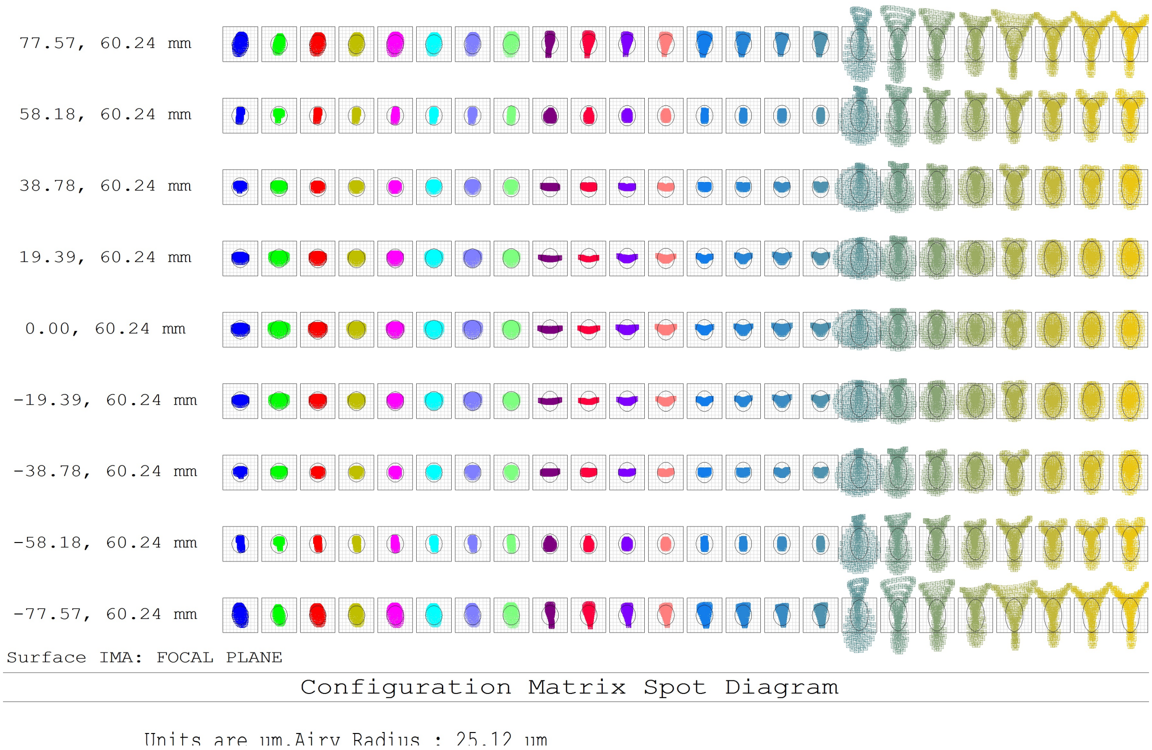

Figure 5.25: Spot diagram obtained for the simultaneous evaluation of 3933 Å, 3968 Å and 4102 Å with the VIS-I spectrograph. The separation of 4102 Å in its optical design with respect to the optical axis is translated into an increase of its aberrations, as shown in the eight columns on the right. Its optical quality is not acceptable for these nominal design, since once tolerances are included, the optical quality could be slightly deteriorated. In order to optimise its optical performances, this wavelength is proposed to be observed alone. 3933 Å and 3968 Å can be observed together keeping the optical quality presented in this spot diagram.

in the design of Fig. 5.31 and the spot diagram of Fig. 5.32.

6. Planets programme:

   The planets programme only requires visible wavelengths: Ca I 4227 Å, Na I 5890 Å, 5896 Å and K I 7699 Å and 7699 Å, where the first one is observed with VIS-I and the others with VIS-II.

   The design and spot diagram of 4227 Å are presented in Figs. 5.33 and 5.34, respectively.

   The rest of the required wavelengths are observed with the VIS-II spectrograph. The following combinations can be observed simultaneously: 5890 Å and 7665 Å, 5890 Å and 7699 Å, 5896 Å with 7665 Å and 5896 Å with 7699 Å. Fig. 5.35 shows the layout for 5890 Å and 7699 Å.

   The optical quality of the design of Fig. 5.35 is presented in Fig. 5.36. If 5890 Å were observed with 7665 Å instead of 7699 Å, the results would be those shown in Figs. 5.37

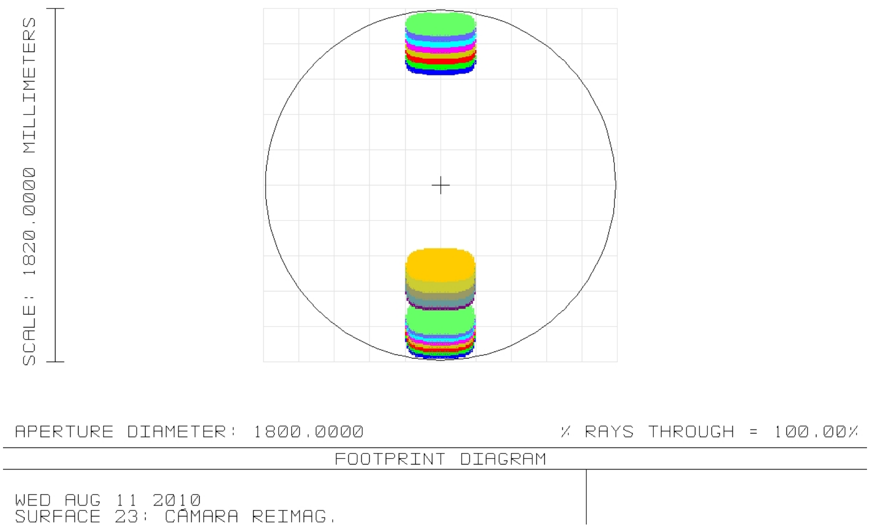

Figure 5.26: ZEMAX footprint of the VIS-I spectrograph camera mirror. If 3933 Å, 3968 Å and 4102 Å are to be observed simultaneously, the camera mirror, using the selected grating, requires a diameter of 1.82 m.

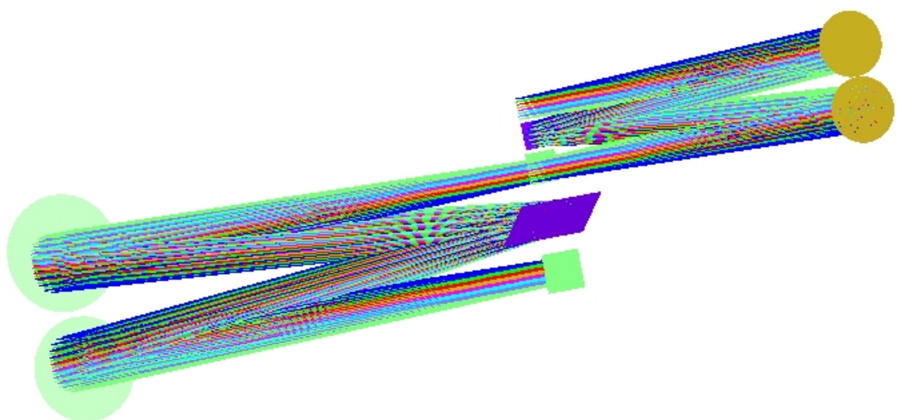

Figure 5.27: Layout of the VIS-I spectrograph for the sequential observation of 4102 Å.

and 5.38.

If 7665 Å and 7699 Å are to be observed together, they would not overlap at the spectrograph image focal plane but they would be too close to each other if the mounts of the detectors are considered, as shown in Fig. 5.39. The optical quality is presented in Fig. 5.40.

7. Sunspot programme:

   This science programme only requires the observation of Ti I 22300 Å. The optical design is shown in Fig. 5.41. The layout of the IR-II spectrograph offers an excellent optical quality with very compensated spots centred within the Airy disk (see Fig.

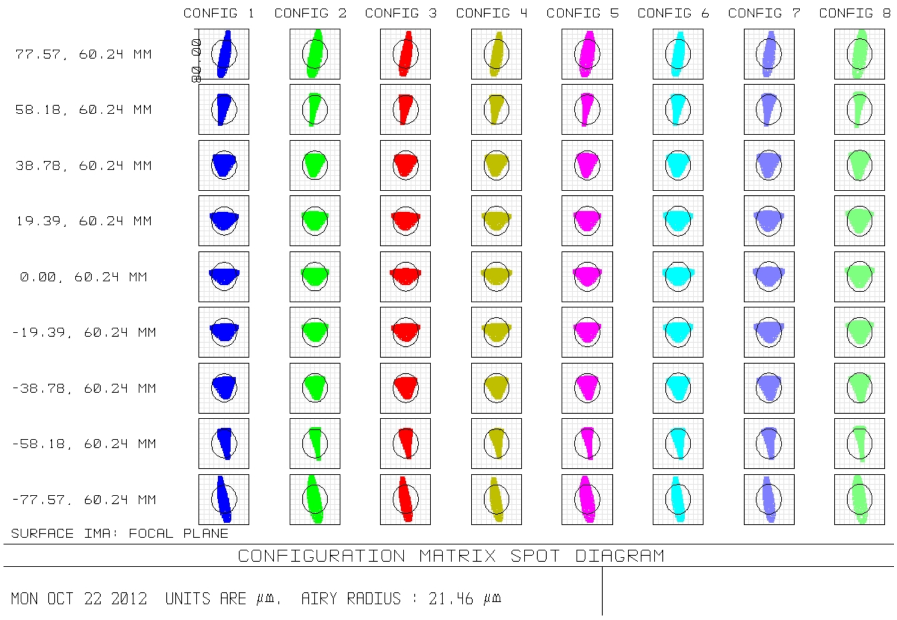

Figure 5.28: Spot diagram of the VIS-I spectrograph for the sequential observation of 4102 Å. The optical quality improves when this wavelength is observed sequentially, as can be seen if this figure is compared with Fig. 5.25.

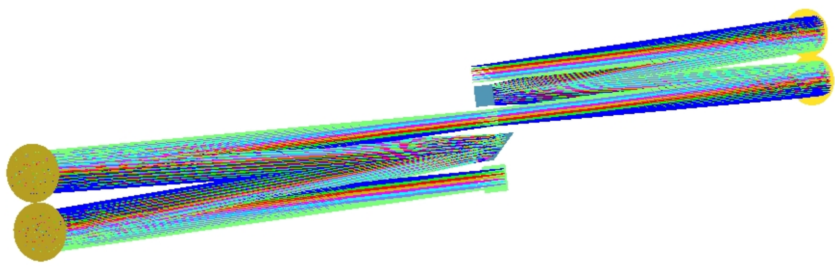

Figure 5.29: Layout of the VIS-II spectrograph, evaluated for 6563 Å for the Flares science programme.

5.42).

The optical designs, evaluated for the different combinations of wavelengths associated to the main science programmes considered for its optimisation, present an optical quality limited by diffraction. These results are much better than the requirement (0.1 arcseconds at 5000 Å) and, although the tolerances have not still been considered, there is a margin that guarantees that this requirement will be satisfied.

5.1.3 Study of off-axis distances

The nominal optical designs of the spectrographs are presented in the previous subsection, evaluated for the different science programmes. These nominal layouts present the minimum possible decentred distances with respect to the optical axis. However, larger decentred

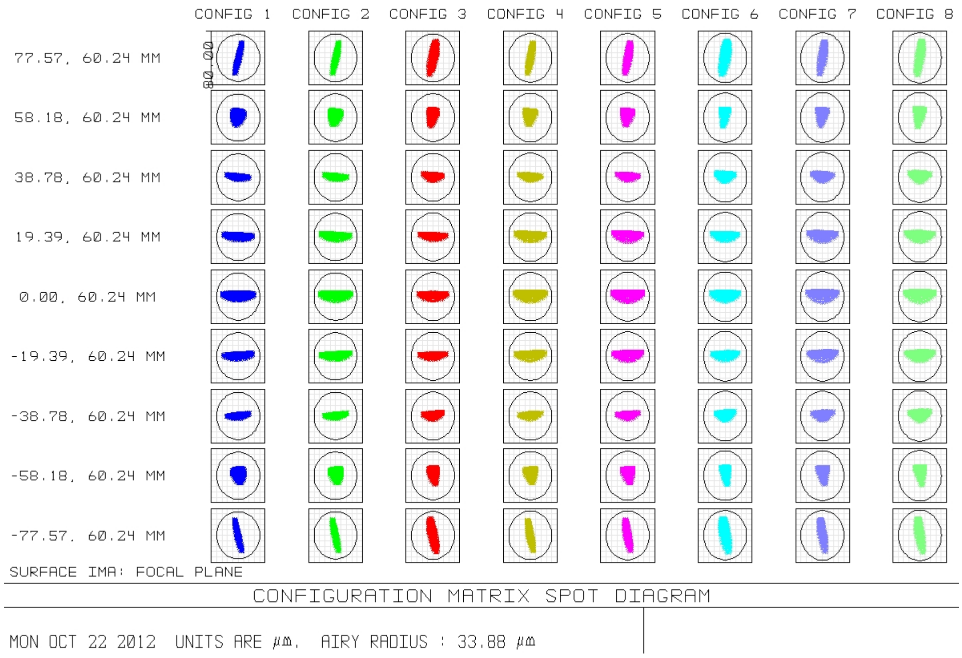

Figure 5.30: Spot diagram associated to the design of Fig. 5.29, for the observation of 6563 Å using the VIS-II spectrograph. The optical quality is at diffraction limit.

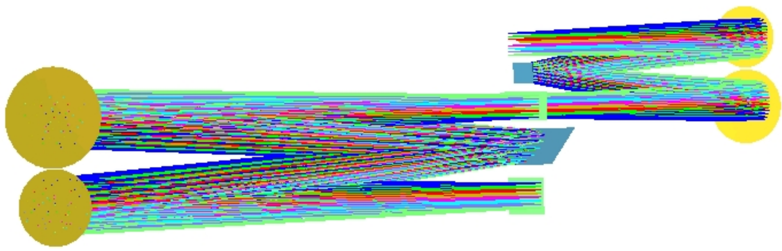

Figure 5.31: ZEMAX optical design of the IR-II spectrograph at Si I 10827 Å.

distances, taking into account the mechanical mountings of the different optical elements, have also been considered.

The considered margins have been defined from the mechanical point of view. For the spectrographs gratings, whose weight is of the order of 20-30 kg, the mounting has been estimated as 40 mm at each side. For the predisperser gratings, with a weight around 12 kg as maximum, the decentred distances have been increased by 20 mm at each side of the gratings. These figures have been summed up to the initial optical designs, in order to increase the separation between neighbouring surfaces or between some surfaces and the beam. The designs and optical quality have been reevaluated under these considerations for each combination of wavelengths. Even with these increases, the optical performances of the spectrographs are maintained, and the spot diagrams continue being diffraction limited. An example is shown in Fig. 5.43, which can be compared with Fig. 5.18. Both present the

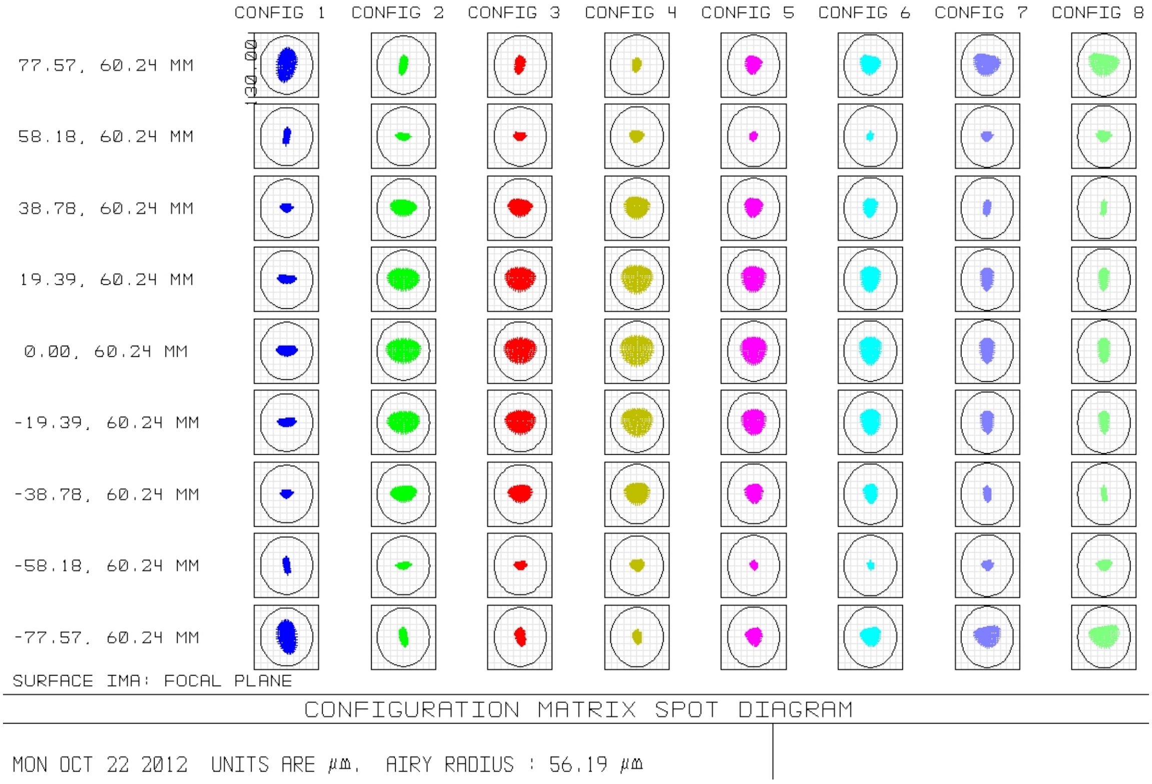

Figure 5.32: Diffraction limited optical quality associated to the design of Fig. 5.31, for the IR-II spectrograph at Si I 10827 Å.

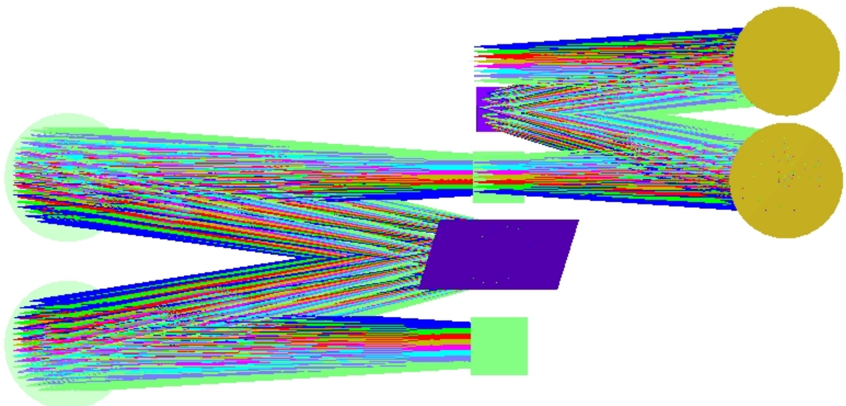

Figure 5.33: Optical design of the VIS-I spectrograph at 4227 Å associated to the planets science programme.

same optical quality.

This study shows that, even with larger decentred distances in order to avoid possible vignetting caused by the mechanical mountings, the design of the four spectrographs,

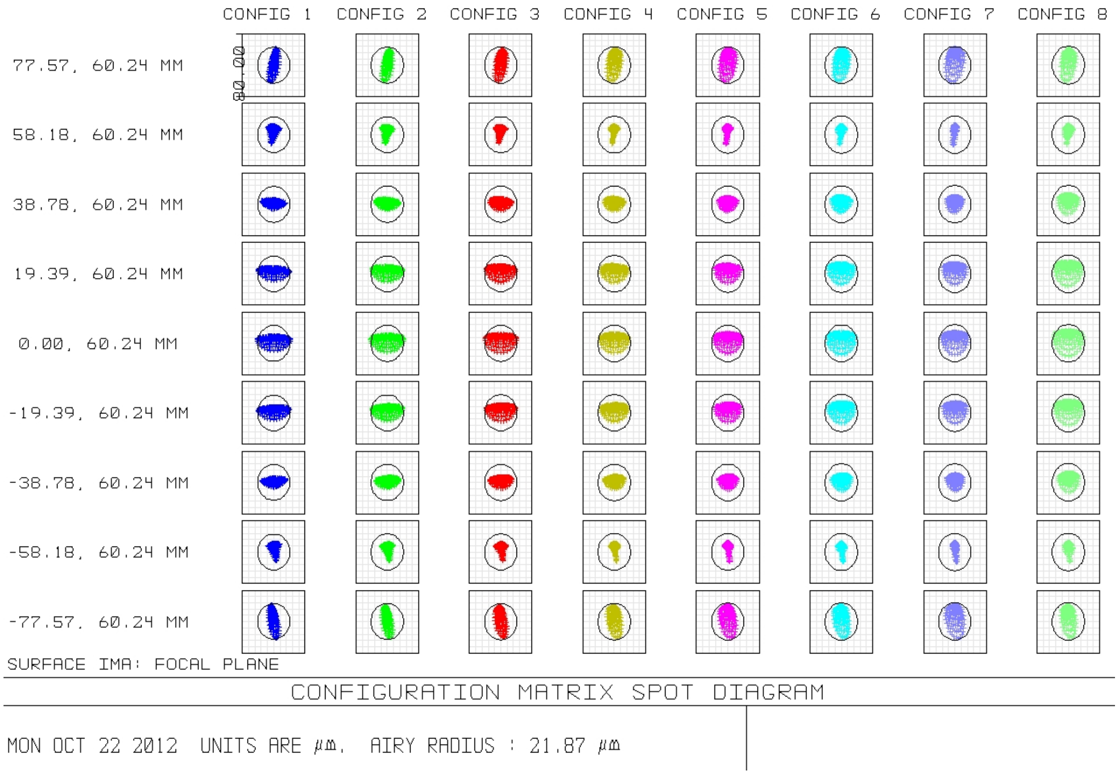

Figure 5.34: Spot diagram of the design of Fig. 5.33. The rays are contained within the Airy disk for all the fields, showing an optical quality at diffraction limit.

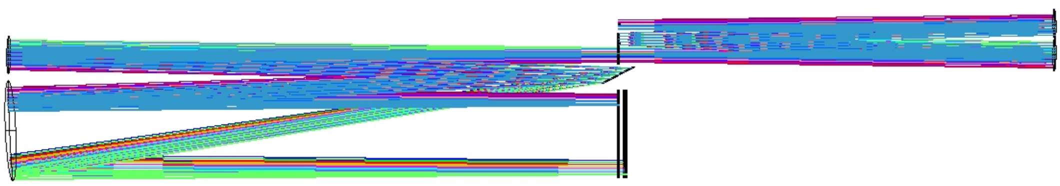

Figure 5.35: ZEMAX optical design of the VIS-II spectrograph evaluated at 5890 Å and 7699 Å.

evaluated for the different combinations of wavelengths, present an excellent optical quality limited by diffraction.

5.1.4 Camera mirror diameter

The camera mirror is, in each case, the optical element with the largest diameter, since it has to collect the image of the eight entrance slits of 200 arcsec length for each wavelength once dispersed by the diffraction grating. Depending on the characteristics of the grating and the order in which the wavelengths are observed, the spectral separation can lead to a large camera mirror. Those wavelengths close to each other or approximately multiple of others with which they are observed together will be closer in the camera and at the image

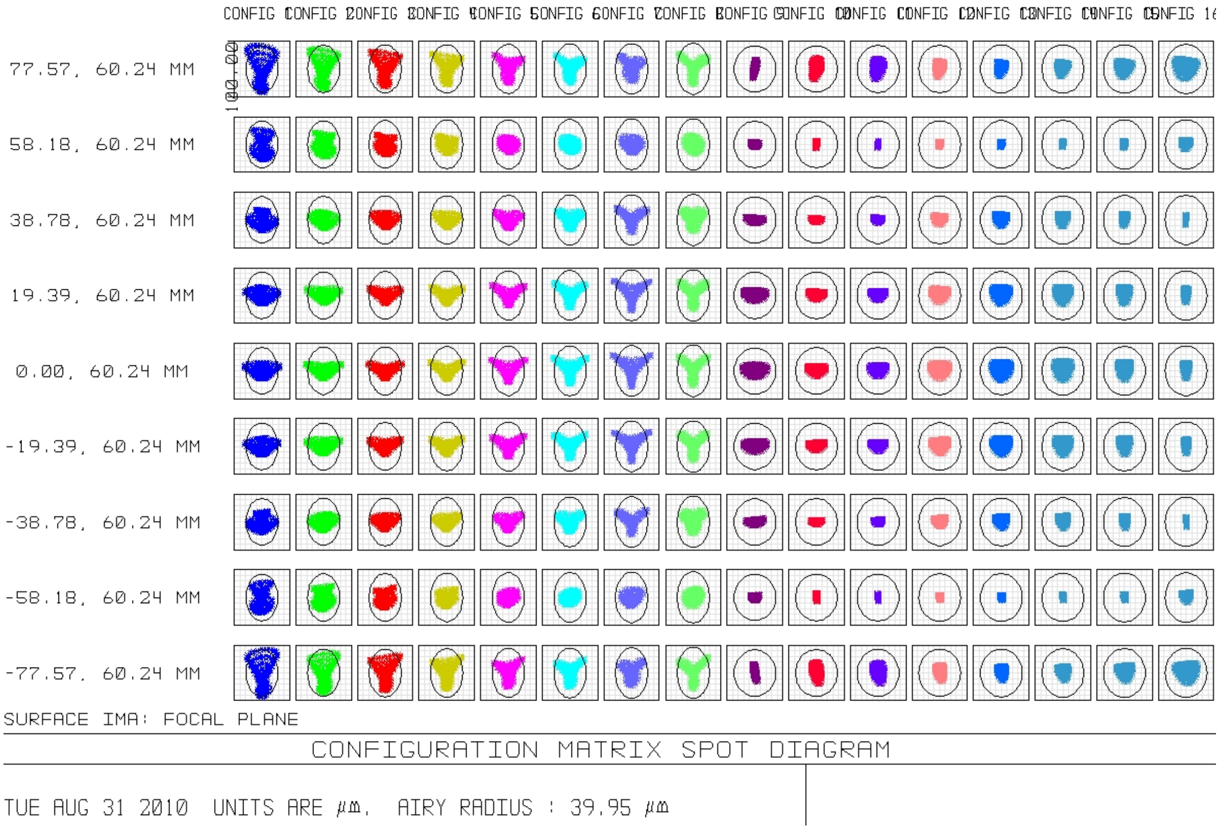

Figure 5.36: Spot diagram of the VIS-II spectrograph evaluated for 5890 Å and 7699 Å.

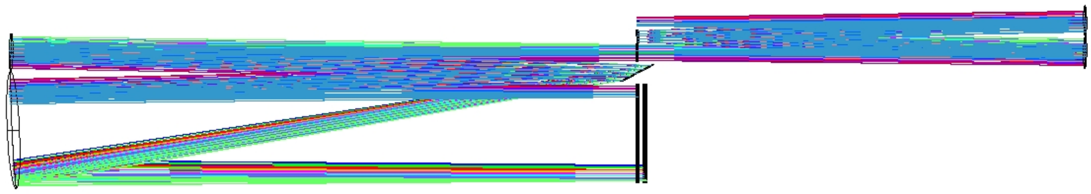

Figure 5.37: ZEMAX optical design of the VIS-II spectrograph evaluated for 5890 Å and 7665 Å.

focal plane. After the evaluation of the designs for the different science programmes, the largest camera mirror defines the final diameter (presented in Table 4.11). Tables 5.1 to 5.4 show the diameter required for each programme in the different spectrographs.

5.1.5 Degrees of freedom

The degrees of freedom for the different elements of predispersers and spectrographs are listed below:

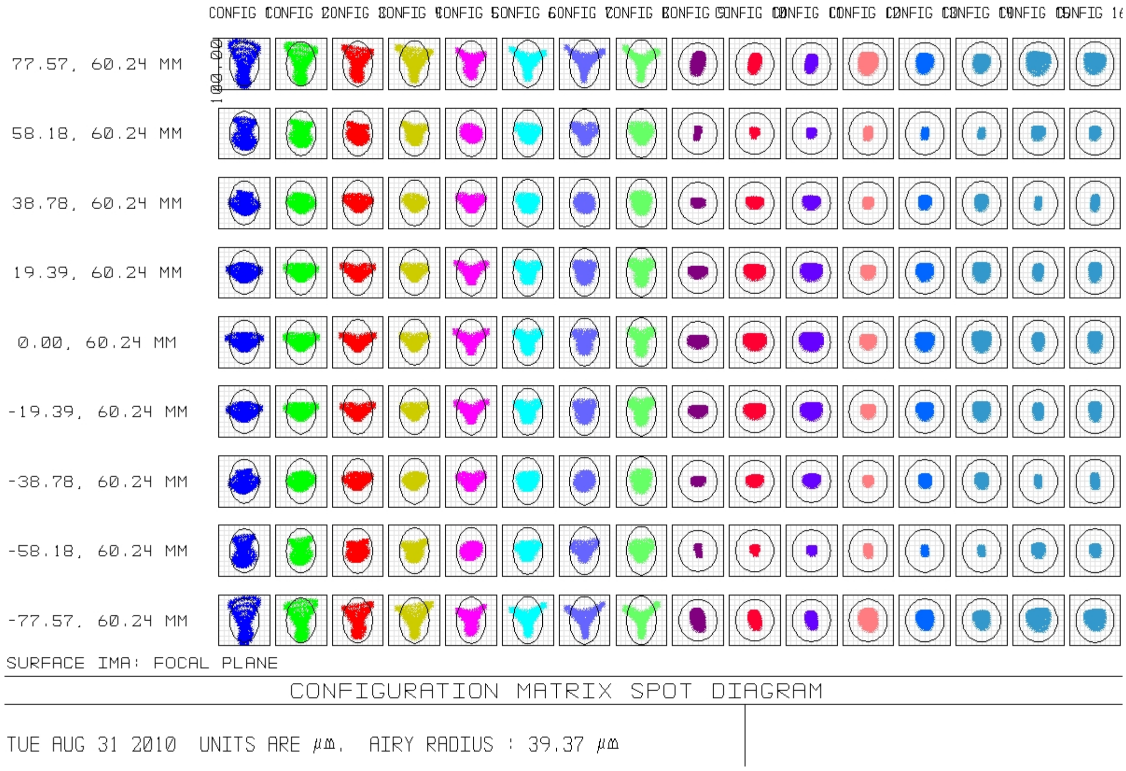

Figure 5.38: Spot diagram corresponding to the layout of Fig. 5.37. If this spot is compared with that of Fig. 5.36, the results show equivalent optical qualities, so, if 7699 Å is changed for 7665 Å, the optical quality is maintained.

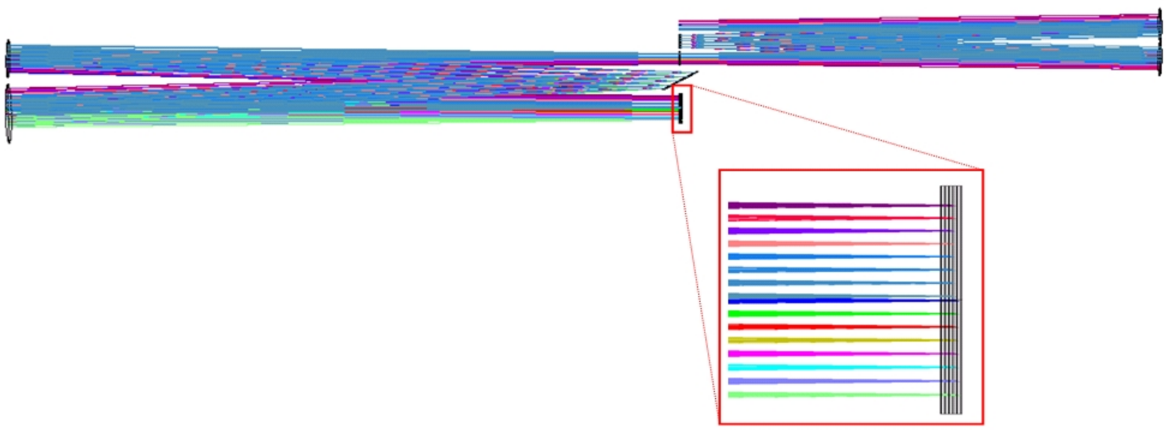

Figure 5.39: Optical design of the VIS-II spectrograph evaluated for 7665 Å and 7699 Å. A zoom of the spectrograph image focal plane (without reimaging system) is pointed out, showing that, although the wavelengths do not overlap, they are too close to each other to be observed in different detectors.

1. collimator and camera mirrors:

   they will present orientation, inclination, focusing, lateral and vertical movements.

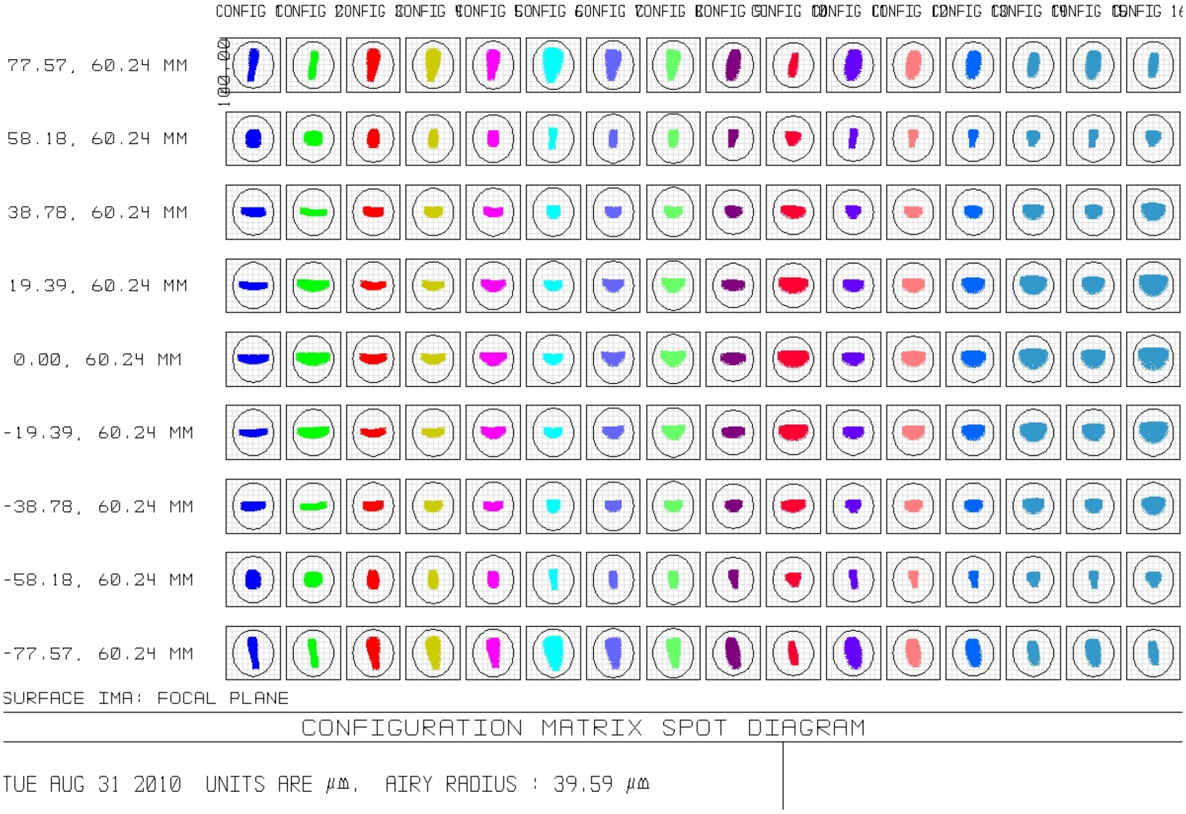

Figure 5.40: Diffraction limited spot diagram of the VIS-II spectrograph evaluated for 7665 Å and 7699 Å.

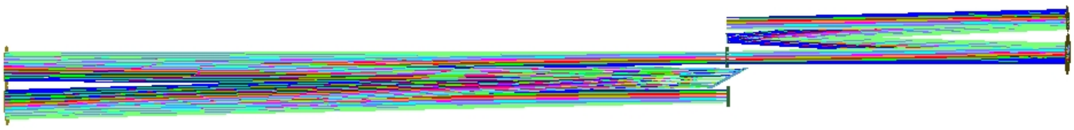

Figure 5.41: ZEMAX layout for 22300 Å evaluated with the IR-II spectrograph.

Table 5.1: VIS-I spectrograph camera diameter for the different science programmes.

SCIENCE PROGRAMME	CAMERA DIAMETER (mm)
Flares	600.00
Flux tube	820.00
Network elements	400.00
Hanle effect	600.00
Planets	400.00
Maximum diameter	820.00

2. gratings:

   the considered degrees of freedom are inclination, rotation and vertical movements.

Figure 5.42: Spot diagram of the IR-II spectrograph evaluated for 22300 Å for the sunspot science program. The rays are contained within the Airy disk, showing that the optical quality of the design is at diffraction limit.

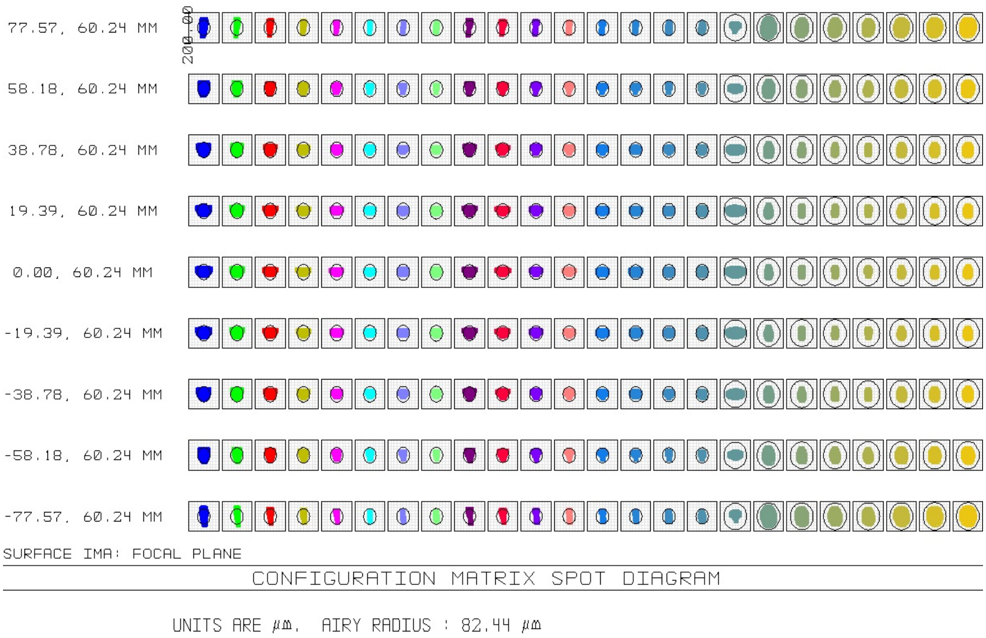

Figure 5.43: Spot diagram of the IR-I spectrograph for the simultaneous observation of 8542 Å, 8498 Å and 15650 Å. This spot diagram can be compared with the one of Fig. 5.18. Although in this case the decentred distances have been increased considering the mechanical mountings, the optical quality of both are the same.

Table 5.2: VIS-II spectrograph camera diameter for the different science programmes.

SCIENCE PROGRAMME	CAMERA DIAMETER (mm)
Flares	400.00
Flux tube	400.00
Magnetic canopies	400.00
Hanle effect	400.00
Planets	400.00
Maximum diameter	400.00

Table 5.3: IR-I spectrograph camera diameter for the different science programmes.

SCIENCE PROGRAMME	CAMERA DIAMETER (mm)
Flares	400.00
Flux tube	660.00
Magnetic canopies	640.00
Network elements	400.00
Hanle effect	410.00
Maximum diameter	660.00

Table 5.4: IR-II spectrograph camera diameter for the different science programmes.

SCIENCE PROGRAMME	CAMERA DIAMETER (mm)
Flares	380.00
Flux tube	380.00
Sunspots	360.00
Maximum diameter	380.00

3. detectors:

   lateral movements in order to observe different wavelengths, focusing and rotation.

5.2 Calculations

The parameters for the wavelengths associated to the four spectrographs, diffraction order (obtained from Eq. 1.12), output angle (β, obtained from Eq. 1.13), grating efficiency (Eq. 1.15) and linear dispersion (Eq. 1.23), are shown in Tables 5.5 to 5.8 for the predispersers and in Tables 5.9 to 5.12 for the spectrographs. The curves of the predisperser gratings efficiency are presented in Figs. 5.44 to 5.47. The grating of the IR-I predisperser is optimised for 15500 Å, which is the blaze wavelength at first order. For the wavelengths close to this value, the theoretical efficiency is 1, as shown in Table 5.7. Those wavelengths obtained as the division of the blaze wavelength by the order, as explained in Eq. 4.8, will also present this efficiency. For this reason, the wavelengths around 8500 Å present a very high efficiency at second order and the grating efficiency decays for wavelengths far away from the blaze wavelength. In particular, the lowest value is obtained around 10000 Å. This wavelength and its multiple $\sim$ 20000 Å is observed with the IR-II predisperser, for which the grating efficiency is very high (∼0.98-0.99). The IR-II predisperser grating also presents the minimum for those wavelengths optimised for the IR-I. Thus, the combination of these diffraction gratings cover the near-infrared spectral range with a very good efficiency.

Table 5.5: VIS-I predisperser calculated parameters.

VIS-I PD			
λ(Å)	order	Eff_{PD}	L_{PD}^{-1}(Å/mm)
3933	1	0.99	6.66
3968	1	0.99	6.66
4102	1	1.00	6.65
4227	1	1.00	6.65
5177	1	0.88	6.64
5250	1	0.87	6.64
5576	1	0.81	6.63

Table 5.6: VIS-II predisperser calculated parameters.

VIS-II PD			
λ(Å)	order	Eff_{PD}	L_{PD}^{-1}(Å/mm)
5890	2	0.74	27.66
5896	2	0.75	27.66
6302	2	0.93	27.66
6563	2	0.99	27.66
7665	2	0.83	27.65
7699	2	0.82	27.65
7770	2	0.80	27.65

Table 5.7: IR-I predisperser calculated parameters.

IR-I PD			
λ(Å)	order	Eff_{PD}	L_{PD}^{-1}(Å/mm)
8498	2	0.91	6.14
8542	2	0.90	6.14
15260	1	1.00	12.36
15650	1	1.00	12.34

The curves of the spectrographs grating efficiency are presented in Figs. 5.48 to 5.51. The efficiency curve is clearly different for the predisperser gratings and for the echelle spectrograph ones. For the predisperser gratings, for which the blaze angle is small, the efficiency curve presents the maximum for the blaze wavelength and decays slowly at both sides. Nevertheless, the echelle gratings are characterised for an inclination of the grooves of the order of 60°. The curves for the efficiency in the case of the spectrographs present different relative maximums. The width of the peaks at half height depends on the blaze

Table 5.8: IR-II predisperser calculated parameters.

IR-II PD			
λ(Å)	order	Eff_{PD}	L_{PD}^{-1}(Å/mm)
10827	2	0.98	17.74
10828	2	0.98	17.74
22300	1	0.99	35.47

Table 5.9: VIS-I spectrograph calculated parameters.

VIS-I SP				
λ(Å)	order	Eff_{SP}	β(°)	L_{SP}^{-1}(Å/mm)
3933	14	0.72	-4.90	0.16
3968	14	0.87	-3.18	0.15
4102	14	0.78	4.48	0.11
4227	13	0.72	-5.28	0.17
5177	11	0.96	2.32	0.16
5250	11	0.75	6.05	0.14
5576	10	0.96	-2.42	0.21

Table 5.10: VIS-II spectrograph calculated parameters.

VIS-II SP				
λ(Å)	order	Eff_{SP}	β(°)	L_{SP}^{-1}(Å/mm)
5890	28	0.79	2.25	0.19
5896	28	0.74	2.52	0.18
6302	26	0.98	0.65	0.21
6563	25	0.97	0.96	0.22
7665	21	0.73	-3.33	0.30
7699	21	0.85	-2.40	0.29
7770	21	1.00	-0.35	0.27

Table 5.11: IR-I spectrograph calculated parameters.

IR-I SP				
λ(Å)	order	Eff_{SP}	β(°)	L_{SP}^{-1}(Å/mm)
8498	26	0.75	-2.40	0.31
8542	26	0.91	-1.36	0.30
15260	15	0.59	5.72	0.40
15650	14	0.79	-4.01	0.60

angle. The larger the angle, the narrower the peaks. Attending to the expression of the theoretical efficiency (Eq. 4.18), it is a function of: wavelength, order, blaze angle, groove density, and input and ouput angles of the beam with respect to the diffraction grating. This is expressed in Eq. 5.1.

Table 5.12: IR-II spectrograph calculated parameters.

IR-II SP				
λ(Å)	order	Eff_{SP}	$\beta(°)$	L_{SP}^{-1}(Å/mm)
10828	21	0.60	3.99	0.35
10827	21	0.60	3.99	0.35
22300	10	1.00	-0.51	0.86

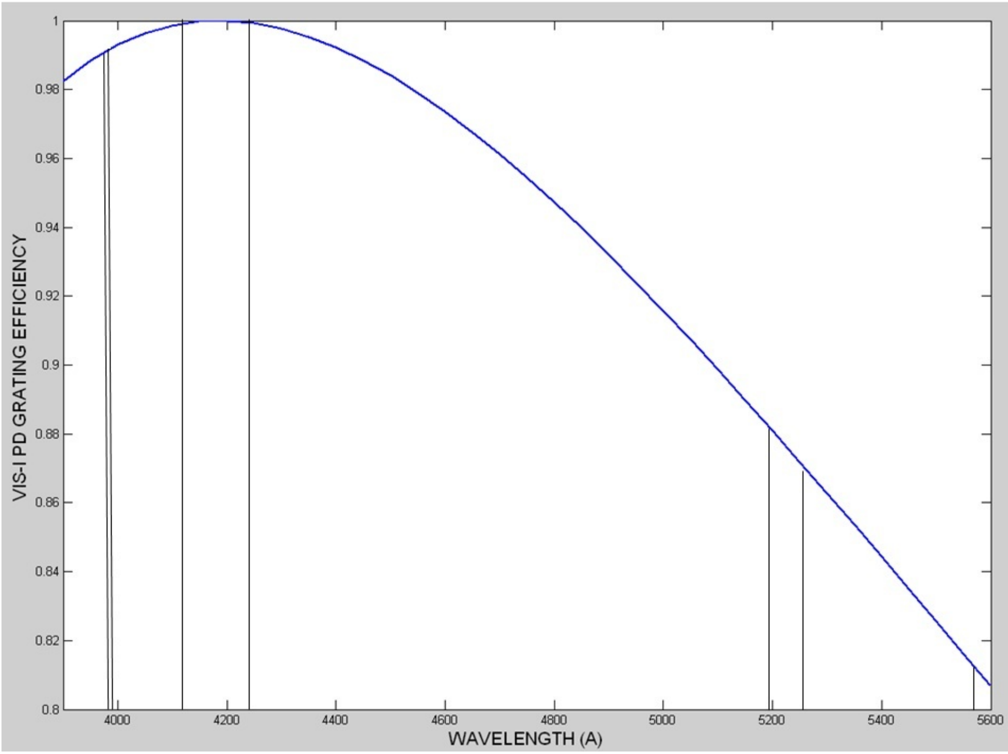

Figure 5.44: VIS-I predisperser grating efficiency curve. The vertical lines represent the wavelengths studied within the spectral range.

$$Eff = f(\lambda, m, \varphi_B, \sigma, \alpha, \beta) \tag{5.1}$$

The angle of incidence of the beam over the diffraction grating takes part in the efficiency value. Thus, the angle can be adjusted in order to improve the efficiency. This is done with the predisperser, whose grating output angle is adapted to improve the spectrograph grating efficiency.

The dependence with the order considerably affects the efficiency value. This effect is higher the bigger the blaze angle, as explained in Fig. 4.22.

For all types of gratings, the efficiency value depends on wavelength. This is represented in Fig. 5.52, in which the efficiency curve for a grating with 79 grooves/mm and a blaze angle of 62° has been evaluated for a spectral range between 10000 Å and 24000 Å, considering the same order for all of them (m=10). The curve is represented by a squared sinc function with

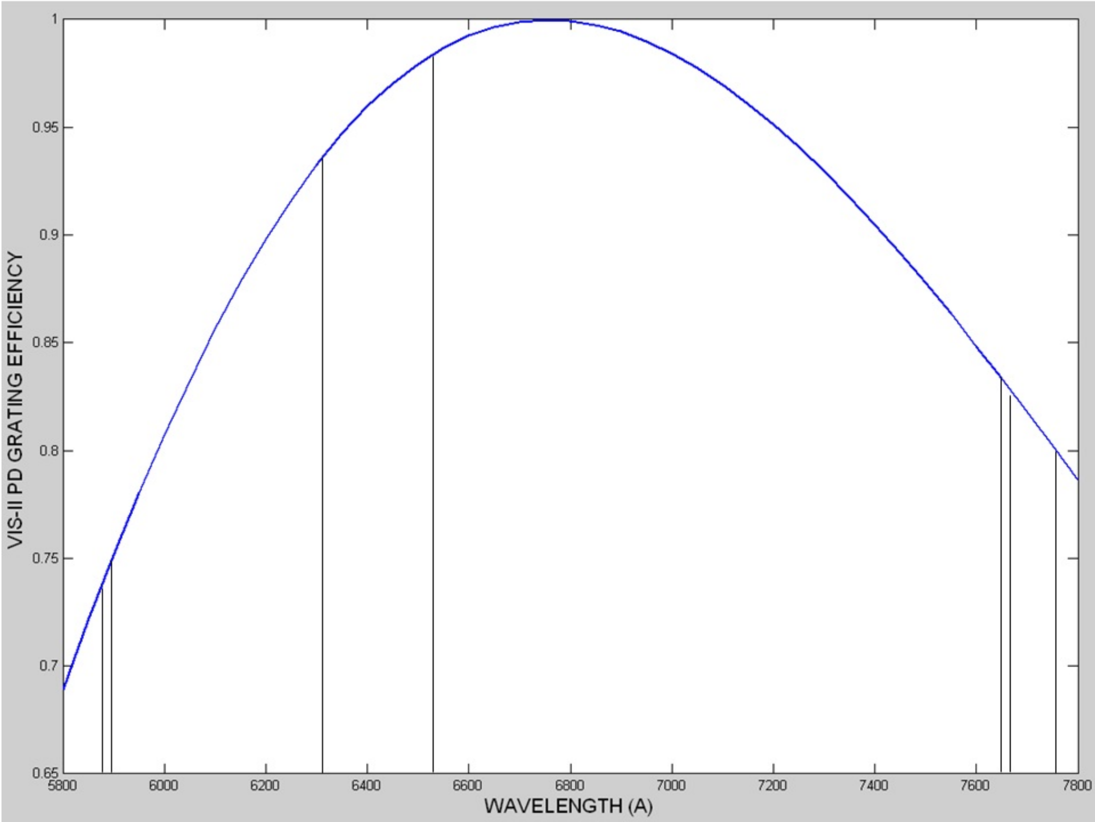

Figure 5.45: VIS-II predisperser grating efficiency curve. The vertical lines represent the wavelengths studied within the spectral range.

the absolute maximum at the blaze wavelength for this order and other relative maximums with gradually decreasing efficiencies. The curves of efficiency for the spectrographs gratings, in which a spectral range is considered, can be decomposed in curves like the one of Fig. 5.52 for each wavelength.

This grating has the blaze wavelength at 223531 Å at first order. Applying Eq. 4.8, the wavelengths at higher orders for which the theoretical efficiency is also maximum can be calculated. For this grating, those wavelengths are shown in Table 5.13.

A very important calculated parameter is the spectral resolution. There are three elements that define the spectral resolution of a spectrograph: the slit, the diffraction grating and the detector. Their resolution elements, denoted as $\delta\lambda_s$, $\delta\lambda_g$ and $\delta\lambda_d$, are defined in Eqs. 1.20, 1.24 and 1.26. A slit width of 40 μm, corresponding to 0.05 arcsec for a focal ratio F/40 and 2 pixels as the resolution element, according to the Nyquist sampling theorem, have been considered. The total resolution element, $\delta\lambda_T$ is calculated using Eq. 1.27. The sampling (S), defined by Eq. 1.31 as the spectral width contained within a pixel, has been calculated too.

Although the grating spectral resolving power is defined by Eq. 1.30, the total spectral resolving power of the spectrograph is given by R_T, defined in Eq. 1.29. The calculated

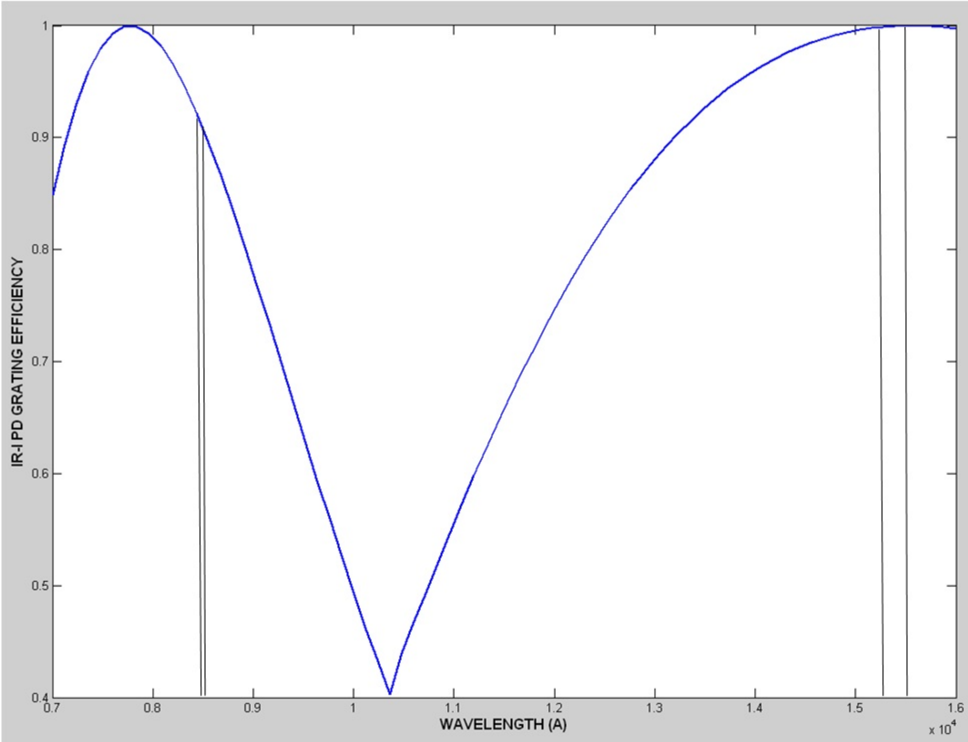

Figure 5.46: IR-I predisperser grating efficiency curve.

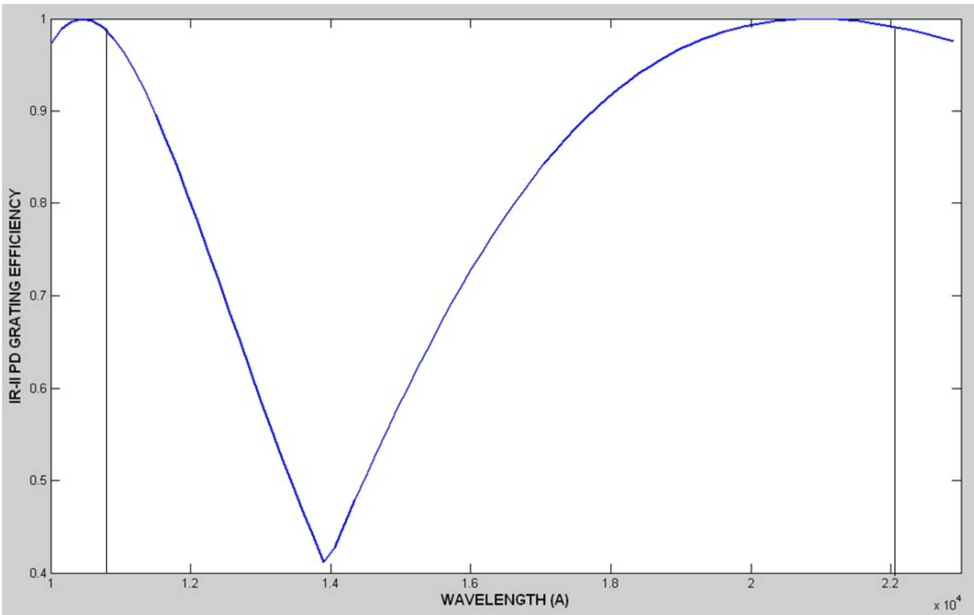

Figure 5.47: IR-II predisperser grating efficiency curve.

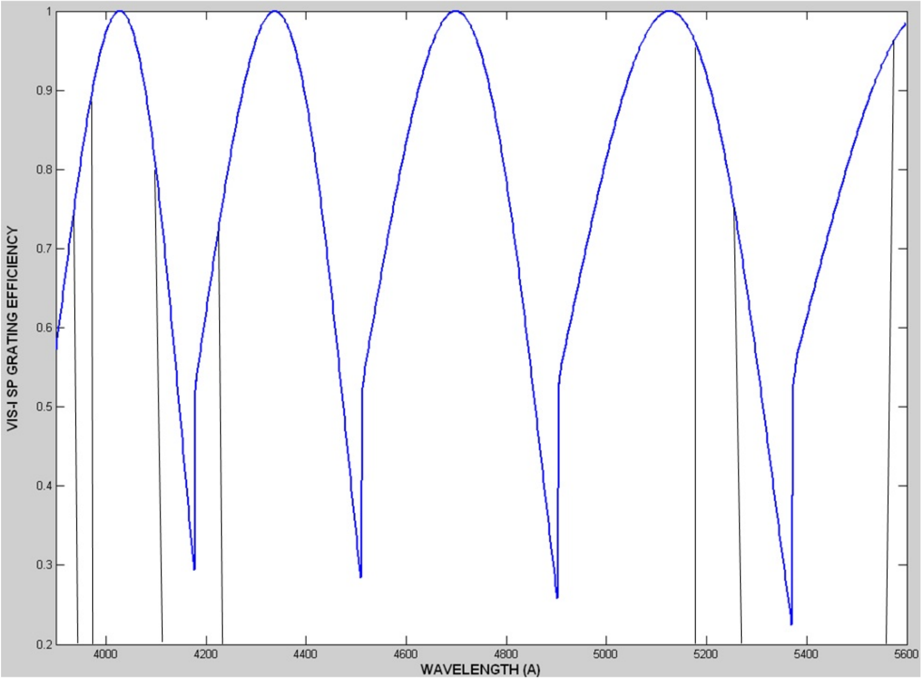

Figure 5.48: VIS-I spectrograph grating efficiency curve. The vertical lines represent the wavelengths studied within the spectral range.

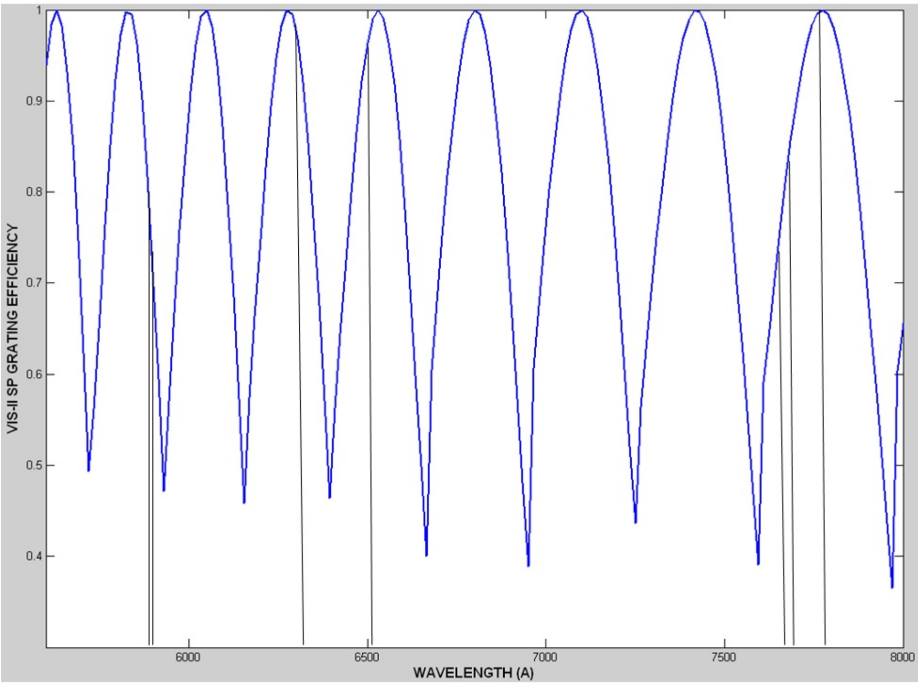

Figure 5.49: VIS-II spectrograph grating efficiency curve. The vertical lines represent the wavelengths studied within the spectral range.

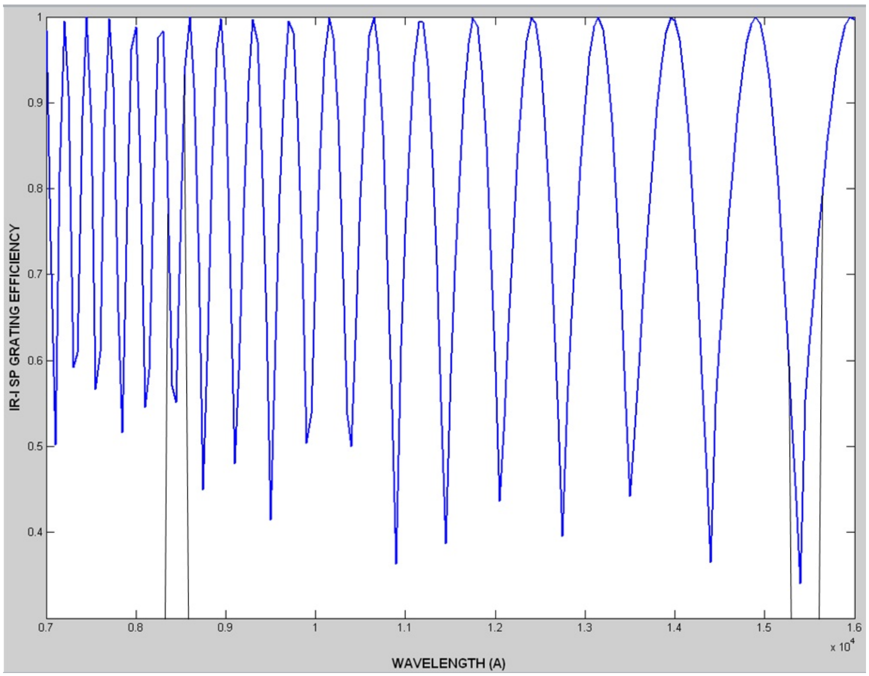

Figure 5.50: IR-I spectrograph grating efficiency curve. The vertical lines represent the wavelengths studied within the spectral range.

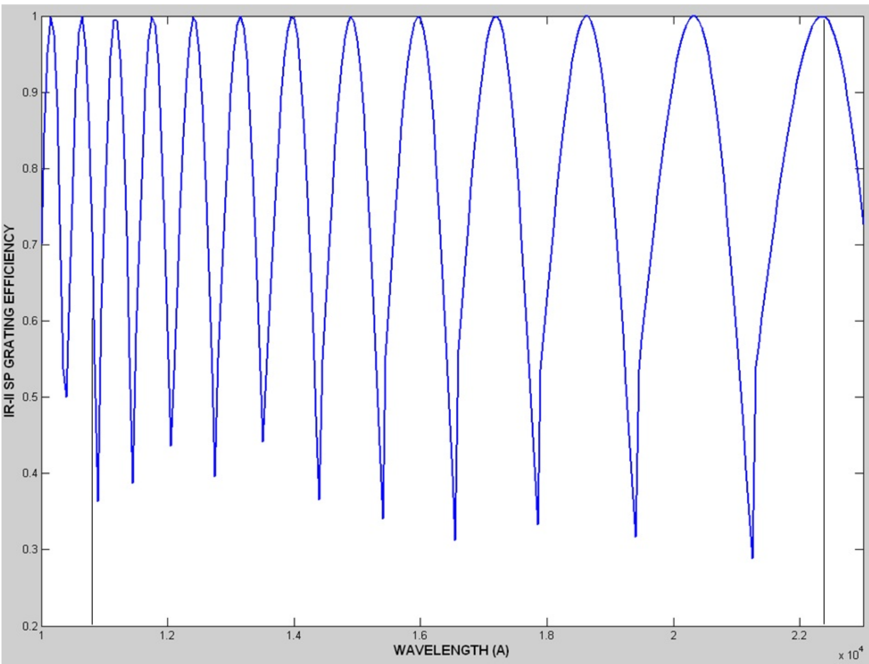

Figure 5.51: IR-II spectrograph grating efficiency curve. The vertical lines represent the wavelengths studied within the spectral range.

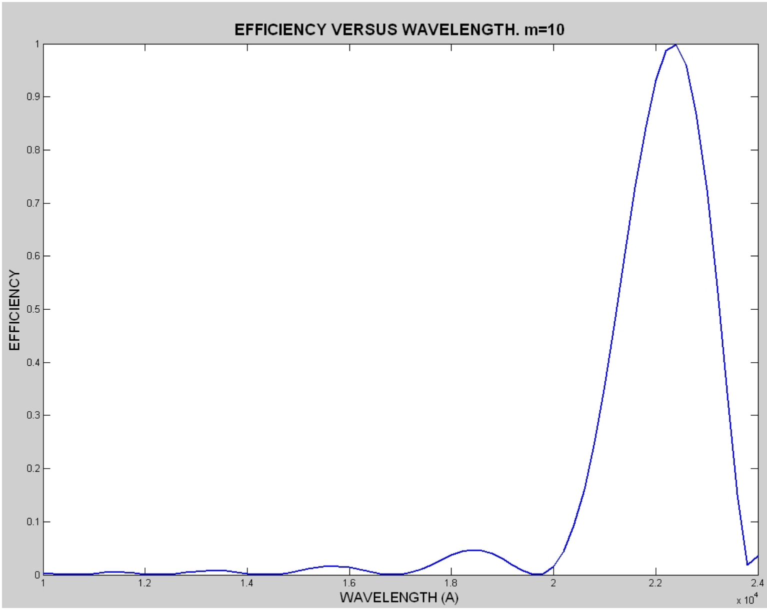

Figure 5.52: Grating efficiency versus wavelength. The curve is described by a squared sinc function with the absolute maximum at the blaze wavelength for this order and other relative maximums with gradually decreasing efficiencies.

Table 5.13: Wavelengths for which the infrared spectrograph grating efficiency is maximum.

Order	$\lambda(\mathring{A})$	Order	$\lambda(\mathring{A})$
1	223531	14	15967
2	111766	15	14902
3	74510	16	13971
4	55883	17	13149
5	44706	18	12418
6	37255	19	11765
7	31933	20	11177
8	27941	21	10644
9	24837	22	10161
10	22353	23	9719
11	20321	24	9314
12	18628	25	8941
13	17195	26	8597

values associated to the spectral resolution are presented in Tables 5.14 to 5.17. For the largest wavelength of the spectrograph spectral range, 22300 Å, the total spectral resolving power is slightly lower than the requirement. Considering the same grating, this can be solved decreasing the magnification of the reimaging system for this wavelength, using a larger final f-number.

Table 5.14: VIS-I spectrograph calculated resolutions. The values obtained for the total spectral resolving power are, for all the wavelengths of the VIS-I spectral range, higher than the requirement (300,000).

λ(Å)	S (Å/pixel)	$\delta\lambda_s$(Å)	$\delta\lambda_g$ (Å)	$\delta\lambda_d$ (Å)	$\delta\lambda_T$ (Å)	R_g	R_T
3933	0.0062	0.0064	0.0022	0.0125	0.0140	1827,100	280,929
3968	0.0058	0.0060	0.0022	0.0117	0.0130	1827,100	305,231
4102	0.0043	0.0044	0.0022	0.0086	0.0099	1827,100	414,343
4227	0.0066	0.0068	0.0025	0.0133	0.0150	1696,600	281,800
5177	0.0062	0.0064	0.0036	0.0125	0.0145	1435,600	357,528
5250	0.0055	0.0056	0.0037	0.0109	0.0128	1435,600	410,156
5576	0.0082	0.0084	0.0043	0.0164	0.0189	1305,100	295,026

Table 5.15: VIS-II spectrograph calculated resolutions. The total spectral resolving power, R_T is higher than the requirement.

λ(Å)	S (Å/pixel)	$\delta\lambda_s$(Å)	$\delta\lambda_g$ (Å)	$\delta\lambda_d$ (Å)	$\delta\lambda_T$ (Å)	R_g	R_T
5890	0.0074	0.0076	0.0048	0.0148	0.0170	1229,600	346,471
5896	0.0070	0.0072	0.0048	0.0140	0.0160	1229,600	368,500
6302	0.0082	0.0084	0.0055	0.0164	0.0190	1141,700	331,684
6563	0.0086	0.0088	0.0060	0.0172	0.0200	1097,800	328,150
7665	0.0117	0.0120	0.0083	0.0234	0.0276	922,200	283,889
7699	0.0113	0.0116	0.0083	0.0226	0.0267	922,200	288,352
7770	0.0105	0.0108	0.0084	0.0211	0.0250	922,200	310,800

Table 5.16: IR-I spectrograph calculated resolutions. The resolution requirement is fulfilled for all the wavelengths of the interval.

λ(Å)	S (Å/pixel)	$\delta\lambda_s$(Å)	$\delta\lambda_g$ (Å)	$\delta\lambda_d$ (Å)	$\delta\lambda_T$ (Å)	R_g	R_T
8498	0.0121	0.0124	0.0097	0.0242	0.0287	875,030	296,098
8542	0.0117	0.0120	0.0098	0.0234	0.0281	875,030	305,071
15260	0.0156	0.0160	0.0302	0.0312	0.0460	504,820	331,739
15650	0.0234	0.0240	0.0332	0.0468	0.0620	471,170	252,419

Table 5.17: IR-II spectrograph calculated resolutions. For the largest wavelength of the spectrograph spectral range, the total spectral resolving power is slightly lower than the requirement. Considering the same grating, this can be solved decreasing the magnification of the reimaging system for this wavelength, in order to have a larger final f-number.

λ(Å)	S (Å/pixel)	$\delta\lambda_s$(Å)	$\delta\lambda_g$ (Å)	$\delta\lambda_d$ (Å)	$\delta\lambda_T$ (Å)	R_g	R_T
10828	0.0136	0.0140	0.0175	0.0273	0.0350	618,410	309,343
10827	0.0136	0.0140	0.0175	0.0273	0.0350	618,410	309,343
22300	0.0335	0.0344	0.0757	0.0671	0.1010	294,480	223,000

5.2.1 Throughput budget

Another important point is the throughput budget that gives an estimation of the percentage of the incoming light that is measured at the image focal plane after the different reflections. The values have been calculated by estimating the reflectivity of each surface (assuming protected silver coating). Taking into account the different subsystems: field of view scanning system, integral field unit, predisperser and spectrograph (but not the detector quantum efficiency), for every wavelength.

Taking into account Fig. 3.25 (a), the values considered for the protected silver coating are: 0.94 for wavelengths ~ 3000 Å, 0.95 for $\lambda \sim 4000$ Å, 0.96 for $\lambda \sim 5000$ Å and 0.98 for $\lambda \geq 6000$ Å.

In the case of the grating, the theoretical efficiency is also multiplied by the reflectivity of its surface. The gratings have been chosen as those that offer the optimum efficiency for most of the wavelengths. It can be observed that for some wavelengths the efficiency is really high. For others, the value is not so good, due to the fact of using commercial gratings for the simultaneous observation of several wavelengths. The gratings present their optimum behaviour for a given wavelength but might not work so well for others. The simultaneity increases the difficulty of the system. Nevertheless, the diffraction gratings have been selected based not only on efficiency criteria. Other requirements like spectral resolution, linear dispersion in order to have the smallest camera mirrors as possible and wavelength overlapping at the image focal plane that has been avoided in all the cases, have also taken part in the decision.

The total throughput value is obtained by multiplying the values for each subsystem, getting the following average values between the results obtained for the studied wavelengths of each interval: 40% for VIS-I, 52% for VIS-II, 55% for IR-I and 55% for IR-II. The values per wavelength are presented in Tables 5.18, 5.19, 5.20 and 5.21.

5.3 Combination of possible simultaneous wavelengths

After studying the combinations of wavelengths of Table 1.1 for the different science programs, Table 5.22 summarises those wavelengths that can be observed simultaneously with the current design and those that have been proposed to be observed individually in a sequential mode. A reason that has led to this suggestion is the spectrograph camera mirror diameter, which increases too much in some cases if all the proposed wavelengths were observed together and with the restriction of the commercial gratings. After studying all the catalogue gratings, there is none that fulfills better the requirements.

A proposal to satisfy the simultaneous observation of the listed wavelengths is the application of the white pupil optical concept (Baranne, 1988). It is based on the reimagination of the dispersed beam in front of the camera, reducing the pupil size. Monochromatic beams intersect each other in the new pupil which has to be superimposed before the camera mirror. The size of the beams on the camera mirror, as well as the separation between the monochromatic beams, are reduced. This provides several advantages to the system: assuming smaller sizes it is possible that all the required wavelengths can be observed together using reasonable camera diameters. It would also facilitate the design of the detector reimaging systems. The demagnification for the white pupil would reduce the one of the final reimaging systems. In addition, if the sizes are reduced, commercial optical components could be considered for their designs. The last advantage is that the size reduction implies smaller off-axis distances of the beams with respect to the spectrograph optical axis, what improves the optical quality.

Table 5.18: Throughput budget for the wavelengths of the VIS-I spectrograph, considering the different subsystems. The average value is 0.40.

	3933 Å	3968 Å	4102 Å	4227 Å	5177 Å	5250 Å	5576 Å
FoV SCANNING SYSTEM							
M1	0.94	0.94	0.95	0.95	0.96	0.96	0.96
M2	0.94	0.94	0.95	0.95	0.96	0.96	0.96
M3	0.94	0.94	0.95	0.95	0.96	0.96	0.96
M4	0.94	0.94	0.95	0.95	0.96	0.96	0.96
TOTAL SCANNING SYSTEM	0.78	0.78	0.81	0.81	0.85	0.85	0.85
IMAGE SLICER							
Macro-slicer+slicer mirror array	0.94	0.94	0.95	0.95	0.96	0.96	0.96
Collimator mirror array	0.94	0.94	0.95	0.95	0.96	0.96	0.96
Camera mirror array	0.94	0.94	0.95	0.95	0.96	0.96	0.96
TOTAL IFU	0.83	0.83	0.86	0.86	0.88	0.88	0.88
PREDISPERSER							
Collimator mirror	0.94	0.94	0.95	0.95	0.96	0.96	0.96
Diffraction grating	0.93	0.93	0.95	0.95	0.84	0.84	0.78
Camera mirror	0.94	0.94	0.95	0.95	0.96	0.96	0.96
TOTAL PD	0.82	0.82	0.86	0.86	0.77	0.77	0.72
SPECTROGRAPH							
Collimator mirror	0.94	0.94	0.95	0.95	0.96	0.96	0.96
Diffraction grating	0.68	0.82	0.74	0.68	0.92	0.72	0.92
Camera mirror	0.94	0.94	0.95	0.95	0.96	0.96	0.96
TOTAL SP	0.60	0.72	0.67	0.61	0.85	0.66	0.85
REIMAGING SYSTEM							
Collimator mirror 1	0.94	0.94	0.95	0.95	0.96	0.96	0.96
Camera mirror 1	0.94	0.94	0.95	0.95	0.96	0.96	0.96
Collimator mirror 2	0.94	0.94	0.95	0.95	0.96	0.96	0.96
Camera mirror 2	0.94	0.94	0.95	0.95	0.96	0.96	0.96
TOTAL REIMAGING SYSTEM	0.78	0.78	0.81	0.81	0.85	0.85	0.85
TOTAL	0.25	0.30	0.40	0.32	0.42	0.32	0.39

Table 5.19: Throughput budget for the wavelengths of the VIS-II spectrograph, considering the different subsystems. The average value is 0.52.

	5890 Å	5896 Å	6302 Å	6563 Å	7665 Å	7699 Å	7770 Å
FoV SCANNING SYSTEM							
M1	0.96	0.96	0.98	0.98	0.98	0.98	0.98
M2	0.96	0.96	0.98	0.98	0.98	0.98	0.98
M3	0.96	0.96	0.98	0.98	0.98	0.98	0.98
M4	0.96	0.96	0.98	0.98	0.98	0.98	0.98
TOTAL SCANNING SYSTEM	0.85	0.85	0.92	0.92	0.92	0.92	0.92
IMAGE SLICER							
Macro-slicer+slicer mirror array	0.96	0.96	0.98	0.98	0.98	0.98	0.98
Collimator mirror array	0.96	0.96	0.98	0.98	0.98	0.98	0.98
Camera mirror array	0.96	0.96	0.98	0.98	0.98	0.98	0.98
TOTAL IFU	0.88	0.88	0.94	0.94	0.94	0.94	0.94
PREDISPERSER							
Collimator mirror	0.96	0.96	0.98	0.98	0.98	0.98	0.98
Diffraction grating	0.71	0.72	0.91	0.97	0.81	0.80	0.78
Camera mirror	0.96	0.96	0.98	0.98	0.98	0.98	0.98
TOTAL PD	0.65	0.66	0.87	0.93	0.78	0.77	0.75
SPECTROGRAPH							
Collimator mirror	0.96	0.96	0.98	0.98	0.98	0.98	0.98
Diffraction grating	0.76	0.71	0.96	0.95	0.71	0.83	0.98
Camera mirror	0.96	0.96	0.98	0.98	0.98	0.98	0.98
TOTAL SP	0.70	0.65	0.92	0.91	0.68	0.80	0.94
REIMAGING SYSTEM							
Collimator mirror 1	0.96	0.96	0.98	0.98	0.98	0.98	0.98
Camera mirror 1	0.96	0.96	0.98	0.98	0.98	0.98	0.98
Collimator mirror 2	0.96	0.96	0.98	0.98	0.98	0.98	0.98
Camera mirror 2	0.96	0.96	0.98	0.98	0.98	0.98	0.98
TOTAL REIMAGING SYSTEM	0.85	0.85	0.92	0.92	0.92	0.92	0.92
TOTAL	0.29	0.27	0.63	0.67	0.42	0.49	0.56

Table 5.20: Throughput budget for the wavelengths of the IR-I spectrograph, considering the different subsystems. The average value is 0.55.

	8498 Å	8542 Å	15260 Å	15650 Å
FoV SCANNING SYSTEM				
M1	0.98	0.98	0.98	0.98
M2	0.98	0.98	0.98	0.98
M3	0.98	0.98	0.98	0.98
M4	0.98	0.98	0.98	0.98
TOTAL SCANNING SYSTEM	0.92	0.92	0.92	0.92
IMAGE SLICER				
Macro-slicer+slicer mirror	0.98	0.98	0.98	0.98
Collimator mirror	0.98	0.98	0.98	0.98
Camera mirror	0.98	0.98	0.98	0.98
TOTAL IFU	0.94	0.94	0.94	0.94
PREDISPERSER				
Collimator mirror	0.98	0.98	0.98	0.98
Diffraction grating	0.89	0.88	0.98	0.98
Camera mirror	0.98	0.98	0.98	0.98
TOTAL PD	0.85	0.85	0.94	0.94
SPECTROGRAPH				
Collimator mirror	0.98	0.98	0.98	0.98
Diffraction grating	0.73	0.89	0.58	0.77
Camera mirror	0.98	0.98	0.98	0.98
TOTAL SP	0.70	0.86	0.56	0.74
REIMAGING SYSTEM				
Collimator mirror	0.98	0.98	0.98	0.98
Camera mirror	0.98	0.98	0.98	0.98
TOTAL REIMAGING SYSTEM	0.96	0.96	0.96	0.96
TOTAL	0.49	0.60	0.44	0.58

An advantage of having 4 spectrographs is that, since for some programmes only some of them are used, more than one programme could be observed simultaneously in the case that the solar region observed by the telescope is the same. Or even other wavelengths could be observed by the available spectrographs together with a required science programme.

5.4 Integration at EST

5.4.1 Compatibility with the multi-purpose grating spectrograph of EST

The spectrograph described in this thesis is one of the four proposals that compose the multi-purpose spectrograph of EST (Calcines et al., 2010a). This family of spectrographs is composed by a long-slit standard spectrograph (LsSS), two devices based on the subtractive double pass (the NEW-GENERATION MSDP (Sayède et al., 2010) and TUNIS (López

Table 5.21: Throughput budget for the wavelengths of the IR-II spectrograph, considering the different subsystems. The average value is 0.55.

	10827 Å	10828 Å	22300 Å
FoV SCANNING SYSTEM			
M1	0.98	0.98	0.98
M2	0.98	0.98	0.98
M3	0.98	0.98	0.98
M4	0.98	0.98	0.98
TOTAL SCANNING SYSTEM	0.92	0.92	0.92
IMAGE SLICER			
Macro-slicer+slicer mirror	0.98	0.98	0.98
Collimator mirror	0.98	0.98	0.98
Camera mirror	0.98	0.98	0.98
TOTAL IFU	0.94	0.94	0.94
PREDISPERSER			
Collimator mirror	0.98	0.98	0.98
Diffraction grating	0.96	0.96	0.97
Camera mirror	0.98	0.98	0.98
TOTAL PD	0.92	0.92	0.93
SPECTROGRAPH			
Collimator mirror	0.98	0.98	0.98
Diffraction grating	0.59	0.59	0.98
Camera mirror	0.98	0.98	0.98
TOTAL SP	0.57	0.57	0.94
REIMAGING SYSTEM			
Collimator mirror	0.98	0.98	0.98
Camera mirror	0.98	0.98	0.98
TOTAL REIMAGING SYSTEM	0.96	0.96	0.96
TOTAL	0.43	0.43	0.73

Ariste et al., 2011b) and this integral field spectrograph. They are compatible with the use of the same base spectrographs (Calcines et al., 2012b). The base spectrographs are those described in this thesis. The integral field spectrograph proposal described in this thesis requires the largest entrance slits (200 arcsec) and the base spectrographs are optimised for this field of view. The spectrograph alternatives that use a slit of 120 arcsec have better optical performances or at least the same than that des-cribed in this chapter. The spectral range is common for all of them. Each proposal will use specific removable subsystems in order to be adapted to the base spectrograph. The combination of the four concepts support different science cases and provide versatility to the telescope. Fig. 5.53 shows the location of the spectrographs in the layout of the telescope.

The telescope offers two optical paths after the field of view scanning systems for the multi-purpose spectrograph. The main one drives directly to the base spectrographs. This is

Table 5.22: Combinations of possible simultaneous wavelengths observed in the different sepctrographs for the science programmes of Table 1.1.

SPECTROGRAPH	λ(Å)
FLUX TUBE	
VIS-I	5177 and 5250
VIS-II	6302
IR-I	8542 and 15650, 15250 sequentially
IR-II	10830
NETWORK ELEMENTS	
VIS-I	5576
VIS-II	6302
IR-I	15650
MAGNETIC CANOPIES	
VIS-II	5896
IR-I	8498, 8542 and 15650
HANLE EFFECT	
VIS-I	3933 and 3968
VIS-II	7770
IR-I	8542
FLARES	
VIS-I	3933 and 3968, 4102 sequentially
VIS-II	6563
IR-I	8542
IR-II	10827
PLANETS	
VIS-I	4227
VIS-II	5890-5896 and 7665-7699
SUNSPOTS	
IR-II	22300

the optical path for LsSS, NG-MSDP and TUNIS. Since the predispersers are too big to be a removable subsystem, a specific optical path is offered for the integral field spectrograph, where the image slicer and the predisperser are fixed. The optical path from the field of view scanning system is compensated using a folding mirror to locate the telescope focus at the image slicer entrance. Image slicer and predisperser are then coupled to the base spectrographs.

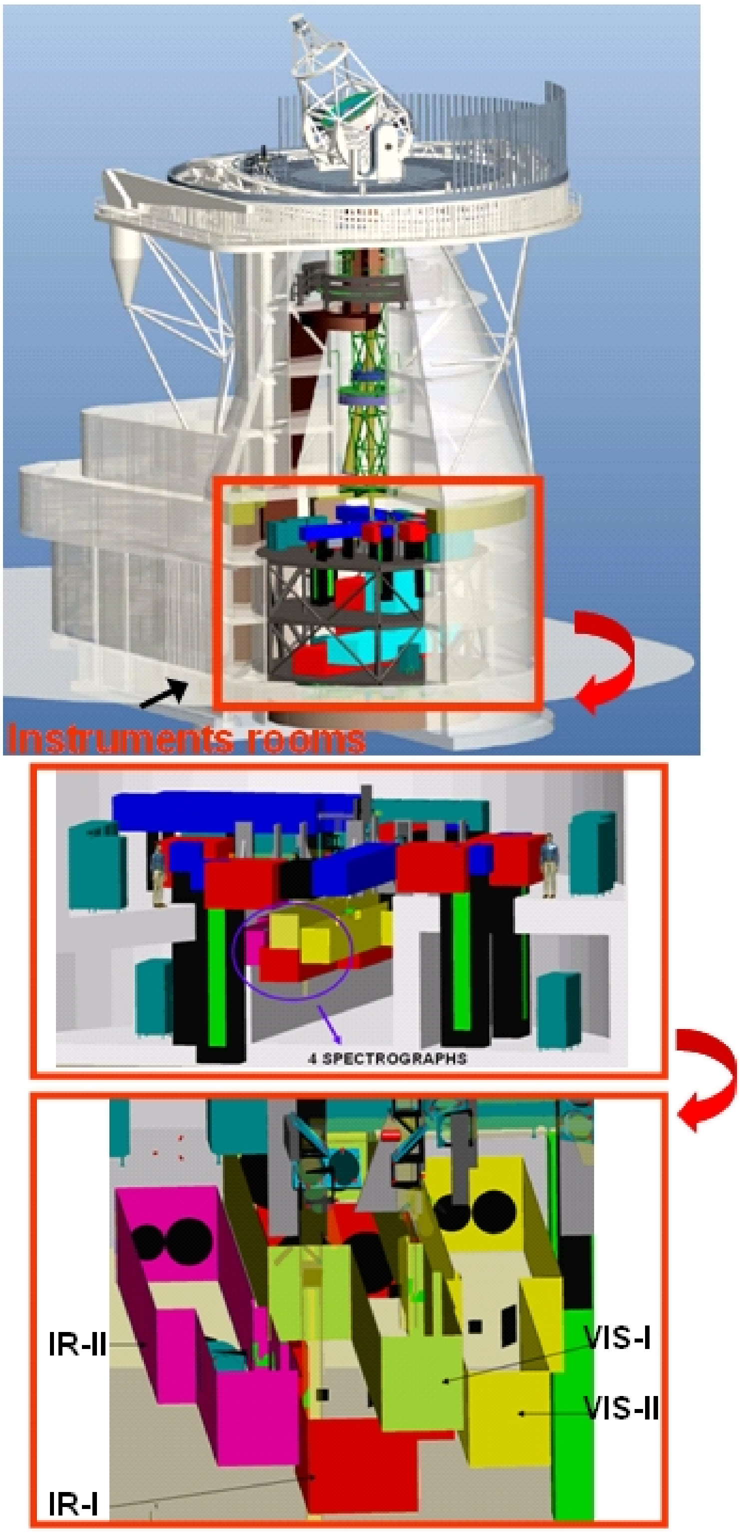

Figure 5.53: Location of the four base spectrographs in the European Solar Telescope layout. The four spectrographs are pointed out. They are, from left to right: IR-II, IR-I, VIS-I nad VIS-II.

6

Conclusions and Future Perspectives

Along the chapters of this thesis, the design of the integral field spectrograph for the European Solar Telescope, according to the requirements, has been described. The expectations for this instrument are very high and the compatibility of the several requirements and specifications has been a hard design process. Both, the calculation and the design of the different subsystems have been done progressively, as pieces of a puzzle that must fit perfectly to make this spectrograph become a great tool that allows us to study all those aspects of the Sun that are still unknown.

Insomuch as some subsystems are innovative, as the considered image slicer, a thorough technologic study has been carried out to investigate the state-of-the-art integral field units and propose an avant-garde concept.

With the development of this design some conclusions can be inferred, which are listed below.

In addition, during the design some other points of interest have emerged, like the next steps before the fabrication and other aspects that could improve the instrument performance, which are presented below.

6.1 Conclusions

- The best focal-ratios in order to fulfil the requirements are those within the interval F/40-F/50. The spectrograph can be illuminated with a beam whose focal-ratio belongs to this range. In this thesis, the proposed focal-ratio is F/40, because it offers the highest spectral resolution for 22300 Å.

- The integral field unit is based on the image slicer concept. The image slicer of this instrument, MuSICa, has been specifically designed for it. It decomposes a bidimensional field of view of 80 arcsec^2 and reorganises it into eight slits of 200 arcsec length $\times$ 0.05 arcsec width, minimizing the number of optical components (three arrays of mirrors). It is a telecentric system and, although it works as an image-side telecentric system at EST, it is designed as a both-side telecentric system, whose concept can be adapted either to solar spectrographs or to nigh-time astronomical instruments. As a difference with other referenced image slicers, MuSICa uses flat slicer mirrors and makes it possible their combination with the macro-slicer array (also flat) in order to optimise the throughput. The other two arrays of mirrors are spherical and have an antisymmetric arrangement. The rays of each configuration are overlapped at the pupil position and the pupil mask, used to avoid scattered light contribution, presents only one circular aperture. The symmetry of the layout presents some advantages: facilitates the manufacturing process, the alignment and reduces the costs. Another important aspect to point out is that the image slicer is compatible with the two modes of operation of the spectrograph: spectroscopic (reorganizing an 80 arcsec^2 field of view into eight slits of 200 arcsec length $\times$ 0.05 arcsec width) and spectro-polarimetric (reorganizing a 40 arcsec^2 field of view into eight slits of 100 arcsec length $\times$ 0.05 arcsec width that are later duplicated by the beam-splitter of a polarimeter).

- Collimator and camera mirrors of the image slicer has been distributed in two columns, whose height is comparable to the generated slit height. This minimizes the angles of incidence and improves the optical quality that is limited by diffraction.

- The spectrograph is preceded by a predisperser that acts as a prefilter. At the predisperser image focal plane a mask selects the combination of wavelengths at the appropriate diffraction order. The slits of the mask are then the spectrograph inputs.

- Both predisperser and spectrograph are 1:1 systems. The integral field unit makes the focal-ratio conversion from the telescope F/50 to F/40. This demagnification is done by the last optical component of the integral field unit without adding any extra surface. A reimaging system per wavelength, located in pre-focus configuration in front of the detectors converts the spectrograph focal-ratio into F/10.3 for visible wavelengths and F/20.6 for the infrared ones.

- Off-axis parabolic mirrors have been used for predispersers and spectrographs. In each case, collimator and camera mirrors are two subapertures that belong to the same global parabola, which is centred in the optical axis.

- Commercial diffraction gratings have been considered, what has implied a restriction of the design in terms of pupil size, linear dispersion and grating efficiency. In order to optimise the efficiency using this type of gratings, the spectral range is divided into four and four spectrographs (VIS-I, VIS-II, IR-I and IR-II), conceptually identical, are proposed, which can work simultaneously.

- The predisperser masks have eight slits per wavelength. The specifications and the fabrication of the slits have to be done with high accuracy. The homogeneity and parallelism of the slits edges are crucial, since small modifications with respect to the specified values could deteriorate the spectrum. The typical tolerance using milling machines is $\pm 20\ \mu$m, which is not enough for very thin slits like those of this spectrograph. Currently, the best technique is photodeposition.

- Since the slits of the masks are very thin, the mask has to present adequate mechanical degrees of freedom needed to orient them. These are translation (using a rail) and orientation (integrating the mask on a calibrated rotator).
- The proposed field of view scanning system allows to scan along two orthogonal axis. Its design, with four flat mirrors orthogonal to each other, is polarimetrically compensated and can also be used as a focusing mechanism.
- For those combinations of wavelengths in which one of them is proposed to be observed on a sequential mode, the white pupil optical principle can be implemented in order to reduce the pupil size before the camera mirror what would reduce the camera diameter for the simultaneous observation of all the wavelengths. In addition this reimaging of the pupil after being dispersed will facilitate the detectors reimaging systems design.
- The calculated values for the spectral resolving power fulfils the requirement except for 22300 Å, for which it is slightly lower. This can be improved by modifying the magnification of its reimaging system for a final slower beam.
- The throughput budget has been calculated for each wavelength considering the different subsystems, except for the detectors, and assuming protected silver coatings. The average obtained values are: 0.40 for VIS-I, 0.52 for VIS-II, 0.55 for IR-I and 0.55 for IR-II. These numbers represent the fraction of the light that reaches the image focal plane after the different reflections.
- The optical quality of the instrument is diffraction limited and has been evaluated for all the combinations of wavelengths associated to the science programmes.
- The spectrograph offers two modes of operation, spectroscopic and spectro-polarimetric, what offers a great versatility.
- The instrument verifies the telecentrism condition. The exit pupil is sent to infinity and the monochromatic beams illuminate homogeneously the detectors.

6.2 Future perspectives

- During the next months a scattered light study will be done for the prototype image slicer. This is an important point that has to be analysed before fabrication. This study will also be done for the image slicer of EST.
- It is interesting to implement the white pupil concept in order to satisfy the simultaneity for the combinations of wavelengths of every science programme. In addition, the detectors reimaging systems will be redesigned for the new beam sizes and magnifications.
- Another future task is the study of the tolerances of the spectrograph, including all the subsystems.
- The design of the spectrograph has considered the possibility to couple a polarimeter. The design of the polarimeter itself will be addressed in a near future.

7

Conclusiones y Perspectivas Futuras

A lo largo de los capítulos de esta tesis se ha descrito el diseño del espectrógrafo de campo integral para el Telescopio Solar Europeo, cumpliendo los requerimientos impuestos. Las expectativas para este instrumento son muy altas y compatibilizar todos los requerimientos y especificaciones ha resultado ser un duro proceso de diseño. Tanto los cálculos como el diseño de los diferentes subsistemas se han realizado progresivamente, como piezas de un puzzle que deben encajar perfectamente para convertir este espectrógrafo en una gran herramienta que nos permita estudiar todos aquellos aspectos del Sol que nos son aún desconocidos.

Debido a que algunos de los subsistemas son innovadores, como es el caso de la unidad de campo integral, se ha llevado a cabo un minucioso estudio tecnológico para investigar las unidades de campo integral que pueden ser consideradas como el estado del arte y proponer un concepto de vanguardia.

Del desarrollo del diseño pueden inferirse una serie de conclusiones que se detallan a continuación.

Asimismo, otros puntos de interés han ido surgiendo durante el diseño, los cuales se presentan más adelante. Algunos de ellos consisten en los siguientes pasos que deben estudiarse antes de la fabricación y otros, en cambio, son aspectos cuya implementación podría mejorar las prestaciones del instrumento.

7.1 Conclusiones

- Las mejores relaciones focales que satisfacen los diferentes requerimientos están comprendidas entre F/40 y F/50. El espectrógrafo puede iluminarse con un haz cuya relación focal pertenezca a dicho intervalo. En esta tesis se propone la relación focal F/40, debido a que ofrece la resolución espectral más alta para 22300 Å.

- La unidad de campo integral está basada en el concepto de image slicer. El image slicer de este instrumento, MuSICa, ha sido diseñado específicamente para él. Descompone un campo de visión bidimensional de 80 segundos de arco cuadrados y lo reorganiza en ocho rendijas de 200 segundos de arco de largo por 0.05 de ancho, minimizando el número de componentes ópticos (tres arrays de espejos). Es un sistema telecéntrico y, aunque en EST funcione como un sistema telecéntrico a la salida, se ha diseñado como un sistema doblemente telecéntrico, cuyo concepto puede ser aplicado tanto a espectrógrafos solares como nocturnos. A diferencia de otros image slicers mencionados en las referencias, los espejos que cortan el campo de entrada en rebanadas son planos en el caso de MuSICa. Esto hace posible que puedan combinarse con los espejos que dividen el campo de visión en ocho subcampos (los cuales también son planos), lo que optimiza la fracción de luz obtenida tras las diferenets reflecciones. Los otros dos arrays de espejos son esféricos y antisimétricos. Los rayos de cada configuración se superponen en la posición de pupila por lo que la máscara de pupila, utilizada para evitar la contribución de luz difusa, presenta una única abertura circular. La simetría del diseño presenta una serie de ventajas: facilita el proceso de fabricación, el alineado y reduce los costes. Otro aspecto importante a destacar es que la unidad de campo integral es compatible con los dos modos de operación del espectrógrafo: espectroscópico (en el que un campo de visión de 80 segundos de arco cuadrados es reorganizado en ocho rendijas de 200 segundos de arco de largo por 0.05 de ancho) y espectro-polarimétrico (en el que un campo de 40 segundos de arco de cuadrados es reorganizado en ocho rendijas de 100 segundos de arco de largo por 0.05 de ancho, las cuales son posteriormente duplicadas por el divisor de haz de un polarímetro).

- Los espejos colimadores y cámaras del image slicer se distribuyen en dos columnas de altura comparable a la de la rendija generada. Esto minimiza los ángulos de incidencia y mejora la calidad óptica, la cual está limitada por difracción.

- El espectrógrafo está precedido por un predispersor que actúa como prefiltro. En el plano focal imagen del predispersor una máscara selecciona la combinación de longitudes de onda en los órdenes apropiados. Las rendijas de la máscara son la entrada del espectrógrafo.

- Tanto el predispersor como el espectrógrafo son sistemas 1:1. La conversión de la relación focal del telescopio, F/50 a F/40, la realiza la unidad de campo integral con sus propios elementos ópticos, sin necesidad de añadir ninguna otra superficie extra. Para cada longitud de onda, un sistema de reimaginación en configuración pre-foco situado delante de cada detector convierte la relación focal del espectrógrafo a F/10.3 para longitudes de onda visibles y F/20.6 para las infrarrojas.

- Los predispersores y los espectrógrafos utilizan espejos parabólicos fuera de eje. En cada caso, tanto el colimador como la cámara son dos subaberturas que pertenecen a la misma parábola global, la cual está centrada en el eje óptico.

- La elección de redes comerciales ha implicado una restricción de diseño en términos de tamaño de pupila, dispersión lineal y eficiencia de la red. Para optimizar la eficiencia de la red se ha dividido el rango espectral en cuatro. Se proponen, por tanto, cuatro espectrógrafos (VIS-I, VIS-II, IR-I and IR-II) conceptualmente idénticos, los cuales pueden operar simultáneamente.

- Las máscaras del predispersor tienen ocho rendijas por longitud de onda. Las especificaciones y fabricación de las rendijas tiene que hacerse con alta precisión. Es muy importante la homogeneidad en los bordes de las rendijas, así como el paralelismo de las mismas, puesto que pequeñas modificaciones respecto a los valores especificados deteriorarían el espectro. Las tolerancias típicas en caso de utilizar fresadora es de ± 20 μm, lo que no es suficiente para rendijas muy finas como las de este espectrógrafo. Actualmente la mejor técnica para su fabricación es la fotodeposición. Por tanto, la precisión es crucial tanto para la fabricación como para el acabado y pulido de las máscaras.

- Debido a que las rendijas de la máscara son muy finas, todos los grados de libertad necesarios para el correcto posicionado de la máscara deben estar mecanizados. Éstos son traslación (utilizando un raíl) y orientación (integrando la máscara sobre un rotador calibrado).

- El sistema de barrido de campo propuesto permite hacer un barrido bidimensional. Su diseño con cuatro espejos planos ortogonales entre sí está compensado en polarización y puede ser también utilizado como mecanismo de enfoque.

- En los casos en los que proponemos que alguna de las longitudes de onda sea observada de modo secuencial, puede implementarse el principio óptico de pupila blanca lo que disminuiría el tamaño de la pupila delante del espejo de cámara y reduciría el diámetro necesario para la observación simultánea de todas las longitudes de onda. Esta reimaginación de la pupila después de dispersar el haz facilitaría el diseño de los sistemas de reimaginación de los detectores.

- Los valores calculados para el poder de resolución espectral satisfacen el requerimiento excepto para 22300 Å, para el que se obtiene un valor ligeramente inferior. Esto puede mejorarse modificando la magnificación de su sistema de reimaginación para tener una relación focal final mayor, correspondiente a un haz más lento.

- El presupuesto de transmisión de luz se ha calculado para cada longitud de onda considerando los diferentes subsistemas excepto los detectores y suponiendo plata protegida para el recubrimeinto de los espejos. Los valores medios obtenidos son: 0.40 para VIS-I, 0.52 para VIS-II, 0.55 para IR-I y 0.55 para IR-II. Estos números representan la fracción de luz medida en el plano focal imagen tras las diferentes reflexiones.

- La calidad óptica del instrumento está limitada por difracción y ha sido evaluada para todas las combinaciones de longitudes de onda asociadas a los programas científicos.

- El espectrógrafo ofrece dos modos de operación, espectroscópico y espectro-polarimétrico, lo que ofrece una gran versatilidad.

- El instrumento satisface la condición de telecentrismo. La pupila de salida se envía al infinito y los haces monocromáticos iluminan los detectores de un modo homogéneo.

7.2 Perspectivas futuras

- El estudio de luz difusa para el prototipo de image slicer se realizará durante los próximos meses. Éste es un punto importante que tiene que ser tenido en cuenta antes de la fabricación. El estudio de luz difusa se realizará también para el image slicer de EST.

- Es interesante implementar el concepto de pupila blanca para intentar satisfacer la simultaneidad de las combinaciones de longitudes de onda para cada programa científico. Los sistemas de reimaginación de los detectores serán rediseñados para este concepto considerando los nuevos tamaños de los haces y los aumentos.
- Otra tarea futura es el estudio de las tolerancias del espectrógrafo, incluyendo todos los subsistemas.
- El espectrógrafo está preparado para acoplar un polarímetro, cuyo diseño es otro de los próximos objetivos.

Bibliography

1988, Optics, optical systems and applications (Adam Hilger)

Abetti, G. 1957, THE SUN (The MacMillan Company)

Allington-Smith, J. 2007, in Science Perspectives for 3D Spectroscopy, ed. M. Kissler-Patig, J. R. Walsh, & M. M. Roth, 3–540

Allington-Smith, J., Dubbeldam, C. M., Content, R., et al. 2007, MNRAS, 376, 785

Allington-Smith, J., Gerssen, J., & Robertson, D. 2006, , 50, 235

Allington-Smith, J. R., Dubbeldam, C. M., Content, R., et al. 2004, in Society of Photo-Optical Instrumentation Engineers (SPIE) Conference Series, Vol. 5492, , 701–710

Alvarez-Herrero, A., Uribe-Patarroyo, N., García Parejo, P., et al. 2011, in Proc. SPIE. 8160, Polarization Science and Remote Sensing V 81600Y

Anusha, L. S., Nagendra, K. N., Bianda, M., et al. 2011a, ApJ, 737, 95

Anusha, L. S., Stenflo, J. O., Frisch, H., et al. 2011b, in Astronomical Society of the Pacific Conference Series, Vol. 437, Solar Polarization 6, ed. J. R. Kuhn, D. M. Harrington, H. Lin, S. V. Berdyugina, J. Trujillo-Bueno, S. L. Keil, & T. Rimmele, 57

Bacon, R., Accardo, M., Adjali, L., et al. 2010, in Society of Photo-Optical Instrumentation Engineers (SPIE) Conference Series, Vol. 7735, Society of Photo-Optical Instrumentation Engineers (SPIE) Conference Series

Bacon, R., Adam, G., Baranne, A., et al. 1995, A&AS, 113, 347

Ball, D. W. 1962, Field Guide to Spectroscopy (SPIE PRESS)

Baranne, A. 1988, in Very Large Telescopes and their Instrumentation, Vol. 2, 1195–1206

Baranne, A. 1991, Academie des Sciences Paris Comptes Rendus Serie B Sciences Physiques, 312, 1521

Barden, S. C., Arns, J. A., & Colburn, W. S. 1998, in Society of Photo-Optical Instrumentation Engineers (SPIE) Conference Series, Vol. 3355, , 866–876

Bettonvil, F., Cavaller, L., Collados, M., et al. 2011a, EST project internal documentation, IAC, RPTEST0001A-part1.pdf

Bettonvil, F., Cavaller, L., Collados, M., et al. 2011b, EST project internal documentation, IAC, RPTEST0001A-part2.pdf

Bettonvil, F., Cavaller, L., Collados, M., et al. 2011c, EST project internal documentation, IAC, RPTEST0001A-part1.pdf

Bianda, M., Ramelli, R., Stenflo, J. O., et al. 2011, in Astronomical Society of the Pacific Conference Series, Vol. 437, Solar Polarization 6, ed. J. R. Kuhn, D. M. Harrington, H. Lin, S. V. Berdyugina, J. Trujillo-Bueno, S. L. Keil, & T. Rimmele, 67

Born, M. & Wolf, E. 1999, Principles of Optics: Electromagnetic Theory of Propagation, Interference and Diffraction of Light (Cambridge University Press)

Brückner, G. 1963, Veroeffentlichungen der Universitaets-Sternwarte zu Goettingen, 7, 459

Calcines, A. 2011a, EST project internal documentation, IAC, RPTIAC73071B.doc

Calcines, A. 2011b, EST project internal documentation, IAC, RPTIAC73091B.doc

Calcines, A., Collados, M., Feller, A., et al. 2012a, in Society of Photo-Optical Instrumentation Engineers (SPIE) Conference Series, Vol. 8446,

Calcines, A., Collados, M., Feller, A., et al. 2012b, in Society of Photo-Optical Instrumentation Engineers (SPIE) Conference Series, Vol. 8446,

Calcines, A., Collados, M., Feller, A., et al. 2010a, in Society of Photo-Optical Instrumentation Engineers (SPIE) Conference Series, Vol. 7735,

Calcines, A., Collados, M., & López, R. L. 2010b, in Society of Photo-Optical Instrumentation Engineers (SPIE) Conference Series, Vol. 7735,

Calcines, A., Collados, M., & López, R. L. 2011, in Highlights of Spanish Astrophysics VI, ed. M. R. Zapatero Osorio, J. Gorgas, J. Maíz Apellániz, J. R. Pardo, & A. Gil de Paz, 660–664

Calcines, A., L. López, R., & Collados, M. 2012c, in Proc. SPIE 8446, Ground-based and Airborne Instrumentation for Astronomy IV, 844674

Casini, R. 2011a, in AAS/Solar Physics Division Abstracts #42, 805

Casini, R. 2011b, in AAS/Solar Physics Division Abstracts #42, 805

Casini, R. & Manso Sainz, R. 2005, ApJ, 624, 1025

Clark, D. M., Eikenberry, S. S., Raines, S. N., et al. 2013, MNRAS, 428, 2290

Collados, M. 2008, in European Solar Physics Meeting, Vol. 12, , 6

Collados, M., Bettonvil, F., Cavaller, L., et al. 2010, in Society of Photo-Optical Instrumentation Engineers (SPIE) Conference Series, Vol. 7733,

Collados, M., Calcines, A., Diaz, J. J., et al. 2008a, in Society of Photo-Optical Instrumentation Engineers (SPIE) Conference Series, Vol. 7012,

Collados, M., Calcines, A., Díaz, J. J., et al. 2008b, in Society of Photo-Optical Instrumentation Engineers (SPIE) Conference Series, Vol. 7014,

Collados, M., López, R., Páez, E., et al. 2012, Astronomische Nachrichten, 333, 872

Cuby, J.-G., Morris, S., Bryson, I., et al. 2008, in Society of Photo-Optical Instrumentation Engineers (SPIE) Conference Series, Vol. 7014,

Cuevas, S., Eikenberry, S. S., Sánchez, B., et al. 2008, in Society of Photo-Optical Instrumentation Engineers (SPIE) Conference Series, Vol. 7014,

de Wijn, A. G., Casini, R., Nelson, P. G., & Huang, P. 2012, in Society of Photo-Optical Instrumentation Engineers (SPIE) Conference Series, Vol. 8446,

del Toro Iniesta, J. 2003, Introduction to Spectropolarimetry (Cambridge University Press)

Dodson, H. W. & Hedeman, E. R. 1970, Sol. Phys., 13, 401

E.Collett. 1934, Field Guide to Polarization (SPIE PRESS)

Eikenberry, S., Andersen, D., Guzman, R., et al. 2006a, in Society of Photo-Optical Instrumentation Engineers (SPIE) Conference Series, Vol. 6269,

Eikenberry, S., Hinkle, K., Joyce, D., et al. 2006b, in Society of Photo-Optical Instrumentation Engineers (SPIE) Conference Series, Vol. 6271,

Eikenberry, S., Raines, S. N., Gruel, N., et al. 2006c, in Society of Photo-Optical Instrumentation Engineers (SPIE) Conference Series, Vol. 6269,

Elmore, D. F., Lites, B. W., Tomczyk, S., et al. 1992, in Society of Photo-Optical Instrumentation Engineers (SPIE) Conference Series, Vol. 1746, , 22–33

EST Science Group. 2011, EST project internal documentation, IAC, RPTEST20012B.doc

Fowles, G. R. 1968, Introduction to Modern Optics (Holt, Rinehart and Winston, Inc., New York)

Frazier, E. N. & Stenflo, J. O. 1978a, A&A, 70, 789

Frazier, E. N. & Stenflo, J. O. 1978b, A&A, 70, 789

Gaulme, P., Schmider, F.-X., Grec, C., et al. 2008, Planet. Space Sci., 56, 1335

Gelly, B. F. 2007, in Astronomical Society of the Pacific Conference Series, Vol. 368, The Physics of Chromospheric Plasmas, ed. P. Heinzel, I. Dorotovic, & R. J. Rutten, 593

Gelly, B. F. & THEMIS Team. 2007, Mem. Soc. Astron. Italiana, 78, 13

Glenn, P. E., Hull-Allen, C. G., Hoffman, J., et al. 2004, in Society of Photo-Optical Instrumentation Engineers (SPIE) Conference Series, Vol. 5492, , 1254–1263

Gorlova, N., Steinhauer, A., & Lada, E. 2010, ApJ, 716, 634

Gray, D. F. 1976, The observation and analysis of stellar photospheres, 2nd edn. (Cambridge University Press)

Guimond, S. & Elmore, D. 2004, SPIE oemagazine

H. Gross, H. Zügge, M. P. F. B. 2007, Handbook of Optical Systems (WILEY-VCH)

Haberreiter, M. & Finsterle, W. 2010, Sol. Phys., 263, 51

Harvey, J. 1971, Publications of the Astronomical Society of the Pacific, 83, 539

Harvey, K. L., Tang, F., & Gaizauskas, V. 1986, in NASA Conference Publication, Vol. 2442, , 359–363

Hecht. 2000, Optica, 3rd edn. (Addison Wesley)

Iserlohe, C., Tecza, M., Eisenhauer, F., et al. 2004, in Society of Photo-Optical Instrumentation Engineers (SPIE) Conference Series, Vol. 5492, , 1123–1134

Keller, C. U. 1992, Nature, 359, 307

Kiselman, D. 1993a, A&A, 275, 269

Kiselman, D. 1993b, A&A, 275, 269

Kiselman, D., Pereira, T. M. D., Gustafsson, B., et al. 2011, A&A, 535, A14

Lagg, A., Solanki, S. K., Riethmüller, T. L., et al. 2010, ApJ, 723, L164

Laurent, F., Henault, F., Renault, E., Bacon, R., & Dubois, J.-P. 2006, PASP, 118, 1564

Laurent, F., Renault, E., Kosmalski, J., et al. 2008, in Society of Photo-Optical Instrumentation Engineers (SPIE) Conference Series, Vol. 7018,

Lee, D., Haynes, R., Ren, D., & Allington-Smith, J. 2001, PASP, 113, 1406

Lin, H. 2003a, in Society of Photo-Optical Instrumentation Engineers (SPIE) Conference Series, Vol. 4853, , 215–222

Lin, H. 2003b, in Society of Photo-Optical Instrumentation Engineers (SPIE) Conference Series, Vol. 4853, , 215–222

Lin, H. 2012, in Society of Photo-Optical Instrumentation Engineers (SPIE) Conference Series, Vol. 8446,

Loewen, E. G. & Popov, E. 1997, Diffraction gratings and applications (Marcel Dekker, Inc.)

López, J. A., Bringas, V., Cuevas, S., et al. 2007, in Revista Mexicana de Astronomia y Astrofisica, vol. 27, Vol. 28, , 69–72

López Ariste, A., Le Men, C., & Gelly, B. 2011a, Contributions of the Astronomical Observatory Skalnate Pleso, 41, 99

López Ariste, A., Le Men, C., & Gelly, B. 2011b, Contributions of the Astronomical Observatory Skalnate Pleso, 41, 99

López Ariste, A., Le Men, C., Gelly, B., & Asensio Ramos, A. 2010, Astronomische Nachrichten, 331, 658

McMullin, J. P., Rimmele, T. R., Keil, S. L., et al. 2012, in Society of Photo-Optical Instrumentation Engineers (SPIE) Conference Series, Vol. 8444,

Mein, P. 1991, A&A, 248, 669

Mein, P. 1992, in ESA Special Publication, Vol. 344, , 153–155

Mein, P. 2002, A&A, 381, 271

Mein, P. & Rayrole, J. 1985, Vistas in Astronomy, 28, 567

Mein, P. & Rayrole, J. 1991, in Le Soleil - une Étoile et Son Domaine, ed. D. Benest & C. Froeschlé, 291–299

Nelson, P. G., Casini, R., de Wijn, A. G., & Knoelker, M. 2010, in Society of Photo-Optical Instrumentation Engineers (SPIE) Conference Series, Vol. 7735,

P. Léna, F. L. & Mignard, F. 1998, Observational Astrophysics (Springer)

Palmer, C. 2005, DIFFRACTION GRATING HANDBOOK OF NEWPORT, 6th edn. (Newport corporation)

Pereira, T. M. D., Asplund, M., & Kiselman, D. 2009a, VizieR Online Data Catalog, 350, 81403

Pereira, T. M. D., Kiselman, D., & Asplund, M. 2009b, VizieR Online Data Catalog, 350, 70417

Phillips, K. J. year, GUIDE TO THE SUN (Cambridge University press)

Powell, J. & Southall, C. 1918, Mirrors, prisms and lenses (The Macmillan company)

Rayrole, J. & Mein, P. 1993, in Astronomical Society of the Pacific Conference Series, Vol. 46, IAU Colloq. 141: The Magnetic and Velocity Fields of Solar Active Regions, ed. H. Zirin, G. Ai, & H. Wang, 170

Rimmele, T. R., Keil, S., McMullin, J., et al. 2012, IAU Special Session, 6

Rossi, B. 1957, Optics (Addison-Wesley Publishing Company, Inc., Reading Massachusetts)

Rueedi, I., Solanki, S. K., Livingston, W., & Harvey, J. 1995, A&AS, 113, 91

Sánchez-Capuchino, J. 2011, EST project internal documentation, IAC, RP-TIAC41021A.pdf

Sánchez-Capuchino, J., Collados, M., Soltau, D., et al. 2010, in Society of Photo-Optical Instrumentation Engineers (SPIE) Conference Series, Vol. 7733,

Sayède, F., Mein, P., Amans, J.-P., & Moity, J. 2010, in Society of Photo-Optical Instrumentation Engineers (SPIE) Conference Series, Vol. 7735,

Scharmer, G., Henriques, V., Hillberg, T., et al. 2008, in European Solar Physics Meeting, Vol. 12, , 2

Schmelz, J. T. & Brown, J. C. 1992, The Sun:A Laboratory for Astrophysics (Kluwer Academis Publisher)

Schmidt, W., Beck, C., Denker, C., Soltau, D., & Volkmer, R. 2008, in European Solar Physics Meeting, Vol. 12, , 2

Schmidt, W., Beck, C., Kentischer, T., Elmore, D., & Lites, B. 2003, Astronomische Nachrichten, 324, 300

Schmidt, W., Kentischer, T. J., Bruls, J., & Lites, B. W. 2001, in Astronomical Society of the Pacific Conference Series, Vol. 236, Advanced Solar Polarimetry – Theory, Observation, and Instrumentation, ed. M. Sigwarth, 49

Schmidt, W., von der Lühe, O., Volkmer, R., et al. 2012, ArXiv e-prints

Schroeder, D. J. 1987, Astronomical Optics (Academic Press, INC.)

Skumanich, A., Lites, B. W., Martinez Pillet, V., & Seagraves, P. 1997, ApJS, 110, 357

Slyusarev, G. G. 1984, Aberration and Optical Design Theory (Adam Hilger)

Socas-Navarro, H., Elmore, D., & Lites, W. 2004, ArXiv Astrophysics e-prints

Socas-Navarro, H., Elmore, D., Pietarila, A., et al. 2006, Sol. Phys., 235, 55

Soltau, D., Berkefeld, T., Sánchez Capuchino, J., et al. 2010, in Society of Photo-Optical Instrumentation Engineers (SPIE) Conference Series, Vol. 7736,

Staiger, J. 2011, A&A, 535, A83

Steiner, O. 2000, Chromosphere: Magnetic Canopy, ed. P. Murdin

Stenflo, J. O. 1982, Sol. Phys., 80, 209

Stenflo, J. O., Gandorfer, A., Holzreuter, R., et al. 2002a, A&A, 389, 314

Stenflo, J. O., Gandorfer, A., Holzreuter, R., et al. 2002b, A&A, 389, 314

Stern, D., Willis, J., Ledlow, M., et al. 2002, in Bulletin of the American Astronomical Society, Vol. 201, American Astronomical Society Meeting Abstracts, 603

T. Roca Cortès, F. S. 1996, The Structure of the Sun (Cambridge University Press)

Tecza, M., Eisenhauer, F., Iserlohe, C., et al. 2003, in Society of Photo-Optical Instrumentation Engineers (SPIE) Conference Series, Vol. 4842, , 375–383

Tecza, M., Thatte, N. A., Eisenhauer, F., et al. 2000, in Society of Photo-Optical Instrumentation Engineers (SPIE) Conference Series, Vol. 4008, , 1344–1350

Trujillo-Bueno, J., Moreno-Insertis, F., & Sánchez, F. 2000, Astrophysical Spectropolarimetry (Cambridge University Press)

Tull, R. G., MacQueen, P. J., Sneden, C., & Lambert, D. L. 1995, PASP, 107, 251

Vandenberg, D. A. 1992, ApJ, 391, 685

Vives, S., Prieto, E., Salaun, Y., & Godefroy, P. 2008, in Society of Photo-Optical Instrumentation Engineers (SPIE) Conference Series, Vol. 7018,

Volkmer, R. 2008, in European Solar Physics Meeting, Vol. 12, , 6

Volkmer, R., von der Lühe, O., Denker, C., et al. 2010, in Society of Photo-Optical Instrumentation Engineers (SPIE) Conference Series, Vol. 7733,

Volkmer, R., von der Lühe, O., Kneer, F., et al. 2007, in Modern solar facilities - advanced solar science, ed. F. Kneer, K. G. Puschmann, & A. D. Wittmann, 39

Wright, G., Ivison, R., Hastings, P., et al. 2002, in Scientific Drivers for ESO Future VLT/VLTI Instrumentation, ed. J. Bergeron & G. Monnet, 128

Yamashita, Y. & Okida, K. 1990, Report of the National Astronomical Observatory of Japan, 1, 23

Zuccarello, F. 2011, in IAU Symposium, Vol. 274, , 310–313

List of Figures

List of Tables

Agradecimientos

He dejado para el final una de las partes más importantes: dar las gracias a todas las personas que han hecho posible que esta tesis sea hoy una realidad. Los tres primeros nombres que me vienen a la cabeza corresponden a las personas que me dieron la primera oportunidad en el apasionante mundo de la instrumentación. Me ofrecieron un proyecto de fin de carrera que resultó ser el primer peldaño de una escalera que he ido subiendo con esfuerzo y felicidad y en la que, afortunadamente, me queda aún un largo camino por recorrer. Esos tres nombres son: Roberto López, Manolo Collados y Ramón García López. Muchísimas gracias. Cada día de todos estos años en los que he disfrutado tanto con el trabajo les he tenido presentes y nunca olvidaré que su ayuda lo ha hecho posible.

Me gustaría agradecer especialmente a Roberto López todo lo que me ha enseñado. Leí en alguna parte que "quien te regala su tiempo te está dando algo muy valioso que nunca recuperará ". Hoy quisiera darte las gracias por emplear una gran parte de tu tiempo en mi formación, por creer en mis posibilidades, por tu paciencia y por no rendirte, por muy duras que se volviesen las conversaciones sobre pupilas. También por alentar mis ilusiones de diseñar instrumentos de vanguardia, de creer que todo es posible y que el esfuerzo siempre vale la pena. Me ha encantado encontrar en el camino a alguien con mis mismas ganas de imaginar instrumentos que vayan un paso más allá, que no vea barreras que el trabajo y el esfuerzo no puedan derribar y que siempre tenga ganas de aprender algo nuevo. Has sido y eres un gran apoyo. Para mí es un orgullo y un privilegio poder aprender de ti. Si esta tesis es hoy una realidad, en gran parte es por ti. Todo lo que te agradezca será poco, pero comencemos con "muchísimas gracias ".

Quiero dar las gracias a mi director de tesis: Manolo Collados. En estos años has sido: mi profesor, mi director de proyecto de fin de carrera, I.P. de diferentes proyectos, mi director de tesis... siempre has estado ahí. Muchas gracias por enseñarme tantas cosas. Yo siempre te veré como mi profesor de instrumentación. Un profesor tan bueno, con la capacidad de hacer que te encante lo que te está explicando que, desde la primera clase de instrumentación astronómica en la facultad, supe que eso era exactamente a lo que me quería dedicar en mi vida. Y, tras esa primera clase, ya no había vuelta atrás. Estoy muy orgullosa de que seas mi director. Te agradezco tu voto de confianza contando conmigo para tus diferentes proyectos: GREGOR, el primer instrumento con el que he trabajado y al que siempre tendré un cariño especial y, sobretodo, por dejarme formar parte de EST. Por darme la responsabilidad del diseño de un instrumento como el que presentamos en esta tesis, a pesar de mi edad y mi poca experiencia. Gracias por creer que, a pesar de todo, lo conseguiríamos. Éste es el primer instrumento que diseño y me ha encantado la experiencia. Espero que en el futuro, esté donde esté, sigas contando conmigo para tus próximos proyectos. Desde luego mi ayuda y mi apoyo siempre lo tendrás.

A Ramón García López, coordinador del área de instrumentación del IAC, por permitirme desarrollar mi tesis en las instalaciones del área y por dedicar su esfuerzo a apoyar proyectos instrumentales como EST.

Durante el proceso de diseño de este instrumento he conocido a gente maravillosa de la que he aprendido mucho y que, de una manera u otra, han aportado algo al diseño. Una de esas personas es Steve Eikenberry, al que quiero dar las gracias por tener siempre algún momento para resolverme alguna duda y para hablar sobre image slicers. También por presentarme a grandes personas, como Salvador Cuevas, al que agradezco sus explicaciones sobre IFUs cuando yo aún estaba empezando y las interesantes conversaciones sobre ellas que hemos seguido teniendo a lo largo de los años. Gracias también a Florence Laurent, por ofrecerme siempre su ayuda y por el gran trabajo que ha hecho que nos sirve de referencia a todos los demás.

A Bernard Gelly y Claude Le Mèn, muchas gracias por permitirnos realizar pruebas en THEMIS, por toda la ayuda que me han ofrecido y todo lo que me han enseñado. A Claude, gracias por el tiempo que has dedicado a explicarme la óptica que no se cuenta en los libros. He aprendido mucho de ti.

A Valentín Martínez Pillet y a José Carlos del Toro por el apoyo que he recibido de ustedes y los ánimos que me han dado después de cada charla. A Valentín le agradezco además haber aceptado ser el revisor de esta tesis. Y a José Carlos le debo la idea de espectroscopía 5D que, con su permiso, he tomado prestada para la explicación de mi espectrógrafo. A ambos, gracias por ser parte de mi tribunal de tesis.

Quisiera agradecerle a José Luis Rasilla, mi jefe de Departamento de Óptica, las facilidades que me ha dado para que termine mi tesis y el apoyo que me ha ofrecido, muchas gracias. Gracias también a Jorge Sánchez Capuchino-Revuelta, con el que he tenido el placer de trabajar en EST. Muchas gracias por animarme en los momentos más difíciles y por ser tan buen compañero.

Gracias a todos mis compañeros de proyecto, a los que he tenido el placer de conocer y de los que he aprendido mucho. Sobretodo a mis compañeros de paquete de trabajo, con los que he compartido más tiempo y donde incluyo también a Christine Grivel. A Elvio Hernández Suárez, ingeniero mecánico de GREGOR y EST, gracias por los diseños 3D mecánicos que he añadido en la tesis. A otros cuyo afecto hace que les tenga especial cariño, como Ilaria Ermolli, Marco Stangalini o Martina Cocciolo. A todos ellos, incluido Fabio Giannattasio, muchísimas gracias.

Quiero agradecer a todas las personas que confiaron en mí y me ofrecieron una oportunidad, como son: Ismael Pérez Fournon, Begoña García o John Beckman. Gracias. Y a todos los miembros de mi tribunal por formar parte de este momento.

Me gustaría dedicar unas palabras de agradecimiento a mis compañeros de universidad. A los de primer año y, especialmente, a los de especialidad, que se convirtieron en mi familia en Tenerife: Christoph, Dan, Tobías, Julio, Elisa, Yamil, Adal, Jeza, Kike, Aythami, Héctor, entre otros, gracias por compartir tantos buenos momentos y por hacer que los tiempos duros fuesen más agradables. También a Juanjo Piqueras, compañero de beca de verano y buen amigo.

En último lugar pero no por ello menos importante, agradecer a mi familia, especialmente a mis padres y mi hermano por enseñarme a luchar por los sueños y por los valores que me han inculcado. A Lucho por alegrarnos la vida. A mis abuelos, con todo mi corazón, a los que echo tantísimo de menos, por haberme enseñado a tener una actitud positiva ante la vida. Y a mis abuelas, especialmente a mi abuela Carmencita, por interesarse por mi trabajo y por la Astronomía.

Echo la vista atrás y todos estos años están llenos de recuerdos de todos ustedes. Muchísimas gracias por ser parte de algo tan importante para mí y por ayudarme a conseguirlo. “Nadie dijo nunca que sería fácil, pero estaba segura de que merecería la pena”.